The Strontium Optical Lattice Clock: Optical Spectroscopy with Sub-Hertz Accuracy

by

Andrew D. Ludlow

B.S. Physics, Brigham Young University, 2002

A thesis submitted to the

Faculty of the Graduate School of the

University of Colorado in partial fulfillment

of the requirements for the degree of

Doctor of Philosophy

Department of Physics

2008

This thesis entitled:
The Strontium Optical Lattice Clock: Optical Spectroscopy with Sub-Hertz Accuracy
written by Andrew D. Ludlow
has been approved for the Department of Physics

Jun Ye

Leo Hollberg

Date

The final copy of this thesis has been examined by the signatories, and we find that both the content and the form meet acceptable presentation standards of scholarly work in the above mentioned discipline.

Ludlow, Andrew D. (Ph.D., Physics)

The Strontium Optical Lattice Clock: Optical Spectroscopy with Sub-Hertz Accuracy

Thesis directed by Assoc. Prof. Adjoint Jun Ye

One of the most well-developed applications of coherent interaction with atoms is atomic frequency standards and clocks. Atomic clocks find significant roles in a number of scientific and technological settings. State-of-the-art, laser-cooled, Cs-fountain microwave clocks have demonstrated impressive frequency measurement accuracy, with fractional uncertainties below the 10^{-15} level. On the other hand, frequency standards based on optical transitions have made substantial steps forward over the last decade, benefiting from their high operational frequencies. An interesting approach to such an optical standard uses atomic strontium confined in an optical lattice. The tight atomic confinement allows for nearly complete elimination of Doppler and recoil-related effects which can otherwise trouble the precise atomic interrogation. At the same time, the optical lattice is designed to equally perturb the two electronic clock states so that the confinement introduces a net zero shift of the natural transition frequency. This thesis describes the design and realization of an optical frequency standard using ^{87}Sr confined in a 1-D optical lattice. Techniques for atomic manipulation and control are described, including two-stage laser cooling, proper design of atomic confinement in a lattice potential, and optical pumping techniques. With the development of an ultra-stable coherent laser light source, atomic spectral linewidths of the optical clock transition are observed below 2 Hz. High accuracy spectroscopy of the clock transition is carried out utilizing a femtosecond frequency comb referenced to the NIST-F1 Cs fountain. To explore the performance of an improved, spin-polarized Sr standard, a coherent optical phase transfer link is established between JILA and NIST. This enables remote comparison of the Sr standard against optical standards at NIST, such as the cold Ca standard.

The high frequency stability of a Sr-Ca comparison (3×10^{-16} at 200 s) is used to make measurements of Sr transition frequency shifts at the fractional frequency level below 10^{-16}. These systematic shifts are discussed in detail, resulting in a total uncertainty of the Sr clock frequency at 1.5×10^{-16}, smaller than that of the best Cs standards of the time. Considerations relevant for future performance improvements are also discussed.

Dedication

to Sharah,

we did it Together

Acknowledgements

Acknowledging in one written space all of the people who played an important role in the training and successful completion of my Ph.D. dissertation research is perhaps the impossible task. My interest in science was cultivated early on by individuals like Mr. Woodruff, my high school chemistry teacher. At the collegiate level, I had the opportunity to work with Scott Bergeson and Mark Nelson at BYU and here had my first in-depth exposure to experimental physics in the laboratory. Through the stimulating research experiences in Scott's lab and with an interest and fascination in atomic and optical physics, I began graduate school at the University of Colorado. I benefitted greatly from my involvement in the Optical Science and Engineering program, which gave me the opportunity to see up-close different research settings (academia, national lab, and industry) and to get to know and work with talented scientists like Jun Ye, Chris Oates, Leo Hollberg, Charles Garvin, Charley Hale, Ross Hartman, Dana Anderson, and Victor Bright.

I settled into Jun's lab and while working on the strontium project, have had the great pleasure of working and developing friendships with many very gifted scientists. Xinye Xu, Tom Loftus, Tetsuya Ido, Tanya Zelevinsky, and Gretchen Campbell were postdocs on the strontium project at various times over the years. Each one has made critical contributions to the evolution of the strontium experiment. Perhaps even more significantly to me personally, they have taught, guided, and worked alongside me and a good part of my graduate education has come through interaction with them. Marty

Boyd and I were graduate students working together on the Sr experiment for "the duration". Our research relationship has proven that two minds focused on a common goal can surely accomplish more than could be done separately. Sebastian Blatt has been an invaluable 'wiz' on many aspects of the Sr experiment and I look forward to seeing the strontium team's continued research in subsequent years. Seth Foreman has been much more than the frequency comb master and played an important role in various aspects of the strontium experiment, particularly remote frequency transfer and laser phase noise measurements across the optical spectrum.

Mike Martin and Marcio de Miranda have done a great job continuing that work and enabling the amazingly precise optical frequency measurements in our laboratory. Benefitting greatly from his expertise, it was largely through working with Mark Notcutt that I got my feet wet in very-high-stabilization of lasers. I enjoyed many stimulating discussions with Thomas Zanon-Willette, who helped open the beauty of three-level atomic systems to me. I've genuinely enjoyed interaction with Jan Thomsen, Xueren Huang, and Long Sheng Ma during their visits to JILA. Our work has benefitted from many others in the lab, Kevin Holman, Jason Jones, Eric and Darren Hudson, Matt Stowe, Kevin Moll, Mike Thorpe, Adela Marian, Brian Sawyer, Avi Pe'er and Dylan Yost to name a few.

I give much thanks to my advisor, Jun Ye. There are innumerable positive things I could say of him, his talent as a physicist, and his leadership in the lab. I have benefitted immensely from the environment he cultivates and the opportunities and experiences in his lab. I deeply respect him and am a better scientist and person for having worked under his tutelage. He has continued on the tradition of excellence from the lab's founder Jan Hall. It is a special opportunity to interact with Jan, ask a question, and open up the floodgates of his vast expertise. It was Jan and Alan Gallagher who collaborated on the original Sr experiment in JILA, and I benefitted greatly from continued interaction with both of them.

JILA is a special place, and there are many reasons for its success as a research institute. Among these, the electronics and machine shops play a key role. I make particular mention of fruitful interactions I had with Terry Brown in the JILA electronics shop.

It has been the combined efforts of the strontium team which made possible the exciting exploration into the strontium atom, a part of which I could play a role. Furthermore, our collaboration with other scientists outside the strontium team has made many of our efforts possible, including some of the results described in this thesis. Among these are: P. Naidon, P. Julienne, and R. Ciurylo (ultracold atomic collisions, including density shifts and photoassociation), J. Stalnaker, S. Diddams, and J. Bergquist (coherent optical carrier transfer), T. Fortier, J. Stalnaker, S. Diddams, Y. le Coq, Z. W. Barber, N. Poli, N. Lemke, K. Beck, and C. Oates (remote optical clock evaluation with NIST), T. Parker, S. Jefferts, and T. Heavner (NIST H-maser and Cs fountain measurements), E. Arimondo (three-level interactions in strontium), and C. Greene (theoretical work and guidance).

I reserve a very special acknowledgement to my family. Through my parents, Alex and Clyda Ludlow, I learned the value of education and the work ethic to pursue it. They taught by example the most important principles and attributes, and I recognize their enormous role in who I am and what I may become. My parents-in-law, Steve and Judy Smith, provided constant love and support to me and my family during the laborious years of school. And most importantly, it is together with my dear wife Sharah and my children Rachael, David, and Evan that I have travelled this road. They have been my strongest support, my most meaningful inspiration, and the origin of my most precious moments. The effort which has culminated in the pages of this thesis has been a worthwhile endeavor. But its most important characteristic is that it was done together with them.

Contents

Chapter

1 Introduction: Atomic Clocks and Strontium 1

1.1 Dimensions and Standards 1

1.2 Atomic Frequency Standards 3

1.3 Optical Frequency Standards 6

1.4 Strontium: Electronic Structure 9

1.5 The Need for Cold Atoms 14

1.6 Precision Timing Applications 15

1.7 Thesis At-a-Glance 16

2 Atomic Manipulation and Control 18

2.1 Laser Cooling: Basic Concepts 18

2.2 Laser cooling strontium: $^1S_0$-$^1P_1$ MOT 23

2.2.1 Laser cooling properties of $^1S_0$-$^1P_1$ MOT 23

2.2.2 Experimental details of the $^1S_0$-$^1P_1$ MOT 29

2.3 Laser cooling strontium: Narrow line laser cooling in the $^1S_0$-$^3P_1$ MOT 36

2.3.1 Narrow line laser cooling dynamics 36

2.3.2 Experimental details of the $^1S_0$-$^3P_1$ MOT 45

2.4 Laser cooling and trapping ^{87}Sr 49

2.4.1 The $^1S_0$-$^1P_1$ MOT 49

2.4.2 The $^1S_0$-$^3P_1$ MOT 52
2.5 Interrogation of Tightly Confined Atoms 56
2.5.1 Free Space Atom Interrogation 56
2.5.2 Confinement in a Harmonic Potential 58
2.5.3 Uniform Confinement Regime 66
2.5.4 Well resolved sideband regime 67
2.5.5 Lamb-Dicke regime 70
2.6 Atomic Confinement with a Far-Detuned Optical Wave 72
2.6.1 Dipole Potential 72
2.6.2 Dipole Polarizability 74
2.6.3 1-D Lattice Confinement 85
2.6.4 Benefits of 1-D Lattice Confinement 88
2.6.5 Further Details of 1-D Lattice Confinement 90
2.7 State Preparation via Optical Pumping: Nuclear spin polarization . . . 96

3 Coherent Light-Matter Interaction: Hz level spectral linewidths in the optical domain 99
3.1 The Need for Atomic and Optical Coherence 99
3.2 Atomic Coherence 100
3.3 Optical Coherence: Laser Frequency and Phase Stabilization 102
3.3.1 Laser Stabilization Design Considerations 103
3.3.2 Sub-Hz Sr clock laser 113
3.4 Atomic spectra of the optical clock transition with Hz level linewidth . . 121
3.4.1 Experimental Setup 121
3.4.2 Spectra 124
3.4.3 Sideband structure 129

4 Development of the Sr Optical Standard: High Accuracy Spectroscopy 133

4.1 Counting optical frequencies: the fs frequency comb 133

4.2 Frequency reference 137

4.2.1 Microwave fiber transfer 138

4.3 Evaluation of the Frequency Shifts and their Uncertainty 140

4.4 Absolute frequency measurement of the $^1S_0$-$^3P_0$ transition 147

5 The Strontium Optical Frequency Standard at 10^{-16} Uncertainty: Remote Optical Comparison of Optical Clocks 150

5.1 Design Improvements in the Sr Optical Standard 151

5.1.1 Atomic Polarization 151

5.1.2 Laser Stabilization to the Atomic Transition 153

5.1.3 Other System Improvements 156

5.2 Optical Carrier Remote Transfer 160

5.3 Stability Evaluation of the Sr Optical Frequency Standard 165

5.4 Accuracy Evaluation of the Sr Optical Frequency Standard 176

5.4.1 Measurement Description 176

5.4.2 Lattice AC Stark shift 178

5.4.3 1^{st}- and 2^{nd}- order Zeeman shifts 186

5.4.4 Density shift 188

5.4.5 Blackbody radiation induced Stark shift 202

5.4.6 Probe laser induced AC Stark shift 206

5.4.7 Line-pulling 207

5.4.8 Servo Error 207

5.4.9 Other residual 1^{st}-order Doppler shifts 208

5.4.10 2^{nd}-order Doppler shift 210

5.4.11 Other effects 210

5.4.12 Uncertainty Summary 211
5.5 Absolute Frequency Measurement 213
5.6 Outlook 215

Bibliography 217

Tables

Table

1.1 Sr transition parameters 11

1.2 The natural abundances of strontium isotopes 13

2.1 Transition parameters used to calculate the atomic polarizability of the Sr clock states 80

4.1 Measurement 1 systematic uncertainties 144

4.2 Measurement 2 systematic uncertainties 146

5.1 Dick effect limited instability of the JILA Sr standard for various values of experimental cycle time T_c and transition probing time t_p 174

5.2 Experimentally measured values of λ_{magic} 184

5.3 Systematic shifts and their uncertainties for the ^{87}Sr $^1S_0$-$^3P_0$ clock transition (2007) 212

Figures

Figure

1.1 Length measurement precision using different rulers 8

1.2 Term diagram for ^{88}Sr 10

2.1 Abbreviated term diagram for $^1S_0$-$^1P_1$ MOT 24

2.2 Two-level steady state excitation and saturation 26

2.3 Spatial confinement in a $J = 0$ - $J = 1$ MOT 29

2.4 Experimental apparatus 30

2.5 $^1S_0$-$^3P_1$ MOT as a function of detuning 39

2.6 $^1S_0$-$^3P_1$ MOT as a function of intensity 40

2.7 $^1S_0$-$^3P_1$ MOT temperature 42

2.8 $^1S_0$-$^3P_1$ MOT timing diagram 48

2.9 ^{87}Sr energy level diagram 50

2.10 Laser cooling ^{87}Sr on the $^1S_0$-$^3P_1$ transition 53

2.11 Absorption spectrum of a confined atom 62

2.12 Absorption spectrum of an atomic ensemble from weak to strong confinement 69

2.13 Sr clock transition atomic polarizability 79

2.14 Schematic of the optical layout for the 1-D optical lattice 86

2.15 Atomic confinement energy band structure in the optical lattice 91

2.16 Rabi frequency for pure electronic excitation from a given motional state 94

2.17 Optical pumping used for nuclear spin polarization state preparation . . 98

3.1 Stable laser-cavity system 114

3.2 Stable-cavity field ringdown 116

3.3 Sub-Hz laser linewidth 118

3.4 Clock laser instability and frequency noise 119

3.5 Clock laser distribution 122

3.6 Spectra of the $^1S_0$-$^3P_0$ clock transition 125

3.7 Ultra-narrow spectra of the $^1S_0$-$^3P_0$ clock transition 127

3.8 Motional sideband spectra 130

4.1 The frequency comb 134

4.2 Remote microwave frequency transfer schematic 139

4.3 Remote microwave frequency transfer results 141

4.4 Measurement 1 clock transition uncertainty evaluation (2005) 142

4.5 Measurement 2 clock transition uncertainty evaluation (2006) 145

4.6 Measurement 1 and 2 absolute frequency measurements 148

5.1 Laser stabilization to the clock transition with a spin-polarized atomic sample 154

5.2 Phase coherent optical carrier transfer schematic 161

5.3 Phase coherent optical carrier transfer performance 163

5.4 Sr frequency counting with both optical and microwave references . . . 166

5.5 Sr frequency counting with both optical and microwave references . . . 167

5.6 Instability of the Sr frequency standard 173

5.7 Experimental setup for Sr-Ca remote measurements 177

5.8 Lattice AC Stark shift sensitivity of the clock transition 183

5.9 First and second order Zeeman shift sensitivity of the clock transition . 187

5.10 Density shift sensitivity of the clock transition 190

5.11 Atomic excitation as a function of time 194

5.12 Density shift sensitivity as a function of $^1S_0$ population 196

5.13 Improving the blackbody shift uncertainty: the blackbody chamber . . . 205

5.14 Absolute frequency measurements of the ^{87}Sr clock transition 214

Chapter 1

Introduction: Atomic Clocks and Strontium

1.1 Dimensions and Standards

As we model the world around us, we neatly categorize the fundamental properties of matter into dimensions. Some dimensions are so common in everyday experience that most people are accustomed to intuitively perceiving the outside world using these dimensional basis sets. Among these are length (in all three spatial directions), time, and mass. Others like electric charge, intrinsic spin, quark flavor, and quark color are less well-known to the general public, but are predominantly accepted as basic quantities. Still others, like additional spacetime dimensions included in string theories attempting to unify gravity with the other fundamental interactions, have been proposed and are currently being scrutinized by the scientific community.

To be fully useful, any dimension must be sufficiently characterized or defined. This is equivalent to having a well-defined unit for each dimension. Many systems of units exist, and different fields of study frequently have their own natural system of units. The International System of Units (SI) has emerged as the most widely used system of units, both internationally and scientifically. The SI unit system employs seven fundamental base units from which many other derived units originate. The seven SI base units are: meter (length), second (time), kilogram (mass), ampere (electric current), kelvin (thermodynamic temperature), mole (quantity), and candela (luminous intensity). The quantitative utility of the SI system rests on how well-defined each base

unit is. From a practical perspective, the job of providing this definition ultimately lies with a primary standard. A standard is some type of physical exemplar which realizes the definition of a dimensional unit. As the name denotes, a primary standard is usually the highest performance standard to which the secondary standards refer back. As an example, the current primary standard for the SI kilogram is given by the international prototype kilogram (IPK). The IPK is a cylindrically shaped piece of platinum-iridium alloy which is maintained by the International Bureau of Weights and Measures (referred to as BIPM, which is abbreviated from its French name, this institution provides uniformity and traceability to the SI system). A piece of material is designated to have a mass of one kilogram when it has the same measurable mass as the IPK.

Several basic figures of merit relating to any standard can be highlighted by considering the case of the IPK standard of the kilogram. The first such figure of merit is the stability of the standard - does the standard provide a fixed definition of the unit or does it change. For example, by comparing the IPK mass to similarly constructed and cared-for replicas of the IPK, it has been found that the IPK mass changes over time due to airborne contamination and cleaning processes [1, 2]. For this reason, a standard born of nature and unsusceptible to mass fluctuations is preferred over man-made artifacts such as the IPK. For example, the mass of a single unbound electron could, in principle, serve as the definition of mass. In this case, the mass definition would be expected to be constant (highly stable) over time. Technical limitations have impeded the development of a natural standard realizing this kind of fundamental mass definition (the kilogram remains the last unit defined by an artificial prototype). However in 2005, motivated in part by the potential improvement in stability, the International Committee for Weights and Measures (abbreviated CIPM, which is the supervisory committee to the BIPM) recommended that the kilogram be defined in terms of fundamental natural constants.

Another figure of merit is related to how the standard changes under different

environments. For example, how does temperature and humidity affect the mass of the IPK, and how well controlled can these environmental parameters be maintained during storage and usage. Standards which have small and well-understood sensitivity to their environment can realize the unit definition more uniformly as the environment changes through space and time. Furthermore, the standard's utility is limited by the technology and science of the relevant measurement itself. If we find a chunk of steel which has the same measurable mass as the IPK, to how many digits can we trust the measurement that they are, in fact, the same mass. It is thus useful to choose a standard for which the related measurement science and technology is well-understood. Each of these considerations relates to what degree of accuracy the standard realizes the definition of the unit. (Note that for the unique case of the IPK, one can argue that because the IPK is both the standard and the actual definition of the SI kilogram, environmental sensitivity is not important for its accuracy, since they change together.)

Finally, two similar standards ideally provide the same definition when compared to each other. This figure of merit is related to the properties which determine the standard's accuracy and is typically referred to as reproducibility. A proper choice of standard, therefore, includes consideration of the standard's stability, accuracy, and reproducibility. With these in mind, we now consider the standard of time, the most well-defined unit in the SI system.

1.2 Atomic Frequency Standards

In practice, time is and has been measured in units of periodic events which repeat themselves. The earth's rotation around the sun or the earth's rotation around its own axis has served as an astronomical standard for which hours, days, and years have been measured in many civilizations. The pendulum clock uses gears which effectively counts the periodic swinging back and forth of a physical pendulum, and in so doing has provided timekeeping for centuries. Since the frequency of these periodic devices

is related trivially to the period (frequency is the inverse of the period), the role of a time (interval) standard is essentially equivalent to that of a frequency standard. As physics has evolved from the time of Newton, so did our understanding of how these standards quantitatively operated. Experience and improved physical models revealed how these standards change over time and under different conditions, dictating their limited accuracy and stability. This led to the search for other physical processes that nature provides which would better suit the role of a time/frequency standard. Early understanding of atomic behavior in the nineteenth century and development of quantum mechanics in the twentieth century revealed that atomic systems can be very well suited for just such a task [3]. Electronic excitation of an atom, acting as nature's pendulum, resonates at the same, well-defined frequency and does so largely insensitive to the environment around it. In addition, the excitation energy required to observe this process is low enough (microwave and optical frequencies) for the laboratory environment. It did not take long (decades) after quantum mechanic's advent that atomic systems emerged as the natural choice for frequency standards and ultimately as the definition of the SI base unit of the second.

For most of their half-century history, frequency standards based on atomic cesium have provided the performance best suited for a primary frequency standard. For this reason, since 1967, the SI second has been defined as follows: "The second is the duration of 9 192 631 770 periods of the radiation corresponding to the transition between the two hyperfine levels of the cesium 133 atom" [4]. To illuminate the basic operation of an atomic frequency standard, I describe the Cs standard in outline detail. The ground state of Cs has two hyperfine states $F = 3$ and $F = 4$ (F denotes the total angular momentum of the state, given by the vector sum of the electronic and nuclear angular momentum terms, I and J respectively). When Cs atoms are illuminated by radiation resonant with exactly the energy difference between the two states $F = 3$ $m_F = 0$ and $F = 4$ $m_F = 0$ (m_F, the magnetic quantum number, denotes the

projection of F along the quantization axis), a weak electronic transition is excited. As a consequence, electronic population is moved between the hyperfine states and the radiation is absorbed and then re-emitted by the atomic sample. By detecting electronic population movement or radiation intensity as a function of radiation frequency, the radiation frequency can be stabilized or locked to the resonant frequency of the atomic excitation. This is the approach of a passive frequency standard, where the radiation is generated externally but stabilized through spectroscopy of the atomic sample. The frequency of the atomic resonance is $f_{Cs} = 9.192631770$ GHz (by definition). By counting 9,192,631,770 periods of the radiation, a time interval equal to one second is measured.

One of the critical properties of the Cs hyperfine transition frequency is its small sensitivity to environmental perturbations which shift its frequency. However, since no standard is completely insensitive to perturbation by its environment, it is important to specify under what conditions the Cs standard must operate to properly define the SI second. A natural choice is to specify a completely ideal environment, free of any perturbations. By controlling the environment as close to ideal as possible, and by quantitatively evaluating the effect of excursions from the ideal environment, a determination can be made of the uncertainty with which the Cs standard realizes the unperturbed, true definition of the SI second. For the operating frequency of the Cs standard f_{Cs}, this uncertainty can be smaller than 10 μHz. Expressed as a fraction of f_{Cs}, this impressively small uncertainty, δf, is less than 1×10^{-15}. This is equivalent to saying that, for state-of-the-art Cs standards, the SI second can be realized with a fractional inaccuracy of less than 1 part per quadrillion, making it (pragmatically speaking) the most well-defined unit in the present SI system.

Unfortunately, this small inaccuracy is not always experimentally accessible in a time/frequency measurement. Noise processes intrinsic to the Cs standard operation degrade the stability of the frequency output at short timescales. The frequency output must be accumulated over long times to average through these noise processes and

reach a measurement instability at the level of the inaccuracy. Depending on the details of operation, the required averaging time can exceed 1 day [5, 6, 7, 8]. For some applications, this long averaging time can be prohibitive. Efforts have been made to reduce the intrinsic noise processes and subsequently reduce the required averaging time [9, 10, 11]. However, an altogether different approach could yield a frequency standard with instability smaller than the fundamental limitation of the Cs standards, as well as provide further reduction in the system's inaccuracy. This different approach is to use a standard operating at much higher frequencies in the optical domain.

1.3 Optical Frequency Standards

A common tool for measurement of length is the ruler. As simple as a long stick of wood with regularly spaced tick marks, the ruler makes length measurement possible by counting the number of ticks between two points of interest. The knowledge that the ticks have been placed at calibrated intervals allows one to extract the length measurement. It is instructive to consider what determines the precision to which a ruler, such as those in Figure 1.1, can measure length. For a given length, the more tick marks which are indicated on the ruler, the more precisely the ruler can measure. For example, we suppose that a cm on ruler A is indicated by 5 tick marks and by 25 tick marks on ruler B. Measuring a 5 cm long object would give 25 ticks from ruler A and 125 ticks from ruler B. Pressed by an observer as to how precisely these measurements were made, one could naturally respond that the uncertainty was less than one tick, since the toy clearly measured close to the 25^{th} tick on ruler A and the 125^{th} tick on ruler B. By simply having more ticks, the measurement using ruler B has a fractional uncertainty ($< 1/125$) smaller than the measurement with ruler A ($< 1/25$).

Now imagine a scenario where we measure two different objects which are nearly but not quite the same length. Ruler C is identical to ruler A, only with an additional set of minor tick marks between each major tick. Using ruler A, both objects measure

to approximately the 25^{th} large tick, one a bit short of it and the other reaching nearly exactly the tick. On ruler C, the second object again falls at nearly exactly the 25^{th} major tick, and the first falls short of it. In this case, however, it is clear that the object is two minor ticks away from the large tick, and the distance between major ticks can be divided down more precisely.

These examples illustrate two important features of the ruler which determine the measurement precision: the number of tick marks for a given length and how well defined the distance between (major) tick marks is. The same is true for the measurement of time. A clock operates by counting the time ticks generated by its frequency standard. More ticks in a second (i. e. higher frequency from the standard) gives higher measurement resolution for a given time interval. More well-defined ticks from the frequency standard (i.e. a low-phase-noise standard with a narrowband frequency output) also gives higher resolution. This can be stated more formally by considering an atomic standard which operates by stabilization to an atomic transition with frequency ν_0 and linewidth $\delta\nu$. Assuming the instability is limited by an unspecified white frequency noise process (equal noise amplitude at all Fourier frequencies), the fractional instability of such a standard is given by [12]:

$$\sigma(\tau) = \frac{\delta\nu}{\nu_0}\frac{\eta}{(S/N)\sqrt{\tau}} \tag{1.1}$$

Here S/N indicates the signal to noise ratio of the atomic transition measurement (rms, 1 Hz BW), τ is the averaging time, and η is a parameter close to unity whose exact value depend on details of the clock operation, including the type of atomic spectroscopy implemented. As stated previously, one way to reduce the final instability is to average for longer times (although this averaging occurs only as the inverse square root). Another way is to increase the measurement S/N, although fundamental limitations exist on how large this can be. As illustrated in the ruler analogy, instability can be reduced with an atomic transition of very narrow linewidth. This will be discussed later in the

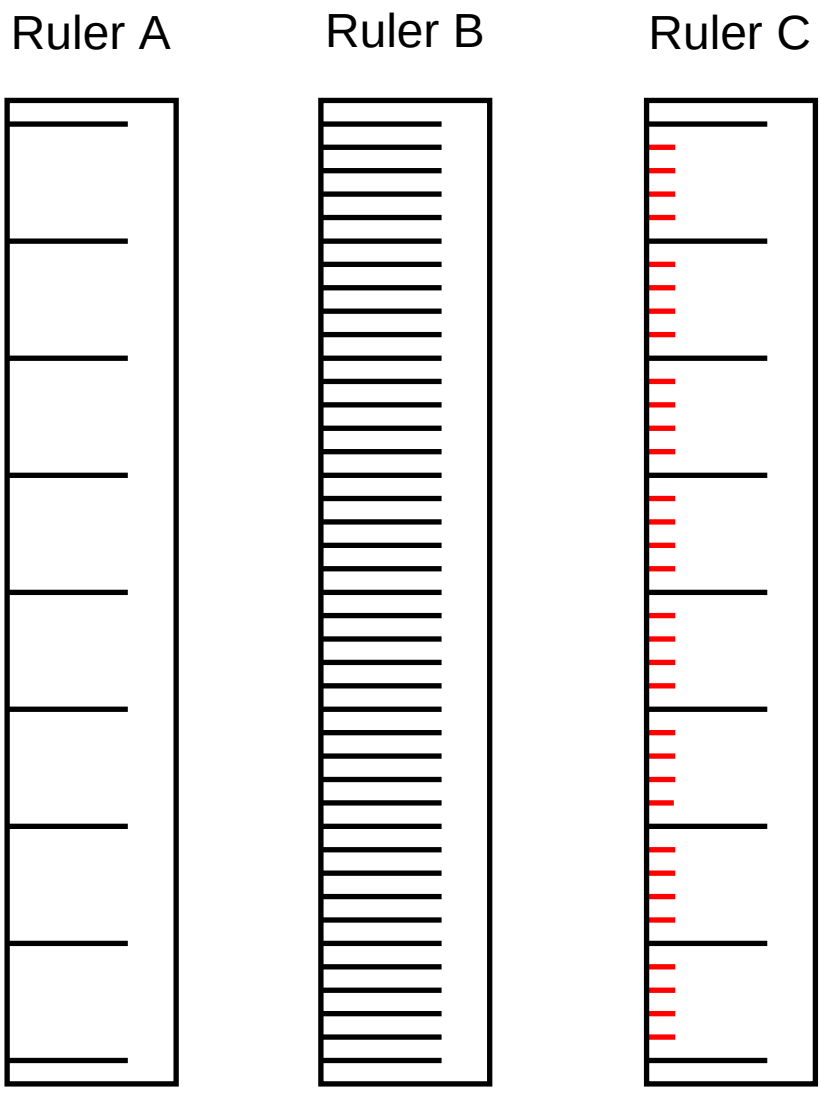

Figure 1.1: Three rulers used to make length measurements. The number of major ticks per length and the discrimination between major ticks (represented by the minor ticks of Ruler C) determine the measurement precision of each ruler.

context of strontium (Sr). Most notably, a straightforward way to reduce the instability is to operate the standard at higher frequencies, ν_0. This can be accomplished with an atomic transition at optical frequencies, which can be five orders of magnitude higher frequency than the microwave transitions used in Cs standards. In principle, this same argument holds not just for the instability but also for the inaccuracy of the standard as well. For a given sensitivity to environmental perturbations, moving to an optical atomic transition can reduce the uncertainty in realizing the ideal frequency output. This is easier said than done, as a change to the optical domain requires a substantial change in the tools and technology required to construct such a standard. However, as we see in the next section, there are atomic systems very well suited to be optical frequency standards.

1.4 Strontium: Electronic Structure

Elements are organized in the periodic table according to their electronic configuration. Elements in the same group (column) have similar electronic configuration and thus similar atomic and chemical properties. Group 1 atoms, the alkali metals, have only one valence electron and thus have electronic structure similar to that of hydrogen. The simplicity associated with having just one valence electron has made alkali atoms a popular choice for experimental and theoretical work in atomic physics. Their ground states, with orbital angular momentum $L = 0$, have a variety of allowed transitions to other electronic states, all spin doublet states. The alkaline earth atoms, located in Group 2 of the periodic table, have two valence electrons. The presence of a second valence electron creates a rich mixture of electronic states, neatly divided into spin singlet (intrinsic electronic spin $S = 0$) and spin triplet ($S = 1$) states. Among the alkaline earth atoms are elements such as beryllium, magnesium, calcium, and strontium. Similar to the alkaline earth metals, elements such as the lanthanide ytterbium, the transition metals zinc, cadmium, and mercury, and the synthetically prepared ac-

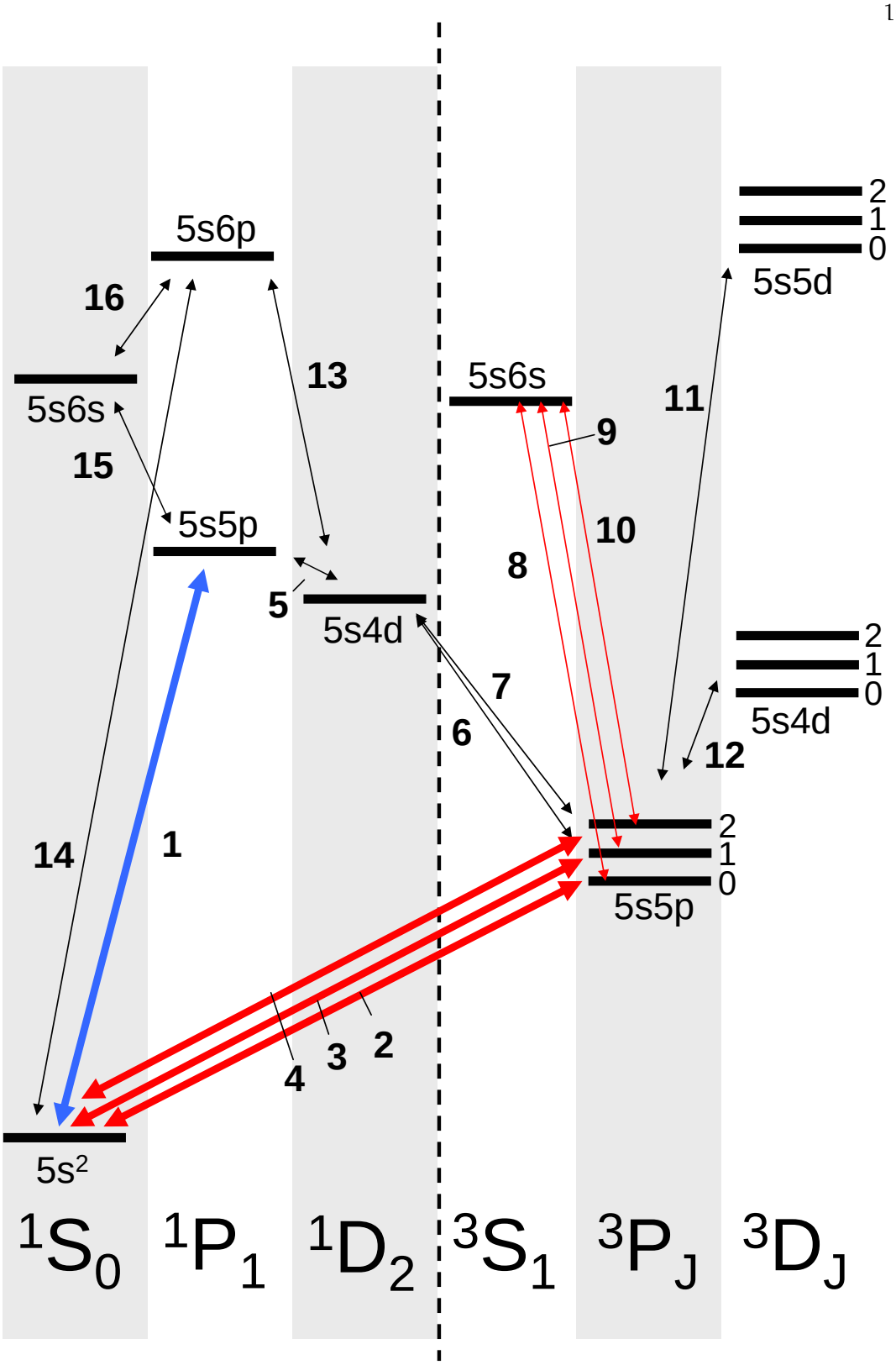

Figure 1.2: Term diagram for ^{88}Sr. The states are organized horizontally by their electronic spin. The dashed line indicates the separation between the singlet and triplet spin states originating from the dipole selection rule, $\Delta S = 0$. The electronic configuration for each state is listed next to it. Transitions are numbered, with the corresponding transition wavelength and decay rate given in Table 1.1. Note that for the case of ^{87}Sr, further hyperfine structure is present.

Table 1.1: Sr transitions and their transition wavelength and Einstein A coefficients. Transition number corresponds to those shown in Figure 1.2.

Transition	λ (nm)	A (1/s)
1	461	1.9×10^8
2	698	7×10^{-3} (^{87}Sr)
3	689	4.7×10^4
4	671	2×10^{-3}
5	6.5×10^3	3.9×10^3
6	1.8×10^3	2.2×10^3
7	1.9×10^3	1.1×10^3
8	679	9×10^6
9	688	2.8×10^7
10	707	4.6×10^7
11	490	6.1×10^8
12	3×10^3	3.5×10^5
13	717	1.6×10^7
14	293	1.9×10^6
15	1.12×10^3	2×10^7
16	2.85×10^3	3×10^6

tinide nobelium have two valence $L = 0$ electrons. The energy level term diagram for strontium is shown in Figure 1.2. While details of the energy level structure are different for each alkaline earth atom, many major features are shared among them. The ground state is $^1S_0$. Strong dipole allowed transitions exist from the ground state to higher lying $^1P_1$ states. For strontium and several other alkaline earth atoms the very first excited state is a triplet state ^3P, with allowed dipole transitions to a variety of ^3S and ^3D states. No dipole transitions are allowed between the spin singlet and spin triplet states due to the dipole selection rule $\Delta S = 0$. As a consequence, these states are predominantly isolated from each other, except for a set of weaker, multipole couplings connecting them.

One notable exception to the lack of dipole couplings between the singlet and triplet states is between the ground $^1S_0$ and the excited $^3P_1$ states. As a result of $L \cdot S$ interaction among the excited states, the $^3P_1$ state acquires a small admixture of the $^1P_1$ state, which does have dipole coupling to $^1S_0$. As a result, a weak dipole transition $^1S_0$-$^3P_1$ exists [13, 14, 15, 16].

There are four stable isotopes of strontium: ^{88}Sr, ^{87}Sr, ^{86}Sr, and ^{84}Sr. The isotopes and their natural abundance are found in Table 1.2 [17]. As a general rule, due to spin pairing of the nucleons, isotopes with an even atomic number Z and an even atomic mass number A have a nuclear spin $I = 0$ [18]. This is the case for the even isotopes of Sr, which have $Z = 38$. The odd isotope ^{87}Sr has $I = 9/2$. In this case, the presence of nuclear spin allows hyperfine interaction to perturb the ^3P states shown in Figure 1.2. Significantly, the hyperfine interaction weakly mixes $^3P_0$ with the $^1P_1$ and $^3P_1$ states. Consequently, like $^3P_1$, $^3P_0$ acquires a very weak dipole coupling (although much weaker than $^3P_1$) to $^1S_0$ [13, 14, 15, 16, 19].

As shown in Figure 1.2, the ground state $^1S_0$ has at least three noteworthy transitions each with very different strengths. The diversity in these transitions facilitate their use for a variety of atomic manipulations, each useful for application to optical frequency

Table 1.2: The natural abundances of strontium isotopes.

Atomic Mass Number	Natural Abundance
88	82.56%
87	7.02%
86	9.89%
84	0.56%

standards. The $^1S_0$-$^1P_1$ transition is strong (Einstein A coefficient, $A = 2.1 \times 10^8$ s^{-1}) and the lowest $^1P_1$ state has only very weak decay rates to states other than $^1S_0$. As a result, this transition is well-suited for traditional laser cooling, permitting a thermal beam of dilute Sr gas to be cooled to mK temperatures and collected in a magneto-optical trap. The $^1S_0$-$^3P_1$ transition is weaker ($A = 4.7 \times 10^4$ s^{-1}) and is a closed transition. This transition complements the $^1S_0$-$^1P_1$ nicely, by permitting a secondary stage of laser cooling to further cool the atomic sample below the fundamental limit for the $^1S_0$-$^1P_1$ transition. In this way, the atomic sample can be cooled and trapped at or below μK temperatures, where thermal energy is small enough for atomic confinement in a traditional optical dipole potential.

Finally, the $^1S_0$-$^3P_0$ is extremely weak ($A = 7 \times 10^{-3}$ s^{-1}). According to the criteria expressed above, a good atomic transition for an optical frequency standard has at least two important qualities: a narrow linewidth and weak sensitivity to perturbations. $^1S_0$-$^3P_0$ exhibits a serendipitously narrow (but not too narrow) transition linewidth of ~ 1 mHz. Furthermore, the sensitivity of this transition to most relevant perturbations, including magnetic fields and optical radiation, is comparatively small. The effect of blackbody radiation, although fractionally smaller than that for Cs, is non-negligible but controllably sized [20]. Together with other properties discussed later in this text, Sr stands as a very favorable candidate for a high performance optical frequency standard. Many laboratories around the world are actively developing standards based on Sr [21, 22, 23, 24, 25, 26, 27, 28, 29] or similar atoms like Yb [30, 31] and Hg [32, 33]. Along with other optical frequency standards, these systems hope to reach eventual

inaccuracies of 1×10^{-18}, or approximately 100 times smaller than the expected limit to the Cs standard inaccuracy.

1.5 The Need for Cold Atoms

It is already worth mentioning one important detail which needs to be addressed for a high performance atomic clock: the Doppler effect. Almost anyone has experienced a car drive by honking its horn. From this everyday experience, it is no surprise that the horn frequency we hear is chirped as the car approaches or leaves. This Doppler effect is a consequence of the frequency (sound) source and observer originating from two different reference frames, and can be calculated (to first order) with a simple Galilean transformation between the frames (to second order, a Lorentz transformation including relativistic effects is required) [34]. The same holds true for an atom in motion: the atom sees radiation which is frequency shifted from the laboratory frame. This can lead to dephasing when probing the atomic transition of a large atom ensemble. Furthermore, it can lead to frequency shifts which depend on the geometry of the probing radiation relative to the atomic motion. Since the Doppler effect scales with the relative velocity between the atom and laboratory reference frame, the best way to reduce it is to slow the atom down. Laser cooling techniques have demonstrated their ability to reduce atomic velocity from thermal sources with hundreds of m/s velocity to cm/s scale velocities [35]. As will be discussed in more detail, some caveats exist with respect to the importance of the Doppler effect. Tightly trapped atoms can be excited with limited Doppler effects. Nonetheless, most of the useful traps only have sufficient depth to trap laser cooled atomic samples with low thermal energy. Furthermore, the recoil shift associated with the absorption of a photon grows to a larger fraction of the transition frequency for increasing transition frequency, making this shift more significant for optical transitions than for microwave ones. For all of these reasons, development of state-of-the-art optical frequency standards currently requires the use of cold or ultracold atomic samples.

1.6 Precision Timing Applications

With the possibility that optical frequency standards could allow clocks to offer 10^{-18} timing accuracy and precision, one might naturally ask "Why do we need this?". Indeed, on the human timescale, such a clock would not help us arrive to an important meeting any more promptly than a decent wristwatch. But high performance timekeeping is a powerful tool which finds many applications. Some of these applications already require state-of-the-art technology and will directly benefit from improved primary frequency standards. Many other applications use more robust, proven clocks that operate below state-of-the-art. But as the best clocks improve, the technology trickles down to improve other clocks as well. To help motivate the need for more advanced optical frequency standards, I list here some areas of application which benefit from high performance timekeeping.

- global positioning system (GPS) [36]
- computer network and electrical power grid synchronization
- deep space navigation
- radio telescopy (very long baseline interferometry)
- definition of the SI second
- measurement of other fundamental units (volt, ampere, ohm, meter)
- tests of fundamental physics (time variation of fundamental constants, symmetry postulates, graininess of space)
- geodesy (gravitational red shift)
- secure communications [37]
- tests of special and general relativity

- gravitational wave detection and long baseline gravitational interferometry [38]
- space clock missions [9, 39]

1.7 Thesis At-a-Glance

With the basic concepts and motivation described in this introduction, I now turn to the details. In Chapter 2, I describe the tools which were implemented to prepare and manipulate the Sr atomic sample for use in high accuracy spectroscopy. This includes a general description of laser cooling techniques and our work on narrow-line Doppler cooling. It describes atomic confinement in an optical lattice and resonant laser interactions with confined atoms. I also describe the optical pumping techniques we used for nuclear spin state preparation.

In Chapter 3, I describe the development of a highly stable, sub-Hz linewidth laser source, a critical ingredient for high precision atomic spectroscopy. This leads to the realization of coherent atom-light interactions approaching the one second timescale. In doing so, we report the observation of optical atomic spectra with 2 Hz linewidths.

Towards the development of an optical frequency standard based on ^{87}Sr, in Chapter 4 I describe tools such as the optical frequency comb and precision frequency references. Using these tools, we performed a spectroscopic evaluation of the Sr clock transition, including several absolute frequency measurements.

In Chapter 5, I describe the current operation of the ^{87}Sr optical frequency standard at JILA. This system was carefully characterized via a remote optical comparison of the Sr optical standard to other optical standards at the National Institute of Standards and Technology (NIST). A detailed description of the systematic shifts of the clock frequency is given, including the total systematic shift uncertainty of 1.5×10^{-16}. Furthermore, an improved absolute frequency measurement of the Sr clock transition was made with an uncertainty $< 9 \times 10^{-16}$. Finally, I conclude by briefly considering

the future direction of ultracold strontium, both in the context of optical frequency standards as well as other physical investigations.

Chapter 2

Atomic Manipulation and Control

As described in the introductory chapter, ^{87}Sr exhibits strong potential as an optical frequency standard. As with any atomic system, that potential is not necessarily achievable under the conditions that nature freely provides. In this chapter, I give a basic introduction to the tools and techniques used for atomic manipulation, which prepare Sr for use in a high accuracy optical frequency standard. I discuss Doppler laser cooling and trapping techniques in the broad and narrow line regimes, atomic confinement and interrogation in optical potentials (such as optical lattices), and atomic state preparation using optical pumping techniques.

2.1 Laser Cooling: Basic Concepts

Laser cooling has proven to be a rich and flexible tool. Much research has been successfully dedicated to understanding and implementing a wide variety of laser cooling techniques. The interested reader is referred to a few of the many well-written review and research articles on the topic [35, 40, 41, 42, 43, 44, 45]. Here, I give a brief conceptual introduction, after which I discuss how these techniques are implemented in two different regimes in strontium: (1) a primary stage of traditional Doppler cooling to pre-cool and collect an atomic sample at 1 mK from a hot, thermal beam source and (2) a secondary stage of narrow line Doppler cooling using the $^1S_0$-$^3P_1$ transition to reach photon-recoil-limited temperatures below 1 μK. These techniques will be discussed first

in a generic context, with broad applicability to ^{88}Sr. Later I will give details relevant specifically to the ^{87}Sr case.

Like matter, light has both energy and momentum. The idea that light can be used to reduce the (thermal) kinetic energy of atoms can be broadly termed laser cooling. The basic ideas behind laser cooling were first proposed independently by Hänsch and Schawlow [46] and Wineland and Dehmelt [47], both in 1975. The description and language used in each proposal were distinct, the former lending itself more naturally to cooling freely moving atoms and the latter to cooling atoms bound to an external potential. Nonetheless, the two proposals shared the same core principles, and the laser cooling phenomenon they described can be qualitatively motivated by a simple consideration of momentum and energy.

When an atom absorbs a photon of light, conservation of momentum dictates that the photon momentum, $\vec{p}_{ph} = \hbar\vec{k}$, is absorbed by the atom. Here $\hbar$ is Planck's constant divided by 2π and $\vec{k}$ is the light wave vector, where $|\vec{k}| = 2\pi/\lambda$ and λ is the wavelength of the light. We consider the case where light illuminates an atom (for simplicity, we assume an atom with two coupled internal states and mass, m) whose velocity $\vec{v}$ is antiparallel to the light k-vector $\vec{k}$. As the photon is absorbed, exciting the atom from the ground to the excited internal state, the atomic momentum is changed from $\vec{p}_{atom} = m\vec{v}$ to $\vec{p}_{atom} = m\vec{v} + \hbar\vec{k}$. Since $\vec{k}$ and $\vec{v}$ are antiparallel, this corresponds to a reduction in the atomic momentum and velocity. When the atom relaxes from the excited to the ground internal state via spontaneous decay, a photon is re-emitted and the atom experiences the corresponding momentum impulse from photon emission. However, due to the isotropic decay process, the photon is emitted in a random direction, and averaged over many decay events, the atom experiences a net zero momentum change due to spontaneous emission (i. e. $\vec{k}_{emis}$ averages to zero). In this way, repeated photon absorption-emission cycles reduce the atomic velocity $\vec{v}$ and cool the atom.

Due to the Doppler effect, radiation emerging from a laser in the laboratory-

stationary reference frame is seen by an atom in motion to have a frequency shift relative to the laboratory frame. In the reference frame of the atom, we label the energy spacing between the internal states of the atom as $\hbar\omega_0$, where ω_0 is the angular frequency of the transition between the two states. Furthermore, we consider laser light which is essentially resonant with the internal transition of the atom *in motion*. In this case, the frequency of the light absorbed (in the laboratory-stationary frame) is given by:

$$\omega_{abs} = \omega_0 + \vec{k} \cdot \vec{v} + \frac{\hbar k^2}{2m} \tag{2.1}$$

The second term on the right hand side accounts for the Doppler shift between the moving atom and the stationary laboratory frames. The third term is the recoil frequency which originates as a natural consequence of conservation of momentum and energy as the atom takes up the photon momentum. Similarly, the photon frequency emitted by the atom after internal relaxation is:

$$\omega_{emis} = \omega_0 + \vec{k'} \cdot \vec{v'} - \frac{\hbar k^2}{2m} \tag{2.2}$$

Again, in the case of emission, averaging over the isotropic, random emission direction results in the Doppler shift term in Equation 2.2 averaging to zero. Consequently, the average change in kinetic energy of the atom (the negative of the energy difference between absorbed and emitted photons) is:

$$\Delta E = -\hbar(\omega_{abs} - \omega_{emis}) = \vec{k} \cdot \vec{v} + 2\frac{\hbar k^2}{2m} \tag{2.3}$$

With $\vec{k} \cdot \vec{v} < 0$ (antiparallel) and $|\vec{k} \cdot \vec{v}| > 2\frac{\hbar k^2}{2m}$ (generally true for optical transitions of non ultracold atoms), the kinetic energy of the atom is reduced (the atom is cooled) and this energy is taken away by the photons.

This simple picture is particularly relevant for laser cooling an atomic beam from a hot thermal source. In practice, the frequency range over which proficient laser cooling occurs is given by the linewidth of the cooling transition. For most of the transitions

used, this is on the order of MHz, corresponding to speeds of m/s. To cool a thermal beam source starting at velocities of hundreds of m/s, some mechanism must be employed to maintain laser cooling efficacy after the Doppler shift experienced by the cooled atom is reduced by an amount comparable to the transition linewidth (where photons would no longer be absorbed efficiently). Several approaches can be employed, the most popular being a tapered magnetic field which generates a spatially dependent Zeeman shift that compensates the change in Doppler shift as the atoms are slowed.

Once cooled to where the total remaining Doppler shift is close to the transition linewidth, counterpropagating laser beams in each Cartesian dimension (red-detuned of the natural transition in the lab frame) can be utilized to further cool the atoms three dimensionally. The atom sees light travelling against (with) its motion with a blue (red) Doppler shift. Since the laser light is red-detuned, the atom preferentially absorbs the blue-Doppler shifted photons (travelling antiparallel to the atom) which appear on resonance. Thus, whatever direction the atom travels, its motion will be reduced (cooled). Its trajectory constantly changes as it absorbs photons from the 3 pairs of orthogonal laser beams. It is straightforward to show (for the simplified 1-D case) that this effect results in a mean velocity-dependent cooling force which drives the atomic velocity towards zero. However, the random absorption of a photon from any direction by an atom at rest and the random emission direction of any emitted photons result in velocity fluctuations which effectively heat the atom. This heating competes with the mean cooling force, and the competition between the two yields the temperature to which the atomic sample can be cooled [41]. The coldest temperatures are obtained with laser light red-detuned from the atomic transition by one half the natural linewidth, γ. This Doppler-cooling temperature limit is:

$$k_B T_{min} = \frac{h\gamma}{2} \tag{2.4}$$

where k_B is Boltzmann's constant. Since the atom's photon scattering rate is deter-

mined by the relative size between the laser detuning (δ) and the natural transition linewidth (γ), it is no surprise that the temperature limit corresponds to a thermal energy approximately equal to the energy width of the transition.

The laser cooling described above can generate samples of millions or billions of cold atoms. By providing a viscous force on the atoms, the laser fields have been dubbed "optical molasses" [41, 35]. As the optical molasses yields only a velocity-dependent force to damp atomic motion, the atoms are not truly trapped since no critical spatially-dependent forces are present. To provide the necessary confinement, a spatially dependent magnetic field is introduced to complement the optical molasses. In a direct analog to the velocity dependent Doppler shift, the spatially dependent Zeeman shift pushes atoms toward the trap minimum [48]. Usually, the magnetic field is generated by a pair of anti-Helmholtz coils, which gives a zero magnetic field at the trap center and a nonzero field away from the center which varies linearly with distance from the center. Optical molasses combined with this magnetic confinement is referred to as a magneto-optical trap (MOT), and was first demonstrated by Pritchard and Chu [49]. The MOT has emerged as an extremely powerful tool for the study and manipulation of neutral atoms, and is the starting point for a large subset of today's experimental studies in atomic physics. Several MOT configurations exist, using different atomic transition types and different laser polarization. Furthermore, some atomic systems lend themselves to additional cooling mechanisms which can generate temperatures below the Doppler limit of a standard MOT. The broad field of laser cooling includes a variety of cooling techniques such as polarization gradient cooling, Sisyphus cooling, cooling using velocity selective coherent population trapping, and Raman cooling (e. g. [45, 50, 51, 52]).

2.2 Laser cooling strontium: $^1S_0$-$^1P_1$ MOT

2.2.1 Laser cooling properties of $^1S_0$-$^1P_1$ MOT

Figure 2.1 highlights the energy level structure of Sr relevant to laser cooling using the $^1S_0$-$^1P_1$ dipole transition. The diagram does not show the hyperfine structure relevant for ^{87}Sr, as this will be discussed later. Please refer back to Figure 1.2 for a more complete energy level diagram including other electronic states. The $^1S_0$-$^1P_1$ transition has several characteristics which make it well-suited for cooling and trapping Sr from a thermal source.

1. Dipole moment. Since laser cooling and trapping relies on atom-laser interaction, the dipole moment, d, of an atomic transition plays a key role in the laser cooling dynamics. The atom-laser dipole interaction strength is given by the Rabi frequency:

$$\Omega = \frac{\vec{d} \cdot \vec{E}}{\hbar} \tag{2.5}$$

where E is the amplitude of the laser electric field. Conversely, the coupling between the dipole moment and the vacuum field yields the spontaneous decay rate for the transition:

$$\Gamma = \frac{4\alpha}{3e^2c^2}\omega_0^3|d|^2 = \frac{2\omega_0^3}{6\pi\epsilon_0\hbar c^3}|d|^2 \tag{2.6}$$

where $\alpha \simeq 1/137$ is the fine structure constant, c is the speed of light in vacuum, e is the electron charge, and ϵ_0 is the permittivity of free space. The solution to the rate equations for a two level atom indicate that the absorption of near resonant laser radiation, moving population between the ground and excited states, saturates when these two rates are approximately equal. In steady state, the excited state fraction, ρ_{exc}, is found to be:

$$\rho_{exc} = \frac{1}{2}\frac{s}{1 + s + 4\frac{\Delta^2}{\Gamma^2}} \tag{2.7}$$

Here $\Delta = \omega_L - \omega_0$ is the detuning of excitation laser from the atomic resonance, and s

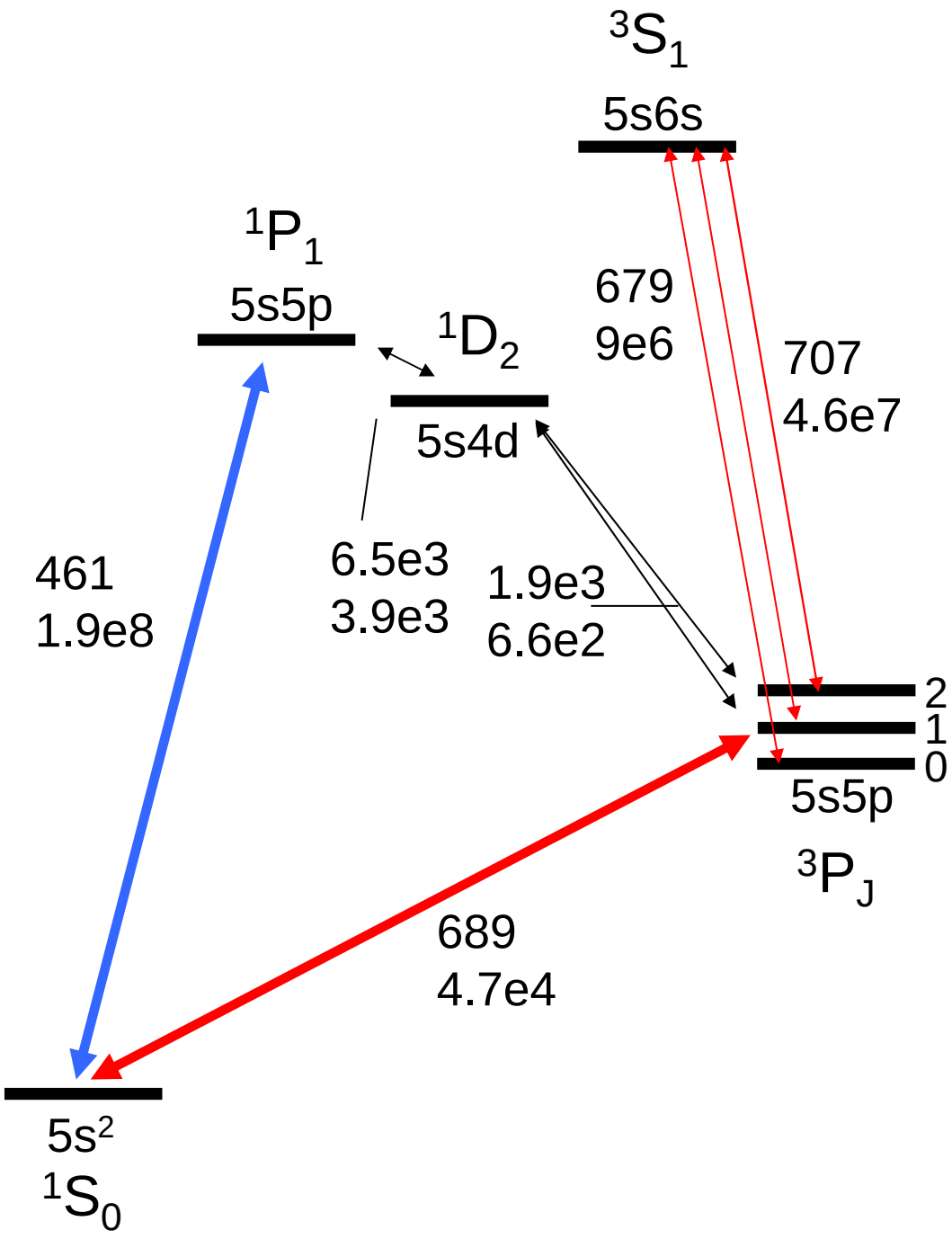

Figure 2.1: Abbreviated term diagram with states relevant for operation of the $^1S_0$-$^1P_1$ MOT. Arrows indicate the transitions, with their associated wavelength (in nm) and decay rates (Einstein A coefficients in 1/s). Decay loss from the excited $^1P_1$ state is shown, as well as the transitions used to repump this population loss back to $^1S_0$.

is the saturation parameter for the laser-atom interaction and is given by:

$$s = 2\frac{\Omega^2}{\Gamma^2} \tag{2.8}$$

s can also be written in terms of the laser intensity, I, as $s = I/I_{sat}$. Here, I_{sat} is given by:

$$I_{sat} = \frac{\hbar^2 c\epsilon_0}{2}\frac{\Gamma^2}{|d|^2}. \tag{2.9}$$

A plot of Equation 2.7 is shown in Figure 2.2 as a function of the saturation parameter s. Note that when $s \simeq 1$ ($\Omega^2 \simeq \Gamma^2$), ρ_{exc} begins to saturate to the steady state limit of 1/2. This places a key limitation on laser cooling and trapping performance. Since laser cooling requires many repeated cycles of photon absorption and spontaneous emission, the fastest rate at which the atomic momentum can be reduced by a photon recoil $\hbar k$ is $\Gamma\rho_{exc}$ (maximizing to $\Gamma/2$). This is equivalent to saying that the maximum deceleration possible from laser cooling using a transition with decay rate Γ is:

$$a_{max} = \frac{\hbar k\Gamma}{2m}. \tag{2.10}$$

For the $^1S_0$-$^1P_1$ transition, $a_{max} \simeq 10^6 \mathrm{m/s}^2$. This has important implications for both slowing the atoms from a thermal source as well as loading them into a MOT. The temperature of a thermal beam source is primarily constrained by the need for sufficient atom beam flux (higher temperature = higher vapor pressure = higher flux). Of course, higher temperatures also yield higher initial velocities, and this initial velocity and a_{max} determine the minimum length over which the atoms must travel to be slowed to near rest ($\Delta x = v_0 t + 1/2at^2$ and $\Delta v = at$). For a typical atomic velocity of 500 m/s, approximately 12 cm is required to slow the Sr atomic beam using the $^1S_0$-$^1P_1$ transition. Transitions with weaker dipole moments (and hence smaller decay rates) would require longer slowing paths, experimentally complicating the process. Note also that longer slowing paths typically mean lower atom beam flux, due to loss of atoms from atomic motion perpendicular to the beam axis.

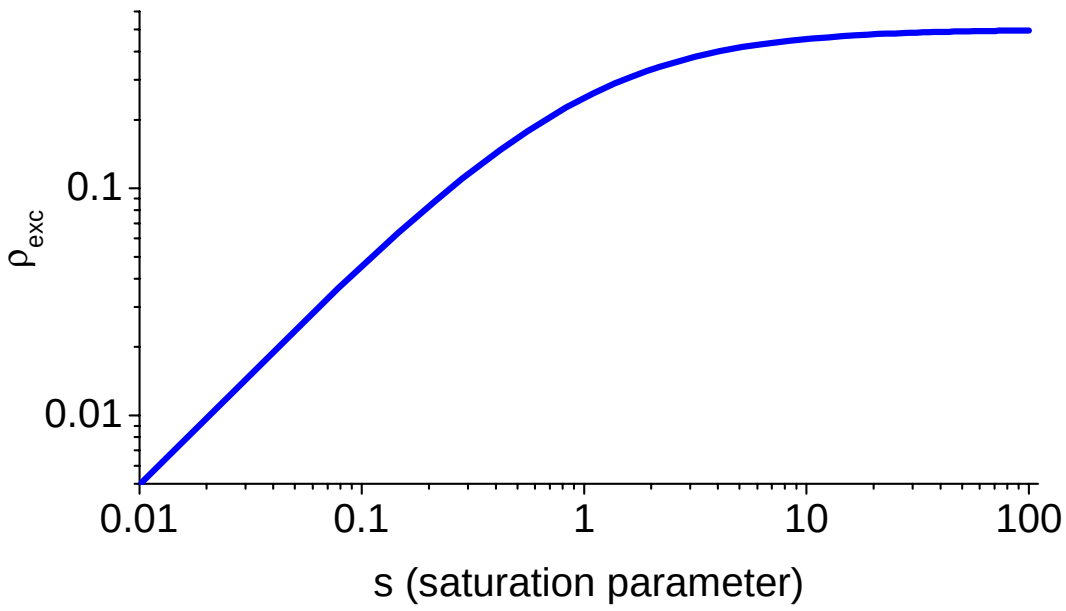

Figure 2.2: Excitation fraction, ρ_{exc}, as a function of saturation parameter, s, for a two level atom in steady state. The excited state fraction saturates to one half around $s \simeq 1$.

For efficient loading of atoms from a slowed beam into a MOT, the capture velocity of the MOT can be estimated as [53]:

$$v_c = \sqrt{a r_c} \tag{2.11}$$

where r_c is the capture radius of the trap, typically set by the radii of the trapping/cooling lasers. Using the $^1S_0$-$^1P_1$ transition and with $r_c = 1$ cm, v_c can be as much as 100 m/s, a healthy capture velocity for robust trapping of large atom number.

It is important to remember that a tradeoff exists in the laser cooling process due to the transition linewidth. Although a large transition linewidth can experimentally facilitate the cooling and trapping process as described above, this also results in higher temperatures (see Equation 2.4). A good deal of experimental work requires ultracold, μK atomic temperatures. Although the $^1S_0$-$^1P_1$ Doppler limit is a relatively warm 770 μK, this temperature is small enough to conveniently and efficiently load the atoms into a secondary MOT using the $^1S_0$-$^3P_1$ transition where much colder temperatures are achievable. In this way, the $^1S_0$-$^1P_1$ MOT serves as means to collect and pre-cool large Sr samples, readying them for further cooling.

2. Closed transition. The discussion in Section 2.1 assumed an ideal atom with only two levels. A realistic many-level atom usually has a rich network of couplings among its internal states. In some cases, two levels can behave nearly isolated from the remainder, approximating a two-level system. This is the case for the $^1S_0$-$^1P_1$ transition in Sr. Atoms excited from the ground $^1S_0$ state to the $^1P_1$ state decay nearly completely back to $^1S_0$. A weak decay channel exists from $^1P_1$ to $^1D_2$ ($\Gamma = 3.9 \times 10^3$ s^{-1}), where decay continues to the $^3P_1$ and $^3P_2$ states with a branching ratio of 2/3 and 1/3 respectively. Atoms falling to the $^3P_1$ state further decay back to the ground $^1S_0$ state, and so are able to continue the $^1S_0$-$^1P_1$ laser cooling process. $^3P_2$ is a metastable state (lifetime, $\tau = 1/A = 500$ s) and so atoms that decay here are lost from the $^1S_0$-$^1P_1$ MOT. Fortunately, this loss rate ($1/3 \times 3.9 \times 10^3 = 1.3 \times 10^3$ s^{-1}) is much smaller than

the $^1P_1$ spontaneous decay rate to $^1S_0$ ($A = 2.1 \times 10^8$ s^{-1}). As a consequence, the MOT can operate without the assistance of any extra lasers to "repump" atoms from the loss channels back to the laser cooling states. This is in contrast to alkali atom MOTs, which require a repump laser for operation.

Nonetheless, the Sr MOT atom number is enhanced when introducing extra lasers to pump $^3P_2$ population back to $^1S_0$. Several repumping schemes are feasible [54]. We accomplish this task with two lasers (refer to Figure 2.1). The first, at 707 nm, resonantly pumps $^3P_2$ to $^3S_1$. From here, decay occurs to $^3P_2$, $^3P_1$, and $^3P_0$ with branching ratios of 5/9, 3/9, and 1/9, respectively. Population decay to $^3P_2$ is simply excited to $^3S_1$ again via the 707 nm repump laser. Population decay to $^3P_1$ subsequently decays further to $^1S_0$ for more MOT cycling. Decay to $^3P_0$ remains stuck there ($\tau =$ 150 s for ^{87}Sr and thousands of years for ^{88}Sr) and so requires application of a second repump laser at 679 nm, which pumps the $^3P_0$ population back to $^3S_1$. In this way, all lost population is eventually returned to $^1S_0$ via $^3P_1$. Experimentally, the presence of repump lasers can enhance the MOT atom number by more than an order of magnitude.

3. J to J+1 transition. Pure Doppler cooling (optical molasses) exploits the sign of the Doppler shift (blue shift for $\vec{v}$ antiparallel to $\vec{k}$ and red shift for $\vec{v}$ parallel to $\vec{k}$) to favor photon absorption from the counterpropogating direction to slow (rather than heat) the atoms. The spatial confinement added in a MOT exploits the spatially dependent Zeeman shift of the atomic states. Consider an atom which is located 1 mm to the right side of the MOT trap center. Absorption of a photon coming in from the right side will give the atom recoil which will push it to the left towards the trap center. However, to successfully trap the atoms, the atom must preferentially absorb a photon from the right rather than from the left, as one from the left would push it further away from the trap center. This is accomplished by optical polarization and the use of two magnetic states with equal but opposite Zeeman shifts ($m_J = \pm 1$, refer to Figure 2.3). Counterpropogating laser beams have opposite polarization with respect to the

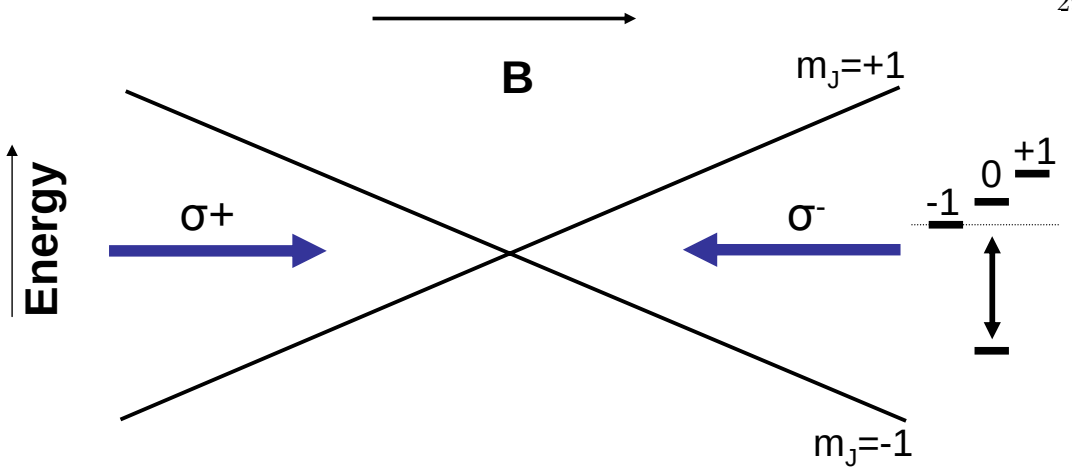

Figure 2.3: The combination of σ^+ and σ^- light with a magnetic field to provide spatial confinement using a $J = 0$ - $J = 1$ laser cooling transition. The Zeeman shift of the $m_F = \pm 1$ states permit preferential absorption of the polarized light field, pushing the atom towards the trap center.

atomic quantization axis. The σ^- polarized light coming in from the right side can drive transitions from $^1S_0$ $m_J = 0$ to $^1P_1$ $m_J = -1$ and the σ^+ polarized light coming in from the left side can drive transitions from $^1S_0$ $m_J = 0$ to $^1P_1$ $m_J = +1$. The red-detuned laser light, however, is only resonant with the $m_J = 0$ - $m_J = -1$ transition because of the negative Zeeman shift of the $m_J = -1$ state from the (positive) B-field aligned along the quantization axis. Thus absorption is preferentially made by the photons from the right, pushing the atom back towards the trap center. The same is true for an atom to the left of the trap center absorbing the photon from the left. The $J = 0$ to $J = 1$ transition is the simplest transition in the J to $J + 1$ family which facilitates this polarization and Zeeman shift dependent absorption for successful spatial confinement. With a single magnetic sublevel, the $J = 0$ ground state is optimal for efficient Doppler cooling since population does not undesirably decay to unwanted substates.

2.2.2 Experimental details of the $^1S_0$-$^1P_1$ MOT

The general schematic of the experimental apparatus used to laser cool and trap strontium (with emphasis on the $^1S_0$-$^1P_1$ MOT) is given in Figure 2.4. We use a

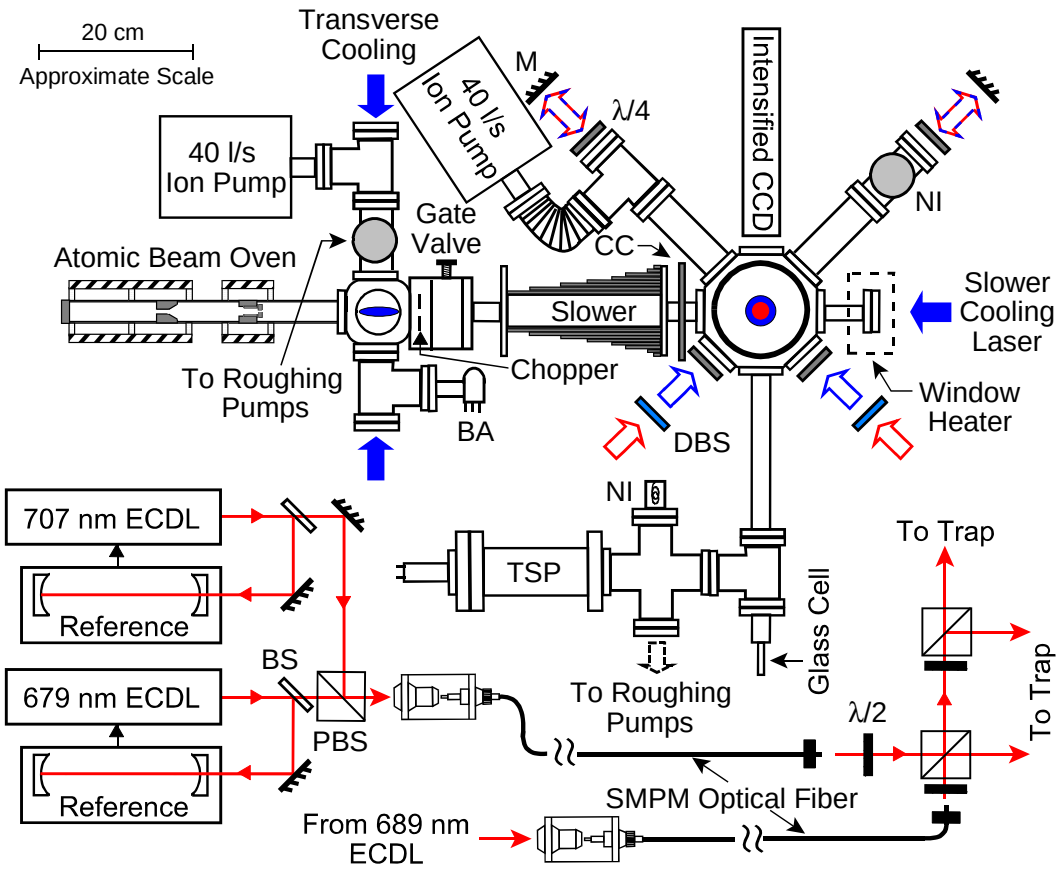

Figure 2.4: Schematic of the experimental apparatus for cooling and trapping strontium. From the oven, the thermal atomic beam traverses a collimator, the transverse cooling stage, a mechanical shutter used to chop the atomic beam, a gave valve, a differential vacuum tube, and the Zeeman slower region. It then travels to the main vacuum chamber for collection in the MOT. The laser light for the $^1S_0$-$^1P_1$ MOT (461 nm) and the $^1S_0$-$^3P_1$ MOT are combined with a dichroic mirror before entering the chamber. The repump lasers (679 and 707 nm) are either stabilized to a reference cavity (as shown here) or strongly frequency modulated. TSP: titanium sublimation pump, BA: Bayard-Alpert vacuum gauge, DBS: dichroic beam splitter, BS: beam splitter, PBS: polarizing beam splitter, ECDL: external cavity diode laser, SMPM: single mode polarization maintaining, M: mirror, NI: nude vacuum gauge, CC: compensation coil

standard six-beam (3 retroreflected beams) 461 nm $^1S_0$-$^1P_1$ MOT that is loaded by a Zeeman slowed and transversely cooled atomic beam. The atomic beam is generated by an effusion oven (2 mm nozzle diameter) whose output is angularly filtered by a 3.6 mm diameter aperture located 19.4 cm from the oven nozzle. Separate heaters maintain the oven body (nozzle) at 575 ^{o}C (850 ^{o}C). The vapor pressure of Sr as a function of temperature is given in [55]. We have previously measured the atomic beam flux (divergence half-angle) to be approximately 3×10^{11} atoms/s (19 mrad) after the filtering aperture. The atomic beam is then transversely cooled by 2-dimensional 461 nm optical molasses. This laser beam, as well as the trapping and slowing beams described below, all have active intensity stabilization. Furthermore, the transverse cooling and trapping beams are mode filtered by transmission through a single mode optical fiber (before the intensity stabilization detector). Using cylindrical lenses, the transverse cooling beam is given an elliptical cross-section. These linearly polarized molasses laser beams have a $1/e^2$ diameter of $\sim$ 3 cm ($\sim$ 4 mm) along (normal to) the atomic beam propagation axis, contain 10 - 20 mW of power, and are detuned from the $^1S_0$-$^1P_1$ resonance by -10 to -15 MHz. Stray magnetic fields in the transverse cooling region are less than 1 G. After the transverse cooling region, the atomic beam passes through a 6.4 mm diameter electro-mechanical shutter and a gate valve that allows the oven to be isolated from the rest of the vacuum system.

The atomic beam then enters a water cooled 20 cm long constant deceleration σ^- Zeeman slower [56] with a peak magnetic field of $\sim$ 600 G, corresponding to a capture velocity of $\sim$ 500 m/s. The 461 nm Zeeman slowing laser is detuned from the $^1S_0$-$^1P_1$ resonance by -1030 MHz, contains roughly 60 mW of power, and is focused to approximately match the atomic beam divergence (although we have seen similar performance from a small, collimated beam). The window opposite the atomic beam is a z-cut Sapphire optical flat that is vacuum sealed via the Kasevich technique [57], broadband anti-reflection coated on the side opposite the chamber, and heated to 200 ^{o}C

to prevent the formation of Sr coatings. The alternating current (ac) window heater, which produces a small stray magnetic field, is only operated during the $^1S_0$ - $^1P_1$ MOT pre-cooling phase. A separate compensation coil reduces the slower magnetic field magnitude (gradient) to $<$ 100 mG ($<$ 8 mG/cm) at the trapping region, located 15 cm from the slower exit. Stray magnetic fields at the trap can be further nulled by three sets of orthogonally oriented Helmholtz coil pairs.

The trapping chamber is a cylindrical octagon with six 2 3/4" (two 6") ports in the horizontal x-y plane (along gravity z-axis). All windows are broadband anti-reflection coated. The MOT anti-Helmholtz coils, oriented such that the axial magnetic field gradient dB_z/dz lies along gravity, are mounted on a computer controlled precision linear track that allows the coil center to be translated from the trapping chamber to a 1 cm $\times$ 1 cm $\times$ 4 cm rectangular glass cell. The coils are constructed to provide window-limited optical access to the geometric center of the trapping chamber and produce axial gradients of 0.819 G/(cm-A). They are made by winding Kapton-insulated copper tubing with a square cross section (width $\simeq$ .41 cm) and a hollow core. The hollow core enables internal water cooling to remove the heat generated from the current flow (typically 61 A). The gradient is linear over a spatial range of $\pm$ 3 cm in both the axial and transverse directions. Current in the coils is regulated by a computer controlled servo and monitored with a Hall probe. For the $^1S_0$ - $^1P_1$ MOT, the axial magnetic field gradient $dB_z/dz = 50$ G/cm.

The trapping and oven chambers are each evacuated by a 40 l/s ion pump and a titanium sublimation pump. The two chambers are separated by a 6.4 mm diameter $\times$ 16 mm long cylindrical differential pumping tube located between the electro-mechanical shutter and the gate valve. Typical vacuum levels in the oven, trapping, and glass cell chambers during operation of the atomic beam are 2×10^{-8} Torr, 1.5×10^{-9} Torr, and 3×10^{-10} Torr, respectively.

461 nm cooling and trapping light is produced by frequency doubling the optical-

fiber-filtered-output of a tapered diode MOPA (Master Oscillator Power Amplifier) amplifier (Eagleyard Photonics) at 922 nm (we have previously used a single mode Ti:Sapphire ring laser with intracavity optical diode, birefringent filter, and dual etalons instead of this diode system). This amplifier (which outputs 1.5 W, giving 1 W after the optical fiber) is seeded by an external cavity diode laser (ECDL) (seeding power $\sim$ 45 mW). Although the polarization-maintaining optical fiber acts as a Gaussian mode filter, the high intensity injected into the fiber seems to induce polarization rotation which occasionally occurs on relatively short time scales (mrad in minutes or less). Future design could benefit from the use of large-core single mode fiber which tolerates higher input powers. The frequency doubling occurs by splitting the 922 nm light (approximately 2/3 and 1/3) and injecting the two beams into two external buildup cavities with intracavity nonlinear crystals[58]. Together, these cavities produce $>$ 250 mW of single-mode light at 461 nm. We chose these short standing wave buildup cavities (input coupler $R > 95\%$ at 922nm, back side of crystal HR at 922 nm), together with a temperature phase matched (150 ^{o}C) $KNbO_3$ nonlinear crystal (high nonlinear coefficients), because of the very high second harmonic conversion efficiency that could be achieved (typical 50%, best 60%). We could not achieve these same efficiencies with longer running wave bow-tie cavities. The motivation for splitting the light into two cavities was rooted in thermally-induced instability which developed when the generated 461 nm light exceeded $\sim$175 mW. This thermal effect led to non-Gaussian transverse mode features (ring structures) that were temperature and phase-matching dependent, and which limited the amount of useful 461 nm power.

The resulting 461 nm light is then offset locked to the $^1S_0$ - $^1P_1$ resonance by saturated absorption feedback to the ECDL seed laser at 922 nm (laser piezo-electric transducer, PZT). The saturated absorption spectrometer utilizes a commercially available "see-through" Sr hollow cathode lamp (Hamamatsu). The probe beam is phase modulated by an electro-optic modulator (EOM), and the pump beam is amplitude

modulated by an acousto-optic modulator (AOM). The probe absorption signal then undergoes two stages of phase-sensitive demodulation to recover the dispersion shaped signal used for stabilizing the 922 nm laser. Relative frequencies of the transverse cooling, Zeeman slower, and trapping laser beams are controlled with acousto-optic modulators (AOMs) which are also used as shutters. Additional extinction of 461 nm light is provided by mechanical shutters. The intensity stabilized trapping beams have $1/e^2$ diameters of $\sim$ 3 cm, are detuned from the $^1S_0$-$^1P_1$ resonance by -40 MHz, and typically have a combined one way power of 30 mW (all three dimensions are retroreflected). For these settings, we find the $^1S_0$-$^1P_1$ MOT population is maximized. Further increases in, for example, the trapping beam power usually only increase the cloud temperature. $^1S_0$-$^1P_1$ MOTs are monitored with a charge-coupled-device (CCD) camera and a calibrated photodiode. Typical trap lifetimes, populations, and temperatures are 20 ms, 3×10^7, and 2.5 mK, respectively (without repumping). The atom population is determined by collecting 461 nm fluorescence from the MOT. This fluorescence is collected with a 2" lens located 15 cm from the MOT atoms and focused on a calibrated photodiode. The photon scattering rate is determined either by empirical measure of the incident trapping laser intensities or directly by the MOT lifetime in the absence of repumping [59].

Operation of the $^1S_0$-$^1P_1$ MOT efficiently populates the ground-state-like $^3P_2$ metastable excited-state (see Figure 2.1, $\sim$ 500 s radiative lifetime [60, 61]) via $^1P_1 \rightarrow {}^1D_2 \rightarrow {}^3P_2$ radiative decay. Consequently, $^1S_0$-$^1P_1$ MOT loading times are typically limited to 10 - 50 ms [62, 63, 59]. As described in Section 2.2.1, this is overcome by applying repumping lasers at 707 nm and 679 nm to optically pump this population to $^3P_1$ where atomic decay returns it to $^1S_0$. These two ECDLs have been operated in two modes. In the first mode, typically used for ^{88}Sr, each laser is locked to a reference cavity that is simultaneously locked to a frequency stabilized helium neon laser utilizing an intracavity iodine cell for stabilization. Double-passed AOMs are then used

to tune the absolute laser frequencies to the atomic transitions. In a second scheme, more recently used with ^{87}Sr, the lasers not locked to stabilization cavities but are instead strongly frequency modulated by application of a sawtooth waveform to their drive current and intracavity laser piezo transducer (PZT). The center frequency and modulation depth and frequency are empirically tuned to optimize MOT size. The modulation approach seems particularly useful for ^{87}Sr, which possesses a large number of nondegenerate hyperfine states which can become populated during optical pumping or re-pumping. After passing through a single-mode polarization-maintaining optical fiber, the co-propagating 707 nm and 679 nm laser beams are expanded to a $1/e^2$ intensity diameter of $\sim$ 1 cm and delivered to the $^1S_0$ - $^1P_1$ MOT. An AOM and mechanical shutter located before the beam expansion optics allows for rapid and complete intensity extinction ($<$ 1 μs transition time with AOM). At the trap, the 707 nm (679 nm) beam contains $\sim$ 1 mW ($\sim$ 2.5 mW) of power, resulting in an optical re-pumping time of $<$ 100 μs. With both lasers operating, the $^1S_0$-$^1P_1$ MOT population and lifetime are typically enhanced by 10$\times$ and 15$\times$, respectively.

It should be noted that along with contributing to $^1S_0$-$^1P_1$ MOT loss, $^1P_1 \rightarrow {}^1D_2 \rightarrow {}^3P_2$ radiative decay continuously loads mK atoms in the $^3P_2(m_J = 1,2)$ states into a magnetic trap formed by the $^1S_0$ - $^1P_1$ MOT quadrupole magnetic field [59, 64, 65, 66]. Importantly, these samples are expected to display a wealth of binary collision resonances that arise due to an interplay between anisotropic quadrupole interactions and the local magnetic field [67, 68, 69]. Qualitatively similar processes and hence, collision resonances, are predicted for polar molecules immersed in electrostatic fields [70]. Studies of metastable Sr collision dynamics will thus likely impact the understanding of a diverse range of physical systems. To pursue these studies, the trapping apparatus was designed to first load $^3P_2$ state atoms into the quadrupole magnetic trap and then mechanically translate [71] the sample to the glass cell chamber. Subsequently, a tight Ioffe-Pritchard magnetic trap could be used to perform a variety of collision

experiments.

2.3 Laser cooling strontium: Narrow line laser cooling in the $^1S_0$-$^3P_1$ MOT

The $^1S_0$-$^1P_1$ MOT described above conveniently cools and traps Sr at mK temperatures. Unfortunately, this temperature still corresponds to an rms (root-mean-squared) velocity of 50 cm/s. The Doppler effect resulting from a gaussian velocity distribution with $v_{rms} = 50$ cm/s yields a Doppler broadened, spectroscopic profile of 1 MHz. This would make observation and precise measurement of the very narrow clock transition difficult. Still colder temperatures are required to reduce this effect, which scales with the square root of the temperature. In addition, ultimately tight atomic confinement is desired for probing the clock transition. Because this confinement is achieved with the relatively weak interaction of a laser intensity gradient with the induced atomic dipole polarizability, colder atoms relax the laser intensities required for trap depths which exceed the atom thermal energy. Although ^{88}Sr lacks the ground state substructure for sub-Doppler cooling mechanisms, the relatively weak $^1S_0$-$^3P_1$ intercombination transition is well-suited to Doppler cooling and has a low Doppler limit of T= 200 nK. Laser cooling on this transition explores the novel regime where the transition linewidth ($\gamma = 7.6$ kHz) is similar to the atomic recoil frequency ($\omega_r/2\pi = 4.7$ kHz), hence the name narrow line cooling.

2.3.1 Narrow line laser cooling dynamics

Fully understanding narrow line laser cooling requires first clarifying the difference between broad and narrow Doppler cooling lines. Broad lines, historically used for the vast majority of laser cooling experiments [44], are defined by $\Gamma/\omega_r >> 1$. The 461 nm ^{88}Sr $^1S_0$ - $^1P_1$ transition shown in Fig. 1(a), which typifies a broad line, has, for example, $\Gamma/\omega_r \sim 3\times10^3$. In this case, Γ, or more generally the power-broadened linewidth

Γ_E, is the natural energy scale. Here, $\Gamma_E = \Gamma\sqrt{1+s}$ is defined by the saturation parameter $s = I/I_S$ where I (I_S) is the single-beam peak intensity (transition saturation intensity). Semiclassical physics thus governs the cooling process and the photon recoil, although essential to quantitatively understanding energy dissipation [43], serves more as a useful conceptual tool than a dominant player in system dynamics. Moreover, gravity is essentially negligible since the ratio of the maximum radiative force to the gravitational force, $R = \hbar k\Gamma/2mg$, is typically on the order of 10^5, where g is the gravitational acceleration.

In contrast, narrow Doppler cooling lines are characterized by $\Gamma/\omega_r \sim 1$. The 689 nm ^{88}Sr $^1S_0$ - $^3P_1$ transition used in this work, for example, has $\Gamma/\omega_r = 1.6$ where $\Gamma/2\pi$ ($\omega_r/2\pi = \hbar k^2/4\pi m$) is 7.5 kHz (4.7 kHz). In this case, the relevant thermal-mechanical energy scale and thus the underlying semiclassical or quantum mechanical nature of the cooling depends on s. Details of a given cooling process are then set by the laser detuning $2\pi\delta = \Delta = \omega_L - \omega_A$ where ω_L (ω_A) is the laser (atomic resonance) frequency. In particular, $\delta < 0$ $^1S_0$-$^3P_1$ MOT cooling and trapping dynamics can be divided into three qualitatively distinct regimes, hereafter labelled (I - III), defined by the relative size of $|\Delta|$, $\Gamma \sim \omega_r$, and Γ_E. In regime (III), corresponding to trapping beam intensities on the order of $I_S = 3\mu\mathrm{W/cm}^2$ or $s \sim 1$ ($\Gamma_E \sim \omega_r$), ω_r is the natural energy scale. Here, single photon recoils and consequently, quantum physics, govern trap dynamics. Temperatures as low as roughly half the photon recoil limit ($T_r = 2\hbar\omega_r/k_B = 460$ nK) are possible despite the incoherent excitation provided by the trapping beams [72, 42, 73].

Conversely, for $s \gg 1$ the system evolves toward semiclassical physics where $\Gamma_E \gg \omega_r$ and hence Γ_E is the dominant energy scale. In this case, cooling and motional dynamics are determined by the relative size of Γ_E and Δ. In regime (II), the $\Delta < \Gamma_E$ radiative force produces damped harmonic motion and, in analogy to standard Doppler cooling, MOT thermodynamics set entirely by the velocity dependence of the force [41, 74]. For these conditions, the expected δ- and s-dependent temperature minima are observed,

although with values globally smaller than standard Doppler theory predictions. Alternatively, in regime (I) where $\Delta > \Gamma_E$, the atom-light interaction is dominated by single-beam photon scattering and trap thermodynamics become intimately linked to both the velocity and the spatial dependence of the force. Here, gravity plays an essential role as the ratio R for the $^1S_0$ - $^3P_1$ transition is only ~ 16. Consequently, the atoms sag to vertical positions where the Zeeman shift balances Δ, leading to Δ-independent equilibrium temperatures.

More insight into regime (I) and (II) thermal-mechanical dynamics is provided by the semiclassical radiative force equation [41]

$$\begin{aligned} \vec{F}(\vec{v},\vec{x}) &= \frac{\hbar\vec{k}\Gamma}{2}\Big[\frac{s}{1+s'+4(\Delta-\vec{k}\cdot\vec{v}-\mu d\vec{B}/dx\cdot\vec{x})^2/\Gamma^2} \\ &- \frac{s}{1+s'+4(\Delta+\vec{k}\cdot\vec{v}+\mu d\vec{B}/dx\cdot\vec{x})^2/\Gamma^2}\Big] \\ &- m\vec{g}. \end{aligned} \tag{2.12}$$

where $\vec{x} = \{x, y, z\}$, $d\vec{B} = \{dB_x, dB_y, dB_z\}$, and $\mu = (g_J\mu_B/\hbar)$ where $g_J = 1.5$ is the $^3P_1$ state Lande g-factor and μ_B is the Bohr magneton. The parameter $s' > s$ accounts, along a single axis, for saturation induced by the remaining four trapping beams. Figure 2.5(a) shows the $^1S_0$ - $^3P_1$ radiative force at $s = s' = 248$ for a range of δ values while Figure 2.6(a) shows the force at δ = -520 kHz for a range of $s = s'$ values. As described earlier, the qualitative nature of the force and hence the resulting trap mechanical dynamics depends on the relative size of Δ and Γ_E. For regime (I), corresponding to $|\delta| > 120$ kHz in Figure 2.5 or $s < 248$ in Figure 2.6, $\Delta > \Gamma_E$ and the 3D radiative force acts only along a thin shell volume marking the outer trap boundary. Here, the trap boundary roughly corresponds to positions where the radiative force is peaked. This situation, as shown by Figures 2.5 and 2.6, produces a box potential with a gravitationally induced z-axis tilt. Hence, in the x-y plane, motion consists of free-flight between hard wall boundaries while along the z-axis, mechanical dynamics are set by the relative size of the radiative force "kicks," gravity, and the cloud thermal energy.

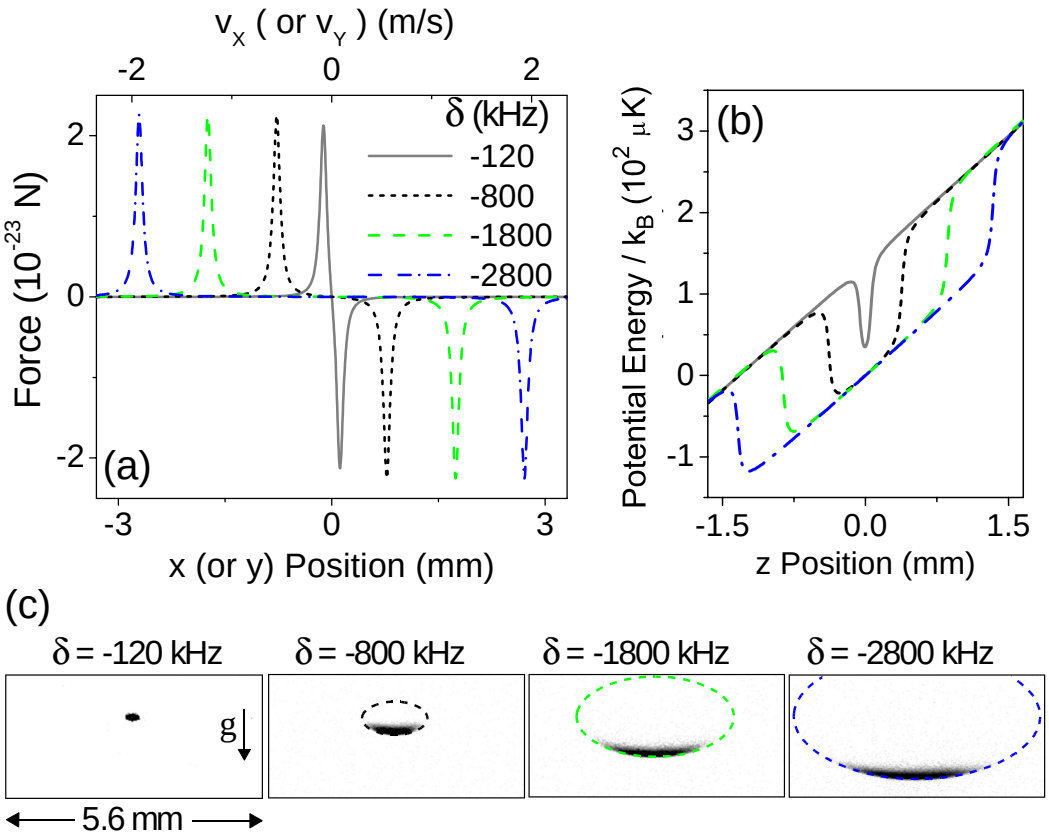

Figure 2.5: (a) Semiclassical radiative force versus position (bottom axis, $v_x = v_y = 0$) and velocity (upper axis, x=y=0) for different detunings. The corresponding trap potential energy in the z direction (b) and in situ images of the $^1S_0$-$^3P_1$ MOT (c). Dashed lines in (c) are calculated maximum force contours (with s =248).

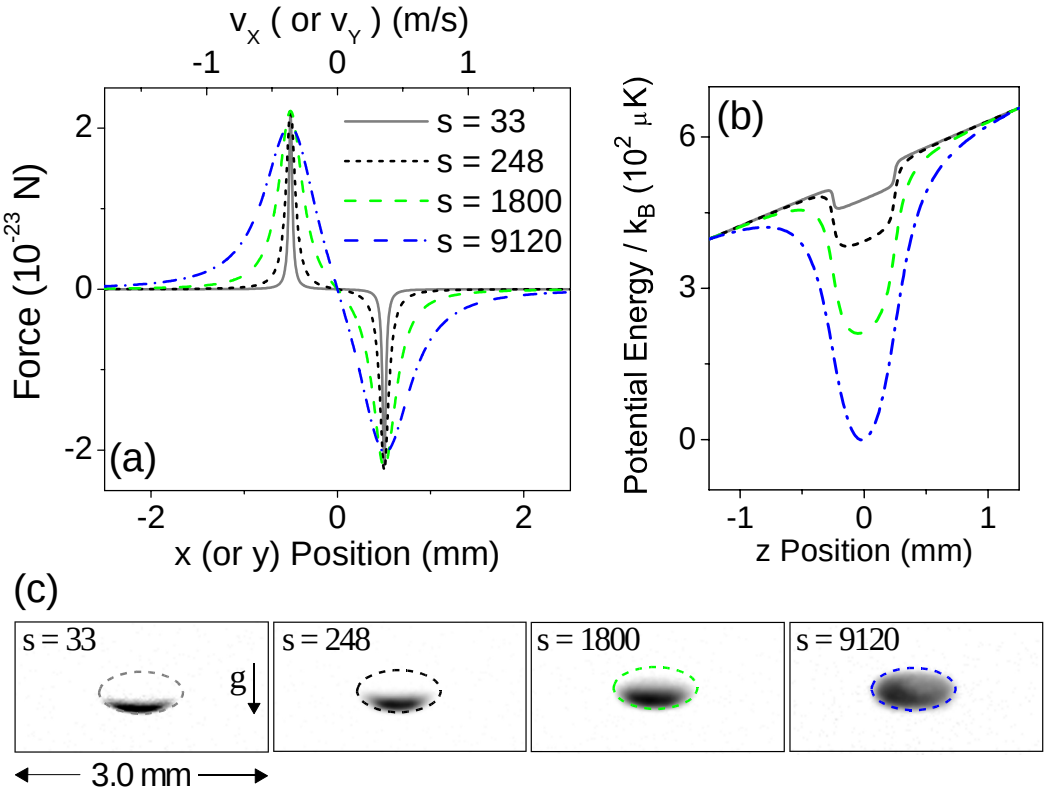

Figure 2.6: (a) Semiclassical radiative force versus position (bottom axis, $v_x = v_y = 0$) and velocity (upper axis, $x = y = 0$) for different intensities. The corresponding trap potential energy in the z direction (b) and in situ images of the $^1S_0$-$^3P_1$ MOT (c). Dashed lines in (c) are calculated maximum force contours. For each, $\delta = -520$ kHz.

The thermal energy is small compared to the gravitational potential energy. Moreover, the ratio of the maximum radiative force to the gravitational force is $R \sim 16$. Thus, the atoms sink to the bottom of the trap where they interact, along the z-axis, with only the upward propagating trapping beam.

As δ decreases in Figure 2.5(a) or s increases in Figure 2.6(a), the trap mechanically evolves to regime (II) where $\Delta < \Gamma_E$ produces a linear restoring force and hence, damped harmonic motion [41, 74]. Consequently the trap potential energy assumes the U-shaped form familiar from standard broad line Doppler cooling. As the trap moves more fully into regime (II), perturbations to the potential energy due to gravity become less pronounced. One expects, therefore, that the cloud aspect ratio will evolve toward the 2:1 value set by the quadrupole magnetic field.

The intuitive descriptions developed above are directly confirmed by Figures 2.5(c) and 2.6(c) which show in-situ images of the $^1S_0$ - $^3P_1$ MOT along with overlaid maximum force contours calculated from Equation 2.12. For excitation conditions corresponding to regime (II), the cloud approaches the 2:1 quadrupole magnetic field aspect ratio. In contrast, for regime (I) the cloud x-y width is determined largely by the separation between x-y force maxima or alternatively, by the wall separation for the x-y potential energy box. In the vertical direction, the atoms sink to the bottom of the trap where the lower cloud boundary z_0 is defined by the location of the z-axis potential energy minima which is, in turn, proportional to the position where the Zeeman shift matches the laser detuning. As δ increases, z_0 shifts vertically downward, an effect predicted in Figure 2.5(b) and clearly revealed in Figure 2.5(c).

MOTs using the $^1S_0$ - $^3P_1$ transition display a rich variety of thermodynamic behaviors that are directly linked to the mechanical dynamics explored in section IV. Figure 2.7 shows the MOT equilibrium temperature T_M versus δ for saturation parameters ranging from $s = 7.5$ to $s = 1800$. For large δ and s, corresponding to regime (I) where $\Delta > \Gamma_E \gg \Gamma$, T_M is basically δ-independent. Recall that for $\Delta > \Gamma_E$, the

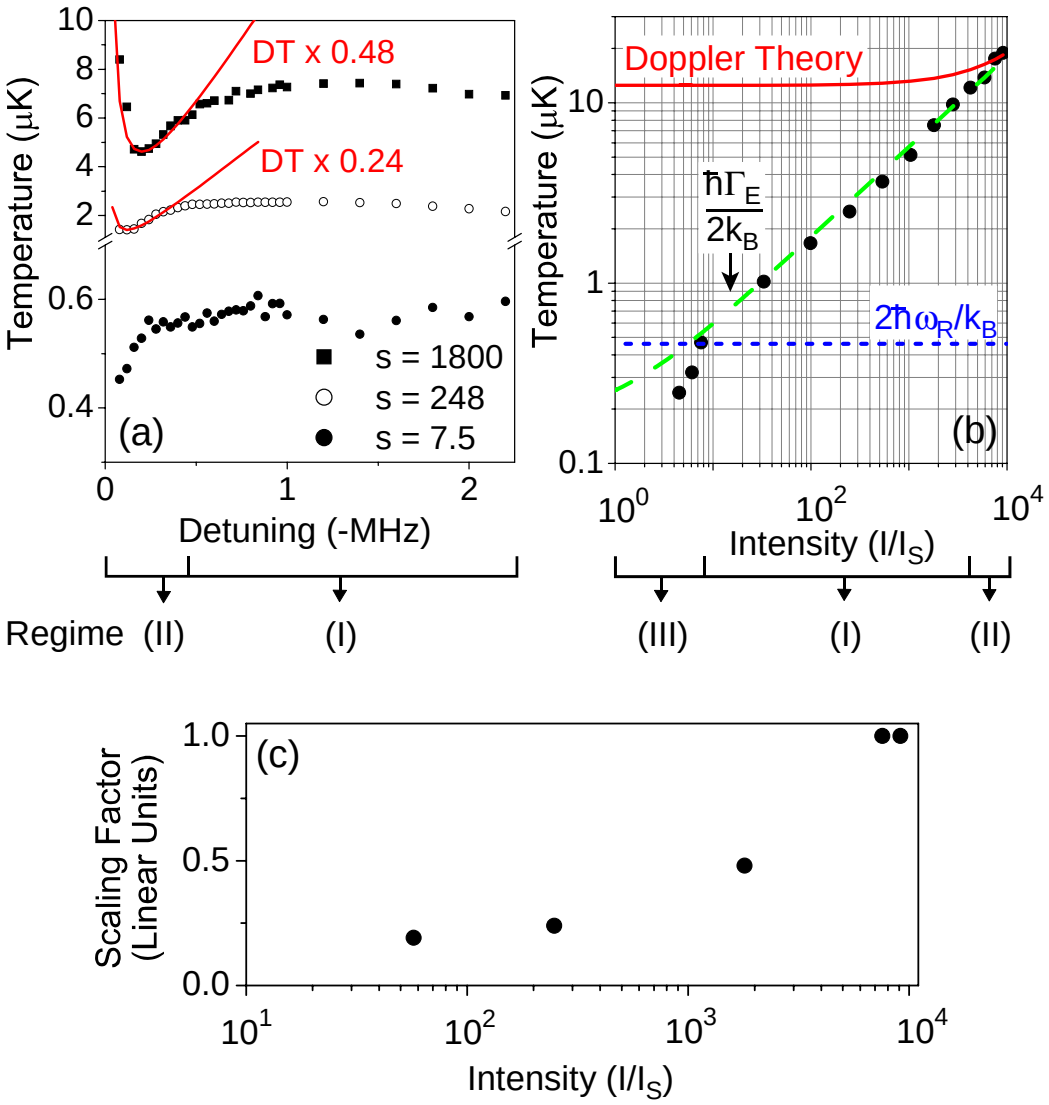

Figure 2.7: $^1S_0$-$^3P_1$ MOT temperature versus (a) detuning (δ) for various intensities and (b) intensity (s) at $\delta = -520$ kHz. In (a), DT is standard Doppler theory. In (b), solid circles are experimental data while the solid, dashed, and short dashed lines give standard Doppler theory, the Doppler limit $\hbar\Gamma/2k_b$, and the single-photon recoil limit $2\hbar\omega_r/k_b$, respectively. (c) Global scaling factor applied to Doppler theory in order to match regime (II) data versus intensity.

cloud sags to the bottom of the trap where interactions occur, along the vertical z-axis, with only the upward propagating trapping beam. Moreover, due to polarization considerations and the free-flight motion executed by atoms in the horizontal plane, horizontal beam absorption rates are more than 4× smaller than the vertical rate. Trap thermodynamics, therefore, are dominated by a balance between gravity and the radiative force due to the upward propagating beam. Here, it is important to realize that as δ changes, the z-axis atomic position z_0 self adjusts such that the effective detuning, Δ - $\mu(dB_z/dz)z_0$, remains constant. Consequently the trap damping and diffusion coefficients, and thus the equilibrium temperature, remain constant.

To obtain a quantitative expression for T_M under these conditions, we first find the damping coefficient α by Taylor expanding the semiclassical force expression

$$\begin{aligned} F(v_z, z) &= \frac{\hbar k \Gamma}{2} \left[\frac{s}{1 + s' + \dfrac{4(\Delta - k v_z - \mu(dB_z/dz)z)^2}{\Gamma^2}} \right] \\ &- mg. \end{aligned} \tag{2.13}$$

where $(\partial F/\partial v) = \alpha$ is evaluated at $v_z = 0$, z = z_0. Solving $F(0, z_0) = 0$ and using $R = (\hbar k \Gamma / 2mg)$, the δ-independent effective detuning is given by

$$\frac{\Delta - \mu(dB_z/dz)z}{\Gamma} = -\frac{\sqrt{Rs - s' - 1}}{2} \tag{2.14}$$

which, in combination with Equation 2.13, states that the scattering rate depends only on R, s, and Γ. Substituting this expression into $(\partial F/\partial v)$, we obtain the damping coefficient

$$\alpha = -\frac{2\hbar k^2 \sqrt{Rs - s' - 1}}{R^2 s} \tag{2.15}$$

Next, the diffusion coefficient D_p is calculated by substituting Equation 2.14 into the single-beam scattering rate. D_p is then given by

$$D_p = \frac{\hbar^2 k^2 \Gamma}{2R} \tag{2.16}$$

Combining Equations 2.15 and 2.16, the predicted δ-independent equilibrium temperature is

$$\begin{aligned} T = \frac{D_p}{|\alpha|} &= \frac{\hbar\Gamma\sqrt{s}}{2k_B}\frac{R}{2\sqrt{R - s'/s - 1/s}} \\ &= \left(\frac{\hbar\Gamma_E}{2k_B}\right) N_R \end{aligned} \tag{2.17}$$

where we have used $\sqrt{s} \sim \sqrt{s+1}$ for $s \gg 1$. The numerical factor N_R is approximately 2 over the entire relevant experimental range. Regime (I) temperatures, therefore, depend only on Γ_E. To test this prediction, Figure 2.7(b) shows T_M versus s for a fixed large detuning δ = -520 kHz. For the central portion of the plot where regime (I) dynamics are relevant, we find good agreement with Equation 2.17 aside from a global scaling factor of two.

For small δ in Figure 2.7(a), the system evolves from regime (I) to regime (II) where $\Delta < \Gamma_E$, $\Gamma_E \gg \Gamma$. As this transition occurs, trap dynamics change from free-flight to damped harmonic motion. Here, one expects thermodynamics similar to ordinary Doppler cooling including δ- and s-dependent minima with equilibrium values having the functional form [41, 74]

$$\begin{aligned} T(s,\Delta) &= T_0\frac{\Gamma_E}{4|\Delta|}\left[1 + 4(\Delta/\Gamma_E)^2\right] \\ T_0 &= (\hbar\Gamma_E)/(2k_B) \end{aligned} \tag{2.18}$$

where T_0, realized at $\Delta = \Gamma_E/2$, is a generalized version of the $s \ll 1$ Doppler limit. As shown by the solid lines in Figure 2.7(a), Equation3 2.18 correctly reproduces the functional shape of the data. As shown by Figure 2.7(c), however, matching the absolute data values requires multiplying Equation 2.18 by a s-dependent global scaling factor (≤ 1) whose value decreases with s, leading to temperatures well below the standard Doppler limit T_0. In contrast to ordinary Doppler cooling, the cloud thermal energy in regime (II) is thus not limited by half the effective energy width of the cooling transition. Notably, we find this surprising result cannot be explained either by analytic treatments

of Equation 2.12 or semiclassical Monte-Carlo simulations of the cooling process. The Monte-Carlo simulations, in fact, simply reproduce standard Doppler theory. Finally, as s approaches unity in Figure 2.7, the trap enters regime (III) where $\Gamma \sim \omega_r \sim \mathrm{k}_B\mathrm{T}/\hbar$ and thus the cooling becomes fully quantum mechanical. Here, we obtain a minimum temperature of 250(20) nK, in good agreement with the quantum mechanically predicted value of half the photon recoil temperature $T_R/2 = \hbar\omega_r/\mathrm{k}_B = 230$ nK [42]. For more information on the dynamical approach to equilibrium, as well as novel heating dynamics for $\delta > 0$, see [75, 76].

2.3.2 Experimental details of the $^1S_0$-$^3P_1$ MOT

Exploring 689 nm $^1S_0$-$^3P_1$ narrow line cooling dynamics requires a laser system whose short-term linewidth is small compared to the 7.5 kHz transition natural width. In addition, the absolute laser frequency must be referenced, with similar stability, to the $^1S_0$-$^3P_1$ transition and be tunable over a range of ~ 10 MHz. The 689 nm laser stabilization and control system consists of a master ECDL, a temperature stabilized and vibration isolated passive optical reference cavity, a Sr saturated absorption spectrometer, and two slave ECDLs phase locked at an offset frequency from the master laser. For ^{88}Sr, having two slave ECDLs is unnecessary, and we have previously operated the master as a seeding laser to injection lock a single second laser. In this approach, the master was stabilized to the cavity (at short time scales) and the Sr spectrometer (at longer time scales) and the injected laser simply acted as an amplifier to give sufficient output power for the $^1S_0$-$^3P_1$ MOT operation. However, as described in the next section, the ^{87}Sr MOT requires two 689 nm lasers. To facilitate fast switching between trapping of ^{87}Sr and ^{88}Sr, we implemented the offset frequency locking of the two ECDLs.

The linewidth of the master ECDL is first narrowed by locking the laser to a stable optical reference cavity via the Pound-Drever-Hall technique [77]. The cavity consists of high reflectivity Zerodur substrate mirrors that are optically contacted to

a Zerodur spacer. The measured cavity finesse (free spectral range) at 689 nm is $\sim$ 3800 (488.9 MHz), giving a linewidth for the TEM_{00} mode of $\sim$ 130 kHz. To isolate the cavity from environmental perturbations, the cavity is suspended by two thin wires inside a temperature stabilized can that is evacuated to $< 10^{-6}$ Torr and mounted on vibration damping material. The 689 laser light is made resonant with the cavity mode by use of a double-passed 1 GHz AOM. The electronic feedback for laser stabilization has a bandwidth of $\sim$ 2 MHz, and is divided between a slow loop that adjusts the piezo-electric mounted ECDL grating and a fast loop to the diode laser current. With the cavity lock engaged, in-loop analysis shows that jitter in the cavity-laser lock is $<$ 1 Hz.

To further evaluate the performance of the 689 nm laser system, the short-term laser linewidth is determined by beating the cavity-locked 689 nm light against a fs comb that is locked to a second optical cavity [78]. Here, we find a short-term linewidth of $<$ 300 Hz, where the measurement is limited by the phase-noise originating from the optical fiber connecting the 689 nm light to the fs comb. Next, the long-term stability of the 689 nm laser is evaluated by beating the cavity locked 689 nm light against a fs comb that is locked to a hydrogen maser via a fiber optical link to NIST [79, 80]. From these measurements, the laser-cavity system drifts $\sim \pm$ 400 mHz/s and exhibits a 1 s stability of $< 4\times10^{-13}$ (i.e., $<$ 180 Hz) with the former value limited by cavity drift and the latter value limited by the short-term maser instability. To eliminate the slow cavity induced drift, the master ECDL is next locked to the $^1S_0$-$^3P_1$ resonance via saturated absorption feedback to the 1 GHz AOM. For added stability, a DC magnetic field is applied to the Sr vapor cell and the spectrometer is set to perform frequency modulation spectroscopy on the $^1S_0(m = 0)$ - $^3P_1(m = 0)$ transition. The $^1S_0$-$^3P_1$ spectrometer is very similar to the $^1S_0$-$^1P_1$ spectrometer described above. The key difference is the atom source: rather than a hollow cathode lamp, the $^1S_0$-$^3P_1$ spectrometer utilizes a simple Sr heat pipe source (with $\sim$ 25 mTorr of argon buffer gas). Saturation spectroscopy with dual

modulation (high frequency phase modulation of the probe beam and low frequency amplitude modulation of the saturation pump beam) and demodulation provides the final error signal for stabilizing the master 689 nm laser to the atomic transition. With the system fully locked, the 1 s stability is then $\sim 4{\times}10^{-13}$ while for time scales < 5 min, the drift rate can be as small as $\sim \pm$ 10 mHz/s. On longer time scales, baseline fluctuations in the error signal cause frequency excursions that are $\sim$ 1 kHz/day.

A portion of the 689 nm master ECDL output is next used to generate heterodyne beats with the two frequency offset slave lasers. Each slave laser output, after double-passing through an AOM used for frequency shifting and intensity chopping, is then coupled into a single-mode polarization-maintaining optical fiber. Upon exiting each fiber, the 689 nm light has up to 6 mW of power and is expanded to a $1/e^2$ diameter of 5.2 mm and divided into three equal intensity trapping beams. Dichroic beamsplitters are then used to co-align the 689 nm and 461 nm trapping beams. The trapping beam waveplates are $3\lambda/4$ ($\lambda/4$) at 461 nm (689 nm).

$^1S_0$ - $^3P_1$ cooling and trapping dynamics are monitored either by in-situ or time-of-flight (TOF) fluorescence images collected with an intensified CCD camera. The camera can view the cloud in either the horizontal x-y plane or nearly along gravity. The x-y plane (along gravity) images have a spatial resolution of 21 μm/pixel (37 μm/pixel). For in-situ images, the 461 nm trapping beams are pulsed on for 10 - 50 μs immediately after the atoms are released from the trap while for TOF images, the atoms are allowed to first freely expand for a variable amount of time. We have verified that in-situ images recorded with 461 nm pulses are identical to direct images of the in-trap 689 nm fluorescence aside from an improved signal-to-noise ratio. Typical TOF flight times are 20 - 35 ms. To determine cloud temperatures, gaussian fits are performed to both the in-situ and TOF images. The temperature T_M is then given by $T_M = (m/4k_B t_F{}^2)(R_F^2 - r^2)$ where t_F is the flight time and R_F (r) is the TOF (in-situ) $1/e^2$ radius of the cloud.

Figure 2.8 depicts the $^1S_0$ - $^3P_1$ MOT loading procedure [81]. A $^1S_0$ - $^1P_1$ MOT

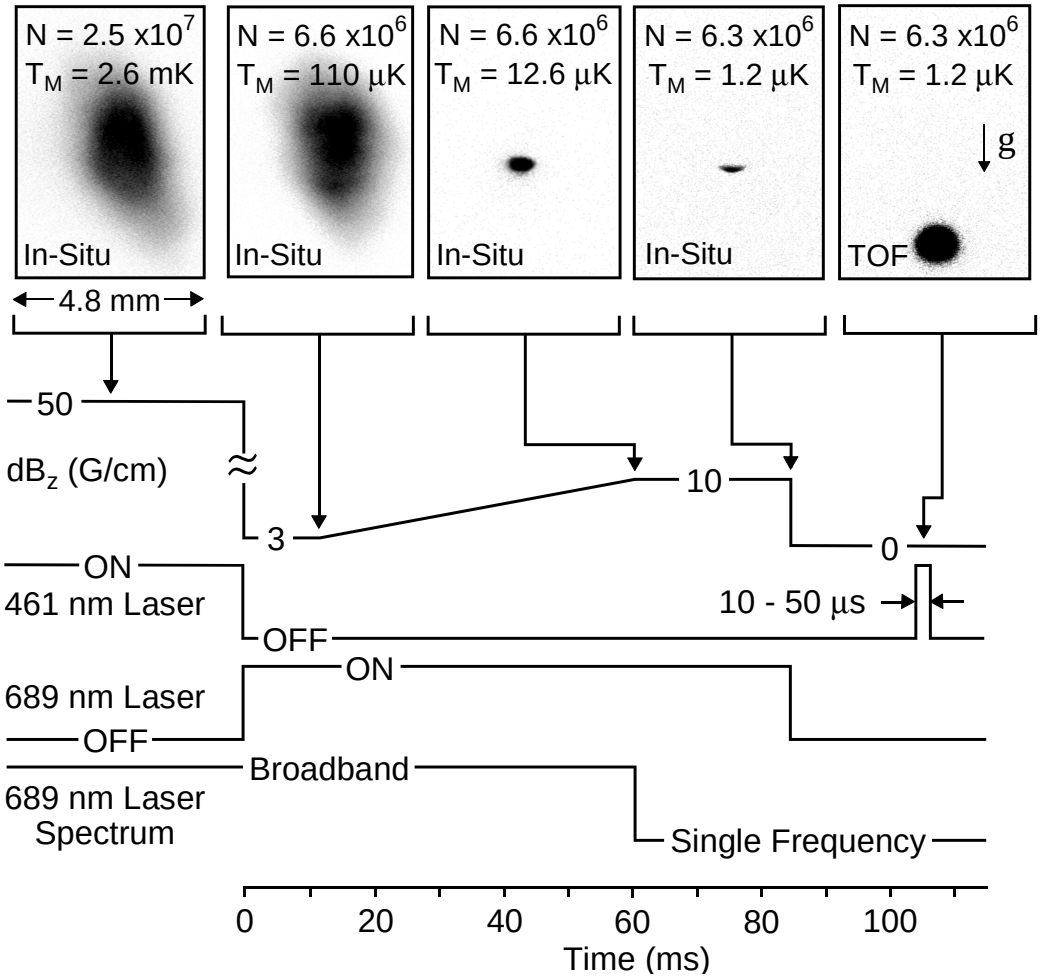

Figure 2.8: $^1S_0$-$^3P_1$ MOT timing diagram. Images at top show the atomic cloud at each stage of the cooling and spatial compression process. Starting from the right, the first four frames are in situ images while the last frame shows the cloud after 25 ms of free expansion from the $\delta = -520$ kHz, $s = 75$ single-frequency MOT. N (T_M) is the cloud population (temperature).

first pre-cools $\sim 3{\times}10^7$ atoms to $\sim$ 2.5 mK (lasting several hundred ms). At time t = 0, the 461 nm light and the atomic beam shutter are switched off, dB_z/dz is rapidly (ms) lowered to 3 G/cm, and red-detuned, broadband frequency modulated 689 nm trapping beams are turned on. 10 ms later and for the following 50 ms (100 ms for ^{87}Sr trapping), the cloud is compressed by linearly increasing dB_z/dz to 10 G/cm. Frequency modulation parameters for the 689 nm trapping beams are set to give complete spectral coverage of the $^1S_0$ - $^1P_1$ MOT Doppler profile and, as shown below, manipulate the cloud size at the end of the magnetic field ramp. Subsequently, at t = 60 ms, the frequency modulation is turned off and the atoms are held in a single-frequency MOT. As shown by the Figure 2.8 images, the best transfer into the 689 nm MOT decreases the sample temperature by more than three orders of magnitude while only reducing the cloud population by a typical factor of 3 - 4, giving final temperatures of ~ 1 μK and populations of $\sim 10^7$. Typical single frequency trap lifetimes and spatial densities are $\sim$ 1 s and $\sim 5{\times}10^{11}$ cm^{-3}, respectively. With 707 nm and 679 nm optical re-pumping of the $^1S_0$ - $^1P_1$ MOT, the $^1S_0$ - $^3P_1$ MOT population (spatial density) can be $4{\times}10^7$ ($3{\times}10^{12}$ cm^{-3}).

2.4 Laser cooling and trapping ^{87}Sr

2.4.1 The $^1S_0$-$^1P_1$ MOT

Hyperfine structure in ^{87}Sr splits the fine structure states as shown in Figure 2.9 [59, 17, 82] for the $^1P_1$, $^3P_1$, and $^3S_1$ states . With nuclear spin $I = 9/2$, the $J = 1$ $^1P_1$ state splits into three hyperfine states, $F = 11/2$, 9/2, and 7/2. Note in Figure 2.9 the unique ordering of the energy of these states, due to the strong role of the electric quadrupole hyperfine interaction. As described in Section 2.2.1, laser cooling and trapping is more straightforwardly achieved in J-$J+1$ transitions (or in the case of hyperfine structure for F-$F+1$ transitions). For this reason, the $^1S_0$ $F = 9/2$ - $^1P_1$

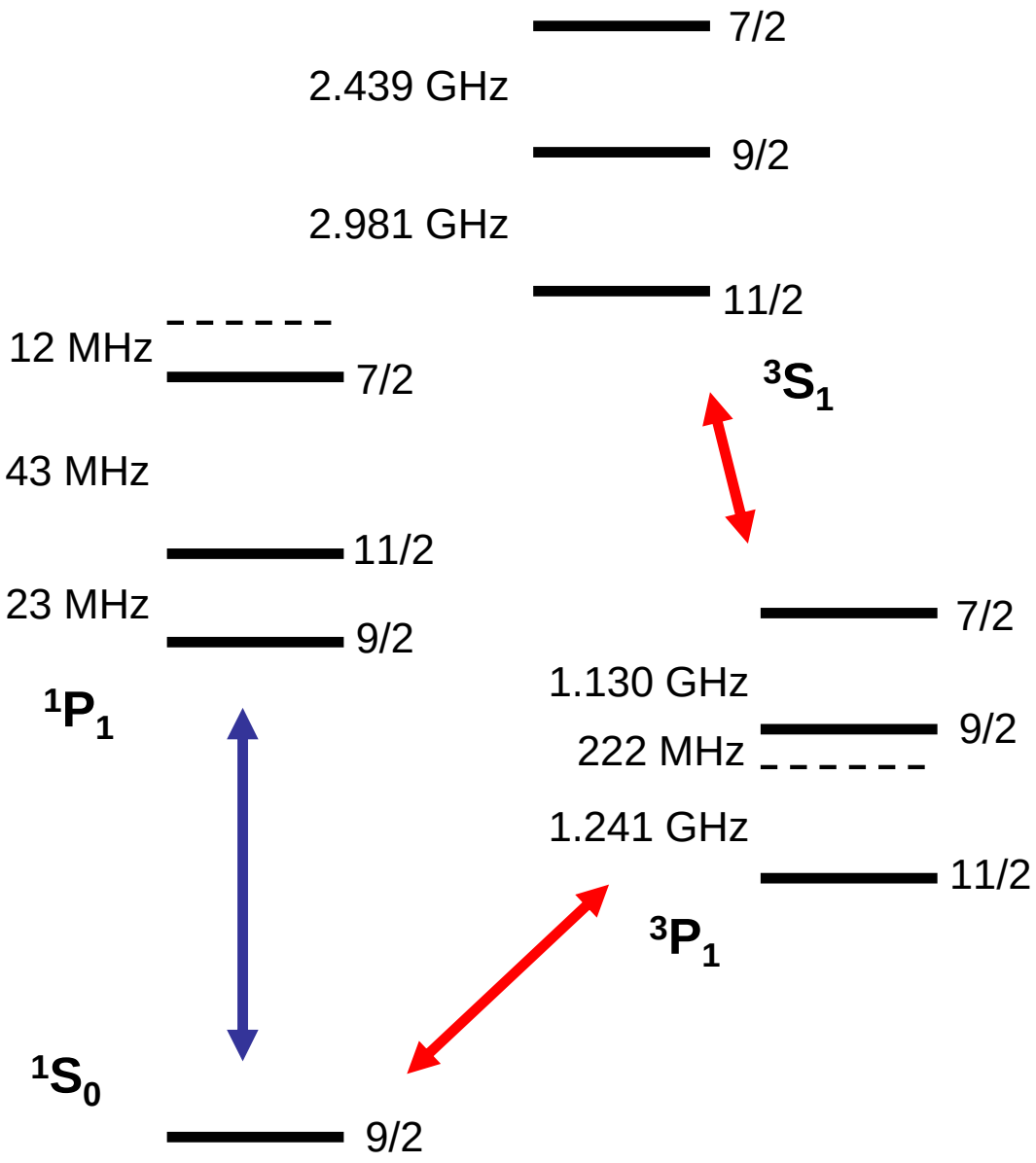

Figure 2.9: Energy level diagram relevant for laser cooling ^{87}Sr with its hyperfine structure. The total angular momentum, F, is denoted on the right side of each level. On the left, frequency shift from the equivalent ^{88}Sr transition is given (indicated by the dashed line).

$F = 11/2$ transition is used as the laser cooling cycling transition. Experimentally, the difference is minor. The cooling 461 nm laser is still locked to the ^{88}Sr spectrometer, but employs an extra 52-55 MHz frequency shift to yield trapping light which is 40 MHz red-detuned from the 9/2 to 11/2 transition.

Perhaps the detail most affected by the ^{87}Sr hyperfine structure is the repumping process. The $^3P_2$ state to which atoms are originally shelved has five hyperfine states with individual state splittings on the order of a GHz. All states are populated by atomic decay and require repumping to $^3S_1$, which has three hyperfine states with 2-3 GHz state separations. The sheer number of states complicates the repumping process. The most successful MOT population enhancement was found by strongly frequency modulating the repump lasers. Modulation is applied to both the laser drive current and the laser PZT of the repump ECDLs, and the modulation frequency and depth are varied to optimize MOT number. The repump spectrum is smeared across many GHz. With this approach, the ^{87}Sr MOT number could be enhanced by the repumping lasers by a factor of 15.

Unfortunately the 87 isotope has a much smaller natural abundance (7%) than the 88 isotope (83%). This means that atomic beam flux of ^{87}Sr emitted from the thermal oven is reduced to $7/83 \simeq 9\%$ of the ^{88}Sr flux. The effect of the reduced flux on the MOT trapped atom number is straightforward. Assuming the simple case of a constant MOT loading rate L, and a loss rate β that scales with the atom number N (e. g. no binary collisions), the atom number rate equation is just:

$$\frac{dN}{dt} = L - \beta N \tag{2.19}$$

whose solution is:

$$N = \frac{1}{\beta}(L - e^{-\beta t}). \tag{2.20}$$

The steady state population is simply $N_{ss} = L/\beta$. Since the loading rate scales linearly with the atom beam flux, the resulting ^{87}Sr MOT atom number is smaller than the ^{88}Sr

MOT number by the ratio of the natural abundances. This is roughly what we observe experimentally.

One bonus associated with cooling the 87-isotope is that the presence of magnetic sublevels in $^1S_0$ permits sub-Doppler cooling. Experimentally, temperatures below 500 μK have been observed, more than a factor of 2 below the Doppler limit for the trap intensities used. Although not directly observed, temperature measurements made at different laser detunings and intensity suggest that temperatures as low as 40 μK could be achieved by operating with low trapping intensity [59]. We have not actively investigated this possibility, although it is an interesting option. Achieving these temperatures with the $^1S_0$-$^1P_1$ MOT could facilitate direct loading of atomic samples into an optical lattice without use of a free space $^1S_0$-$^3P_1$ cooling sequence.

2.4.2 The $^1S_0$-$^3P_1$ MOT

The experimental operation of the $^1S_0$-$^1P_1$ MOT was minimally affected when trapping ^{87}Sr rather than ^{88}Sr. However, this is not the case for the $^1S_0$-$^3P_1$ MOT. The difference originates because of the differences between the $^1S_0$-$^3P_1$ and $^1S_0$-$^1P_1$ transition linewidths, $\Delta\nu$, relative to their recoil frequencies, $\nu_r = \omega_r/2\pi$. These details were first described in the literature in [84]. To appreciate the difference, consider a MOT operating on the F to $F+1$ transition, which like the $^1S_0$-$^1P_1$ MOT, is $F = 9/2$ to $F = 11/2$. Of course, the Zeeman shift of this transition depends on the magnetic quantum number, m_F, of the states and is given by (for simplicity in 1-D):

$$h\Delta\nu = [(m_F \pm 1)\mu_e - m_F\mu_g]B(x) \tag{2.21}$$

where μ_g and μ_e are the Zeeman shift coefficients for the m_F ground and $m_F \pm 1$ excited state respectively, and B(x) is the linearly dependent magnetic field generated by the anti-Helmholtz coils with a zero crossing at the trap center. The complication originates with the case of $\mu_e \gg \mu_g$. To distinguish the cases of $\mu_e \simeq \mu_g$ and $\mu_e \gg \mu_g$, consider

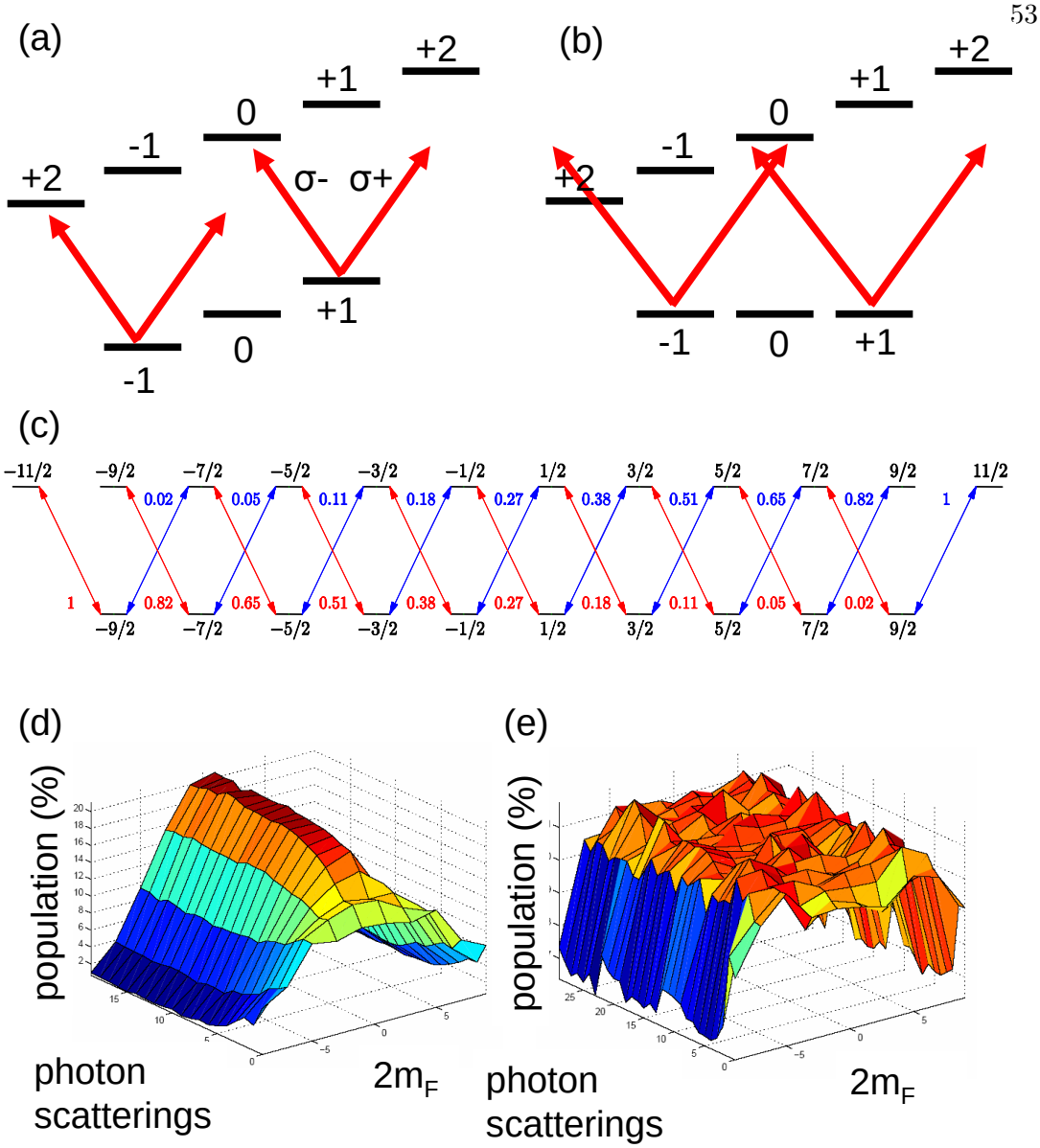

Figure 2.10: Laser cooling ^{87}Sr on the $^1S_0$-$^3P_1$ intercombination transition. (a) when $\mu_g \simeq \mu_e$, atomic population in any ground m_F level favors absorption of light from the appropriate direction for trapping (encoded with polarization). (b) when $\mu_g \gg \mu_e$, absorption of light from a given direction depends on m_F, and some m_F states are thus not suited to provide spatial confinement in a MOT. (c) Clebsch-Gordan (CG) coefficients (squared) among the $^1S_0$-$^3P_1$ $F = 9/2$-$F' = 11/2$ transition. Note that for a given ground m_F state, the CG coefficients are larger to excited states with larger $|m_F|$. This difference in CG coefficients is most dramatic for the $^1S_0$ $|m_F| = 9/2$ states, and can be used with the σ^+ and σ^- configuration to yield spatial confinement. (d) Based upon the CG coefficients, in the $^1S_0$-$^3P_1$ MOT, spontaneous decay from the excited $^3P_1$ $F' = 11/2$ state favors accumulating population in magnetic substates with small m_F where the difference in CG coefficients for absorption from the ground state is reduced [83]. (e) Using σ^+ and σ^- polarized light slightly red-detuned from the $^1S_0$-$^3P_1$ $F = 9/2$-$F' = 9/2$ transition, spontaneous decay evenly distributes population among all magnetic sublevels. Such an optical field can thus rapidly stir and randomize the population among m_F levels. This allows population to move to the m_F states best suited for spatial confinement at a given spatial location in the MOT and thus improve trap performance.

Figure 2.10. We assume the atom is moving relatively slowly (such that $\vec{k} \cdot \vec{v} \leq \Delta\nu$) and is located at x_0 such that $m\mu_g B(x_0) > 0$ (right hand side). Laser light is incident on the atom from both sides, σ^- from the right and σ^+ from the left. Because of the small Doppler shift, the red-detuned laser light remains red-detuned for both laser beams. For $\mu_e \simeq \mu_g$, it is clear that no matter what ground m_F state is occupied, the atom will always favor absorption of the red-detuned σ^- photon, and consequently will experience a net restoring force back to the trap center. For the case of $\mu_e \gg \mu_g$, the scenario is quite different. Due to the approximate degeneracy of the ground spin states, some spin states favor absorption of red-detuned σ^- photon, while others favor the red-detuned σ^+. Which is favored depends strongly not only on the spin state, but also on the atomic position, x_0 (determining the Zeeman shift), and these dependences frustrate the existence of a mean trapping force. Fortunately, an additional mechanism facilitates the trapping process: the relative transition probabilities between σ^+ and σ^- transitions, as given by the Clebsch-Gordan (CG) coefficients. As seen in Figure 2.10, for negative (positive) m_F in the ground state, the CG coefficients are larger (smaller) for σ^+ transitions than for σ^- transitions, thus favoring absorption of a σ^+ (σ^-) photon. The asymmetry between σ^+ and σ^- transition probabilities is small for $|m_F|$ close to 0, and becomes more pronounced as $|m_F|$ approaches F. This transition probability difference, aided by the spatially dependent Zeeman shift, can thus be used to generate a spatially dependent restoring force [85].

In order to work effectively, however, population must be able to move between the ground spin states so that when located at $x = x_0$ ($x = -x_0$), the population resides in negative (positive) m_F to experience the proper restoring force. Furthermore, since the restoring force from the CG asymmetry is most pronounced in the stretched states, ideally the population would not only be in the spin state with the proper sign, but also in the stretched state. Here, the narrow linewidth of the $^1S_0$-$^3P_1$ transition complicates the trap realization. Because the linewidth, $\Delta\nu$, is comparable to the recoil frequency,

ν_r, a few photon recoils are enough to induce a large enough change in the Doppler shift such that the transition is no longer in resonance with the laser field, and the transition is no longer cycled. This means that population is not moved very easily among the spin states by optical pumping effects from the trapping lasers. This non-mobile spin state population then has a high probability to be in the wrong spin state and not experience the efficient restoring force (e.g. in the worse case scenario, the population could be $m_F = +9/2$ for $x_0 > 0$). This is in contrast to a broad transition such as $^1S_0$-$^1P_1$, where many photon recoils yield a change in the Doppler shift equal to a small fraction of the transition linewidth. As a consequence, the atom regularly scatters trap photons and the population is rapidly pumped through all spin states, such that the probability to be in a spin state well-suited for trapping is reasonable. The reduced population "randomization" by optical pumping with $^1S_0$-$^3P_1$ is further exacerbated by the fact that spontaneous decay favors population accumulation in the states with small $|m_F|$. As described above, these states have reduced CG asymmetry, and thus less efficient trapping.

To provide population randomization, a second laser is introduced. Named for its capacity to evenly stir the population among the different spin states, the stirring laser is slightly red-detuned from the $F = 9/2$ to $F' = 9/2$ transition. The effect of scattering this σ^+ and σ^- polarized field is shown in Figure 2.10, where many photon scatterings result in population evenly distributed among the spin states (for simplicity $B = 0$ was assumed). This rapid population stirring ensures that the population can evolve to the needed spin state for efficient trapping. Furthermore, because μ_e for the stirring transition is more than four times smaller than that for the $F = 9/2$ to $F' = 11/2$ transition, the atoms remain in resonance over a longer distance and thus the laser can partly function as an optical molasses cooling laser to complement the trapping laser.

The combination of the stirring and trapping laser allows for operation of a μK temperature MOT with $> 10^5$ ^{87}Sr atoms. Experimentally these lasers are frequency

stabilized with offset locks from the master ECDL locked to the $^1S_0$-$^3P_1$ ^{88}Sr spectrometer. [84] demonstrated a five-fold improvement in the $^1S_0$-$^3P_1$ MOT lifetime by adding the stirring laser to the trapping laser. Still not as efficient as the simpler ^{88}Sr $^1S_0$-$^3P_1$ cooling, when cooling ^{87}Sr we typically allow for longer cooling times (50 ms single frequency cooling compared to 25 ms for ^{88}Sr).

2.5 Interrogation of Tightly Confined Atoms

2.5.1 Free Space Atom Interrogation

In the introduction, I briefly described the motivation for using laser cooled atoms in optical frequency standards: reducing the Doppler effect. More explicitly, in Equation 2.1, we considered the frequency of laser radiation in the laboratory frame which was essentially resonant with a moving atom in its own rest frame:

$$\omega_{abs} = \omega_0 + \vec{k} \cdot \vec{v} + \frac{\hbar k^2}{2m} \tag{2.22}$$

A large atom ensemble can allow for high measurement S/N of the transition. The ensemble usually has a well-defined temperature, T, indicating that the relative distribution of atoms with (1-D) velocity, v, is Gaussian, given by the Boltzmann factor:

$$P(v) = e^{\frac{-mv^2}{2k_bT}} \tag{2.23}$$

For a large atomic sample with rms Doppler shift, kv_{rms}, larger than the natural transition rate, Γ, of the transition being probed, a Gaussian spectroscopic profile is recovered with full width at half maxima (FWHM) equal to:

$$\Delta\nu_D = \sqrt{\frac{8k_bT\ln(2)}{m}}\frac{1}{\lambda_0} \tag{2.24}$$

where $\lambda_0 = 2\pi c/\omega_0$ is the transition wavelength and m is the atomic mass. This inhomogeneous, Doppler broadening originates from the fact that atoms in different velocity groups are resonant at different probe frequencies. The negative effect of Doppler

broadening on a frequency standard is seen by direct consideration of Equation 1.1. Any broadening beyond the natural linewidth degrades the achievable stability of an atomic standard. For decades, Doppler-free spectroscopic techniques such as saturation spectroscopy have been used to probe atomic transitions nearly free of Doppler broadening. Unfortunately, such techniques typically take advantage of only a small fraction of the total atomic sample - those atoms with a small enough atomic velocity that $\vec{k}\cdot\vec{v} < \Gamma$. This corresponds to smaller signal size, eventually affecting S/N in Equation 1.1. More sophisticated techniques, like multiple pulse Ramsey interrogation, can obtain spectroscopic features with a linewidth at or even below the natural transition linewidth while still including the majority of the atomic sample in the laser interaction. Unfortunately, even though this can reduce Doppler broadening effects, these techniques, like all other free space ones, are eventually susceptible to measurement shifts associated with residual Doppler effects. These measurement shifts compromise the standard's realizable accuracy. For example, both saturated absorption and four pulse Ramsey spectroscopy utilize counter-propagating beams (equal but opposite $\vec{k}$) to realize Doppler cancellation. However, experimentally, the ability to create equal but opposite $\vec{k}$ is limited by technical considerations and can subsequently result in residual Doppler shifts of the atomic transition. This problem extends to non-uniform atomic motion due to gravitational acceleration of a free space atomic sample. Many of these sometimes subtle but relevant effects were considered in detail in high precision spectroscopy of free space, laser cooled Ca, developed as an optical frequency standard for now more than a decade [86, 87, 88, 89, 90]. We also investigated some of these effects in a free space spectroscopic interrogation of the $^1S_0$-$^3P_1$ transition in ^{88}Sr [91]. All of these studies carefully considered residual Doppler shifts, and although headway in reducing and controlling these effects has been made, keeping shift uncertainties well below one part per thousand (ppt) of the transition linewidth is technically very challenging and seemingly prohibitive.

It was a reduction of the Doppler effect which motivated the use of laser cooling to begin with. However, even laser cooled samples at μK temperatures have Doppler broadened linewidths of tens of kHz [91]. The weak square root dependence of the Doppler width on temperature ensures that even a Boltzmann-distributed Sr sample at a very cold 1 nK has a Doppler broadened linewidth at the kHz level. It was with this in mind that for many years, some researchers considered large Bose-Einstein condensates (BECs), with all atoms uniformly condensed to the ground state of motion, as an ideal sample for an atomic frequency standard (it has since become clear that strong interactions among the atomic bosons perturb the clock transition frequency [92]). Instead of merely lowering the temperature of a free space atomic sample, tightly confining the atoms can dramatically reduce the (first-order) Doppler effect, as we see in the next section.

2.5.2 Confinement in a Harmonic Potential

We now consider a single atom trapped in a simple harmonic potential. The initial Hamiltonian is composed of two pieces, one for the internal degrees of freedom of the two level atom and one for the external degrees of freedom of motional confinement in the 1-D harmonic potential.

$$H_{int} = \hbar\omega_1|1\rangle\langle 1| + \hbar\omega_2|2\rangle\langle 2| \tag{2.25}$$

$$H_{ext} = \frac{\hat{p}^2}{2m} + \frac{1}{2}m\omega^2\hat{x}^2 \tag{2.26}$$

Here the internal states 1 and 2 have energy of $\hbar\omega_1$ and $\hbar\omega_2$, m is the atomic mass, ω is the trap frequency of the harmonic oscillator, and $\hat{x}$ and $\hat{p}$ are the position and momentum operators. The position and momentum operators of H_{ext} can be re-written in terms of the annihilation and destruction operators [93]:

$$\hat{x} = \sqrt{\frac{\hbar}{2m\omega}}(\hat{a} + \hat{a}^\dagger) \tag{2.27}$$

$$\hat{p} = i\sqrt{\frac{m\hbar\omega}{2}}(-\hat{a} + \hat{a}^\dagger) \tag{2.28}$$

and H_{ext} is given by:

$$H_{ext} = \hbar\omega(\hat{a}^\dagger\hat{a} + \frac{1}{2}) \tag{2.29}$$

The eigenstates of H_{int} are just the internal states $|1\rangle$ and $|2\rangle$, while the eigenstates of H_{ext}, labelled as $|n\rangle$, are characterized entirely by the motional quantum number n. The annihilation and creation operators operate on $|n\rangle$ as follows:

$$\hat{a}|n\rangle = \sqrt{n}|n-1\rangle \tag{2.30}$$

$$\hat{a}^\dagger|n\rangle = \sqrt{n+1}|n+1\rangle \tag{2.31}$$

It can thus be shown that energy eigenstates consist of a ladder of equally spaced motional states $|n\rangle$, with n ranging from 0 to ∞. Each individual state has well-defined harmonic motion, whose wave function in position and momentum space is specified by the motional quantum number, as is the state energy $E = \hbar\omega(n + 1/2)$. In position space, the normalized state wave function can be written as:

$$\psi_n(x) = \sqrt{\frac{1}{\sqrt{\pi}2^n n! x_0}} e^{-\frac{1}{2}(\frac{x}{x_0})^2} H_n\left(\frac{x}{x_0}\right) \tag{2.32}$$

with characteristic length $x_0 = \sqrt{\hbar/m\omega}$, and $H_n(x)$ the Hermite polynomial of order n. The expectation value of x^2 is found to be:

$$\langle\psi_n(x)|x^2|\psi_n(x)\rangle = \frac{x_0^2}{2}(2n+1) \tag{2.33}$$

such that the rms spatial extent of the n^{th} motional state is $x_{rms} = x_0\sqrt{n+1/2}$. The $n = 0$ ground state wave function is gaussian, with a 1/e probability distribution radius of x_0.

The combined eigenstates for H_{int} and H_{ext} are simply product states of the internal states $|1\rangle$ and $|2\rangle$ with the motional states $|n\rangle$. However, we now add a third term to the Hamiltonian corresponding to an atom-light field interaction. This term originates from the introduction of a nearly resonant probe laser for spectroscopic investigation

of the confined two-level atom. This interaction couples internal levels with an electric field and can be expressed as:

$$H_I = -\vec{d} \cdot \vec{E}(x,t) \simeq \frac{\hbar\Omega}{2}(e^{ik\hat{x}}e^{-i\omega_L t}|2\rangle\langle 1| + e^{-ik\hat{x}}e^{i\omega_L t}|1\rangle\langle 2|) \tag{2.34}$$

Here $\Omega = -dE/\hbar$ is the Rabi frequency, d is the atomic dipole moment, k is the 1-D wave vector, and ω_L is the laser frequency. Note that the rotating wave approximation has been made, but that the dipole approximation has not been made and for now we keep all orders of $e^{ik\hat{x}}$. This is important since the confined atomic wavefunction is not necessarily much smaller than the probe laser wavelength, indicating the atom can sample different values of the electric field at a given time. We now transform to a frame rotating at the laser frequency, ω_L:

$$H_I = \frac{\hbar\Omega}{2}(e^{ik\hat{x}}|2\rangle\langle 1| + e^{-ik\hat{x}}|1\rangle\langle 2|) \tag{2.35}$$

This rotating frame also transforms H_{int} to:

$$H_{int} = -\hbar\Delta|2\rangle\langle 2| \tag{2.36}$$

where $\Delta = \omega_L - (\omega_2 - \omega_1)$ is the laser detuning from the atomic transition and $\hbar\omega_1$ is chosen to be the reference point of zero atomic energy. Returning to Equation 2.35, we substitute Equation 2.28 in for $\hat{x}$ to get:

$$H_I = \frac{\hbar\Omega}{2}[e^{i\eta(\hat{a}+\hat{a}^\dagger)}|2\rangle\langle 1| + e^{-i\eta(\hat{a}+\hat{a}^\dagger)}|1\rangle\langle 2|] \tag{2.37}$$

where $\eta = kx_0/\sqrt{2}$. We now write the total system Hamiltonian together [94, 95, 96]:

$$H = H_{int} + H_{ext} + H_I = -\hbar\Delta|2\rangle\langle 2| + \hbar\omega(\hat{a}^\dagger\hat{a} + \frac{1}{2}) + \frac{\hbar\Omega}{2}[e^{i\eta(\hat{a}+\hat{a}^\dagger)}|2\rangle\langle 1| + e^{-i\eta(\hat{a}+\hat{a}^\dagger)}|1\rangle\langle 2|] \tag{2.38}$$

An eigenstate of this Hamiltonian can be written as a linear superposition of product states of the internal and external degrees of freedom:

$$\psi = \sum_{n'=0}^{\infty}(c_{1n'}|1\rangle|n'\rangle + c_{2n'}|2\rangle|n'\rangle) \tag{2.39}$$

Plugging Equation 2.39 into the Schrödinger equation $i\hbar\frac{d\psi}{dt} = \hat{H}\psi$, and then taking the inner product with $|1\rangle|n\rangle$ and $|2\rangle|m\rangle$ gives the coupled equations of motion, for n and m from 0 to ∞:

$$\dot{c}_{1n} = -i\omega(n + \frac{1}{2})c_{1n} - i\frac{\Omega}{2}\sum_{n'=0}^{\infty}\langle n|e^{-i\eta(\hat{a}+\hat{a}^\dagger)}|n'\rangle c_{2n'} \tag{2.40}$$

$$\dot{c}_{2m} = i[-\omega(m + \frac{1}{2}) + \Delta]c_{2m} - i\frac{\Omega}{2}\sum_{n'=0}^{\infty}\langle m|e^{i\eta(\hat{a}+\hat{a}^\dagger)}|n'\rangle c_{1n'} \tag{2.41}$$

Now we impose the assumption that we can near resonantly address the individual transition from $|1\rangle|n\rangle$ to $|2\rangle|m\rangle$ and in so doing ignore far-detuned coherent couplings from $|1\rangle|n\rangle$ and $|2\rangle|m\rangle$ to other states. This allows us to pick out the $m^{th}(n^{th})$ term in the summation of Equation 2.40 (2.41) and reduce our system to two coupled equations:

$$\dot{c}_{1n} = -i\omega(n + \frac{1}{2})c_{1n} - i\frac{\Omega}{2}\langle n|e^{-i\eta(\hat{a}+\hat{a}^\dagger)}|m\rangle c_{2m} \tag{2.42}$$

$$\dot{c}_{2m} = i[-\omega(m + \frac{1}{2}) + \Delta]c_{2m} - i\frac{\Omega}{2}\langle m|e^{i\eta(\hat{a}+\hat{a}^\dagger)}|n\rangle c_{1n} \tag{2.43}$$

To illuminate the solution to these equations of motion, we compare Equations 2.42 and 2.43 to the equations of motion for the well known Rabi flopping solution of a stationary atom (in the dipole approximation):

$$\dot{c}_{1n} = -i\frac{\Omega}{2}c_{2n} \tag{2.44}$$

$$\dot{c}_{2n} = i\Delta c_{2n} - i\frac{\Omega}{2}c_{1n} \tag{2.45}$$

Comparing the first terms in the right hand side of Equations 2.42, 2.43, and 2.45, when $n = m$, the harmonically bound atoms have resonant excitation similar to an atom at rest. When $n \neq m$, the resonant frequency is not simply $\hbar\omega_2$, but rather $\hbar\omega_2+(m-n)\hbar\omega$. In this case, the atom is not only excited internally (electronically), but the atom is also excited (or de-excited) motionally resulting in a change of the motional state within the ladder of harmonic states.

Further comparison indicates that the harmonically trapped atoms experience Rabi flopping similar to the rest atom, but notably the coherent excitation rate is

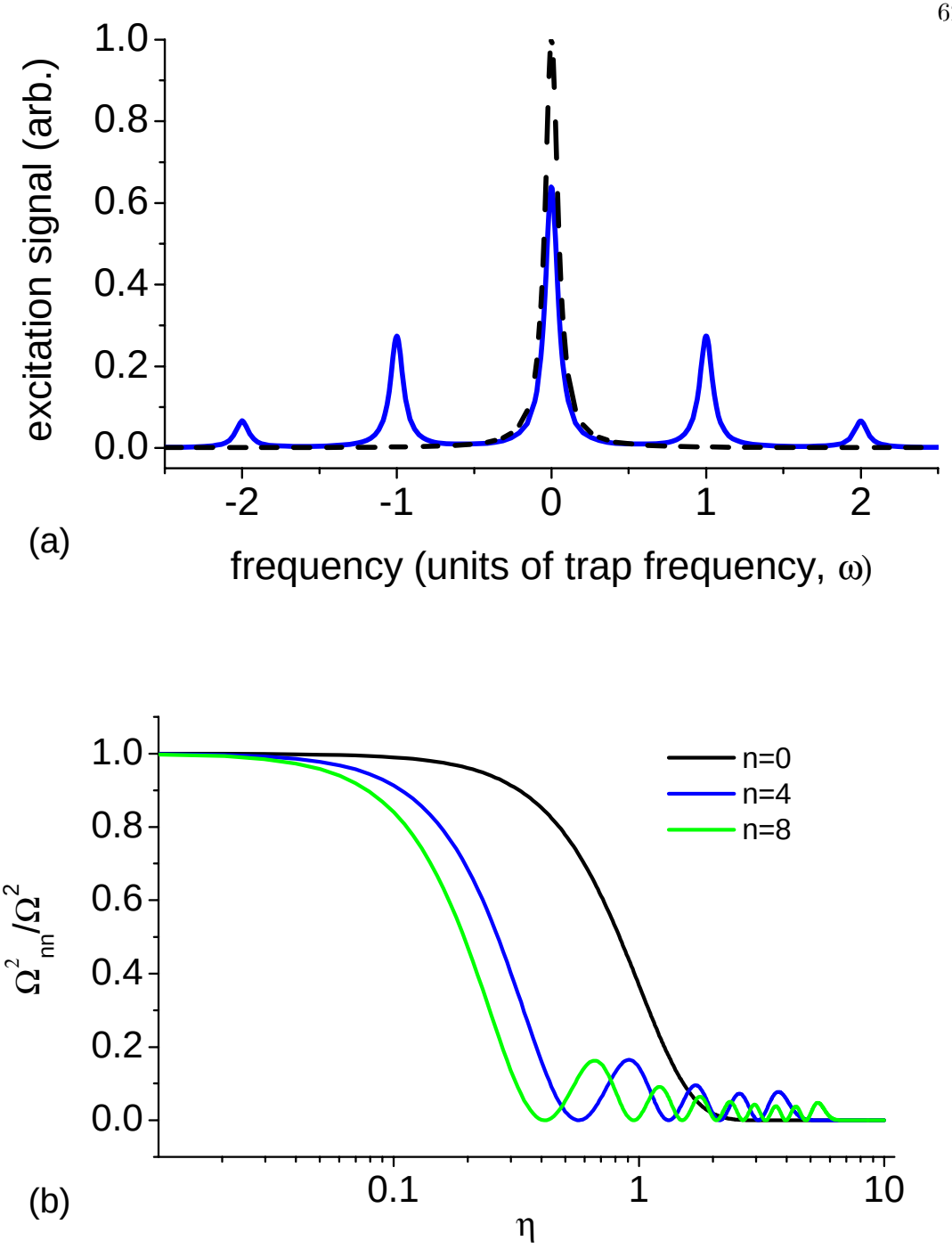

Figure 2.11: (a) Absorption spectrum of a confined atom. Zero detuning frequency corresponds to the natural atomic resonant frequency ω. The atom is also excited at $\omega_0 \pm l\omega$, where l is an integer. This yields the sideband resonances at ± 1, ± 2, etc. It has been assumed that the decoherence rate Γ is less than the trap frequency ω, such that the sidebands are well-resolved from each other and from the resonance at the natural atomic resonance. (b) The effective Rabi frequency (squared) for purely electronic transitions as a function of the Lamb-Dicke parameter η for various ground motional states with quantum number n. With very strong confinement ($\eta \ll 1$), $\Omega^2_{nn}/\Omega^2 \simeq 1$, indicating the atom is excited at a rate comparable to an atom at rest. With very weak confinement ($\eta \gg 1$), $\Omega^2_{nn}/\Omega^2 \ll 1$ as dipole coupling is spread among excitations to other motional states of the excited electronic state.

different than for the rest atom case (Ω). Rather the effective Rabi frequency is given by:

$$\Omega_{mn} = \Omega\langle m|e^{i\eta(\hat{a}+\hat{a}^\dagger)}|n\rangle \tag{2.46}$$

By expanding the exponential term and operating with $\hat{a}$ and $\hat{a}^\dagger$ to the left and right, Ω_{mn} can be explicitly solved to be [94, 95]:

$$\Omega_{mn} = \Omega e^{-\frac{\eta^2}{2}}\sqrt{\frac{n_<!}{n_>!}}\eta^{|m-n|}L_{n_<}^{|m-n|}(\eta^2) \tag{2.47}$$

where $n_<$ ($n_>$) is the lesser (greater) of n and m, and $L_n^\alpha(x)$ is the generalized Laguerre polynomial:

$$L_n^\alpha(x) = \sum_{p=0}^{n}(-1)^p\binom{n+\alpha}{n-p}\frac{x^p}{p!} \tag{2.48}$$

For the cases of electronic and motional excitation ($m > n$), pure electronic excitation ($m = n$), and electronic excitation and motional de-excitation ($m < n$), the effective Rabi rates are explicitly given by:

$$\Omega_{mn} = \begin{cases} e^{-\frac{\eta^2}{2}}\sqrt{\frac{n!}{m!}}\eta^{m-n}L_n^{m-n}(\eta^2) & \text{if } m > n \\ e^{-\frac{\eta^2}{2}}L_n^0(\eta^2) & \text{if } m = n \\ e^{-\frac{\eta^2}{2}}\sqrt{\frac{m!}{n!}}\eta^{n-m}L_m^{n-m}(\eta^2) & \text{if } n > m \end{cases} \tag{2.49}$$

This leads to atomic spectra which may appear like the one in Figure 2.11(a). Shown here is the purely electronic excitation, named the carrier, as well as the red (blue) sidebands associated with de-excitation (excitation) of the atomic motion. The relative amplitudes of these transitions are given by the square of the Rabi frequencies given in Equation 2.49. Also shown is the transition had the atom been at rest. As can be seen, the excitation rate of the carrier transition is diluted due to the decreased coupling between $|1\rangle|n\rangle$ and $|2\rangle|n\rangle$ as a consequence of the confined atomic motion. Shown in Figure 2.11(b) is Ω_{nn} (purely electronic excitation) as a function of η. Further ramifications of η dependence (known as the Lamb-Dicke parameter) on the atomic interrogation will be discussed later. However, note here that at large η (weak confinement so that the

atomic wavefunction characteristic length x_0 is large compared to the wavelength of the probing light), Ω_{nn} can become substantially smaller than Ω. The combined atomic and motional eigenstates constitute a complete and normalized basis set, such that:

$$\sum_{m=0}^{\infty} |\Omega_{mn}|^2 = |\Omega|^2 \tag{2.50}$$

Correspondingly, when Ω_{nn} shrinks as η grows, the total coupling to other motion states (Ω_{mn} for $m \neq n$) grows. At very small η (strong confinement), $\Omega_{nn} \simeq \Omega$. This makes intuitive sense as very strong confinement indicates the atom can not experience large motional displacement, like an atom at rest. Furthermore, stronger confinement means that more of the atoms, Boltzmann distributed in the motional state ladder, occupy the ground motional state.

Another important consequence of Equation 2.49 is that atoms in different initial motional states, n, experience different coherent excitation rates to the excited state. This inhomogeneous excitation is particularly evident when a large number of motional states are occupied. Furthermore, the differences in the excitation rate are more pronounced in weaker confinement. Like other sources of inhomogeneity, this can lead to damped Rabi oscillations, exhibiting contrast collapse and revival. More details are given in Section 5.4.4.

Although the quantum mechanical treatment above gives the most complete analysis of the harmonically bound atomic system, it is worthwhile to consider an alternative semi-classical picture which can provide further intuition into the physical system. In the quantum mechanical treatment, it was useful to move to a reference frame rotating at the laser frequency, ω_L. Here, we choose the rest frame of the atom. The atom in a given motional state $|n\rangle$ is oscillating in the lab frame

$$x(t) = A\sin(\omega t + \phi) \tag{2.51}$$

where A is total oscillation amplitude of displacement, t is time, and ϕ is a phase factor. This means that in the atom rest frame, the atoms sees the incident probe radiation as

a frequency modulated field:

$$\vec{E}_{atom} = \vec{E}_0 \sin(kA \sin \omega t - \omega_L t) \tag{2.52}$$

where ϕ has been chosen to be zero. Equation 2.52 matches the initial expression for signal modulation theory from phase/frequency modulation [97, 43]. Following that analysis, the field in Equation 2.52 can be expanded as a series of Bessel functions:

$$\vec{E}_{atom} = \vec{E}_0\{J_0(kA)\sin[\omega_L t] + J_1(kA)\sin[(\omega_L+\omega)t] - J_1(kA)\sin[(\omega_L-\omega)t] + ...\} \tag{2.53}$$

The electric field seen by the atom has a component at the original frequency ω_L with amplitude given by $J_0(kA)$, but also has sideband components at $\omega_L \pm \omega$ with amplitude $J_1(kA)$. The ". . . " in Equation 2.53 refers to higher l^{th} order sidebands with amplitudes given by $J_l(kA)$. If $\omega_L = \omega_0 = \omega_2 - \omega_1$, then the atom is excited electronically and the absorption and emission spectrum has an intensity proportional to $[J_0(kA)]^2$. For an atom in the motional state $|n\rangle$, the oscillation amplitude A is found to be $x_0\sqrt{2n+1}$ which corresponds to the classical turning point of the harmonically bound atom. This means that $kA = \sqrt{2}\sqrt{2n+1}\eta$ and the intensity is proportional to $[J_0(kA)]^2 = [J_0(\sqrt{2}\sqrt{2n+1}\eta)]^2$. This can be compared to the quantum mechanical result (middle equation in Equation 2.49) by recognizing that:

$$J_0(\sqrt{2}\sqrt{2n+1}\eta) \simeq e^{-\frac{\eta^2}{2}} L_n^0(\eta^2) \tag{2.54}$$

Equation 2.54 is valid for $\eta < 1$, presumably because unlike the quantum mechanical treatment, this semi-classical picture does not properly account for photon recoil (see further discussion below).

The relative size of the red and blue sideband intensities is slightly more complicated. This is because during the excitation, the motional state changes from $|n\rangle$ to $|m\rangle$ and thus the expansion coefficient $J_1(kA)$ changes because of a change in the modulation depth kA. This is in contrast to the carrier excitation, where the atomic motion and hence the modulation seen by the atom are independent of the electronic

state. To deal with the case of sideband excitation, as a simple approach [98] we evenly average the effect of the two motional states on the modulation, i. e. $n \rightarrow (n+m)/2$. For the l^{th} order blue sideband ($l = m - n$), the line intensity is thus proportional to $J_l(\sqrt{2}\sqrt{2n+1+l}\eta)$. Again the similarity of these results with the quantum mechanical treatment can be seen by recognizing numerically that:

$$J_l(\sqrt{2}\sqrt{2n+1+l}\eta) \simeq e^{-\frac{\eta^2}{2}}\sqrt{\frac{n!}{m!}}\eta^{m-n}L_n^{m-n}(\eta^2) \tag{2.55}$$

again valid for $\eta < 1$. The spectrum is thus seen to resemble Figure 2.11.

Already in our discussion on harmonic confinement of atoms, we have implicitly touched on different regimes which may or may not be ideal for performing high resolution spectroscopy. Here, I explicitly list several important regimes and why they are useful for the experimental spectroscopy reported later in this thesis.

2.5.3 Uniform Confinement Regime

We have been implicitly assuming that the harmonic potentials are identical for the ground and excited electronic states. If this were not the case, the carrier transition frequency would not be ω_0, but would instead include a frequency shift given by the energy difference between the confinement of the two electronic states. The electronic degree of freedom and the motional degree of freedom are not cleanly separated unless the motional potential is the same for both electronic states.

The presence of a frequency shift dependent on the confinement details makes it more difficult to maintain a small measurement inaccuracy of the unperturbed clock transition. These confinement details would need to be known and controlled better than in the case that the confinement potentials were uniform for the two clock states. In general, when accuracy and long-term stability are important, it is almost always better to make the measurement as close to an unperturbed case as possible.

Along with a frequency shift comes line broadening due to spatial or temporal in-

homogeneities in the confinement of atomic ensemble. This broadening could ultimately degrade the measurement stability of the transition frequency (see Equation 1.1).

Achieving uniform confinement for the two clock electronic states depends on the type of confinement used. For the case of frequency standards based on single trapped ions, the non-zero charge of the ion is exploited to confine the atoms using a time dependent (RF) electric field. This field interacts strongly with the net charge of the ion, but extremely weakly with the clock electronic states. In this way, the confinement is naturally independent of the electronic state. Neutral atoms, with a net charge of zero, can not be trapped this way. For the work reported here, atomic confinement is achieved with an optical lattice, exploiting a very strong optical electric field gradient interacting with the induced dipole moment of the atom. The optical lattice strongly perturbs the valence electronic wave functions. However, as described in the next section, the field parameters can be chosen so that the dipole polarizabilities of the two clock states are equal. In doing so, the uniform confinement regime is realized, cleanly separating the internal and external degrees of freedom [27, 99, 100, 101].

In many respects, the optical lattice is an ideal atomic trap, providing nearly uniform confinement through its trap sites. This is in contrast to solid state lattice structures, which typically have imperfections which introduce significant inhomogeneities between the confinement at different sites. This leads to decoherence which, despite very strong confinement, prevents the same level of spectroscopy for quantum absorbers bound to a solid state material. The optical lattice has emerged as such a powerful experimental tool because of its defect-free confinement through its various sites.

2.5.4 Well resolved sideband regime

Any real system suffers from relaxation or decoherence. As a consequence, spectroscopic features are broadened in the frequency domain. The relative size of the decoherence rate, Γ, and the trap frequency, ω, strongly influences the two level dy-

namics and the observed spectroscopic features. When $\Gamma > \omega$, the sideband structure in Figure 2.11 is unresolvable. This means that optical excitation at a given frequency cannot neatly discriminate between purely electronic excitation (the carrier transition) or mixed electronic and motional excitation (sideband transitions). This makes spectroscopic measurements much more sensitive to the motional effects of Doppler and recoil shifts. This is in contrast to the case $\Gamma \ll \omega$, where the Doppler effects are moved to high modulation frequencies around the carrier transition. At these high modulation frequencies, the motional effects interfere substantially less with measurement of the purely electronic excitation frequency, which is the frequency that is relevant for high accuracy optical frequency standards. The ability to discriminate carrier and sidebands is sometimes called the well-resolved sideband regime (or the strong binding regime) [43, 102, 103].

To understand this effect more clearly, consider the spectra in Figure 2.12. These absorption spectra are given by Equations 2.42, 2.43, and 2.49 for varying confinement strengths and assume a Boltzmann-distributed population among the motional states. The individual lines are represented in the well-resolved sideband regime (the details of the individual lineshapes are not shown, but they are resolved). As the trap frequency is reduced, the spacing between sidebands is reduced and at the same time additional higher order sidebands appear (η increases as ω decreases). When the trap frequency is reduced to the point that $\Gamma \simeq \omega$, the sideband and carrier lineshapes eventually overlap. As the trap frequency approaches 0, we approach the limit of free space interrogation of the untrapped atomic sample. In that limit, the spectrum is given by the Doppler-broadened profile (whose Gaussian width is given by Equation 2.24) and is shown as the black envelope function of the first spectrum. In this limit, the spectroscopic resolution and accuracy are degraded because of the direct influence of the motional effects. In contrast, in the well-resolved sideband regime, the Doppler effects manifested as far-detuned sideband features, only influence the carrier transition by line-pulling (shift

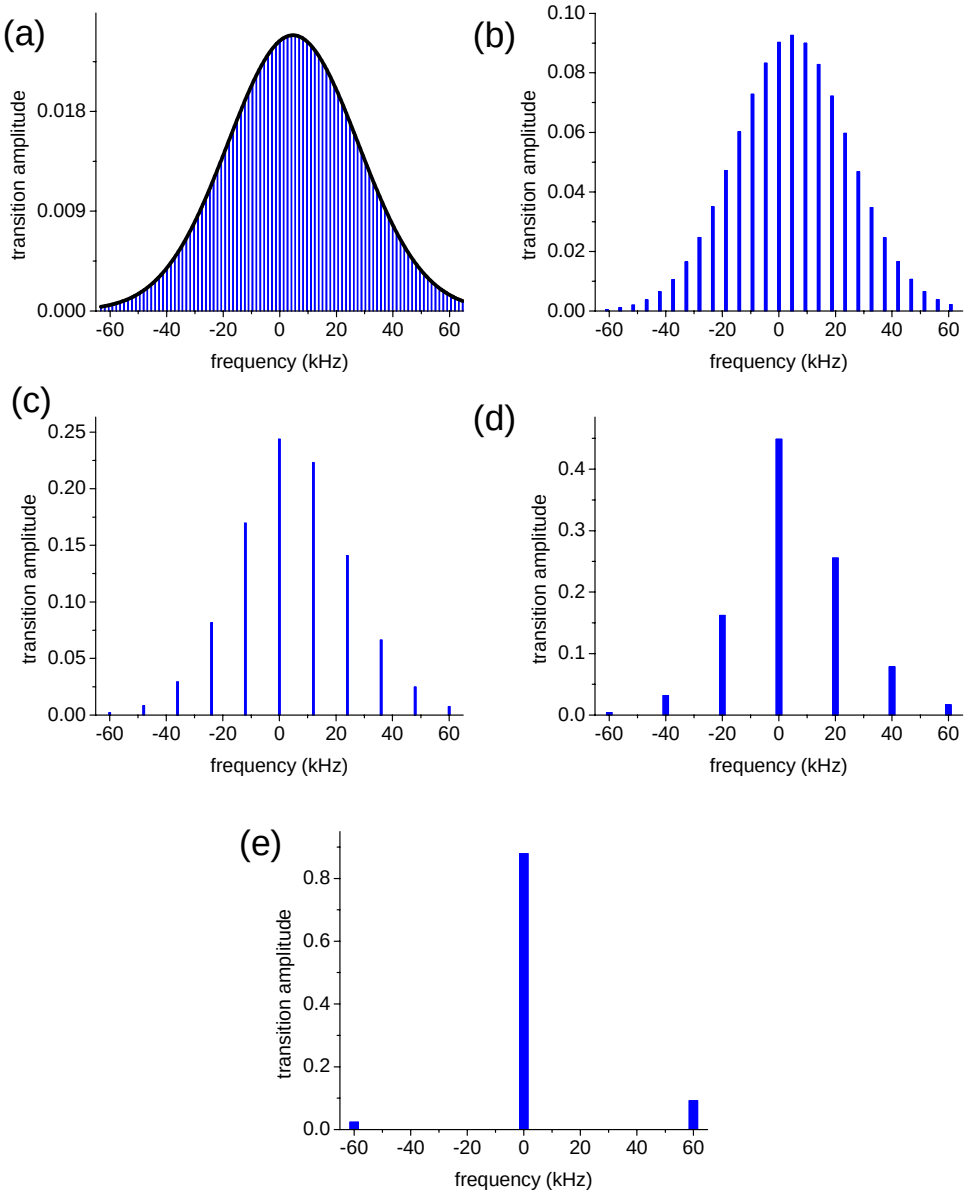

Figure 2.12: Absorption spectrum of an atomic ensemble in the range of very weak confinement (a) to very strong confinement (e). The horizontal axis indicates frequency detuning from the natural transition. The atomic recoil frequency $\omega_r/2\pi$ is taken to be 4.68 kHz, approximately that of the strontium $^1S_0$-$^3P_0$ clock transition. Furthermore, we assume negligible decoherence ($\Gamma \ll omega$). In (a), the black solid curve gives the absorption spectrum of the atomic ensemble in free space, corresponding to the Doppler-broadened profile. This Doppler-broadened profile serves as an envelope for the weak confinement spectrum shown with trap frequency $\omega/2\pi = 1.376$ kHz and Lamb-Dicke parameter $\eta = 1.84$. As the atomic confinement becomes stronger and tighter [(b) $\omega = \omega_r$ and $\eta = 1$ and (c) $\omega/2\pi = 12$ kHz and $\eta = 0.62$], the photon recoil shift (where the spectral amplitude maximum is blue-detuned from the natural transition frequency) is suppressed and the natural atomic transition emerges with the largest transition amplitude [as in (c)]. Furthermore, the spectrum becomes more symmetric around the natural transition frequency and the sideband amplitudes are suppressed relative to the carrier, purely electronic excitation. This recoil suppression effect becomes dramatic far into the Lamb-Dicke regime [(d) $\omega/2\pi = 20$ kHz and $\eta = 0.48$ and (e) $\omega/2\pi = 60$ kHz and $\eta = 0.28$].

from the "wings" of the sidebands). For even the slowly decaying Lorentzian lineshape, in the well-resolved sideband limit this line-pulling effect scales to the third power in Γ/Δ where Δ is the angular detuning of the line responsible for pulling. This effect can thus be made very small.

A remarkable outcome of the quantum mechanical solution to the bound atom is that, despite the photon recoil (recoil frequency $\omega_r = \hbar k^2/2m$ as in Equation 2.22), in the well-resolved sideband regime, the carrier resonance clearly occurs at ω_0 and the sidebands at $\omega_0 \pm l\omega$. With $\eta \geq 1$, the recoil strongly determines the relative line intensities of the carrier and sidebands. As seen in Figure 2.12, the maximum line intensity is at the line closest to $\omega_0+\omega_r$ (just as the free space lineshape peaks at $\omega_0+\omega_r$). The blue detuned sidebands have intensities larger than their red counterparts, just as the free space recoil-shifted line is shifted to the blue. In the well-resolved sideband regime, this asymmetry in the sideband structure around the carrier causes line-pulling shifts which can be made small with sufficiently narrow spectral lineshapes.

2.5.5 Lamb-Dicke regime

In Section 2.5.2, we defined the parameter η, called the Lamb-Dicke parameter, which gave the relative size between the atomic spatial confinement of the ground motional state x_0 and the wavelength of the probing laser field ($\eta = kx_0/\sqrt{2}$). This parameter can be further seen to be equal to:

$$\eta = kx_0/\sqrt{2} = k\sqrt{\frac{\hbar}{2m\omega}} = \sqrt{\frac{\omega_r}{\omega}} \tag{2.56}$$

We look again at Figure 2.12 which gives the absorption spectra for various values of η. As we move further into the Lamb-Dicke regime ($\eta \ll 1$), the recoil effect on the line intensities is reduced: the maximum line intensity moves closer to the carrier transition, the sideband structure becomes more symmetric, and the sideband intensities become smaller relative to the carrier. In this regime, the photon recoil energy and momentum

is taken up less by the atom and more by the confining potential (via lattice photon generation in the case of an optical lattice). Therefore, the Lamb-Dicke effect is the suppression of sideband excitation intensities [104], indicating that the atom does not take up photon recoil. This phenomenon is analogous to the much studied absorption of γ-rays on the Mossbauer line [105]. This recoil suppression roughly begins when $\eta = 1$ or when $\omega = \omega_r$. Here, the atomic recoil momentum from one photon absorption is roughly equal to the rms momentum change from the atom being excited by one motional quantum. Thus as η becomes less than 1, presumably the higher energy and momentum needed to excite the atom motionally results in the recoil being more favorably taken up by the confining potential.

In the Lamb-Dicke regime, the expression for Ω_{nm} becomes simpler. In particular, the first order red and blue sidebands are seen to have excitation rates of

$$\Omega_{n,n+1} = \eta\sqrt{n+1} \tag{2.57}$$

$$\Omega_{n,n-1} = \eta\sqrt{n} \tag{2.58}$$

respectively. Note that while the recoil is suppressed in the Lamb-Dicke regime, it is only completely suppressed in the limit of $\eta \to 0$, as evidenced by the fact that with nonzero η, the blue sideband excitation (Equation 2.57) remains larger than the red one (Equation 2.58). The sidebands continue to get smaller deeper into the Lamb-Dicke regime, with their intensities scaling as η^2. Naturally, as the sidebands get smaller, the carrier excitation rate approaches Ω. This can be seen in Figure 2.11. No matter what n, the Ω_{nn} approaches Ω. This illustrates that in addition to recoil suppression, the Lamb-Dicke regimes helps with another unwanted effect: inhomogeneous atomic excitation as a function of motional state $|n\rangle$. As η gets smaller, for all n, the carrier transition coupling becomes more uniform and the sideband transition couplings become smaller. Thus a large atomic sample distributed over many motional states can be excited more homogeneously.

To clarify further the role of the atomic recoil, we explicitly consider two extreme cases and their intermediate regime. In a free space atom (limit $\omega \to 0$), it is well known that the atomic transition experiences a blue-detuned shift given by the recoil frequency, ω_r. In the case of an atom rigidly bound to a potential (limit $\omega \to \infty$), the photon recoil is taken up by the combined atom-potential, and since the potential has an effective mass much larger than the atom, the recoil shift is tiny and approaches zero. In a very weakly bound, slowly oscillating atom, the atom absorbs the photon recoil. Since the atom is bound, all of this momentum is eventually transferred to the potential. However, because of the huge effective mass of the potential, the energy predominantly remains with the atom ($E_{kinetic} = 1/2Mv^2$) [106, 43]. As the atom becomes more tightly bound, the "recoil energy" is reduced and the recoil momentum is taken up more directly by the combined atom-potential system.

2.6 Atomic Confinement with a Far-Detuned Optical Wave

In the previous sections, we considered properties of atomic confinement that were optimal for high precision spectroscopy. We now consider one method to realize this confinement for neutral atoms: nonresonant interaction with a strong optical field.

2.6.1 Dipole Potential

In Equation 2.38, I listed the Hamiltonian for a two level atom, harmonically confined, and interacting with a laser field with Rabi frequency Ω and detuning Δ. Originally, we considered the resonant or near resonant case where the atom was excited internally. We now focus on the far detuned case, where the atom is illuminated by a laser field with $\Delta \gg \Omega$. Here, no substantial excitation (electronically or motionally) occurs. Rather, the laser field acts as a perturbation on the atomic energy levels, shifting their energy. We assume that the laser field is so far detuned that the details of the motional states are not important ($\Delta \gg \omega$). In other words, the far-detuned laser is

essentially equally far-detuned from all motional and electronic transitions, and because of the normalized couplings between electronic and motional states (Equation 2.50), we can neglect the effect of confinement in the total Hamiltonian. In particular, we exclude H_{ext} as we consider the perturbation induced by the far-detuned laser field. Hence we write the Hamiltonian, this time in matrix form in the $|1\rangle$,$|2\rangle$ basis [44] as:

$$H = H_{int} + H_I = \frac{\hbar}{2}\begin{pmatrix} 0 & \Omega \\ \Omega & -2\Delta \end{pmatrix} \tag{2.59}$$

By direct diagonalization, the eigen-energies of the "dressed" states can be found. Compared to the energies of the bare, unperturbed states, the energy shift is:

$$U = \hbar\Delta\omega = \frac{\hbar\Omega^2}{4\Delta} = \frac{1}{4}E_0^2\frac{|d|^2}{\hbar(\omega_L - \omega_0)} \tag{2.60}$$

where $\Delta \gg \Omega$ has been assumed, and in the last term, the values $\Omega = dE_0/\hbar$ and $\Delta = \omega_L - \omega_0$ have been used. We recall that the Hamiltonian originating from Equation 2.38 exploited the rotating wave approximation. In the near resonant case, this approximation is entirely justified. In our far-detuned case here, keeping the other wave yields a second contribution to the observed frequency shift:

$$\Delta\omega = -\frac{E_0^2}{4}\frac{|d|^2}{\hbar^2}\left(\frac{1}{\omega_0 - \omega_L} + \frac{1}{\omega_0 + \omega_L}\right) = -\frac{E_0^2}{4\hbar}\left(\frac{2|d|^2}{\hbar}\frac{\omega_0}{\omega_0^2 - \omega_L^2}\right) \tag{2.61}$$

The term in parentheses on the right hand side is labelled α, the dipole polarizability.

We now generalize α for a multi-level atom (with far-detuned transitions). We label the state being shifted as state $|a\rangle$. All intermediate states with dipole couplings which contribute to the shift are labelled with the summation index, $|k\rangle$.

$$\alpha_a = \frac{2}{\hbar}\sum_k |d_{ak}|^2\frac{\omega_{ak}}{\omega_{ak}^2 - \omega_L^2} \tag{2.62}$$

$$\Delta\omega_a = -\frac{1}{4\hbar}\alpha_a E_0^2 \tag{2.63}$$

where the transition between states $|a\rangle$ and $|k\rangle$ has angular frequency ω_{ak} and dipole moment matrix element d_{ak}. The shift, $\Delta\omega_a$, is referred to as the dynamic or AC Stark

shift, or alternately the light shift. The corresponding energy level shift can be exploited to confine the atoms. By designing a light field with a spatially dependent intensity, spatial confinement can be achieved at the energy minimum. Classically, the dipole moment induced by an electric field is given by [107]:

$$\vec{d} = \alpha \vec{E} \tag{2.64}$$

The interaction energy between the induced dipole and the field is simply:

$$U = \vec{d} \cdot \vec{E} \tag{2.65}$$

A dipole feels no overall force, only torque, in a uniform field. However, in a nonuniform field, a dipole experiences an overall force:

$$F = (\vec{d} \cdot \vec{\nabla})\vec{E} \tag{2.66}$$

It is clear that the light field plays two roles in trapping the atoms. First, it induces an atomic dipole moment (1^{st} order in E). Second, the spatially varying light field forms a trap for the induced dipole (1^{st} order in E). Together, the resulting trap depth, $\Delta U = \hbar \Delta\omega$, scales with the polarizability, α, and the square of the electric field, E^2. Furthermore, the stronger the field gradient, the tighter the confinement that can be achieved.

2.6.2 Dipole Polarizability

To calculate the dipole polarizability in Equation 2.62, we need the dipole matrix element d_{ak} which is related to state transition rates as in Equation 2.6. While the decay rates from states specified by L and S quantum numbers are commonly reported as experimental and theoretical results, we are concerned with couplings to a very specific quantum state (the clock state), not the entire family of substates in the LS state. Determination of how these couplings are subdivided through fine, hyperfine, and magnetic substructure has been a long-solved problem in angular momentum theory

[108, 109, 110, 111]. We start with a variant of the reduction formula which, as written here, relates the reduced dipole moment matrix element of a composite spin system to a further reduced dipole matrix element which removes one spin dependence. Specifically, here it is used to relate the dipole matrix element in the J,L,S basis to the reduced L,S basis only:

$$X_{ab} = \frac{|\langle J_a L_a S_a \| D^1 \| J_b L_b S_b \rangle|^2}{|\langle L_a S_a \| D^1 \| L_b S_b \rangle|^2} = (2J_a + 1)(2J_b + 1) \left\{ \begin{array}{ccc} L_a & J_a & S_a \\ J_b & L_b & 1 \end{array} \right\}^2 \tag{2.67}$$

The term in curly brackets is the $6 - j$ symbol, which can be related to the Racah W coefficient. Note that the reduced dipole matrix element in the denominator has no J dependence. This matrix element is more directly related to the LS state decay rate. Equation 2.67 gives the relative dipole branching between the states $|J_a L_a S_a\rangle$ and $|J_b L_b S_b\rangle$. When the lower state, indexed by 'a', has fine structure, the dipole coupling between $|L_a S_a\rangle$ and $|L_b S_b\rangle$ is divided among those substates. To calculate the normalized branching ratio between $|J_a L_a S_a\rangle$ and $|J_b L_b S_b\rangle$, consider the following summation:

$$\sum_{J_a} (2J_a + 1)(2J_b + 1) \left\{ \begin{array}{ccc} L_a & J_a & S_a \\ J_b & L_b & 1 \end{array} \right\}^2 = \frac{2J_b + 1}{2L_b + 1} \tag{2.68}$$

Thus the branching ratio between particular fine structures states, each within fine structure manifolds, is given by:

$$\phi_{J_a J_b} = \frac{X_{ab}}{\sum_{J_a} X_{ab}} = (2J_a + 1)(2L_b + 1) \left\{ \begin{array}{ccc} L_a & J_a & S_a \\ J_b & L_b & 1 \end{array} \right\}^2 \tag{2.69}$$

Note that the branching ratio in Equation 2.69 is for the relative transition line strength (dipole moment squared) between fine multiplets.

Because of the frequency dependence of the spontaneous decay rate (see Equation 2.6), the nondegeneracy of fine structure states in a multiplet lead to decay rate branching ratios which are close, but not exactly equal, to those of Equation 2.69. This must

be kept in mind when extracting dipole moments, d, from measured decay rates of LS states. As an example relevant to the ^{87}Sr clock states, we consider coupling between an upper $^3S_1$ state and the $^3P_0$ clock state. Equation 2.69 gives the branching ratio, $\phi_{J_aJ_b}$, from $^3S_1$ to $^3P_2$, $^3P_1$, and $^3P_0$ as 5/9, 3/9, and 1/9 respectively. Using Equation 2.6, the combined decay rate from $^3S_1$ can be written as

$$\Gamma = \Gamma_{^3P_0} + \Gamma_{^3P_1} + \Gamma_{^3P_2} = \frac{2}{6\pi\epsilon_0\hbar c^3}(\omega^3_{^3P_0}\frac{1}{9}|d|^2 + \omega^3_{^3P_1}\frac{3}{9}|d|^2 + \omega^3_{^3P_2}\frac{5}{9}|d|^2) = \frac{2}{6\pi\epsilon_0\hbar c^3}\omega^3_{cm}|d|^2 \tag{2.70}$$

where $\omega_{^3P_X}$ is the ^3P_X-$^3S_1$ transition frequency. It is clear that the relative decay rates to the ^3P multiplet states scale as $\phi_{J_aJ_b}$ and $\omega^3_{J_aJ_b}$. Equation 2.70 also shows that the dipole moment d is most easily calculated with ω_{cm}, the average transition frequency weighted by the branching ratios ("center of mass" frequency). Thus, to generalize Equation 2.6, the dipole moment between LS states is calculated using

$$\Gamma_{L_aL_k} = \frac{2}{6\pi\epsilon_0\hbar c^3}\omega^3_{cm}|d_{L_aL_k}|^2 \tag{2.71}$$

$$\omega^3_{cm} = \sum_{J_a}\phi_{J_aJ_k}\omega^3_{J_aJ_k} \tag{2.72}$$

We are also concerned with the dipole coupling between particular magnetic substates. Here we refer to the well known Wigner-Eckart theorem (written here for the case of dipole coupling only). This theorem indicates how to separate the dipole matrix element between two fully specified quantum states into two terms: one a purely geometric term and the second a dynamical term with no dependence on the magnetic quantum number. The quantum state is specified explicitly by J, L, S, m. Other quantum numbers are assumed but not explicitly shown:

$$|\langle J_aL_aS_am_a|D^1_i|J_bL_bS_bm_b\rangle|^2 = \begin{pmatrix} J_a & 1 & J_b \\ -m_a & i & m_b \end{pmatrix}^2 |\langle J_aL_aS_a\|D^1\|J_bL_bS_b\rangle|^2 \tag{2.73}$$

The first term on the right hand side is the Wigner $3-j$ symbol and can be expressed in terms of the Clebsch-Gordan coefficients [93]. The second term, known as the reduced

dipole matrix element (indicated with double bars '‖' around the dipole operator), is independent of magnetic quantum number m and the dipole polarization i. Only the Wigner $3-j$ maintains dependence of the geometrically determined m and i. Hence, the magnetic substructure coupling is isolated from the coupling between the other quantum degrees of freedom.

One important property of the Wigner $3-j$ is:

$$\sum_{m_a,i} \begin{pmatrix} J_a & 1 & J_b \\ -m_a & i & m_b \end{pmatrix}^2 = \frac{1}{2J_b+1} \tag{2.74}$$

As we consider the appropriate dipole coupling strength between particular magnetic sublevels, the total decay rate from an upper magnetic state must equal that of its parent fine structure state. Thus, the magnetic branching term for a lower state with m_a from upper state with m_b is given by [112]:

$$\phi_{m_a m_b} = (2J_b+1) \begin{pmatrix} J_a & 1 & J_b \\ -m_a & i & m_b \end{pmatrix}^2 \tag{2.75}$$

What states m_b are relevant depend on the experimental details. A well-defined laser polarization may excite only one polarization, i, coupling to a single upper state m_b. On the other hand, an unpolarized field would need to be summed over all three values of i with allowed couplings to more m_b upper states.

As a side note, it is worth mentioning that the fully specified dipole matrix elements in a composite spin system can be related to the fully specified matrix elements in the reduced spin basis. Combining the Wigner-Eckart theorem (Equation 2.73) and the reduction formula (Equation 2.67), it can be shown that:

$$\frac{\sum_{J_k,m_k,m_a} |\langle J_a L_a S_a m_a | D_i | J_k L_k S_k m_k \rangle|^2}{2J_a+1} = \frac{\sum_{m_k,m_a} |\langle L_a S_a m_a | D_i | L_k S_k m_k \rangle|^2}{2L_a+1} \tag{2.76}$$

Thus the sum of the matrix elements for a given J_a in the J basis equals those for a given L_a in the L basis (for an upper state with L_k), each weighted by their state degeneracy in the denominator.

With the appropriate branching parameters determined, we can now specify d_{ak} in Equation 2.62 as:

$$|d_{ak}|^2 = \phi_{J_a J_k}\phi_{m_a m_k}|d_{L_a L_k}|^2 \tag{2.77}$$

for upper state k and lower state a. Here $d_{L_a L_k}$ is the dipole moment between the $|L_a S_a\rangle$ and $|L_b S_b\rangle$ states. This allows us to now calculate the dipole polarizability of the fine structure states. By a similar application of the reduction formula (Equation 2.67) the hyperfine state (F) reduced dipole matrix elements can be rigorously related to those of the fine structure (J). However, as mentioned below, calculating the polarizability while ignoring the ^{87}Sr hyperfine substructure is an approximation that does not limit the present calculation.

The relevant energy levels with dipole coupling to the clock states are determined by the dipole selection rules. The ground clock state, $5s^2\ {}^1S_0$, couples to all higher lying ${}^1P_1$ states. The excited clock state, $5s5p\ {}^3P_0$, couples to the higher lying ${}^3S_1$ and ${}^3D_1$ states, as well as a doubly excited ${}^3P_1$ state. The dipole polarizability is calculated using Equations 2.62, 2.71, and 2.77. The relevant values of ω_{ak}, $\Gamma_{L_a L_k}$, $\phi_{J_a J_k}$, and ω_{cm} are listed in Table 2.1. Note that because both clocks states are $J = 0$ and thus taken to be $m_J = 0$, and since the confining dipole trapping laser is assumed to π-polarized, the $\phi_{m_a m_k} = 1$ for all transitions. Plots of $\alpha_{^1S_0}$ and $\alpha_{^3P_0}$ are shown in Figure 2.13 as a function the radiation wavelength, $\lambda = 2\pi c/\omega_L$. In the bottom panel of Figure 2.13, the difference in the two polarizabilities is plotted, zoomed in around $\lambda = 800$ nm. As can be seen, in this region, the polarizabilities of the two clock states are equal, such that atomic confinement can be made essentially identical for both clock states. This achieves the very important uniform confinement regime discussed earlier in the chapter.

Before moving to the next sections where we consider the details of the ^{87}Sr dipole trapping, I pause here to note the assumptions and imperfections in the above

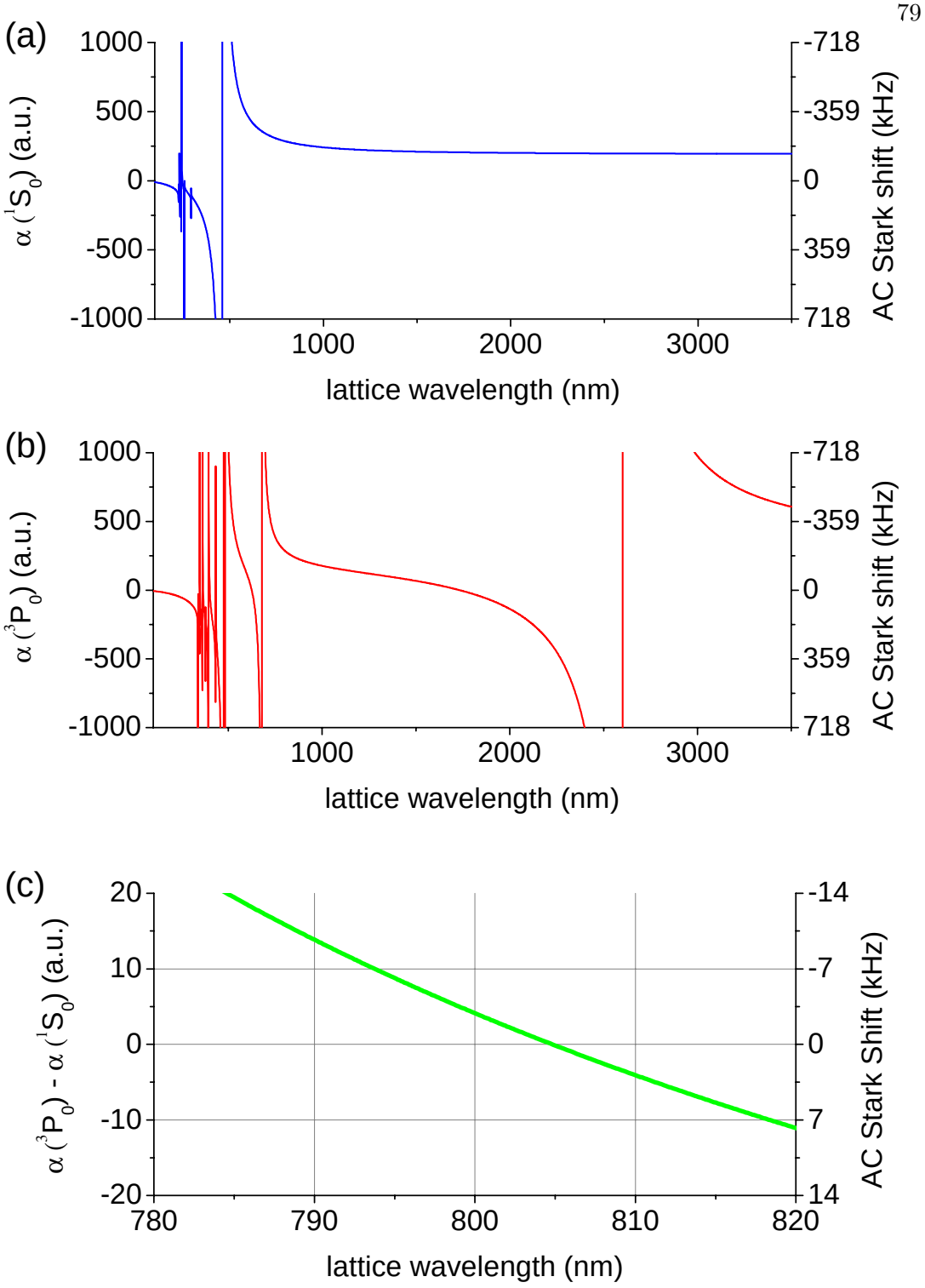

Figure 2.13: Sr atomic polarizability (in atomic units) as a function of wavelength (in nm). (a) $^1S_0$ polarizability (b) $^3P_0$ polarizability (c) difference between $^3P_0$ and $^1S_0$ polarizability, on a magnified wavelength axis around the "magic" zero crossing point near 805 nm. The right hand side axes of each plot gives the corresponding AC Stark shift for the atomic states in a 1-D lattice with one way intensity $I = 5$ kW/cm^2 (see Section 2.6.3).

Table 2.1: Transition parameters used to calculate the atomic polarizability of the Sr clock states. The transition (radial) frequency values ω_{ak} are from [113] (10^{15} 1/s). The decay rates $\Gamma_{L_a L_k}$ (10^6 1/s) are from the references indicated. $\phi_{J_a J_k}$ and ω_{cm} are defined in the text.

clock state	intermediate state	ω_{ak}	$\Gamma_{L_a L_k}$	Reference	$\phi_{J_a J_k}$	ω_{cm}
$5s^2\ ^1S_0$	$5s5p\ ^1P_1$	4.087	190.7(3.0)	avg of [114] and [115] exp	1	4.087
	$5s6p\ ^1P_1$	6.423	1.86	[116] exp		6.423
	$5s7p\ ^1P_1$	7.328	4.3	[116] avg of exp & theor		7.328
	$4d5p\ ^1P_1$	7.755	14.5	[116] avg of exp & theor		7.755
	$5s8p\ ^1P_1$	7.755	16.7	[116] avg of exp & theor		7.755
	$5s9p\ ^1P_1$	7.998	11.7	[116] avg of exp & theor		7.998
	$5s10p\ ^1P_1$	8.161	7.6	[116] theor		8.161
	$5s11p\ ^1P_1$	8.276	4.88	[116] theor		8.276
$5s5p\ ^3P_0$	$5s6s\ ^3S_1$	2.773	75.4	[116] weighted avg of exp	1/9	2.701
	$5s7s\ ^3S_1$	4.353	17.5	[116] theor		4.281
	$5s8s\ ^3S_1$	4.981	8.22	[116] theor		4.909
	$5s9s\ ^3S_1$	5.299	4.53	[116] theor		5.227
	$5s10s\ ^3S_1$	5.483	2.77	[116] theor		5.411
$5s5p\ ^3P_0$	$5s4d\ ^3D_1$	0.724	.345(.024)	[117] exp	5/9	0.707
	$5s5d\ ^3D_1$	3.897	60.9	[116] weighted avg of exp		3.879
	$5s6d\ ^3D_1$	4.778	26.7	[116] theor		4.760
	$5s7d\ ^3D_1$	5.190	14.2	[116] theor		5.172
	$5s8d\ ^3D_1$	5.415	8.51	[116] theor		5.397
	$5s9d\ ^3D_1$	5.555	5.51	[116] theor		5.537
$5s5p\ ^3P_0$	$5p^2\ ^3P_1$	3.961	127	[116] weighted avg of exp	1/3	3.907

dipole polarizability calculation. Firstly, as early as our choice of Hamiltonian, we have assumed the laser radiation is far-detuned from any dipole transition. In other words, we are in the dispersive, not absorptive regime. It is the violation of this assumption which gives infinite resonances in Figure 2.13 as a particular transition is crossed.

As mentioned above, the calculation was made on the fine structure states in the J basis, more appropriate for the hyperfine-free ^{88}Sr states than for ^{87}Sr. Again, the assumption requires a far-detuned laser field, where the sum of the couplings to the individual higher lying hyperfine states is approximately the same as for the fine structure states. Similar to Equation 2.67, the hyperfine reduced matrix elements can be related to the fine structure reduced matrix elements. An equality similar to Equation 2.76 can be found indicating that the hyperfine dipole matrix elements sum to the larger fine structure dipole matrix elements. In fact, for lower states with $J = 0$, it can be shown that all ground magnetic sub-levels experience equal total dipole coupling to the upper states. However, the resonant frequency dependence ω_{ak} in the polarizability (Equation 2.62) indicates that the magnetic sublevels in different nondegenerate upper hyperfine states will yield different contributions to the clock state polarizability. The larger the laser detuning relative to the hyperfine splitting (typically many orders of magnitude larger), the smaller this effect will be. Discussed more in Chapter 5, this small effect results in a m_F dependent polarizability which is included in the dipole polarizability tensor. Furthermore, because the $^3P_0$ clock state is not perfectly $J = 0$ (due to hyperfine mixing), the magnetic sublevels of the $^3P_0$ $F = 9/2$ clock state have different polarizabilities. In this same spirit, the weak nondegeneracy of magnetic sublevels in a bias magnetic field and of motional states of the confined atom yield differential polarizabilities. These splittings, orders of magnitude smaller than hyperfine splitting, yield effects which are negligible at the current level.

We have considered only the dipole polarizability interacting with the second order term in the electric field. Higher order multipole interactions as well as the

atomic hyperpolarizability interacting with the fourth order electric field term will be briefly discussed in Chapter 5.

Perhaps one of the biggest weaknesses of the dipole polarizability calculation is the accuracy of the state decay rates listed in Table 2.1. Unlike the well-known transition frequencies, few decay rates are known at the percent level. With the linear dependence of the polarizability contributions on these decay rates, knowledge of the polarizability better than the percent level is difficult. The lowest lying states typically contribute the most to the polarizability in the near-infrared region we are most concerned with for confinement. Improved measurements of these state decay rates will further improve the polarizability calculation.

Finally, as seen clearly from Table 2.1, the calculation above includes dipole polarizability contributions from states with principal quantum number, n, as high as 11. Of course, all higher lying states actually contribute (to a lesser degree), including Rydberg states and the continuum above ionization. The relative importance of such contributions varies, and cannot be overlooked. As a straightforward estimate of these higher-lying contributions, we first define the oscillator strength for a given transition, related to the dipole moment [118]:

$$f_{ak} = \frac{2}{3}\frac{\omega_{ak} m}{\hbar e^2}|d_{ak}|^2 \tag{2.78}$$

where $e(m)$ is the electron charge (mass). Closely related to the dipole moment squared, the oscillator strength (a dimensionless quantity) obeys the Thomas-Reiche-Kuhn sum rule [119]:

$$\sum_k f_{ak} = N \tag{2.79}$$

where N is the valence electron number (for Sr, $N = 2$). Here the sum is over all higher lying states, k, including Rydberg states and the continuum. By summing up the oscillator strengths for the transitions listed in Table 2.1, we can determine the residual contribution of the unlisted states to the oscillator strength sum of 2. Using

the dipole moments calculated from Table 2.1, the sum of oscillator strengths for the $^1S_0$ clock state from the $nsnp$ $^1P_1$ states (up to $n = 11$) is $\sum f_{^1S_0} \simeq 1.99$. For the $^3P_0$ clock state, the combined contributions from the listed $^3S_1$, $^3D_1$, and $^3P_1$ states gives $\sum f_{^3P_0} \simeq 1.28$. In the $^1S_0$ case, the sum is ~ 2 predominantly because of the very strong dipole coupling to the low lying $5s5p$ $^1P_1$ state. As a result, the effect of higher lying discrete states and the continuum on the $^1S_0$ polarizability are relatively small. However, in the $^3P_0$ case, the total oscillator strength contribution from higher lying states is non-negligible.

As a simple estimate of the effect on the polarizability, we can assume that all of the residual oscillator strength for each state is concentrated at the ionization energy, which corresponds to an angular frequency of $\omega_{ak} = 8.65 \times 10^{15}$ (rad/s) from the $^1S_0$ clock state and $\omega_{ak} = 5.95 \times 10^{15}$ from the $^3P_0$ clock state. We first consider the polarizability in the limit $\lambda \to \infty$, where the dynamic polarizability simplifies to the static polarizability. Using only the states in Table 2.1, the static polarizability of $^1S_0$ ($^3P_0$) is found to be 191 au (351 au) (1 atomic unit of polarizability is 1.64878×10^{-41} in the SI system). By including the residual oscillator strength contribution at the ionization threshold, the $^1S_0$ ($^3P_0$) static polarizability is found to be 192 au (455 au). As expected, the $^1S_0$ static polarizability is barely changed, but the $^3P_0$ static polarizability is increased by more than 30%. This change puts the values of the static polarizability in very good agreement with the currently accepted values of 197.2(2) au and 458.3(3.6) au [20]. However, the effect at near infrared wavelengths is also dramatic for $^3P_0$. As shown in Figure 2.13, using only the states in Table 2.1, a crossing of the $^1S_0$ and $^3P_0$ polarizabilities occurs at 805 nm, close to the experimentally observed value of 813.4 nm. However, the inclusion of the residual oscillator strength at the ionization threshold moves that zero crossing far away from the experimentally observed value, implying that the higher lying contribution is not accounted for properly by this simple estimate. Note that the static polarizability would be less sensitive to the details of

these higher contributions, because these high frequency resonances are far detuned from the limit $\lambda \to \infty$.

A more proper and sophisticated inclusion of these high lying contributions is difficult, mostly due to the lack of knowledge of the oscillator strength spectral distribution for Rydberg states and the continuum. Some experimental and theoretical investigation in this area has been conducted for Sr [120, 121, 122, 123, 124, 125, 126, 127, 128, 129]. By approximating the oscillator strength spectral distribution for Rydberg states and the continuum as reported in the experimental work of [120] corresponding to the $5s5p\ ^3P$- $5snd\ ^3D$ Rydberg series, further polarizability calculations showed qualitatively similar results to those described in the previous paragraph. Unfortunately, knowledge of continuum resonances in the oscillator strength spectral distribution is sparse, which could play an important role.

One approach to including all relevant contributions is making a full ab-initio calculation of the electronic wave functions and the corresponding transition energies and coupling matrix elements. The calculation can include a finite, spatial boundary around the atom, so that the eigenstates always remain discrete, rather than blending into a continuum. A complete basis set can be established so that a properly converging calculation of a quantity such as the polarizability includes all relevant contributions, comparable to a free space atom calculation including both Rydberg states and the continuum [130]. Most of these calculations involve designing the proper system Hamiltonian and finding the wave functions by solving an effective Schrodinger equation, often utilizing perturbation theory. While these calculations are very sophisticated and can become complex, in many cases it is easier to solve ab-initio for the entire polarizability contribution than trying to solve for just the higher lying contributions and add these to the contributions from states with sufficient experimental data [131].

One well known example of the importance of continuum contributions is the Cs microwave clock transition. Agreement between some theoretical and experimental

results on the size of the blackbody radiation (BBR) induced clock shift were in disagreement with other theoretical and experimental results [132, 133, 134, 135, 136, 137, 138]. The disagreement, exceeding the 1×10^{-15} level, was significant considering the role of Cs in defining the SI second and the projected inaccuracy of Cs fountain systems at 10^{-16}. The discrepancy was illuminated by ab-initio calculations which showed the disagreement among theoretical values originated from the lack of continuum contributions in the clock state polarizability for several semi-classical calculations [139, 140, 131]. While it is unclear if technical details caused the discrepancy in experimental values, these calculations helped guide the accepted BBR shift value. For the case of Sr, a complete basis calculation of the Sr dynamic polarizability has been made [136] yielding a crossing point of the two clock state polarizabilities at 795 nm. Further ab-initio calculations, perhaps guided by known experimental values, should provide more knowledge about the Sr polarizability (dynamic and static) and structure details. This information will be useful for several reasons, perhaps most prominently to aid in reducing the uncertainty of the BBR-induced shift of the Sr clock transition. As shown later in this thesis, this uncertainty currently limits the realizable accuracy of the Sr optical frequency standard.

2.6.3 1-D Lattice Confinement

Having considered the atomic dipole polarizability interacting with a generic optical potential, we now look at a specific case of trapping: the 1-D optical lattice. Multiple flavors of the 1-D lattice exist [141]. Here we consider a linearly polarized optical beam which is focused to a minimum beam radius. After propagating some distance beyond the beam waist, the beam is retroreflected without polarization rotation and with the appropriate optics so that the returning beam overlaps and maintains the same beam parameters as the original incident beam (see Figure 2.14). By summing together the electric fields of the two counterpropogating beams travelling in the x direction:

$$\vec{E} = \vec{E_0}\cos(kx - \omega t) + \vec{E_0}\cos(-kx - \omega t) \tag{2.80}$$

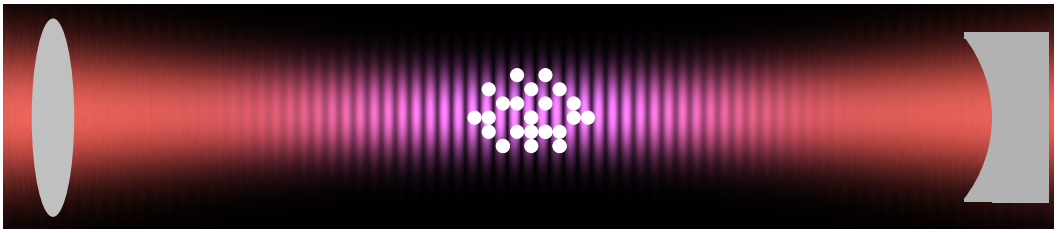

Figure 2.14: Schematic of the optical layout for the 1-D optical lattice. The lattice laser at 813 nm is tightly focused with an achromatic lens and retroreflected with a curved mirror whose radius of curvature matches the optical wavefront curvature. The atoms are confined at the trap focus. Interference along the trap axis and the Gaussian beam profile perpendicular to the trap axis give pancake shaped lattice sites. Many atoms are confined in each site and many sites are occupied. The clock laser propagates along the trap axis and the lattice retroreflector has high transmission ($\sim 99\%$) of the clock laser at 698 nm.

it is straightforward to show that the time average of the square of the electric field for the resulting standing wave is:

$$\langle |E|^2 \rangle = 2|E_0|^2 \cos^2(kx) \tag{2.81}$$

Here $\langle\rangle$ denotes the time average. Referring back to the total trapping energy ($\hbar\omega_a$) in Equation 2.63, and assuming a Gaussian beam profile with $1/e$ field radius of w_0, the time averaged trapping potential energy for an atom in state $|a\rangle$ is found to be:

$$\langle |U_a| \rangle = -\alpha_a \frac{4P}{\epsilon_0 c \pi w_0^2} \tag{2.82}$$

where P is the one way optical power of the incident optical beam, ϵ_0 is the permittivity of free space, c is the speed of light, and w_0 is the 1/e probe beam field radius. This peak trap depth is modulated by the $\cos^2(kx)$ term along the optical axis, and has a Gaussian envelope perpendicular to the optical axis as given by the beam's Gaussian profile. We have assumed that the index of refraction around the atom is unity. Equation 2.82 gives the total trap depth, expressed as energy, for the lattice confined atoms. By dividing by Boltzmann's constant k_B, we express this trap depth as a temperature. Obviously, to confine a substantial fraction of the atomic sample, the sample temperature must be less than the trap depth temperature.

With $\cos^2$ confinement along the trap axis and Gaussian confinement orthogonal to it, we now approximate confinement in all directions as harmonic. This is done in the standard way, by setting the trap "spring constant" in the ith direction equal to the second derivative of the trap depth profile with respect to the ith direction, and evaluating this second derivative at the trap minimum. These trap spring constants can then be related to the trap frequencies by the standard relation $\omega_{trap} = \sqrt{k_{trap}/m}$ with m the atomic mass. By doing so, we get the trap frequencies along (orthogonal) to the lattice axis as f_{long} (f_{trans}):

$$f_{long} = \frac{\omega_{long}}{2\pi} = \frac{1}{\lambda}\sqrt{\frac{2\langle U_a \rangle}{m}} \tag{2.83}$$

$$f_{trans} = \frac{\omega_{trans}}{2\pi} = \frac{1}{\pi w_0}\sqrt{\frac{\langle U_a \rangle}{m}} \tag{2.84}$$

These are the trap frequencies precisely at the trap focus. For a more general expression giving the trap frequencies away from the center of the focus, see Reference [142]. The trap frequencies ω_{long} and ω_{trans} can be used for the trap frequency ω in Equation 2.28 in their respective directions. Thus, these frequencies give the energy spacing between motional states of the confined atom in the different spatial dimensions.

2.6.4 Benefits of 1-D Lattice Confinement

In Section 2.5.2, we suggested that atomic confinement in an optical potential could be made uniform and defect-free for large atom numbers. This is in contrast to traditional crystal lattices which suffer from lattice defects that create inhomogeneities in the confining environment. Although the typically weaker confinement in the transverse dimension and atomic confinement away from the trap focus can allow for some trapping inhomogeneity, these effects are rather small and not particularly prohibitive in the matched potential regime. Overall, the optical standing wave makes for a very clean, defect-free potential, enabling confinement in the uniform potential regime. This is only one of several benefits of using lattice confinement for cold Sr atoms.

In Figure 2.13, we saw that the dipole polarizability of the two clock states have the same value around 805 nm. Experimentally, we have confirmed that the wavelength corresponding to the realization of matched potentials for the two clock states (sometimes referred to as the magic wavelength λ_{magic}) is 813.428 nm [23, 22]. This near infrared wavelength is relatively convenient for generating optical powers exceeding 1 W using optically pumped Ti:Sapph lasers or diode lasers followed by tapered diode amplifiers. Furthermore, we have experimentally observed that the sensitivity of the clock transition to excursions of the lattice laser away from the magic wavelength is approximately 1 GHz of lattice laser excursion to 1 Hz of clock transition shift (for our typical operating power of the lattice laser) [21]. This is in agreement with Figure 2.13,

and means that using standard techniques to frequency stabilize the lattice laser at <MHz level, we can ensure that the lattice laser operating at the magic wavelength will yield AC Stark shifts of the clock transition <1 mHz (1×10^{-18} of the clock transition frequency). Of course, at this level, we must be careful to consider higher order effects. Nevertheless, confinement of ^{87}Sr in an optical lattice is well suited to operating in the matched potential regime. It is also worth noting that because the clock states have $J = 0$ (nearly $J = 0$ for $^3P_0$), the Clebsch-Gordan coefficients (or Wigner $3-j$ values) for all optical polarizations are identical, meaning that the atomic confinement is not very sensitive to rotations of the lattice polarization, further facilitating the experimental realization of the matched potential regime.

Experimentally, it is straightforward to provide several hundred mW of lattice laser power focused to a 65 μm beam radius, corresponding to single beam laser intensities of $5 - 10$ kW/cm^2. Using Equation 2.82 together with the calculated atomic polarizability around λ_{magic}, we can straightforwardly achieve trap depths of 10-20 μK. This depth could be enhanced using an optical power build-up cavity around the atoms [143]. Since our laser cooling provides atomic samples at the μK level, the achievable trap depth facilitates trapping a large atom number from our laser cooled source. Furthermore, the Stark shift of the $^1S_0$-$^3P_1$ cooling transition in the lattice at λ_{magic} is small enough that proper choice of detuning of the cooling laser can still yield efficient cooling. This means that cooling can occur simultaneously during loading of the optical lattice, which enables atoms which "roll" into the conservative lattice potential to be cooled before "rolling" back out.

With this kind of trap depth, we see from Equations 2.83 and 2.84 that longitudinal and transverse trap frequencies exceeding 40 kHz and 150 Hz, respectively, can be achieved. As shown in the next chapter, coherent interrogation of the $^1S_0$-$^3P_0$ clock transition for lattice trapped atoms has yielded transition linewidths, γ, of a few Hz. This means that the 1-D lattice confinement realizes the well-resolved sideband regime

for all dimensions. Furthermore, with a clock transition recoil frequency of $\nu_r = 4.7$ kHz, we can operate in the Lamb-Dicke regime in the longitudinal dimension. For this reason, the clock transition is probed with a laser k-vector aligned parallel to the lattice axis. In doing so, we achieve both the well-resolved sideband and Lamb-Dicke regime, critical for high precision spectroscopy.

2.6.5 Further Details of 1-D Lattice Confinement

In Section 2.6.3, we looked at how the 1-D lattice provides harmonic confinement of Sr atoms. This confinement was shown to be approximately harmonic only by Taylor expanding the real potential around the trap minimum in each dimension. In the longitudinal direction, if we leave the full $\cos^2(kx)$ term in the 1-D confinement Hamiltonian, the Schrodinger equation can be transformed to be written as Mathieu's equation. The eigen-energies are found from well-known solutions to this equation. An example of the resulting energy spectrum is shown in Figure 2.15. The periodic $\cos^2(kx)$ potential results in a band structure, where the quantum states have finite energy bandwidths. Figure 2.15 corresponds to a trap depth that yields approximate harmonic trap frequencies of 80 kHz. In the matched potential and well resolved sideband regimes, while the anharmonicity has no appreciable effect on the purely electronic carrier transition, red and blue sideband transition frequencies depend on the initial quantum state $|n\rangle$. As a consequence, a thermal distribution of many motional states leads to first order sidebands with a range of different frequencies, and their maximum frequency separation from the carrier being ω_{long} [21]. By enabling spectroscopic discrimination, this anharmonicity could prove beneficial for studying the dynamics of individual motional states.

Another consequence of confinement in a finite, periodic potential is the possibility for quantum tunnelling between lattice sites. Such tunnelling can lead to two pernicious effects. The first is that atoms escape the potential, spatially lost to spectroscopic

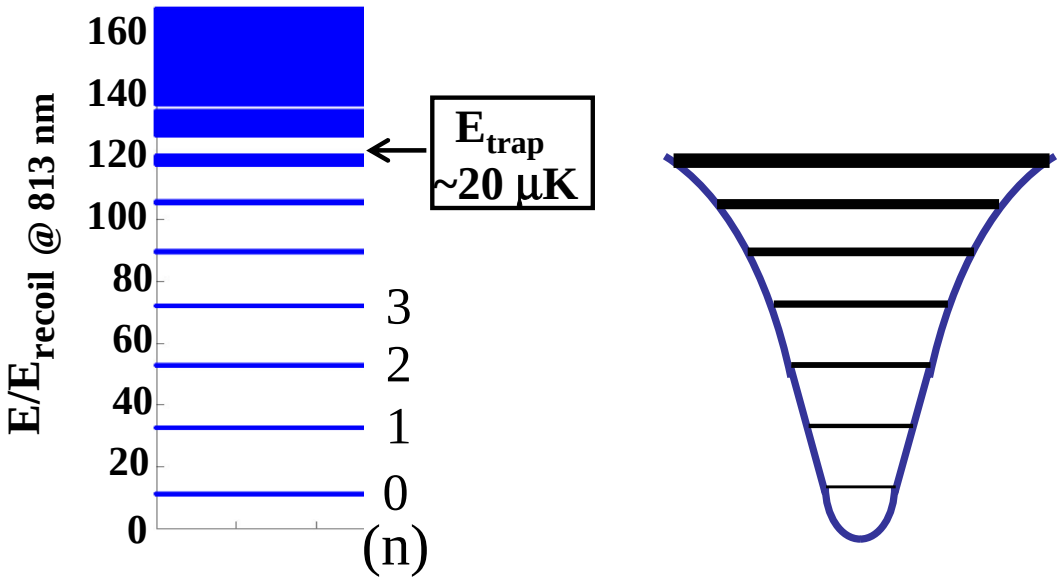

Figure 2.15: Atomic confinement energy band structure due to the anharmonic and periodic $\cos^2(kx)$ potential. The motional state quantum number, n, of the levels is indicated. Here the trap depth $\sim$ 20 μK corresponds to a lattice laser intensity of $I = 10$ kW/cm^2.

probing. More significantly, the corresponding band structure can shift the carrier transition frequency from the pure atomic transition frequency. Furthermore, the finite bandwidth of the motional states leads to line broadening. Both of these effects can be considered as residual Doppler and recoil effects associated with the delocalization of the atom due to quantum tunnelling. These effects have been estimated for the case of Sr in a 1-D optical lattice [144]. It has been determined that to keep them at or below the 10^{-17} fractional frequency level, the lattice depth should be at least 50 to 100 E_r (where $E_r = \hbar\omega_r$ for the magic wavelength lattice photon at 813 nm) to suppress these tunnelling effects. Alternatively, introduction of a term in the system Hamiltonian with linear spatial dependence can lift the degeneracy between neighboring lattice sites and more strongly localize the atom. This can be accomplished simply by aligning the 1-D lattice axis along gravity (as is roughly the case in our experimental setup). In this case, the eigenstates are referred to as Wannier-Stark states, typically organized into a ladder structure, with each state separated from its neighbor by the gravitational energy difference. Transition shifts and broadening are strongly suppressed in this case, and it is estimated that lattice depths of only 5-10 E_r are sufficient to keep these effects below 10^{-17} [144].

As seen in the previous section, confinement in a 1-D lattice can be very spatially asymmetric. For our typical operating conditions, $f_{long} \simeq 40$ kHz and $f_{trans} \simeq 150$ Hz. The much weaker confinement in the transverse axis creates some additional complications. First of all, the weaker confinement means that the atomic wavefunction has a larger spatial extent (see characteristic length x_0 in Section 2.5.2). Because f_{long} becomes smaller away from the optical axis [142], this larger transverse spatial extent can result in longitudinal spectroscopic sidebands which are smeared out, with a maximum frequency f_{long} [21]. The details of the smearing depend on the atomic sample temperature (which determines the population of motional states and thus the spatial extent, for more details see [16, 145]). This effect and the anharmonicity described above yield

broad asymmetric sideband spectra described more fully in Section 3.4.3

Perhaps a more significant consequence of the weak transverse confinement is that probing along that direction is not in the Lamb-Dicke regime. Although we try to probe along the strong confinement axis, for both practical and fundamental reasons, we can never perfectly do this. As a result, some component of excitation occurs in the transverse dimension. This is perhaps most notably observed through the Rabi excitation rate of the confined atom, as given in Equation 2.49. As seen in Figure 2.16, out of the Lamb-Dicke regime, the purely electronic excitation rate Ω_{nn} can become strongly diluted as a function of the initial motional state $|n\rangle$. For a Boltzmann thermal distribution occupying many transverse motional states, significant inhomogeneity in the Rabi frequency for different motional states can lead to a strongly damped Rabi excitation for the total atom ensemble [94, 146, 147]. This inhomogeneous excitation will be discussed more quantitatively in Section 5.4.4. This effect is present for both the transverse and longitudinal dimensions, but because we are in the Lamb-Dicke regime longitudinally, this effect is much smaller there.

Finally, we have shown how the atoms can be confined optically by considering atom-light interactions in the dispersive regime. Of course, even far off resonance, some photon absorption occurs. This leads to residual heating which transfers thermal energy to the atomic sample so that it is no longer confined in the lattice. In the far detuned case, the photon scattering rate (via spontaneous emission) is (see Equations 2.7 and 2.8 or see also [148]):

$$\Gamma_{scatt} = \sum_k \frac{\Gamma_k \Omega_{ak}^2}{4\Delta_{ak}^2} = \sum_k \frac{\Gamma_k}{\Delta_{ak}} \frac{U_{ak}}{\hbar} \tag{2.85}$$

where Γ_k is the (total) spontaneous decay rate from upper state k, Δ_{ak} is the (angular) transition detuning, and in the last equality we have used Equation 2.60 for the Stark energy term U_{ak}. Under current experimental conditions, the atom spends the bulk of its time in the lattice occupying the ground state. The ground state photon scattering

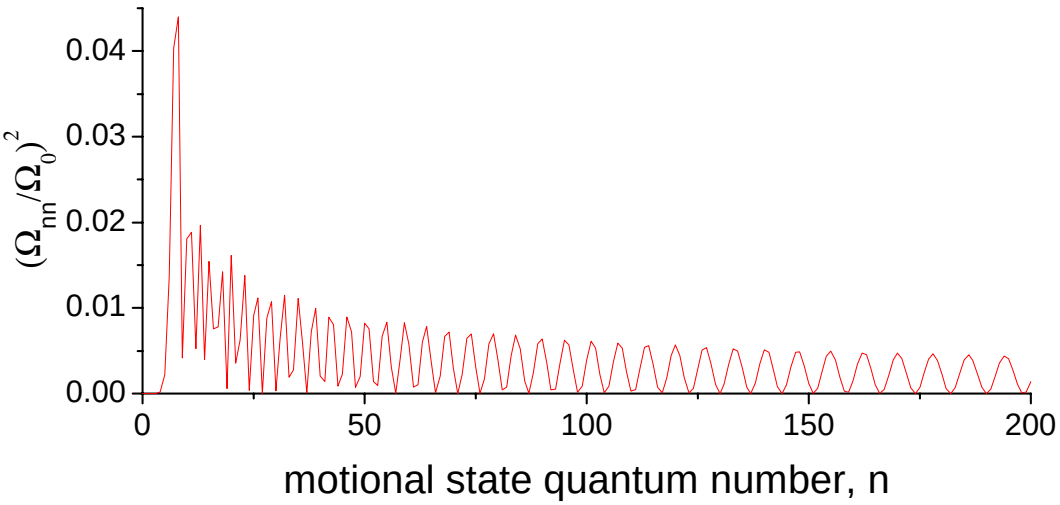

Figure 2.16: The diluted Rabi frequency (squared) for purely electronic excitation from a given motional state with quantum number n. The Rabi frequency is normalized to that of an atom in free space at rest. Here the atoms are not in the Lamb-Dicke regime ($\eta \simeq 5.3$), as is the case for atomic interrogation along the weak transverse axes of the 1-D lattice (as shown here $f_{trans} = 170$ Hz).

contribution is dominated by the very strong $5s^2\ {}^1S_0$- $5s5p\ {}^1P_1$ transition. Assuming each scattering event yields sufficient gain in thermal energy to heat the atom out of confinement, for typical experimental conditions, the trap lifetime due to photon scattering from the ground state ($\tau = 1/\Gamma_{scatt}$) exceeds 5 s. This lifetime is more than sufficient for spectroscopic probing of Fourier limited spectra with state-of-the-art resolution (see next chapter). As the probing times evolve to longer times, this lifetime may become an issue. Furthermore, with longer probing times, the atom spends more time in the excited clock state. This requires consideration of the photon scattering rate from ${}^3P_0$. Using only the dominant contribution from the $5s6s\ {}^3S_1$ state (and typical operating parameters), the trap lifetime of ${}^3P_0$ atoms also exceeds 5 s.

Another important contribution to finite trap confinement time comes from collisions between the trapped Sr with the hot vacuum background gas. Higher vacuum lowers the density of the background particles and thus the trap loss rate. The thermal energy of these hot gas particles is so large compared to the confinement energy, in many cases it is assumed that each collision successfully removes a Sr atom from the trap [149]. This assumption is not always valid, and quantum diffractive background gas collisions can play a role [150]. Accurate calculations of the loss rate due to background gas collisions require some knowledge of interaction potentials between the trapped and hot background particles (e. g. C_5 or C_6 coefficient). Here, empirical measurements can play an important role in determining this loss rate. Some experimental data exists for Sr [64, 115, 60]. Assuming a background-gas-limited-lifetime that is independent of the trap depth, application of the measurement by [64] to our typical vacuum at the trap ($\sim 2 \times 10^{-9}$ torr) yields a loss rate of 1 s^{-1}. This is in reasonable agreement with our observed trap lifetime of 1 s, indicating that background gas collisions could be playing the limiting role in our trap lifetime. Other physical mechanisms worth consideration including tunnelling loss and atomic heating due to phase or amplitude noise on the optical potential.

2.7 State Preparation via Optical Pumping: Nuclear spin polarization

In the case of ^{87}Sr, $I = 9/2$ meaning that the clock states with $F = I$ have a magnetic state degeneracy of $2I + 1 = 10$. Because $J = 0$, each m_F state corresponds to a unique nuclear spin orientation ($m_F = m_I$). In small or negligible background magnetic fields, these nuclear spin states are nearly degenerate. After laser cooling on the narrow $^1S_0$-$^3P_1$ transition, we have observed that the ground state $^1S_0$ population is approximately evenly distributed among all ten nuclear spin substates. Due to the fact that each magnetic substate has different Zeeman and lattice Stark dependence, this mixed population is not ideal for high accuracy and high precision spectroscopy. For this reason, it is desirable to interrogate isolated spin states by applying a magnetic field to split the nuclear spin state degeneracy. Sequential interrogation of opposite spin states ($\pm m_F$) has the added advantage of measuring two transitions whose average frequency is independent of some perturbing fields, like the B-field (to 1^{st} order). Since the spectroscopic signal scales with atom number, it would be efficient to push all of the atomic population into the nuclear spin state to be probed. This also reduces unwanted line pulling effects due to off-resonant transitions from neighboring spin states in a bias magnetic field. This state preparation preceding spectroscopy can be accomplished by optical pumping to one or more nuclear spin states.

Optical pumping has already been discussed in this chapter in different contexts. In Section 2.2 on laser cooling, we discussed unwanted optical pumping as the $^1S_0$-$^1P_1$ transition was cycled with a small spontaneous decay from $^1P_1$ to $^1D_2$, eventually populating the ^3P states. In Section 2.4, we discussed the role of the stirring laser for laser cooling ^{87}Sr on the $^1S_0$-$^3P_1$ transition. One of key roles of the stirring laser was that of optically pumping the population, in this case so that the population could be randomized among the magnetic sublevels. For state preparation, we are interested in

optically exciting the atoms where spontaneous decay favors a particular decay route (via the relative sizes of the Clebsch-Gordan coefficient for different decay routes) so that many pumping cycles move the population to the desired ground nuclear spin state. Like the stirring laser, we can utilize the $^1S_0$-$^3P_1$ transition to accomplish this. Figure 2.17 shows the results of a Monte-Carlo simulation where the atomic population is assumed to be initially distributed evenly among all populations [83]. In one case, the $^1S_0$ $F = 9/2$ - $^3P_1$ $F' = 7/2$ transition is driven using π-polarized light. After < 10 photon scattering events, the population has been pumped to an equal mixture of stretched states $m_F = \pm 9/2$. In the other case, the $^1S_0$ $F = 9/2$ - $^3P_1$ $F' = 9/2$ transition is driven with pure σ^+-polarized light, and the entire population is driven to $m_F = 9/2$. Switching to pure σ^--polarized light drives population to $m_F = -9/2$. Here, degeneracy among all nuclear spin states has been assumed. In practice, we typically apply a very small bias magnetic field (< 50 mG) during the optical pumping. We find optical pumping times of 20-50 ms give sufficient pumping of the population. Details of how well this pumping process works experimentally can be seen spectroscopically in Chapter 5.

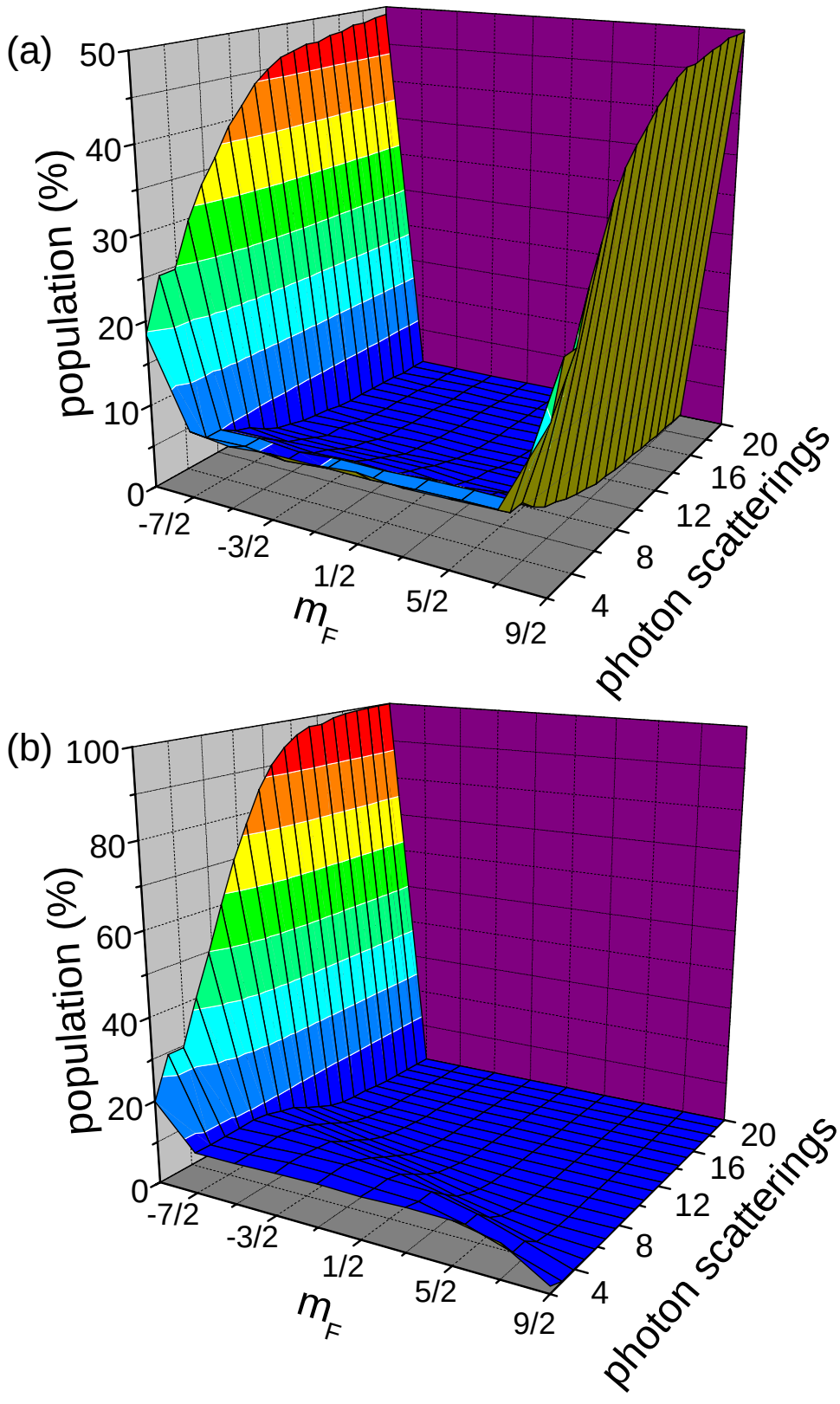

Figure 2.17: Optical pumping used for nuclear spin polarization state preparation. The population is assumed to be initially distributed evenly among all spin states. (a) Optical pumping by scattering π-polarized light on the ${}^1S_0$-${}^3P_1$ $F = 9/2$-$F' = 7/2$ transition. After ~ 10 photon scatterings, the population is evenly shared between the $m_F = \pm 9/2$ states. (b) Optical pumping by scattering σ^--polarized light on the ${}^1S_0$-${}^3P_1$ $F = 9/2$-$F' = 9/2$ transition. After ~ 10 photon scatterings, the population accumulates in the $m_F = -9/2$ states.

Chapter 3

Coherent Light-Matter Interaction: Hz level spectral linewidths in the optical domain

3.1 The Need for Atomic and Optical Coherence

As seen in Chapter 2, the spectroscopic probing of an atomic transition is described by the interaction term of the Hamiltonian, $H_I = \vec{d} \cdot \vec{E}$ (e. g. Equation 2.34). Coherent excitation of the atomic transition requires the individual coherent evolution of both the atomic dipole d and the electric field E. The longer that this coherence can be maintained, the higher the resulting spectral resolution. This is seen in the Rabi flopping solution for the excitation of a two-level atom (with equations of motion as in Equations 2.44 and 2.45):

$$P_e(t, \Delta) = \frac{\Omega^2}{\Omega^2 + \Delta^2} \sin^2 \left(\frac{\sqrt{\Omega^2 + \Delta^2} T}{2} \right) \tag{3.1}$$

where Ω is given in Equation 2.5, Δ is the (angular) detuning from the atomic transition, and T is time. For convenience, we choose $\Omega T = \pi$ (pi pulse). The resulting sinc^2 spectral feature has a Fourier-limited full width at half-maximum equal to $\Delta\nu_{Rabi} \simeq 0.89/T$. Longer times T give narrower features $\Delta\nu_{Rabi}$. Eventually decoherence limits the achievable coherent interaction time T. Regardless of the type of spectroscopy employed, often a primary goal of very high precision spectroscopy is to probe the atomic sample for a maximum time. For atomic frequency standards, the enhanced spectral resolution with long timescale interactions enables very high measurement stability (Equation

1.1), which subsequently improves the precision of systematic shift measurements and thus the accuracy. In some cases, like line-pulling from nearby transitions, the size of the shift itself decreases with narrower linewidths. Also, we saw in Section 2.5.4 that Doppler and recoil effects are reduced with confinement in the well-resolved sideband regime. The narrower transition linewidths relax the potential depths needed to operate in this regime. For all of these reasons, a good deal of effort is made to permit long coherence times for both the atom and the probing electric field.

3.2 Atomic Coherence

The coherence relevant for an atomic frequency standard focuses on the two clock states (and their relative eigen-energies). This coherence must be observable in a reference frame where the probing optical wave is coherent. These important criteria can be frustrated by a multitude of noise processes coupling to the atoms. Among these, motional effects can play a significant role. The recoil and Doppler effects we have already considered in previous sections manifest themselves in a variety of shift mechanisms and inhomogeneities across a thermal velocity distribution of atoms. Although some types of spectroscopy remain less sensitive to these effects, none are completely insensitive. The reduction of the effect itself, by reducing the velocity distribution and by confining the atoms in the well-resolved sideband and Lamb-Dicke regime, is critical. The success of single-trapped ions and now lattice-trapped neutral atoms in achieving the highest resolution optical coherent spectroscopy [151, 152] is made possible through the elimination of motional effects due to the quantum confinement of these cold particles. A key ingredient is uniform confinement, where the two clock states are differentially unaffected by the confinement.

Many mechanisms can perturb the relative phase evolution of the clock states and decohere the atomic sample. One such mechanism is collisions between the cold Sr atoms, which leads to density dependent frequency shifts of the measured transition

frequency. Up until recently, this effect has been unobservable. In Chapter 5, using the high measurement resolution resulting from a direct optical comparison between optical standards, we will see non-negligible collisional effects in the dilute Sr gas and discuss how these effects can be further minimized. Another perturbing mechanism is spatially or temporally varying fields, which can lead to random phase accumulation which decoheres the atomic sample as the atoms sample these fields in space and time [153]. We work to minimize such potential perturbations, including: using low magnetic susceptibility stainless steel vacuum chambers, electrically grounding the chamber, using electromagnetic trim coils to zero residual bias fields (designed with spatial homogeneity in mind) driven by low noise current sources, using optically thick enclosure around vacuum chamber (curtains) to reduce stray optical fields, using mechanical shutters to block unwanted residual laser fields during probing, etc.

Finally, while ideal lattice confinement removes most motional problems, noise in the trap potential itself can re-introduce these problems. For example, phase noise in the lattice standing wave (e. g. shaking lattice retroreflector) may introduce sizeable Doppler effects during spectroscopy. We utilize high stability optical mounts for the lattice and probe lasers, and a large fraction of the optical path for these beams is shared, allowing for partial common mode rejection of vibration. We typically float the optical table on which the spectroscopy takes place, using standard compressed air legs with an isolation roll-off frequency of a few Hz. Furthermore, we mounted a PZT on the lattice retroreflector, and using the lattice standing wave as one arm of a homodyne Michelson interferometer (the other arm serving as a reference arm), we have actively stabilized the retroreflector position along the lattice axis (by monitoring optical phase of the interferometer). For measurements described in this chapter, this active stabilization did not make noticeable improvements and is typically not used. We also took care to avoid amplitude noise in the lattice trap by actively stabilizing the lattice optical power incident on the vacuum chamber viewport.

3.3 Optical Coherence: Laser Frequency and Phase Stabilization

Generation of coherent, single-frequency electromagnetic radiation has a rich history in the radio, microwave, and optical domains. The invention of the laser was a landmark step towards this goal for optical frequencies. Lasers, usually consisting of an excited optical gain medium interior to an optical resonance cavity, can generate high intensity radiation with relatively high spatial and temporal coherence. The laser radiation frequency is given by a resonant frequency of the laser's optical cavity. This resonant frequency is susceptible to a variety of noise processes originating from the driven gain medium, other intracavity optical elements, optical path length changes of the round trip cavity length, and amplified spontaneous emission. These processes give finite temporal coherence to the laser output, with a coherence time often insufficient for the very high resolution desired in precision optical spectroscopy. With the possibility to reduce all of these noise processes, a much more well-defined resonant frequency can be achieved in a properly designed, purely passive optical cavity. Highly coherent optical radiation can be obtained by stabilizing the frequency output of a laser to the passive optical cavity resonance. This stabilization typically exploits electronic feedback to the laser. Several schemes for deriving the stabilization signal exist, the most popular for high performance laser phase and frequency stabilization being the Pound-Drever-Hall (PDH) technique [77]. With the wide use of PDH stabilization in different laboratory and technical environments, a basic review of this technique will not be given here. The interested reader is referred to several useful references in the literature, dealing both with the PDH technique and laser stabilization in general [77, 154, 155, 156, 97]. Rather, I give here a partial list of important design considerations relevant to laser frequency stabilization at the current state-of-the-art.

3.3.1 Laser Stabilization Design Considerations

PDH locking has several advantages over many alternative stabilization schemes. By utilizing the reflected signal ("composed" of both the cavity reflection and the cavity leakage field), PDH stabilization accesses optical phase information at Fourier frequencies above the cavity linewidth ($\delta\nu_{cavity}$) and optical frequency information below it. Unlike the transmitted signal, the feedback bandwidth is not limited to the inverse of the cavity storage time [77]. Furthermore, because detection is moved to a high modulation frequency where the laser intensity noise spectral density can approach the shot noise, PDH locking is typically less sensitive to intensity fluctuations [77]. The PDH error signal is dispersion shaped, and the region between maximum and minimum can be approximated by a line whose slope, called the discriminator slope, is given by [154]:

$$D = \frac{8\sqrt{P_c P_s}}{\delta\nu_{cavity}} \tag{3.2}$$

where P_c is the optical power in the carrier, P_s is the optical power in the one sideband, and it has been assumed that the cavity reflection contrast is unity. The fundamental noise process limiting PDH locking is photon shot noise, with a white spectral density. The shot noise sets a limit on the laser frequency noise spectrum which is achievable using PDH locking, and is given by dividing the shot noise by the discriminator slope. This frequency noise amplitude spectral density of shot noise can be written as [154]:

$$s_f = \frac{\sqrt{hc}}{4}\frac{\Delta\nu_{cavity}}{\sqrt{\lambda P_c}} \tag{3.3}$$

where λ is the laser wavelength. Note that for true white frequency noise, the resulting laser spectrum is Lorentzian with a full width at half maximum given by πs_f^2 [157, 97]. From Equation 3.2, it is clear that in PDH locking, a narrower linewidth cavity can yield a more stable laser (less frequency noise and narrower laser linewidth). It is with this motivation that high reflection, low loss mirrors are used in optical cavities for state-of-the-art laser stabilization, with cavity finesses approaching 10^6 (cavity finesse,

$F = \Delta\nu_{FSR}/\Delta\nu_{cavity}$, where $\Delta\nu_{FSR} = c/2L$ and L is the cavity length). According to Equation 3.2, lower frequency noise could also be achieved using a stronger laser power (higher shot noise signal to noise ratio - S/N). Unfortunately, in practice, this is not generally true for at least two important reasons. It is common that as optical power is turned up, the S/N becomes limited by technical noise which scales with power, limiting Equation 3.2. Second, optical power buildup in high finesse cavities can result in very high circulating powers which can be weakly absorbed by the dielectric thin films of the cavity mirrors. This results in heating which causes cavity length drift/noise and thus degrades the stability of the cavity resonance. How much absorption occurs depends on individual dielectric coatings and surface contaminants. In one case, a cavity with finesse $F \geq 150,000$ experienced a cavity resonance shift of 1 Hz per 1 μW of incident power [158]. To this end, the optical power incident on the cavity (or the reflected or transmitted power) can be stabilized to limit drift/noise from this effect. It should be noted that the mirrors used in these high finesse cavities have optical coatings with very low transmission and absorption/scattering losses. Ideally the absorption/scattering losses would be zero, but are usually not smaller than a few parts per million (ppm). With smaller and smaller transmission losses for high reflectivity, the non-negligible absorption/scattering losses in the cavity mirrors result in less than unity reflection contrast. This degrades the PDH error signal. In this more general case, the photon shot noise limited frequency noise amplitude spectral density can be found to be:

$$s_\nu(f) = \frac{\pi}{rt_1^2 F}\frac{\Delta\nu_{cavity}}{8}\sqrt{\frac{2hc(2P_s + R_{imp}P_c)}{\lambda P_c P_s}} \tag{3.4}$$

where r is the amplitude reflection coefficient of both mirrors of the passive Fabry-Perot cavity, t_1 is the amplitude transmission coefficient of the input mirror, and R_{imp} is the fraction of the resonant carrier power reflected back due to imperfect "impedance matching" of the cavity.

A very high finesse cavity can sometimes have a linewidth much narrower than

the power spectrum of the laser needing to be stabilized. This can lead to several complications. In some cases, pre-stabilization of a laser to a broader linewidth cavity is used to spectrally narrow the laser so that the subsequent laser radiation incident on the high finesse cavity has a spectral linewidth similar to or less than the high finesse cavity linewidth [158, 159]. Such an approach avoids the error signal distortion which otherwise occurs, helping to keep detection and feedback operation in the linear regime. This helps make characterization and optimization of the cavity and cavity lock more straightforward. Furthermore, it can reduce the probability of saturation in the high gain electronic feedback. However, in many cases, this approach is not essential [160]. Several groups developing stable laser sources for optical frequency standards have chosen to lock directly to a high finesse cavity and avoid the complexity of a pre-stabilization cavity [161, 162, 163, 164, 165, 166]. Note that these issues are less relevant for intrinsically frequency stable lasers like Nd:YAG MISER (Monolithic Isolated Single-mode End-pumped Ring) lasers and single mode fiber lasers, whose free running linewidth can sometimes be below the 10 kHz level.

A major weakness of PDH locking is that the required laser phase modulation can never be realized perfectly, but rather there is always some level of residual amplitude modulation (RAM). Time dependent RAM introduces measurement noise where it is least wanted: at the detection frequency. This typically limits the locking performance to worse than the photon detection shot noise, and unfortunately RAM can be quite large (1% level) [167]. There are many physical origins of RAM. Some of these include etaloning effects in the phase-modulation crystal, time dependent crystal birefringence (e. g. temperature induced), spatial inhomogeneity of the modulation field in the crystal, piezo-electric response of the modulation crystal causing beam steering, amplitude noise in the RF drive, and vibration of optical components. Fortunately, steps can be taken to reduce these mechanisms. Active control of amplitude modulation by feedback on a bias electric field in the electro-optic (EO) crystal has demonstrated real-time zeroing

of RAM to reach shot noise limited detection [168]. Furthermore, two tone modulation can reduce RAM effects. We have generally taken a passive approach to limiting RAM. For example, some steps we have taken include: temperature stabilization of the electro-optic phase modulation crystal; anti-reflection (AR) coating on EO crystal faces; use of a crystal with large cross section and large electrodes with center stripe for uniform field generation at crystal center [169]; 4 axis kinematic mount for EO crystal to periodically align crystal to minimize RAM; a high quality polarizer before EO crystal; optical isolator after EO crystal; EO crystal with reduced RAM sensitivity (ADP, reduced piezoelectricity) [167]; low noise RF drive source; mounting of both the EO crystal, high finesse cavity, detection photodetector, and all intermediate optics on a vibration isolation platform; and detection of the entire optical beam after the EOM on a large area photodetector.

With a properly designed feedback system, utilizing high bandwidth components with minimal temporal delay and phase excursions, the PDH error signal is filtered to tightly lock the laser phase/frequency to the resonant optical cavity (error signal analysis can characterize the locking efficacy) [97]. The generation of frequency-stable laser radiation now transforms into the task of designing an optical cavity with a very stable cavity length (resonant frequency), and this is where a large fraction of the effort is spent. As a first effort to maintain length stability, the cavity mirrors are mounted (optically contacted) to a rigid spacer. The optical cavity is also typically placed in vacuum, motivated by several considerations. First, by reducing convective and conductive heat flow through air, the vacuum acts as a thermal insulating layer which aids the effort to temperature stabilize the cavity. Temperature stability is critical due to the coefficient of thermal expansion of the material(s) used to construct the optical cavity. Second, the vacuum acts as an acoustic shield, preventing the optical cavity from being shaken and deformed by airborne acoustic waves. Third, the vacuum helps reduce index of refraction fluctuations which translate into changes in the optical length of the cavity.

For example, the index of refraction, n, at standard temperature and pressure (STP) can be related to n somewhat away from STP by the empirical model:

$$(n-1)_{T,P} = (n-1)_{STP} \times 0.0013882 \frac{P_{Torr}}{1 + 0.003671 T_{Celsius}} \tag{3.5}$$

Temperature change of 1 ^{o}C or pressure change of 5 Torr (the approximate daily pressure change over 24 hours) can result in changes of the index of refraction $\Delta n \simeq 1 \times 10^{-6}$. Remembering the changes in the index of refraction, the cavity length, and the resulting laser frequency drift can be related simply by:

$$\frac{\Delta n}{n} = \frac{\Delta l}{l} = \frac{\Delta f}{f} \tag{3.6}$$

such a large Δn can be prohibitive in obtaining low drift rates of a sub-Hz stable laser.

To estimate the effect while under vacuum, we treat the residual vacuum gas as an ideal gas. From the ideal gas law, the particle density is given by:

$$\rho = \frac{N}{V} = \frac{P}{k_B T} \tag{3.7}$$

Furthermore, we treat the index of refraction with the simple model:

$$n = 1 + \alpha_{chem} \rho \tag{3.8}$$

where α_{chem} is the gas particle polarizability in units of volume ($\alpha_{chem} = \alpha / 4\pi\epsilon_0$, where α is the polarizability as given in Chapter 2). For a typical polarizability of several common vacuum gases ($\alpha_{chem} \simeq 1 \times 10^{-30}$), a pressure change of 5 torr gives a change in the index of refraction of $\Delta n \simeq 1 \times 10^{-11}$. Thus by operating in vacuum and keeping the technical vacuum fluctuations below 10^{-4} torr, index of refraction contributions may be kept sufficiently small for sub-Hz laser stability and minimal vacuum induced laser drifts. Note that this simple model may underestimate the vacuum pressure effect, but experimentally we have observed that a $\sim 10^{-6}$ Torr vacuum level is sufficient to reduce cavity drift levels below thermal induced drifts described below.

Finally, before leaving the topic of vacuum, it should be noted that fundamental vacuum fluctuations can introduce index of refraction noise with a relatively high bandwidth. This noise originates in the Poissonian fluctuations of the number of vacuum gas particles which alter the index of refraction in the volume given by the optical cavity mode. The effect of these fluctuations, expressed as a frequency noise amplitude spectral density, is found to be [170]:

$$s_\nu(f) = 2^{5/2}\pi^{5/4}\frac{\alpha_{chem}c}{\lambda^{5/4}L^{3/4}}\sqrt{\frac{\rho}{\bar{v}}}e^{-\sqrt{2\pi\lambda L}f/\bar{v}} \tag{3.9}$$

where f is the Fourier frequency, L is the cavity length, $\bar{v}$ is the mean gas particle speed, c is the speed of light, and λ is the laser radiation wavelength. This noise from residual gas is regularly considered in the context of large interferometers for gravitational wave detectors. For laser stabilization used by optical frequency standards, the technical sources of vacuum-induced laser drift/noise usually put a more stringent constraint on the required vacuum than this more fundamental effect.

One of the key properties considered in the choice of materials used to make the optical cavity (spacer and mirror substrates) is the coefficient of thermal expansion (CTE). It is, of course, desirable to have as small a CTE as possible. For this reason, glass materials such as Corning ultra-low expansion glass (ULE) and Schott Zerodur are commonly used, with typical CTEs as low as 10 parts per billion (ppb) per K. The vacuum chamber enclosing the cavity is temperature stabilized, where 24 hour temperature stability at the mK level can keep laser frequency drifts at or below the 1 Hz/s level. Note that it is principally the CTE of the cavity spacer which is of interest, but when the cavity spacer and mirror substrates are made of different materials with unmatched CTEs, stress-induced deformation of the mirror substrate can make the overall cavity CTE significantly depend on the mirror substrate CTE [171]. ULE has the added advantage that the CTE has a zero crossing temperature, typically above the freezing point of water. Unfortunately, lack of manufacturing control makes it diffi-

cult to design this CTE zero crossing around a convenient room temperature, however groups have worked to operate around the CTE zero crossing of their particular ULE sample and have seen laser drifts as small as the several mHz/s level [172, 173]. Some materials cooled to cryogenically cooled temperatures, like crystalline sapphire, exhibit remarkably small CTEs or CTE zero crossings [174, 175, 176]. Finally, because ULE and Zerodur glasses are non-crystalline amorphous solids, they experience long-term settling changes referred to as material creep. It seems that the material creep rate reduces as the glass ages. Furthermore, based on the use of a few samples, it seems that ULE has a smaller material creep rate than Zerodur. In one case, using a year-old Zerodur cavity at 698 nm yielded a laser drift rate of ~ 5 Hz/s, which appeared to be limited by material creep. Beyond this long term material creep, small discrete jumps in the cavity length also occur and are commonly attributed to the settling of the amorphous glass or the optical contacts between the spacer and mirror substrates.

Although the optical cavity utilizes a rigid spacer to hold the mirror spacing constant, no material is infinitely rigid, and as such is susceptible to elastic deformation. For the case of optical cavities, acceleration-induced deformation can result in cavity length changes which can seriously degrade both the short and long timescale frequency noise of the spectrum of the laser locked to the cavity. The details depend on the acceleration noise spectrum shaking the cavity. The efforts to reduce this effect are two-fold. First, vibration isolation is implemented to reduce the amplitude of the acceleration noise spectrum affecting the cavity. Different groups have utilized different isolation systems [158, 159, 161, 164], passive or active, commercial or homemade, and the gravitation wave detection community has a good deal of experience in this area (e. g. [177, 178, 179]). For optical frequency standards, particular emphasis must be placed on the very pernicious vibrations at low Fourier frequencies. The second, and somewhat more elegant approach to reducing acceleration-induced cavity noise is making the cavity length less sensitive to acceleration-induced deformation. With the vacuum

limiting airborne noise, acceleration is transferred to the cavity at the points where the cavity is physically held and connected to the vacuum chamber and environment. If the cavity can be designed and held in such a way that length changes from deformations are either reduced in amplitude or enjoy cancellation along different parts of the cavity, then acceleration-induced cavity noise can be reduced. Many cavity mounting techniques in the last few years thus try to exploit symmetry in the acceleration-induced cavity stress to reduce the cavity sensitivity. A number of experimental and theoretical (finite-element-analysis) results have been presented [165, 180, 181, 182]. Cross coupling of deformation must be taken into account with Poisson's ratio. While a typical cavity held with relatively standard techniques might have an acceleration sensitivity of > 100 kHz/(m/s^2) (expressed as a resonance shift for a 1 m/s^2 acceleration), some cavity designs and mounting have shown sensitivities reduced by more than 100 times. As discussed in the next section, the cavity we used exploited a vertical-oriented symmetry to reduce the acceleration sensitivity.

Perhaps the most fundamental limit to cavity length stability is thermal mechanical noise of the cavity components. Any object not at absolute-zero temperature has thermal energy which on the microscopic scale corresponds to the motion of its constituent particles. This thermal energy off-resonantly excites mechanical modes of the mirror substrates, dielectric thin film mirror coatings, and the cavity spacer. In this way, the cavity length dynamically changes according to the random, Brownian thermal motion, introducing frequency noise to the laser which is locked to it. Thermal-mechanical noise has been studied in different contexts, most notably in gravity wave interferometers [183, 184] and recently in rigid cavities for laser stabilization. Thermal mechanical noise in the wires used to hang interferometer mirrors can play a limiting role in the detection sensitivity of gravitational wave detectors. The quantitative relevance of thermal mechanical noise to state-of-the-art cavity stabilization was illuminated by [185]. Using the fluctuation dissipation theorem [186], the authors of [185] derived approximate

formulas for the length noise spectral densities of the cavity spacer, mirror substrates, and dielectric thin films. In most cases, the mirror contributions dominates over the spacer contribution. Expressed as a frequency noise amplitude spectral density (for the cavity), the mirror and dielectric coating thermal mechanical noise is [185]:

$$s_\nu(f) = \frac{c}{L\lambda}\sqrt{\frac{4k_BT}{2\pi f}\frac{1-\sigma^2}{\sqrt{\pi}Ew_0}\phi\eta} \tag{3.10}$$

where E is the Young's modulus of the mirror material, σ is Poisson's ratio, w_0 is the beam radius at the mirror, ϕ is the loss of mirror substrate ($\phi = 1/Q$, where Q is the mechanical quality factor), and η is a correction factor ≥ 1 including the effect of the mirror coating [185]. State-of-the-art cavities at room temperature made from ULE glass with cavity lengths typically in the range of 10-20 cm have a frequency noise spectrum (Equation 3.10) which corresponds to a fractional frequency instability limit in the range of 4×10^{-16} - 1×10^{-15}. This instability limit is consistent with the best experimentally demonstrated instabilities (e. g. [158, 185, 159]), and thermal-mechanical noise is seen as the current limitation to frequency stabilization at the state-of-the-art.

Equation 3.10 gives a straightforward description of how the thermal-mechanical noise can be reduced from its current magnitude. Reduction can be achieved by (1) improved choice of cavity materials (increased E and $Q = 1/\phi$) (2) increased beam radius w_0 (3) increased cavity length L (4) reduced cavity temperature T. Each one of these approaches comes with technical difficulties. Frequently-used ULE has $Q = 6\times10^4$, 20 times larger than that of Zerodur. Fused silica looks attractive, with $Q = 10^6$ [185] and $E \simeq 70$ GPa (E approximately similar to that of ULE and Zerodur). However, the CTE for fused silica is approximately 50 times larger than that of ULE, implying that much more stringent temperature control would need to be employed if using fused silica anywhere in the cavity. With a similar motivation, the gravitational wave detection community is considering at least two other mirror substrate materials: cryogenically cooled crystalline sapphire and silicon. Both have E several times larger than ULE

(measured at room temperature). Near room temperature, both have Q similar to fused silica. However, with cryogenic cooling, both have demonstrated remarkable Q increases, with $Q \simeq 10^8 - 10^9$ (near 4 K) [187, 188]. Furthermore, both materials have been shown to possess remarkably small CTEs at cryogenic temperatures [174, 175, 176]. It must be remembered, however, that as thermal noise contributions from the mirrors decrease, the contribution from the dielectric coating (summarized by η) may dominate. The mechanical Q for high quality dielectric coatings is typically $2 - 3 \times 10^3$, and so far these values are roughly independent of temperature [189]. Again motivated by gravitational wave detectors, work has investigated whether a particular choice of dielectric coating (including coatings with doping) could result in larger Q. Unfortunately, thus far, only small gains (TiO_2-doping of Ta_2O_5 in Ta_2O_5 / SiO_2 coatings has twice the mechanical Q) have been observed [190, 189].

Increasing the beam radius allows further transverse spatial averaging of the thermal mechanical noise. One approach to increasing the effective beam size is by exciting higher order transverse modes of the cavity [191]. Otherwise, thermal noise reduction by beam size is limited by the cavity mode radius for mirrors of available radii of curvature. Another cavity parameter can yield much more noise reduction: of all the parameters in Equation 3.10, cavity length has the strongest dependence, and could thus most reduce thermal noise effects. Unfortunately, extending cavity lengths beyond those now used (typically from $5 - 20$ cm) introduces increased complexity and cost in manufacturing and isolation of the cavity. Furthermore, for some mounting schemes, the acceleration sensitivity scales with the cavity length (e. g. [165]), and longer cavities can prove difficult for keeping acceleration-induced cavity length changes down. Nonetheless, some gains may be available here.

Finally, reducing the thermal energy at lower temperatures reduces the thermal-mechanical noise. To be productive, large temperature reductions must be made (cryogenic cooling). As mentioned above, several candidate materials could be used. Other

important material properties for cooling include the thermal conductivity and heat capacity. Cryogenically cooled sapphire cavities have already been used to demonstrate laser frequency stabilization at the 1 Hz instability level [175]. Perhaps the primary difficulty with cryogenic cooling is the ability to do so without introducing excess vibrational noise, deforming the cavity. Cooling to reduce thermal noise holds promise, and expertise in quiet cooling is already being developed in other fields, such as gravitational wave detection.

As we move to the next section describing particular details of the ^{87}Sr clock laser at 698 nm, I mention in passing one or two other design details. To limit RAM, we discussed the use of optical isolation after the modulation crystal. Generally speaking, etaloning effects from any optical surface can cause problems to the measurement detection. We always implement an optical isolator between the EO crystal and the high finesse cavity and have seen gains from doing so. We also utilize optical isolation after beam pick-offs from the light headed toward the cavity. At times, we have also used isolation immediately before the photodetection. Time dependent electronic biases originating from ground loops, mixers, or input stages to the loop filter used for feedback should also be monitored carefully.

3.3.2 Sub-Hz Sr clock laser

The clock laser source is a diode laser (Hitachi HL6738MG, AR-coated) in an external cavity of the Littman configuration operating at 698 nm (see Figure 3.1). The laser is first pre-stabilized to a simple optical cavity with finesse of $\sim 10,000$ and linewidth of several hundred kHz. The PDH stabilization is accomplished via feedback to the laser diode current and the laser cavity piezoelectric transducer (PZT). The servo bandwidth is 2-3 MHz. The pre-stabilized laser light is first-order diffracted by an acousto-optic modulator (AOM) and fiber coupled to a platform on which an ultra-stable cavity resides. This platform is mounted on a commercially available passive vibration

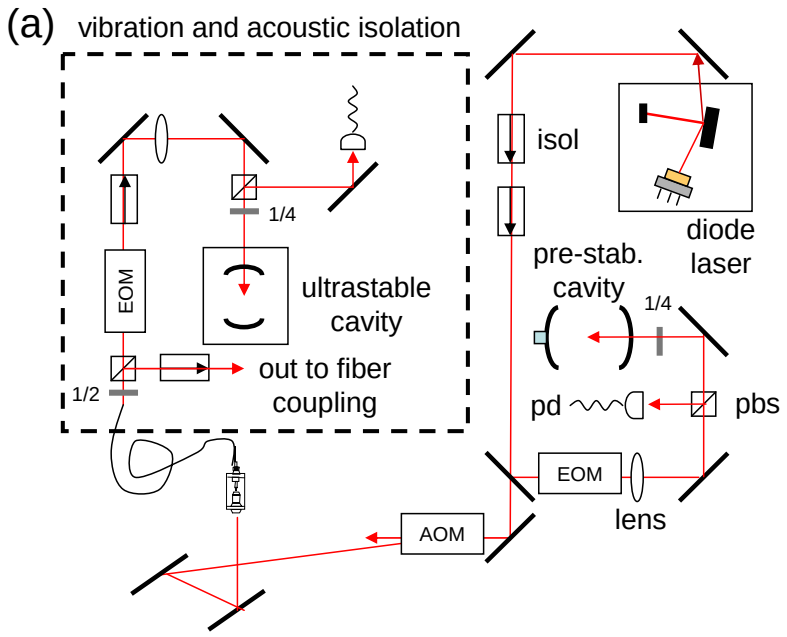

(b)

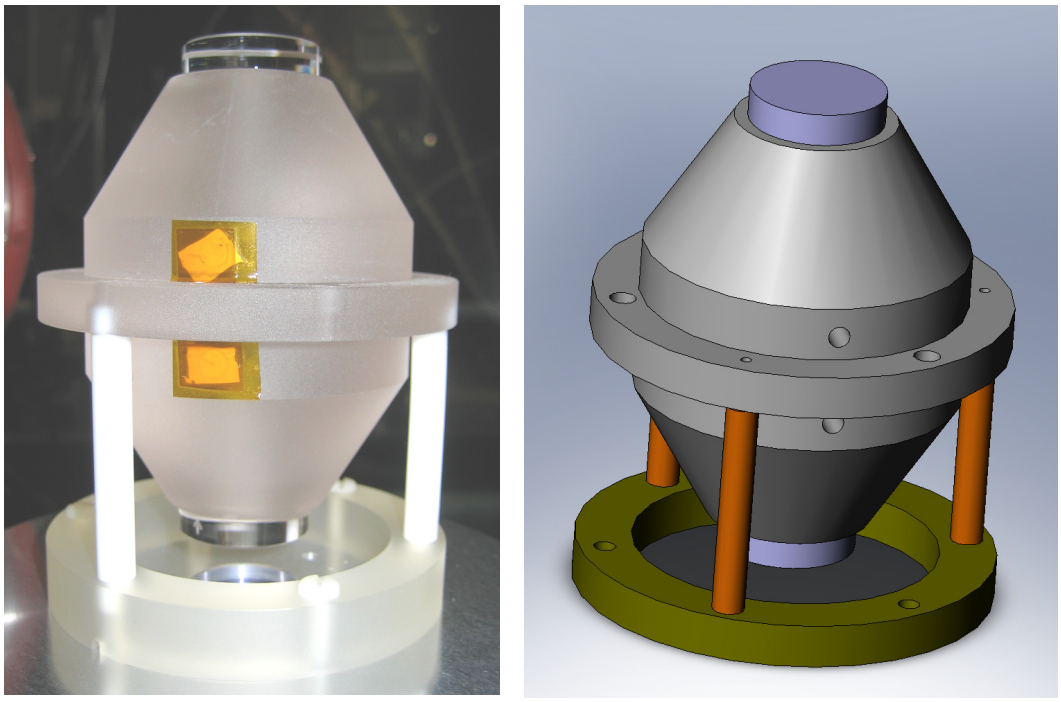

Figure 3.1: (a) Schematic of the laser-cavity system used to probe the ^{87}Sr clock transition. 1/4: quarter wave plate, 1/2: half wave plate, pd: photodetector, EOM: electro-optic modulator, AOM: acousto-optic modulator. The diode laser, in an external cavity configuration, is electronically frequency locked by two stages of Pound-Drever-Hall stabilization, first to the pre-stabilization cavity and ultimately to the high finesse, ultra-stable optical cavity. (b) The tapered, high finesse ultra-stable cavity in the vertical mounting configuration. The mirrors are optically contacted on the spacer. The midplane mounting ring, monolithically integrated to the spacer, loosely rests on three teflon rods which themselves are tightly held by a Zerodur ring fastened to the vacuum chamber.

isolation unit (Minus K, resonant frequency of 0.5-1 Hz). Both the platform and the isolation unit are within an enclosure lined with acoustic-damping foam. At times, this enclosure has been temperature controlled at the 100 mK level. On the platform, the pre-stabilized laser light is phase modulated by an electro-optic modulator operating at 5 MHz. Approximately 10 μW of optical power is incident on the ultra-stable cavity for PDH locking. Stabilization to this cavity is accomplished via feedback to the AOM and a PZT controlling the pre-stabilization cavity length. The servo bandwidth for this final locking stage is $\sim$ 100 kHz, limited in part by the acoustic wave propagation time in the AOM. The useful output of the laser is delivered from a fiber port located near the ultra-stable cavity on the same platform, and utilizes fiber phase noise cancellation [192, 193]. The entire optical setup occupies less than 1 m^3. Further details can be found in [159].

The ultra-stable cavity has a finesse near 250,000 and is 7 cm long (cavity linewidth of $\sim$7 kHz). The high reflectivity mirrors are made from ion beam sputtered dielectric coatings, using alternating quarter wave stacks of SiO_2 (silica) and Ta_2O_5 (tantala). The cavity linewidth is determined by a heterodyne cavity ringdown measurement (Figure 3.2). The cavity reflection contrast was measured to be 50 %. By also measuring the cavity transmission (when locked), each mirror was seen to have transmission losses (power) of 6 ppm and absorption/scattering losses of almost 10 ppm. The laser is locked to the TEM_{00} transverse cavity mode, as observed by a CCD camera image of the cavity transmission. For the results shown below, no stabilization of the incident optical power on the cavity was employed.

Both the spacer and the optically bonded mirror substrates are made of ULE. To maintain a small sensitivity of the cavity length to acceleration, we implemented the following design features. First, the cavity is held at its midplane to achieve symmetric stretching and compressing of the two halves of the cavity during acceleration to suppress vibration sensitivity [165]. The cavity is mounted vertically to exploit the intuitive

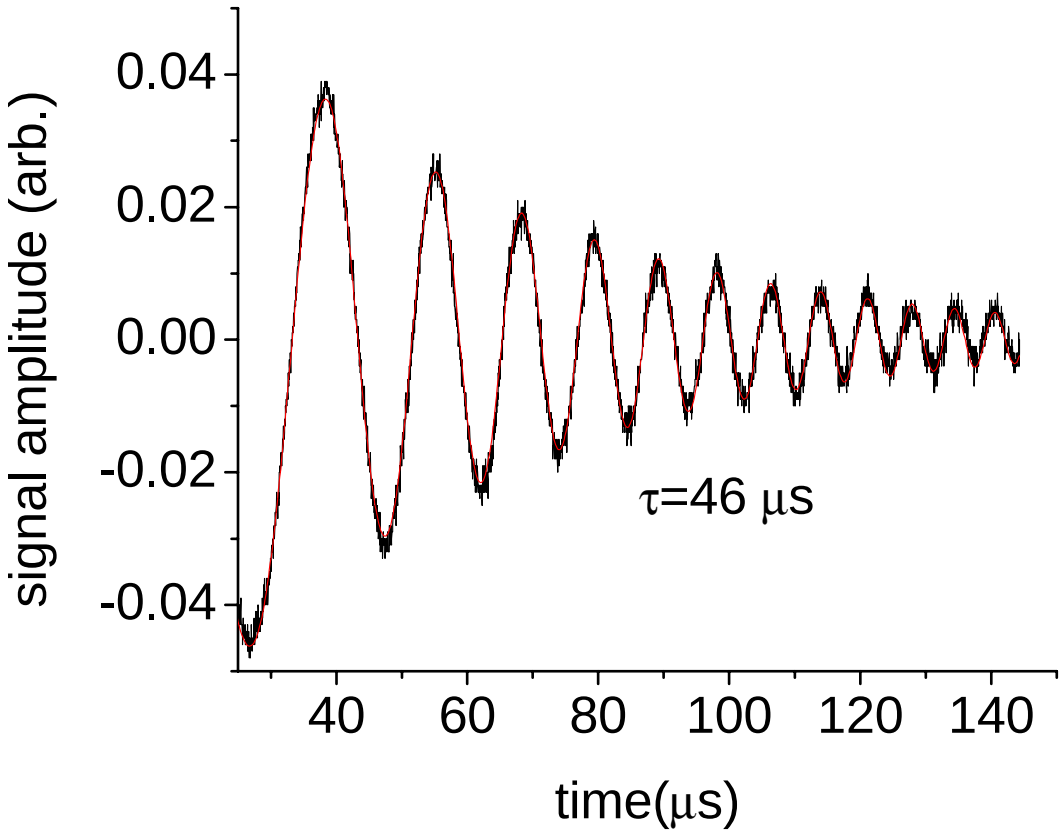

Figure 3.2: Measurement of the cavity field ringdown time from the heterodyne interference of the decaying cavity field and a linearly-frequency-chirped reflected laser field. For this particular ultra-stable cavity, the measured field decay time is 46 μs.

symmetry in the vertical direction (see Figure 3.1). This mounting is accomplished by a monolithically attached midplane ring resting on three Teflon rods. Second, with this mounting design, because the acceleration sensitivity of fractional cavity length scales with the cavity length, we chose a somewhat short cavity spacer [165] (7 cm). Third, the cavity is wider in the middle and tapered at the ends, allowing more rigid construction without excess material. This cavity was designed in our laboratory and constructed in conjunction with a dozen other quantum metrology laboratories around the world. It is now commercially available, facilitating 1 Hz laser stabilization to any interested research lab [159]. The cavity and supporting rods are held in a vacuum enclosure (10^{-6} Torr) pumped by an ion pump (2 l/s); the cavity spacer has symmetric evacuation holes perpendicular to the optical axis. Optical access to the cavity was made through AR-coated, wedged vacuum windows of BK7 glass. The vacuum can is single point temperature controlled to $\sim$305 K within 500 μK (typical best results) over a 24 h period. Since the ion pump is not temperature controlled, we installed a blackbody radiation baffle between the vacuum can and the ion pump.

To evaluate the final laser stability, a second cavity-laser system was constructed with a separate diode laser and a separate ultra-stable cavity mounted on an independent vibration isolation platform in an independent enclosure. Light was transferred from one system to the other via optical fiber (employing fiber-phase-noise cancellation [192]) and a heterodyne beat between the two stabilized lasers was detected (Figure 3.3). A linear drift of $\leq$1 Hz/s of the heterodyne beat was removed by applying a feedforward linear correction to reduce the drift to less than 50 mHz/s. At 300 mHz resolution bandwidth (RBW), the laser linewidth is 400 mHz (full width at half maximum). As the RBW is reduced to 150 mHz, linewidths of 220 mHz can be observed, while some fraction of the carrier power is moved into low-frequency noise sidebands. The fractional linewidth is below 1×10^{-15}.

We have already discussed general expressions for frequency instability of an

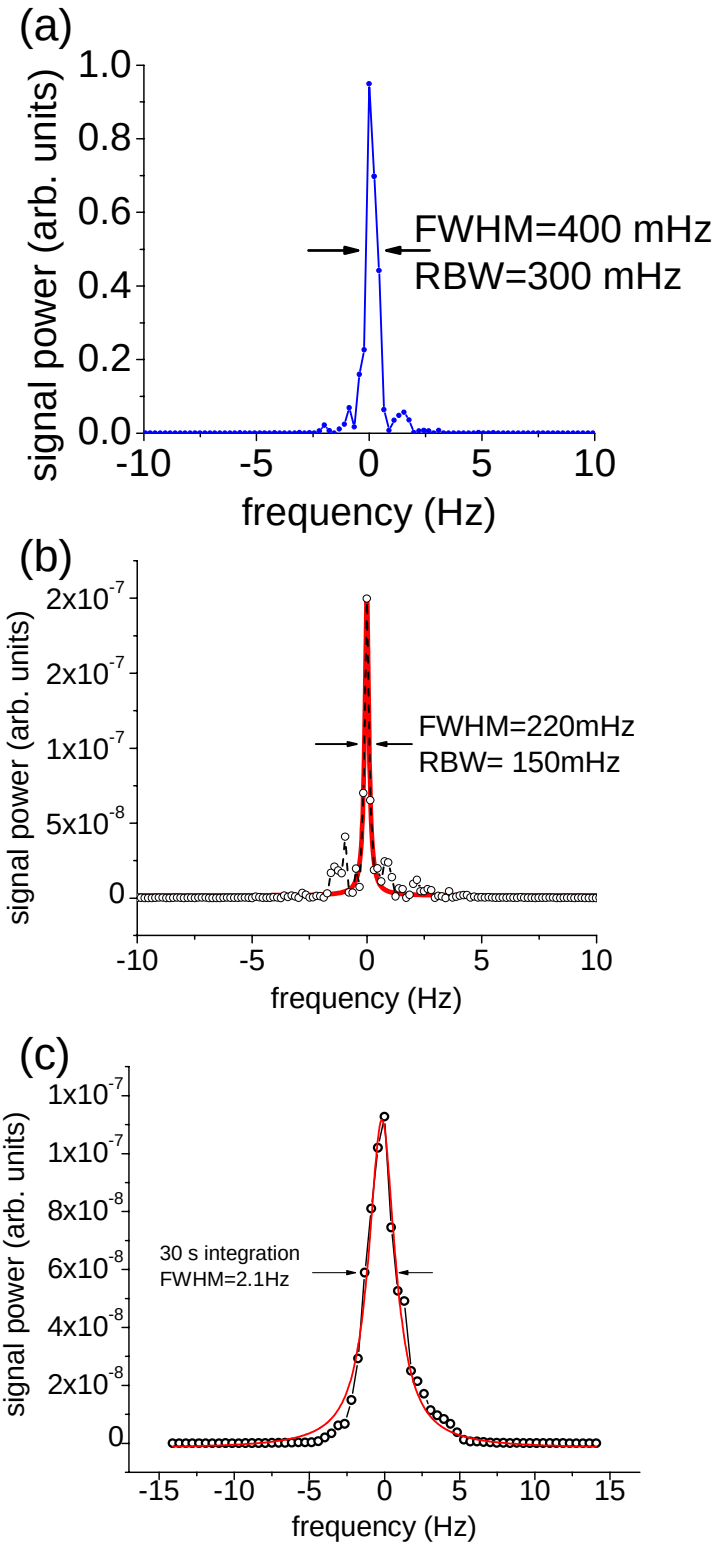

Figure 3.3: After stabilization to the ultra-stable cavity, sub-Hz laser linewidths are measured by detecting the RF heterodyne beat between two similar but independent laser-cavity systems (frequency axis has been scaled by $1/\sqrt{2}$ for equal contributions from both laser systems) are shown in (a) and (b) at 300 mHz and 150 mHz resolution bandwidth, respectively. Spectra with several hundred mHz linewidths are measured. In (b), a feature as narrow as 220 mHz is resolved, as the carrier power decreases due to low frequency noise manifest as enlarged sideband power. In (c), the measurement is integrated over 30 s (with linear drift nominally cancelled), giving a 2 Hz power spectrum linewidth.

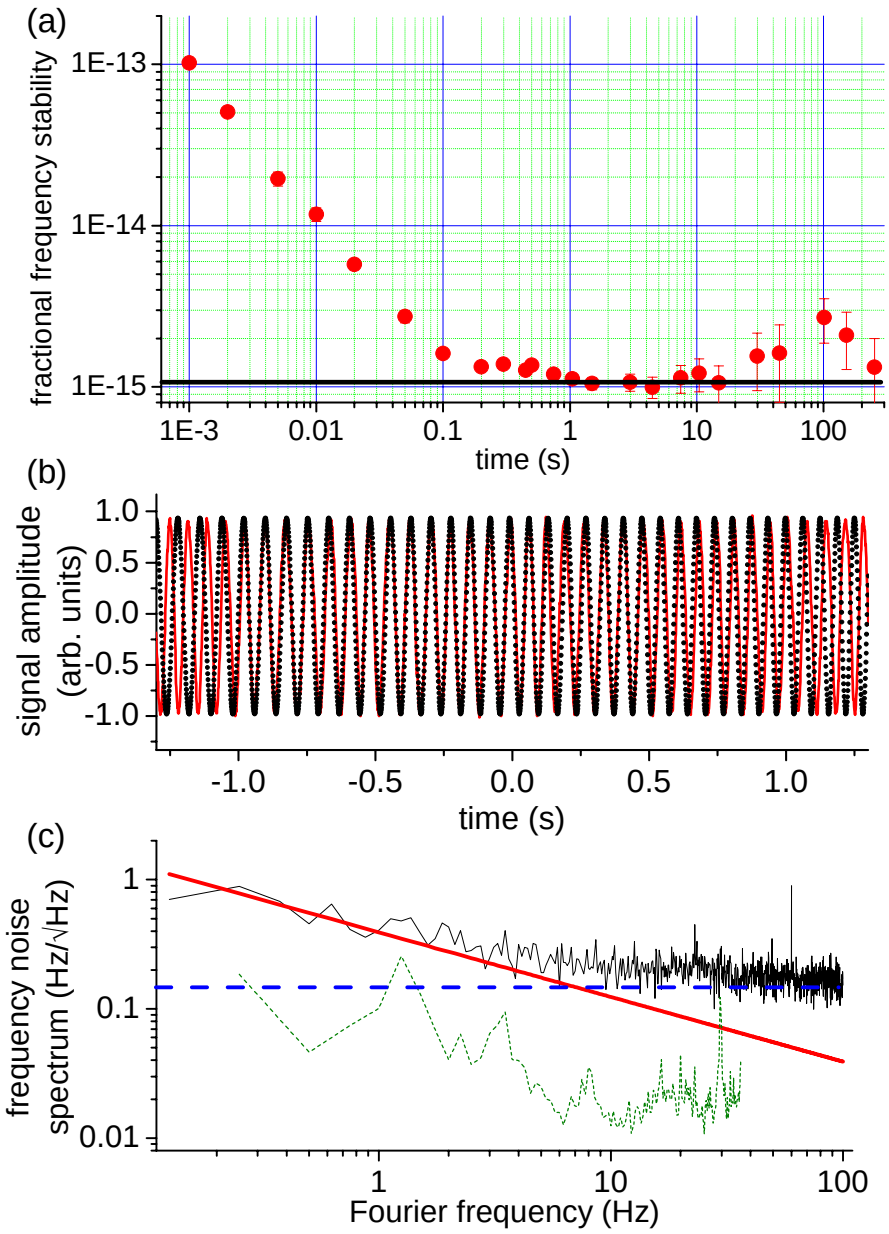

Figure 3.4: (a) The measured fractional frequency instability of the 698 nm clock laser as given by the Allan deviation. The solid, black line indicates the instability limit dictated by the thermal-mechanical noise of the mirror substrates and dielectric coatings in the ultra-stable cavity. Note that except for a noise bump near 100 s, from 100 ms to 100s the laser instability is given by the thermal-mechanical noise limit. (b) Time domain measurement of the heterodyne beat between two similar but independent clock laser systems, mixed down to low frequency. The measurement data is shown by the black dots, whereas a weakly chirped sinusoidal fit is indicated in red. From $t = -1$ s to $+1$ s, the fit matches the data to better than π radians, whereas for $|t| > 1$ s, the fit does not match due to excess accumulation of laser phase noise. This indicates that the clock laser can provide a coherent optical wave for times at or somewhat exceeding 1 s. (c) The measured frequency noise amplitude spectral density of the clock laser (black trace). The frequency noise contribution from acceleration sensitivity of the cavity length is shown in green. The red solid line shows the $1/\sqrt{f}$ flicker frequency noise contribution from the thermal-mechanical noise of the ultra-stable cavity. The black dashed line gives the white frequency noise originating from a technical source: electronic noise in the transimpedance amplifier used in photodetection of the cavity reflection.

atomic frequency standard. One important characterization of the frequency instability of any frequency source is the two-sample Allan deviation, given by [194, 195]:

$$\sigma_y(\tau) = \left[\frac{1}{2(N-1)} \sum_{n=1}^{N-1} (f_{n+1} - f_n)^2 \right]^{1/2} \tag{3.11}$$

for N frequency measurements (y) taken with an averaging (gate) time τ. For more details on the Allan deviation, and relationships between the Allan deviation and the frequency noise spectral density, see [194]. Here we report the Allan deviation as a fraction of the laser frequency (4.29×10^{14} Hz). The instability of one of the lasers as measured by the fractional Allan deviation is also shown in Figure 3.4(a). This measurement was taken directly by counting the heterodyne beat under linear drift cancellation (relative to a stable microwave source). The theoretical estimate of the thermal-noise-limited instability is indicated as a solid horizontal line in the figure. This modelled thermal noise limit (see Equation 3.10) has nearly negligible contribution from the ULE spacer itself, while the contribution from the ULE mirror substrates is approximately 1.5 times that from the dielectric high-reflective coating [185]. Except for a small noise bump at 100 s, the laser stability from 0.5 to 300 s coincides precisely with the modelled thermal noise limit.

Laser phase coherence was also observed via time domain measurements. A 15 Hz heterodyne beat signal between the two lasers and its sine wave fit are shown in Figure 3.4(b), with a linear chirp to account for the simple residual linear drift between the two lasers. The fit shows that the lasers remain phase coherent within 1 rad at the optical frequency of 4.29×10^{14} Hz for a period 2 s.

The sensitivity of the cavity length to accelerations was measured by shaking the cavity and observing the additional frequency noise present on the laser when tightly locked to the cavity resonance. This was also accomplished via an optical heterodyne measurement, with the system that was not shaken serving as the reference oscillator. The vertical acceleration sensitivity was measured to be 30 kHz/(m/s^2). The horizontal

acceleration sensitivity was 20 kHz/(m/s^2) at 5 Hz and it dropped to 5 kHz/(m/s^2) at 15 Hz because of mechanical isolation provided by the Teflon cavity mounting posts. The relatively short cavity used here constitutes a compromise between cavity acceleration sensitivity and the fractional thermal noise contributions (from the mirrors) to the cavity length stability. This compromise facilitates impressive diode laser stability at the 10^{-15} level with relatively straightforward vibration isolation. The difference in performance between this system and that of the highest recorded stability [158] is consistent with the difference in cavity length that scales the fractional thermal noise. To see this compromise more quantitatively, Figure 3.4(c) shows the laser frequency noise spectrum. Below 5 Hz, the laser noise is dominated by thermal noise. Also shown is the laser noise contribution due to cavity acceleration. This is simply the measured acceleration noise spectrum on the vibration isolation platform scaled by the empirically determined acceleration sensitivity given above. The thermal noise contributes roughly a factor of 2 to 4 more than the acceleration noise. Consequently, the system could be further improved by using similar, but longer, mounted optical cavities together with fine tuning of the symmetrical rejection of acceleration sensitivity [165]. In this case, the combined thermal and acceleration noise contributions can be kept small enough for laser fractional frequency instability at the low side of the 10^{-16} decade.

3.4 Atomic spectra of the optical clock transition with Hz level linewidth

With the atomic and optical coherence described above, we are now ready to consider the coherent atom-light interaction during the probing of the clock transition.

3.4.1 Experimental Setup

The stable laser light is transferred from the enclosed vibration isolation platform by noise cancelled fiber link to a second isolated breadboard in a plexiglass enclosure,

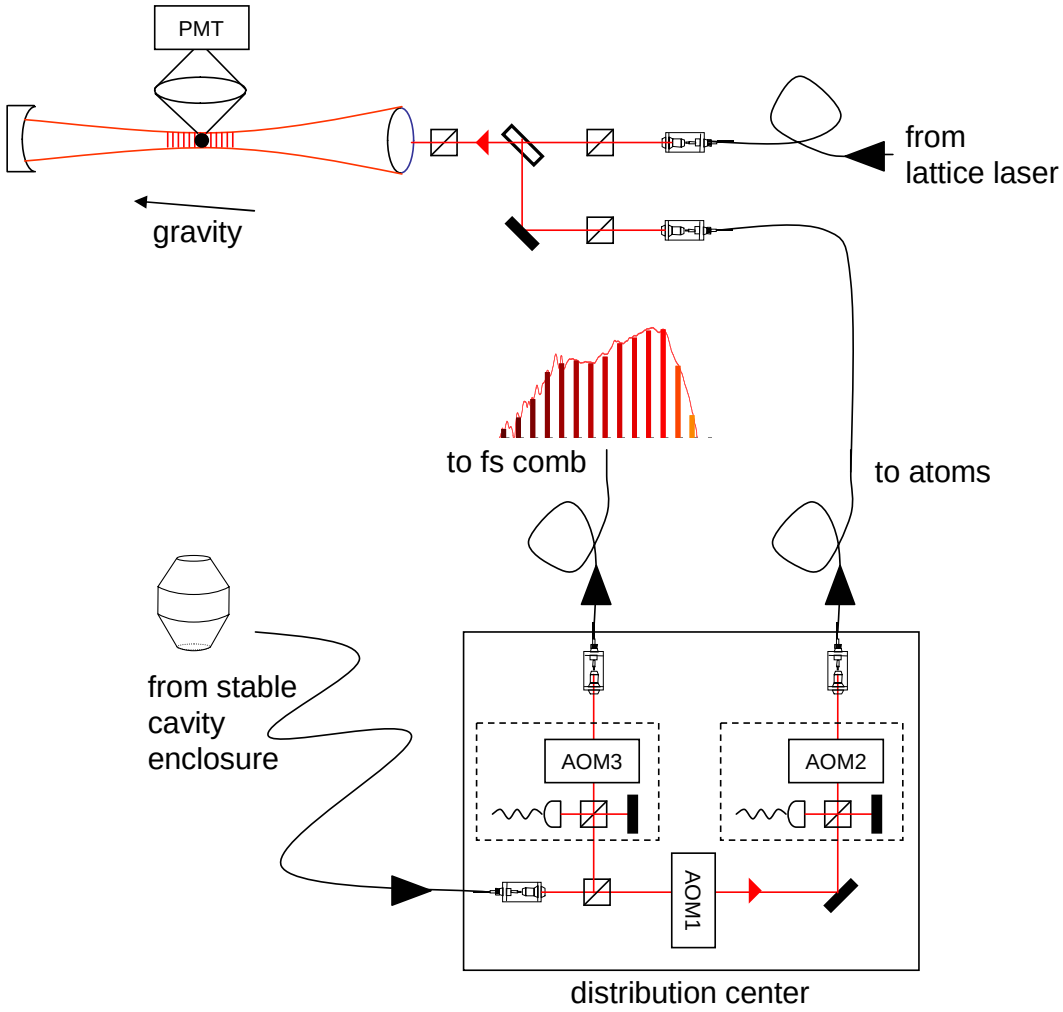

Figure 3.5: Schematic of the distribution of the cavity-stabilized light. From the stable cavity enclosure, the light reaches the enclosed distribution center (via phase-noise-cancelled fiber link) where it is split between two phase-noise-cancelled fiber links: one to the fs frequency comb for counting, and the other to be co-propagated and co-polarized with the lattice laser for interrogation of the clock transition. As described later, AOM1 is used for frequency stabilization to the atomic transition, whereas AOM2 and AOM3 are utilized in the heterodyne Michelson interferometers (dashed line box) for phase-noise-cancellation over the fiber links.

referred to as the distribution center. The fiber phase noise cancellation utilizes a heterodyne Michelson interferometer, where the round trip fiber phase is locked to the phase of a local reference arm [192]. On the distribution center, the light is split into two beams, one going by fiber-phase-noise-cancelled link to the fs optical frequency comb to have its optical frequency counted. The second beam goes through a second fiber-phase-noise-cancelled link to the Sr vacuum chamber (see Figure 3.5). Here the light is passed through a polarizer and a liquid crystal shutter and is co-propagated with the lattice laser using a dichroic mirror. The combined lattice and probe laser pass through a Glan-Taylor polarizer, ensuring identical polarization of the two beams. Furthermore, the optical polarization is oriented for π-polarization (relative to the bias B-field). The lasers are subsequently focused by an achromatic lens ($f = 14$ cm) into the vacuum chamber, with their k-vectors oriented about 15 degrees away from gravity. The collimated probe and lattice beam waists incident on the lens are chosen to give the probe beam a 1/e field radius at the trap focus which is five times larger than the lattice focus radius (assuming diffraction-limited focusing). This is done to prevent probe inhomogeneity along the transverse trap axis due to the Gaussian intensity envelope of the probe beam. The vacuum chamber windows are AR-coated for 698 nm. At the lattice laser wavelength, 813 nm, the vacuum windows are not optimally AR-coated (transmission is 85% per window), but the lasers are incident at an angle so that no etaloning occurs. The 813 nm reflection off the first vacuum window is used for intensity stabilization. After exiting the vacuum chamber, the lattice light is retroreflected by a concave mirror (radius of curvature $R = 15$ cm and reflection 99% at 813 nm) to overlap with the original lattice beam and form the focused lattice standing wave. The retroreflecting mirror is a poor reflector of the probing laser (1% reflection at 698 nm) to reduce probe standing wave effects. The focusing lens is mounted on a translation stage. This translation stage and the lattice/probe beam pointing is walked to optimize lattice overlap with the $^1S_0$-$^3P_1$ MOT. By blocking the back reflection, good overlap is

determined by a large atom number in the dipole trap, which leaks down the trap axis because of gravity. The retroreflector alignment is varied to optimize the amount of lattice light retro-coupled to the optical fiber delivering it to the chamber, as well as the trapped atom number in the focused lattice trap. The retroreflector is also mounted on a translation stage oriented along the trap axis, and this degree of freedom is used to optimize the observed trap frequency (as described below), consistent with good focus overlap between the incident and reflected lattice beam. Co-alignment of the probe and lattice is accomplished by looking for spot overlap over several meters of optical path.

3.4.2 Spectra

Figure 3.6(a) shows a spectrum of the $^1S_0$-$^3P_0$ clock transition (ground state population) with optical-lattice-confined ^{87}Sr atoms. The spectrum is of the purely electronically excited transition carrier, i. e. no motional excitation. The lattice is operated at the magic wavelength, $\lambda_{magic} \simeq 813.428$ nm. Bias coils in all three Cartesian dimensions were used to zero the magnetic field at the atomic sample. This was accomplished by systematically scanning the magnetic field in all dimensions and looking for the narrowest possible spectrum as a function of the field. Under nonzero field, the magnetic states are made non-degenerate, resulting in Zeeman broadening of the observed, overlapped transitions. By probing the atomic sample for 80 ms, allowing Fourier limited linewidths of ~ 10 Hz, this technique could usually determine the field zero within 10 mG. As shown in Figure 3.6(a), narrow resonances with linewidths (FWHM) as small as 5 Hz were observed for longer probing times.

To further push the coherence limit of the system, a small bias magnetic field was applied (along the probing polarization axis) in order to separate out distinct π-polarized transitions from the individual m_F states. A spectrum as shown in Figure 3.6(b) results, where the relative transition strengths are determined by the Clebsch-Gordan coefficients between particular m_F states, and the relative populations of the

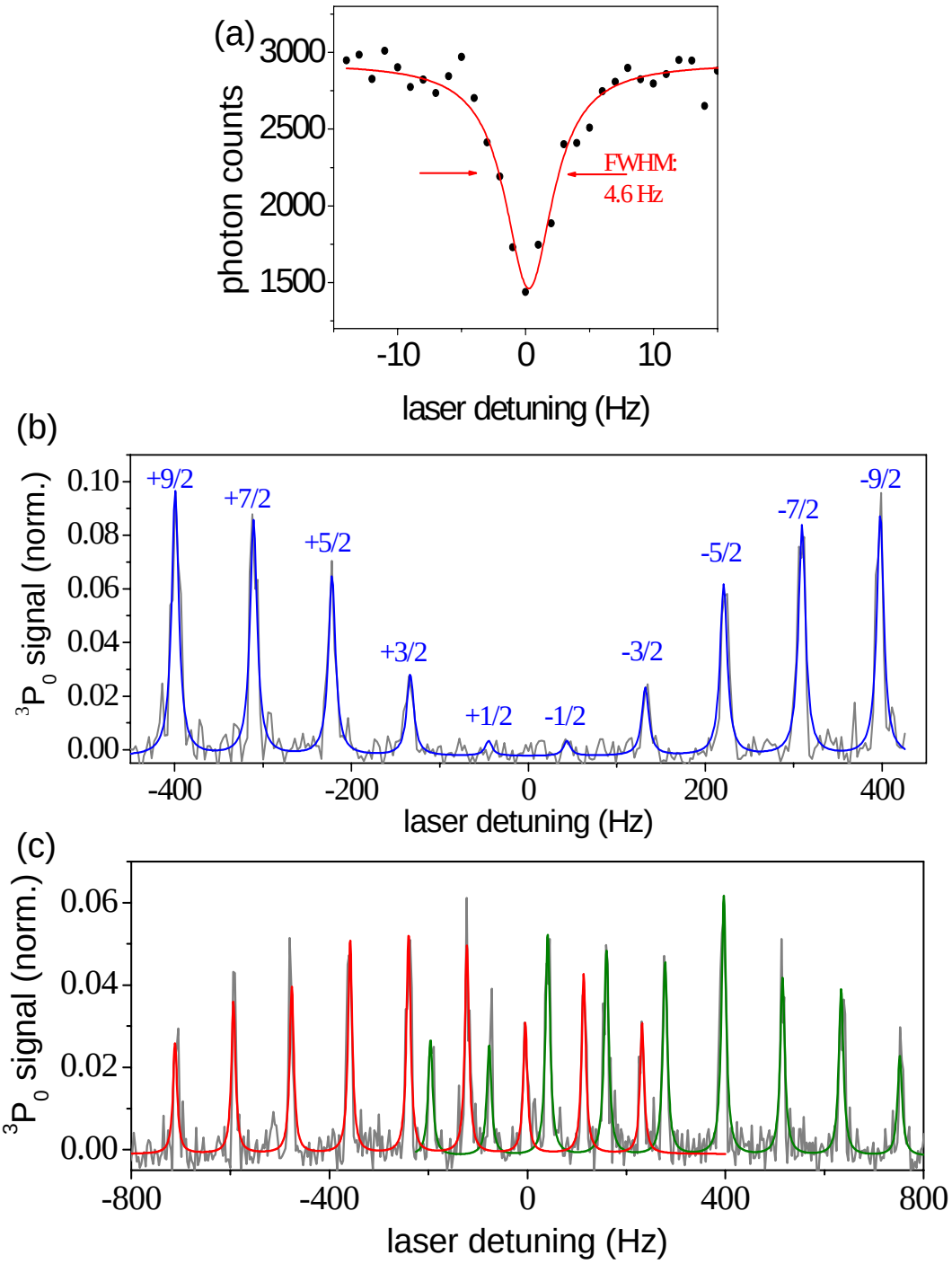

Figure 3.6: (a) Narrow, 5 Hz linewidth dip in the ground state population due to excitation of the clock transition. This is made at near zero B-field with all nuclear spin states degenerate, so that π transitions from all m_F states are excited simultaneously. (b) Applying a non-zero bias magnetic field to lift the nuclear spin state degeneracy, the resolved π transitions from individual m_F states are observed in the excited state population. (c) Same as (b), but with the σ^+ and σ^- transitions.

m_F levels in the ground state (approximately equally distributed). A similar spectrum in Figure 3.6(c) shows the σ^+ and σ^- transitions. Note that the π and σ spectra can be used to determine the differential g-factor ($\Delta g = 7.7 \times 10^{-5}$) for the clock states by determining the relative shifts between different m_F states [151].

If we spectroscopically focus on a particular π-transition (e. g. 5/2 or 7/2) in Figure 3.6(b), a spectrum as shown in Figure 3.7(a) can be revealed. Here, the optical probing time has been extended to 480 ms, corresponding to a Fourier-limited linewidth of 1.8 Hz (FWHM). The linewidth of the spectrum in Figure 3.7(a) is 2 Hz. Repeated measurements of these narrow optical transitions yields a histogram of transition linewidths as shown in the inset of Figure 3.7(a). The distribution spreads out over several Hz due to the residual drift and low Fourier frequency noise of the probing laser. The bare probe laser drift was mostly compensated by applying a feedforward drift via an AOM which kept the spectral peak at a constant frequency. This compensation is never perfect, due to time-dependent changes in the laser drift, and so the direction of the frequency scan across the spectrum was toggled between scans so as to average out the effect of the drift of the measured linewidths. The mean histogram value corresponds well with the Fourier limited width of 1.8 Hz. This corresponds to a line quality factor (ratio of transition frequency ν to the transition linewidth $\Delta\nu$) of $Q \geq 2.3 \times 10^{14}$, currently the highest observed line Q in coherent spectroscopy. This represents coherent atom-light interaction at ~ 0.5 s. Attempts to push probing times to longer time scales (≥ 1 s) did not result in clean, narrower spectra, but rather revealed the low frequency jitter in the laser frequency as noisy spectra. This is seen from the probe laser coherence as seen in Figure 3.4(b). Here two lasers were able to maintain phase coherence over 2 s timescale. However, during narrow scans, while individual points on a scan represent approximately 1 s of probing, they are separated by almost 1 s of dead time during which time the atoms are cooled in the MOT, loaded into the lattice, etc. Made worse by imperfect drift compensation, the laser does not have sufficient temporal coherence

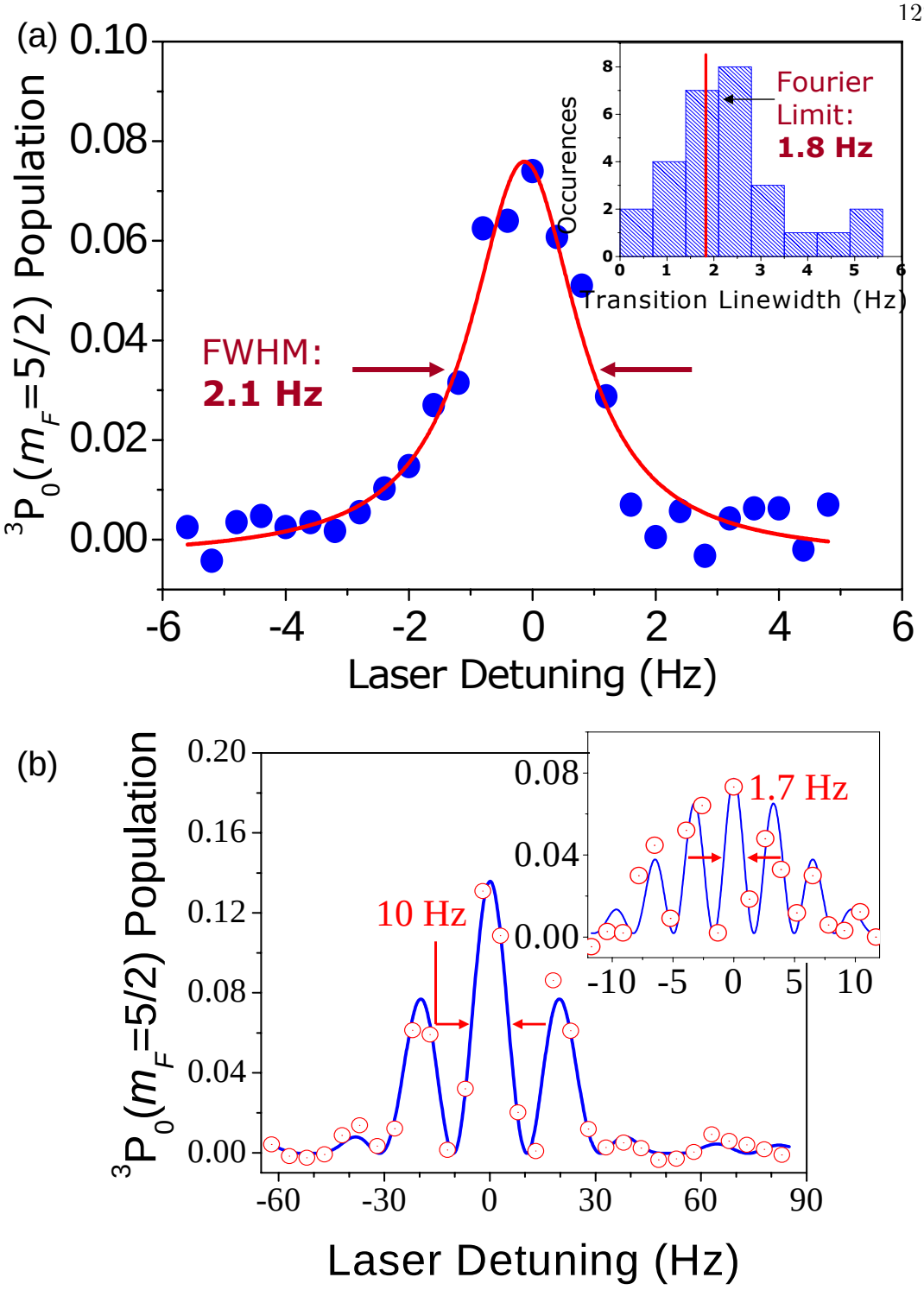

Figure 3.7: (a) With an applied bias field to separate individual π transitions from the different m_F levels, a narrow spectrum of the π transition from the $^1S_0$ $m_F = 5/2$ state is observed. The 2 Hz spectral linewidth of this optical transition is close to the Fourier limit of 1.8 Hz, set by the probing time of 480 ms. The inset shows a histogram of measured spectral linewidths, consistent with the Fourier limit. (b) Similar to (a), the atoms are now probed with two pulse Ramsey spectroscopy. The inset shows Ramsey fringes with a full width at half maximum of 1.7 Hz.

to enable scans of the atomic transition with < 1 Hz spectral linewidth. Shown also in Figure 3.7 is an atomic spectrum taken with two-pulse Ramsey spectroscopy and a linewidth (FWHM) of 1.7 Hz (inset of (b)).

Concerned also with the possibility of noisy Doppler contributions from shaking optical elements around the optical lattice in Figure 3.5, we also considered introducing free space active phase noise cancellation while probing the narrow optical transition. With the optical setup given in Figure 3.5, this is not completely straightforward, since vibration in different places along the optical path affects the probe and lattice phase differently, and it is the relative optical phase at the lattice trapped atom which matters for the Doppler contribution. For example, if the lattice retroreflector alone is shaken, this introduces phase noise in the lattice sites, but does not affect the probe light since (nearly) all probe light is transmitted through the retroreflector. On the other hand, once the probe and lattice beams are combined, shaking elements definitely introduces phase noise on the probe beam. However, the lattice sites are less sensitive to such noise. To see this, we describe the lattice by two counterpropogating waves:

$$\vec{E} = \vec{E_0}\left[\cos(kx + \omega t + \phi_1) + \cos(-kx + \omega t + \phi_2)\right] \tag{3.12}$$

where ϕ_1 and ϕ_2 are time dependent phase noise terms. For the particular case where the second wave is simply the first one retroreflected, the relationship between ϕ_1 and ϕ_2 is determined by applying the boundary condition that the phase of the optical waves are shifted by π at the retroreflector position, x_0:

$$kx_0 + \omega t + \phi_1 = -kx + \omega t + \phi_2 - \pi \tag{3.13}$$

For simplicity, we set $x_0 = 0$ and have $\phi_1 = \phi_2 - \pi$. Equation 3.14 becomes $\vec{E_0}\sin(kx)\sin(\omega t + \phi_2)$, and the standing wave nodes are unaffected by the phase noise. In the current configuration, phase noise from the probe beam is corrected only up to the optical fiber tip, before being combined with the lattice beam. Perhaps the ideal scenario for noise

cancellation would be to have the lattice standing wave defined by a Fabry-Perot cavity around the atoms, with active stabilization of the cavity by feedback to a PZT on the retroreflector. Then the probe light could be phase stabilized to the input reflector of the cavity. In our situation, assuming that the bulk of the optical phase noise would originate from the lattice retroreflector, we mounted this mirror on a PZT and electronically stabilized its position by using the lattice standing wave as one arm of a homodyne Michelson interferometer, and stabilizing the relative phase between it and a short, stable reference arm. Introducing this extra stabilization did not improve the observed narrow spectra.

With optical transition linewidths as narrow as 2 Hz, the ^{87}Sr frequency standard has the potential for very low instability. Looking at Equation 1.1, a mere S/N of 10 could yield a 1 s instability below 10^{-15}. Achieving the narrow optical transition is thus an important step toward development of an optical frequency standard. Before we move to consider the other important pieces for this frequency standard, we look at the part of the atomic spectra far from the carrier clock transition: the sideband structure.

3.4.3 Sideband structure

In Section 2.5, using the Hamiltonian describing harmonically trapped atoms interacting with a resonant light field, we saw that the atom could be excited both electronically and motionally. In the appropriate regimes, this resulted in a spectrum of carrier and sideband transitions. In Section 2.6.5, we discussed how trap anharmonicity resulted in non-degenerate sideband structure for atoms with different initial motional states. This anharmonicity is particularly relevant for the strong confinement axis, since here there are only several discrete motional states present. We also discussed (Section 2.6.5) how the transverse atomic spread (along the weak confinement axes) resulted in asymmetric broadening of the longitudinal sideband structure. These effects combine to yield a spectrum as shown in Figure 3.8(a). With π-polarized interrogation, the

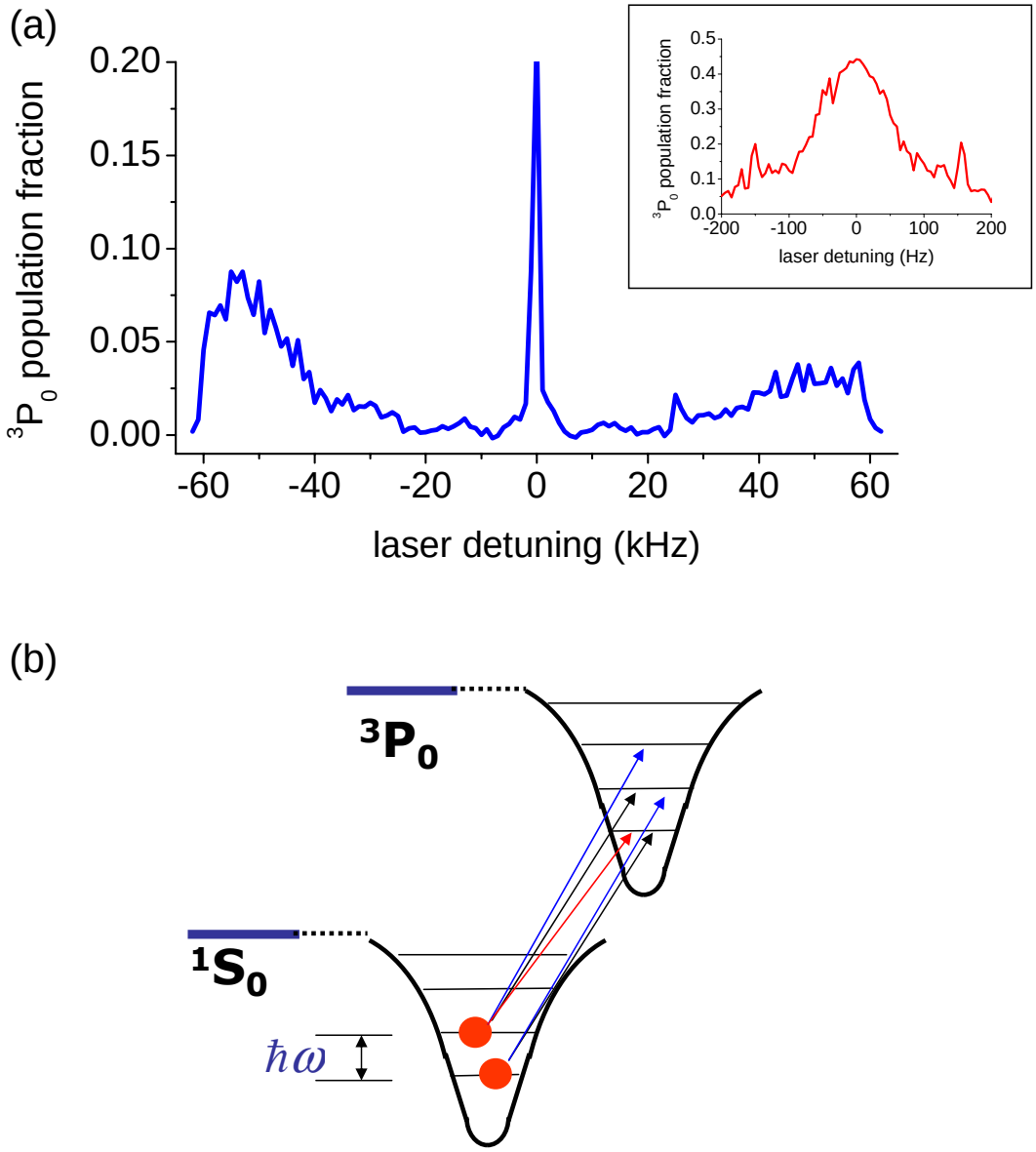

Figure 3.8: Measurement of the motional sideband structure. (a) The first order red and blue longitudinal motional sidebands around the purely electronic carrier transition. The broad asymmetric lineshape of the sidebands originate from the longitudinal anharmonic confinement as well as the transverse spatial extent of the atomic wave function where (off-axis) the trap confinement is weaker. The inset shows observation of the transverse motional sidebands with a strongly saturated carrier. (b) The sideband structure corresponds to motional excitation and de-excitation while the atom is being excited electronically. In the harmonic approximation, the motional states are separated by the trap frequency ω.

carrier and the $\pm 1^{st}$ order red and blue sidebands are shown. In order to accentuate the sideband details, the carrier transition is saturated. This sideband structure is not directly useful for the generation of a well-defined optical frequency, but rather must be considered as a line-pulling mechanism for frequency shift. Furthermore, the structure manifests useful information about the confinement details of the atomic sample.

From Figure 3.8(a), we can directly read off the trap frequency along the longitudinal axis (approximately from the peak of the sideband to the carrier). A finer resolution scan of the carrier may also reveal motional excitation along the transverse axis (see Figure 3.8(a) inset, where the transition is being power broadened with strong saturation). Because of the careful co-alignment of the probe and lattice k-vectors, the transverse sidebands are difficult to excite and hence observe without introducing some relative misalignment. Using Equations 2.83 and 2.84, the measured longitudinal and transverse trap frequencies can be used to determine the trap depth and the lattice beam waist (in the harmonic approximation).

Atoms in the ground motional state of $^1S_0$ cannot contribute to the red sideband (because the motion cannot be de-excited below the ground state, see Figure 3.8(b)). However, these atoms do contribute to the blue sideband. The largest contribution to the red sideband comes from those atoms occupying the first motional state of $^1S_0$. The second biggest contributions to the blue and red sidebands are from the first and second excited motional state of $^1S_0$, respectively. And so on. Typically following a thermal distribution, the atomic population among the different motional states is given by the Boltzmann factor. Thus, the relative size of the blue and red first order sidebands, whose amplitudes are weighted by the population distribution, gives the atomic sample temperature.

$$\frac{P_{red}}{P_{blue}} \simeq \frac{N_1}{N_0} = e^{-\frac{\hbar\omega_{long}}{k_b T}} \tag{3.14}$$

where P_{red} (P_{blue}) is the peak amplitude of the first-order red (blue) sidebands, N_0 (N_1)

is the atomic population in the ground (first excited) $^1S_0$ motional states, and ω_{long} is 2π times the longitudinal trap frequency. In principal, Equation 3.14 holds approximately for the transverse axes (ω_{trans}) as well. For our confinement, however, the transverse trap frequencies are small enough that the difference in the first-order blue and red sideband amplitudes is quite small ($\sim 1\%$) and typically below the measurement S/N.

Note that for the particular case of strong trap anharmonicity (similar to our case), the blue and red sidebands for each motional state are non-degenerate, and the sum of the individual transitions can be fit to the observed spectra. The relative amplitude weighting for the red or blue sideband of each motional state is given by the appropriate Boltzmann factor, and can be alternatively used to determine the sample temperature. The two measures of temperature typically agree [21]. For such fits, we have previously assumed that all transitions from one motional state to the next have a Lorentzian lineshape with a common broadened linewidth. While the previous measurements yield the sample temperature along the longitudinal axis, the shared linewidth of each transition (determined by fit) gives a crude estimate of the sample temperature along the transverse axis. Without dedicated sideband cooling along a particular axis, the measured longitudinal and transverse temperatures typically agree within the fit uncertainties. Efforts are being made to properly account for the asymmetric lineshape of each transition due to the transverse spatial extent and temperature, using a model suitable for fitting the many degrees-of-freedom [145, 16, 196]. Note also that while the Lamb-Dicke parameter can be directly calculated with the known trap frequencies and recoil frequency, the sideband amplitudes can provide further quantitative verification (as in Section 2.5).

Chapter 4

Development of the Sr Optical Standard: High Accuracy Spectroscopy

In Chapter 3, we motivated ^{87}Sr as an optical frequency standard with the observation of Hz-level-linewidth optical spectra. We now discuss the tools and measurements which developed this system as an optical frequency standard.

4.1 Counting optical frequencies: the fs frequency comb

In Section 1.3, the benefits of optical frequency standards were highlighted. For years, these benefits were heavily outweighed by the difficulty of measuring optical frequencies. Except for measurements between optical standards operating at similar frequencies (difference of operational frequencies in microwave regime), comparison among different optical standards was extremely difficult, and thus the utility of optical standards was limited. The behemoth optical frequency chains developed in a few national laboratories laboriously enabled optical frequency measurements referenced to the Cs-defined SI second [197, 198]. Within the last ten years, a revolutionary approach to optical frequency measurement has made the process relatively straightforward. With the pioneers of this technique rewarded by the 2005 Nobel Prize in Physics, these optical measurements are now made regularly with amazing precision in laboratories around the world.

Somewhat paradoxical, the heart of the apparatus used to measure well-defined CW optical frequency sources is a femtosecond (fs) pulsed laser. Consider the optical

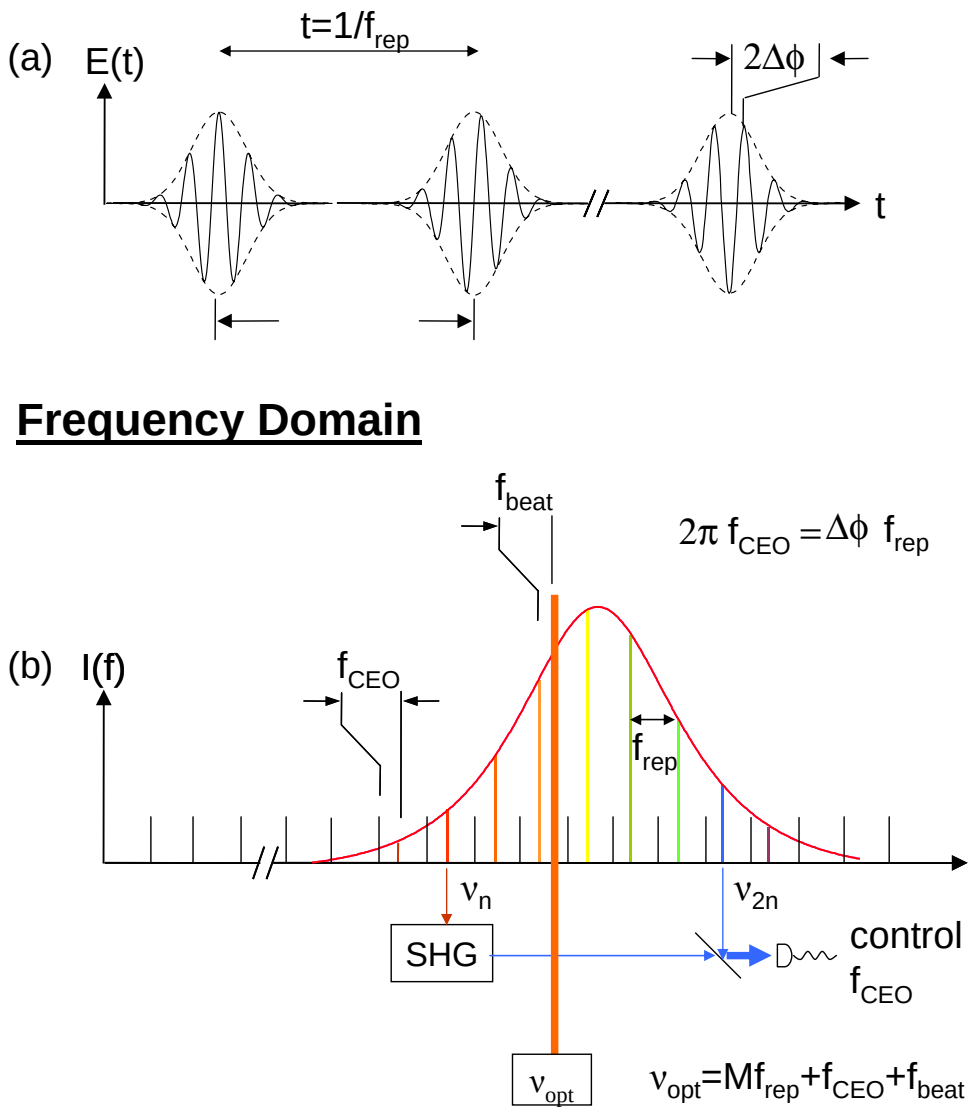

Figure 4.1: Emission from a mode-locked femtosecond (fs) pulsed laser (a) In the time domain, the laser output generates fs pulse-width envelopes separated in time by $1/f_{rep}$. Another important degree of freedom is the phase difference between the envelope maximum and the underlying electric field oscillating at the carrier optical frequency. (b) By Fourier transformation to the frequency domain, the corresponding frequency comb spectrum is revealed. Each tooth in the comb, a particular single frequency mode, is separated from its neighbor by f_{rep}. The relative carrier-envelope phase in the time domain is related to the offset frequency f_{CEO} in the frequency domain. f_{CEO} is given by the frequency of one mode of the comb (e. g. ν_n) modulo f_{rep}, and can be measured and stabilized with a f-2f interferometer. In this interferometer, one comb mode, ν_n, is frequency doubled and heterodyne beat with the comb mode at twice the frequency, ν_{2n}. Thus, by stabilizing f_{CEO} and f_{rep} to a well known frequency reference, each comb mode frequency is well known. Measurement of the frequency of a poorly known optical frequency source (e. g. previously measured at the resolution of a wavemeter) can be determined by measuring the heterodyne beat between the frequency source and the frequency comb. The previously determined coarse frequency knowledge of the optical source can be used to determine which comb mode is adjacent the optical source in the frequency domain.

output of such a laser, as illustrated in Figure 4.1. Pulses with temporal widths of several to tens of fs are generated in a pulse train. The repetition rate of the pulse train (f_{rep}) is given by the inverse of the round trip cavity travel time inside the mode-locked laser. The frequency and phase properties of this pulse train can be fully constrained by control of two degrees of freedom: the relative phase between the carrier wave and the envelope packet (known as the carrier envelope offset), and the repetition rate. Now we apply a Fourier transform to describe the laser output in the frequency domain. The pulse train transforms to a comb of many single frequency modes. The spacing between each mode is given by the laser repetition rate, and the spectral range covered by the frequency comb is related to the temporal width of each pulse. With the repetition rate known, the frequency of the individual modes (comb teeth) could be extrapolated to the mode closest to zero frequency (DC). The extrapolated mode closest to DC has a frequency offset known as f_{CEO} (note that $f_{CEO} < f_{rep}$). It can be shown that f_{CEO} determines the carrier envelope phase offset [199]. Thus the frequency properties can be constrained, in the frequency domain, by control of f_{rep} and f_{CEO}. This is equivalent to saying that each comb mode has a frequency given by $\nu = Nf_{rep} + f_{CEO}$, where N is an integer representing the mode number, counting from the first mode at frequency f_{CEO}.

With an appropriately large spectral bandwidth, determining the value of f_{CEO} is straightforward. Consider the N^{th} comb mode in the low frequency spectrum of the comb, whose frequency is given by $\nu_N = Nf_{rep} + f_{CEO}$. We frequency double this comb mode (using the appropriate nonlinear crystal for second harmonic generation) to compare its frequency with that of $\nu_{2N} = 2Nf_{rep} + f_{CEO}$. The difference between the two frequencies, $2\nu_N - \nu_{2N}$ is seen to equal f_{CEO}. The same holds true for the M^{th} comb component. Thus, if the comb spectrum covers an entire octave, f_{CEO} can be measured by comparing the comb output to the frequency doubled output of the comb. Some mode-locked lasers, exploiting Kerr nonlinearity in the laser gain medium to generate

strong phase modulation, intrinsically produce a full octave output of an optical comb. We use such an octave-spanning frequency comb. In other cases, the fs laser output can be injected into a microstructure optical fiber, where strong nonlinearities broaden the comb spectrum to cover an entire octave. The other comb degree of freedom, f_{rep} (which is typically a value between 100 MHz and a few GHz), can be measured directly with a properly designed photodetector. Thus, both comb degrees of freedom can be measured. By appropriate actuation on the laser cavity [200, 201], it has been shown that the measured values f_{CEO} and f_{rep} can be controlled and stabilized at impressive levels of precision and accuracy [202].

The utility of the comb is now evident. After stabilizing f_{rep} and f_{CEO} to a microwave frequency reference, an unknown laser frequency can be determined by measuring the heterodyne beat between the unknown laser and the stabilized comb (assuming the comb has sufficient spectral overlap with the unknown laser). A coarse, independent measurement of the unknown laser frequency using a commercially available wavelength meter allows one to determine which comb mode, N, makes the heterodyne beat with the laser. The laser frequency is then determined straightforwardly by $\nu_{laser} = N f_{rep} + f_{CEO} \pm f_{beat}$, where f_{beat} is the measured heterodyne beat frequency and the $\pm$ is determined by whether the comb mode or the unknown laser is at higher frequency (straightforward to constrain). Such a measurement can be currently made at the stability level of the best microwave frequency references.

The situation above can also be inverted. If the heterodyne beat is formed with a well-defined optical frequency standard, f_{beat} can be locked by actuating on the fs comb. The repetition rate of the comb can then be measured, which is stabilized to the optical frequency standard. In this way, the comb enables the phase information of an optical frequency standard to be used in the microwave domain. Furthermore, when stabilized to one optical frequency standard, the comb can be compared to a second optical standard at a different frequency and thus enable easy comparison of different

optical standards. The ability of the comb to inherit the accuracy and stability of the optical standard to which it is locked and then transfer this across large spectral gaps for measurement with a second standard has been shown to far exceed the current accuracy and stability of the standards themselves [202].

The fs comb, using relatively standard laboratory techniques, thus enables microwave-to-optical, optical-to-microwave, and optical-to-optical phase-coherent measurements. For this reason, the comb is considered the vital "gear system" which allows an optical frequency standard to be counted. Together, the optical standard and fs comb constitute the heart of an optical atomic clock. Using a stabilized fs comb, we measure and characterize our Sr standard against other well established frequency references, as discussed in the next sections.

4.2 Frequency reference

Experimental characterization of ^{87}Sr as an optical frequency standard includes determination of systematic shifts of the atomic transition frequency and its absolute measurement. Both of these require measuring the Sr transition frequency relative to a well-accepted frequency standard, the later ultimately requiring a Cs standard to link to the SI second. In our laboratory, one reference option was an in-house commercial Cs clock (HP 5071A). These robust clocks have 1 s fractional instabilities of $\leq 5 \times 10^{-12}$ and average down to $\leq 1 \times 10^{-14}$ over 5 days. The factory specified inaccuracy is 2×10^{-13}, although Dr. Judah Levine provides GPS-based steering to the UTC-NIST timebase with an inaccuracy of 1×10^{-14}. This microwave frequency reference would have been usable for our first characterization of the Sr system. However, a superior reference was available from NIST: one hydrogen maser from an ensemble of multiple masers which is periodically calibrated to the NIST-F1 cesium fountain clock (calibration services provided by Dr. Tom Parker and the Cs fountain team at NIST). The H-maser typically exhibits a 1 s instability of 2×10^{-13} and averages down to as

low as 10^{-16} roughly as $1/\sqrt{\tau}$ (averaging time τ). Depending on the behavior of the maser and the details of the Cs-calibration, during the measurements described below, the maser frequency was determined accurately to anywhere from the several 10^{-15} level to 5×10^{-16}. Besides the higher accuracy, the H-maser/Cs reference provides more than an order of magnitude reduced instability beyond our in-lab Cs clock, strongly relaxing the required measurement time for a given measurement precision. The only complication originates from the need to remotely transfer this standard from the NIST Boulder campus to our laboratory in JILA.

4.2.1 Microwave fiber transfer

A schematic of the frequency transfer scheme that we used is shown in Figure 4.2. The H-maser reference signal (typically using H-maser ST-4 or ST-5) at 5 MHz is sent from the H-maser ensemble room at NIST to the lab of Drs. Leo Hollberg and Scott Diddams over a low-temperature-coefficient coaxial cable. This 5 MHz reference signal is frequency doubled and used as the reference for a tunable analog synthesizer (e. g. Agilent E4428C-503). This synthesizer, operating at approximately 950 MHz, is used to amplitude modulate a Nd:YAG laser operating at 1320 nm. This amplitude modulation is realized using a telecom Mach-Zehnder interferometer with an internal electro-optic modulator. The amplitude modulated light is transferred by optical fiber link (part of the Boulder Research Area Network, BRAN) approximately 3.5 km one-way. The amplitude modulation is detected at JILA by illuminating a photodetector (EOT ET-3000A-FC) with the transferred light. This RF signal at $f_{maser} \simeq 950$ MHz serves as the comb frequency reference by counting the difference frequency between f_{maser} and the tenth harmonic of the repetition rate ($f_{count} = 10 f_{rep} - f_{maser} \simeq 40$ kHz) on a frequency counter referenced to the HP Cs standard. More details on the microwave fiber transfer can be found in reference [79, 203, 201, 21, 22]. At short timescales, extra phase noise accumulated by the synthesizer phase lock and dispersion

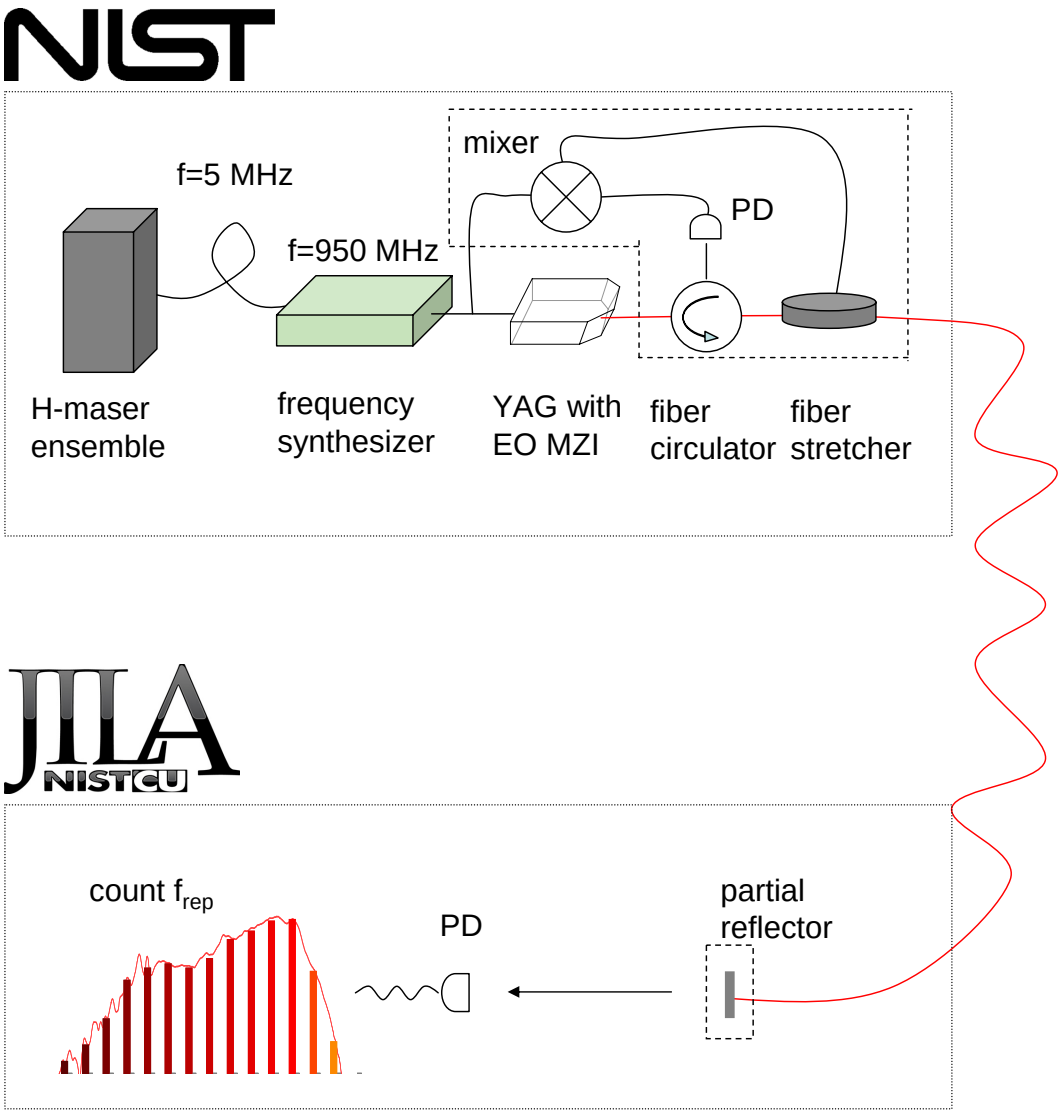

Figure 4.2: The microwave reference frequency transfer from NIST to JILA over optical fiber link. A synthesizer at 950 MHz is phase locked to the hydrogen maser reference at 5 MHz. This synthesizer drives amplitude modulation of a YAG laser at 1320 nm utilizing a commercially available Mach-Zehnder interferometer with an internal electro-optic modulator. This amplitude modulated light is transferred to JILA and detected on a photodetector. This signal is then used as a frequency reference to count the repetition rate, f_{rep}, of the frequency comb which is stabilized to the Sr clock laser. For frequency measurements with an accuracy at or better than the fractional 10^{-14} level, long term phase noise accumulated in the fiber transfer must be compensated. This is done by detecting the round trip microwave phase along the fiber path and stabilizing it to the synthesizer phase reference using a fiber stretcher.

in the optical fiber is relatively small, permitting the use of a passive, uncompensated signal transfer. At 1 s, the H-maser reference transferred to JILA gave instabilities of $2 - 3 \times 10^{-13}$, averaging down like $1/\sqrt{\tau}$ to 100 s. Excess phase noise, presumably originating from thermal drifts, could degrade the instability at many hundred seconds, but never worse than several 10^{-14}. This effect is shown is Figure 4.3(a), where the transferred microwave phase is measured as a function of time. The largest phase drift observed corresponds to a frequency shift of 10^{-14}. For our first measurement of the ^{87}Sr $^1S_0$-$^3P_0$ transition frequency, the passive microwave transfer gave sufficient stability and accuracy. For our second, improved measurement, our measurement uncertainty was on the 10^{-15} level, requiring more accurate control of the fiber phase noise. This was accomplished by adding a fiber stretcher at the NIST fiber end (see Figure 4.2). The modulated light was sent to JILA, with a fraction of it reflected back to NIST for homodyne phase detection with the local microwave copy using a mixer. The detected roundtrip microwave phase was stabilized by actuating on the fiber stretcher with low bandwidth feedback (unity gain bandwidth just below the Hz level). By doing so, the fiber group delay could be compensated and the long timescale phase noise in the microwave signal cancelled, reducing potential frequency shifts well below the 10^{-15} level [22, 203, 201]. This is demonstrated in Figure 4.3(b). Shown here is the stability of the strontium standard measured against the H-maser. At longer timescales, the instability continues to average down as $1/\sqrt{\tau}$, demonstrating control of the group delay noise that would otherwise result from the fiber transfer.

4.3 Evaluation of the Frequency Shifts and their Uncertainty

A very long list of physical mechanisms can systematically shift the measurement of atomic transition frequencies. An atomic system well suited as a frequency standard has very weak sensitivity to most of these mechanisms. Many shift mechanisms are very well understood, and together with excellent knowledge of the environmental conditions,

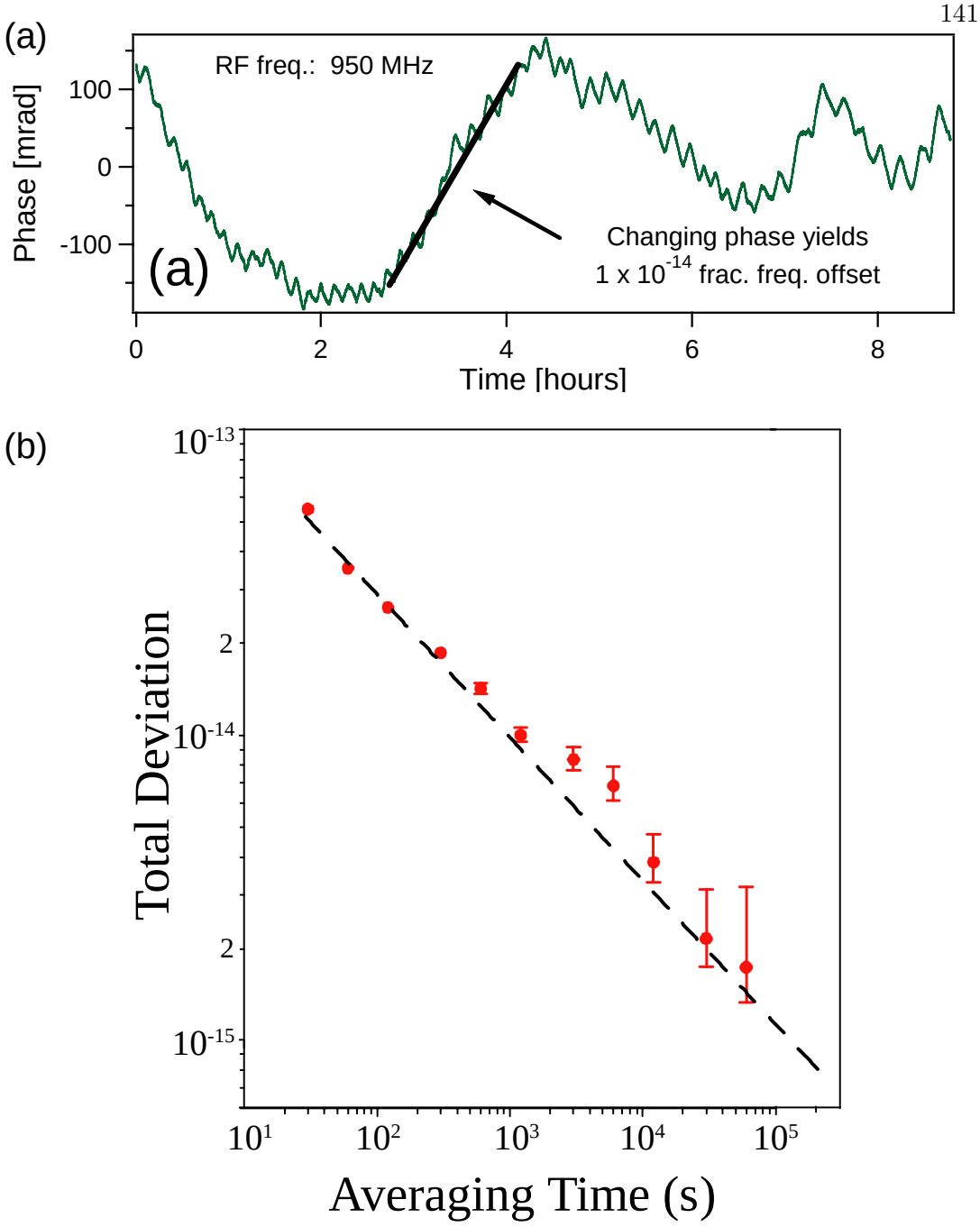

Figure 4.3: (a) Long-term phase noise present in the microwave reference transfer across the optical fiber link when no microwave phase stabilization is utilized. Thermal and other effects can result in phase chirps producing fractional frequency offsets as large as 10^{-14}. Although these effects can be averaged over with measurement durations at or exceeding 24 hours, measurement below the 10^{-14} accuracy level benefits from control of this microwave phase to eliminate any possible offset in the delivered frequency reference. (b) Using the microwave phase noise cancellation (with a fiber stretcher) over the optical fiber link, the relative instability between the Sr clock at JILA and the Cs-fountain-calibrated H-maser at NIST is shown. The instability averages down to 10^{-15} roughly as white frequency noise. If no feedback control of the fiber-link induced microwave phase noise were implemented, large instability bumps beyond the 100s timescale would be observed.

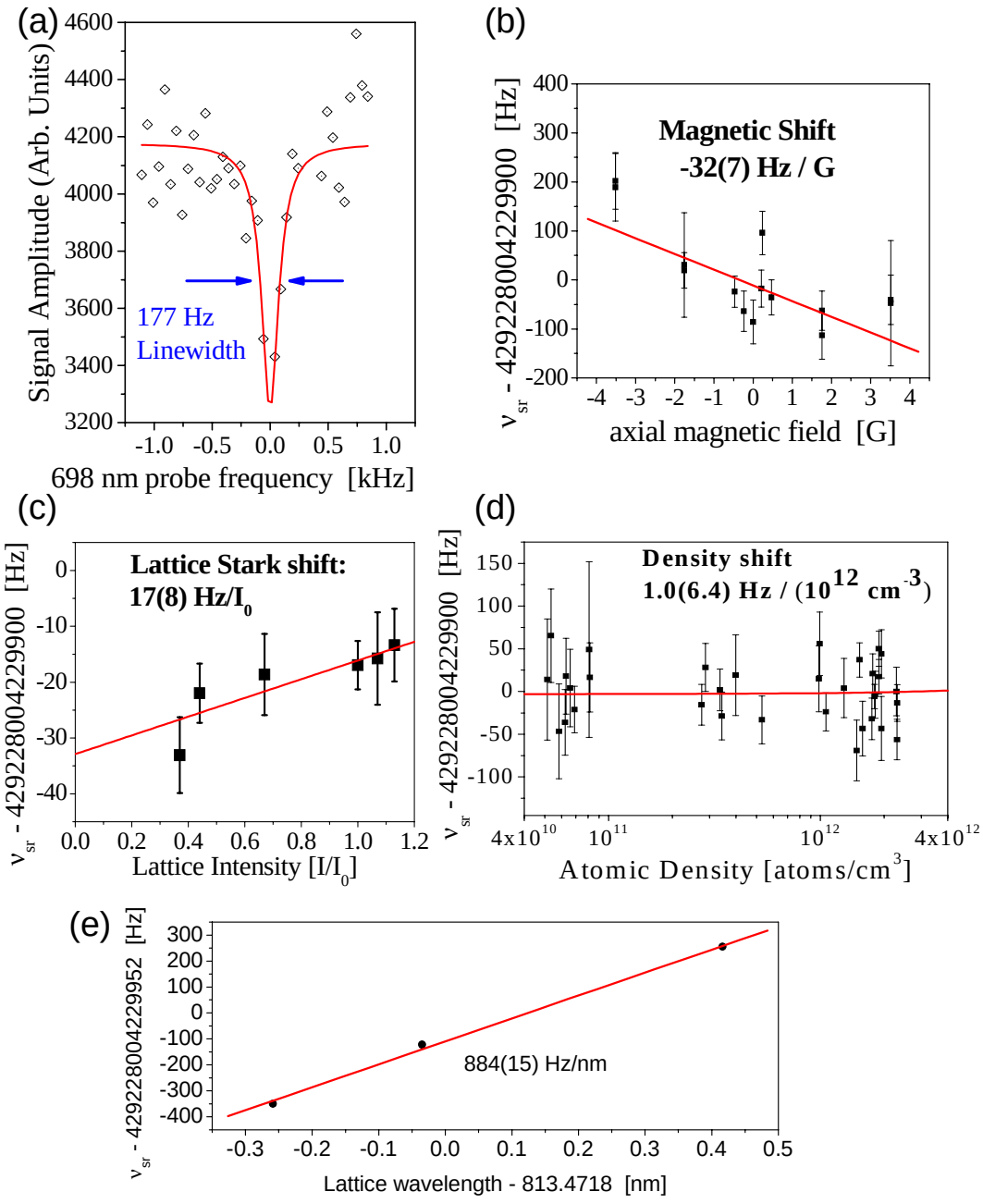

Figure 4.4: Measurement 1 uncertainty evaluation (2005) (a) Clock transition linewidth below 200 Hz. Sensitivity of the clock transition frequency to (b) magnetic field (along the axial direction) (c) AC Stark shift induced by the lattice laser and (d) density shift from interatomic collisions. (e) at a one way lattice laser intensity of 10 kW/cm^2, the clock transition frequency shift as a function of lattice laser wavelength.

the size of these shifts can be estimated computationally. Nonetheless, a rigorous determination of the transition frequency requires experimental investigation of the key systematic shifts. As a first measurement (2005) [21], we investigated critical shifts by spectroscopically scanning the clock transition while systematically varying the environmental parameters. The scans, whose absolute frequency axis was determined using the H-maser reference, were fit to determine the transition line center. Figure 4.4(a) shows one particular scan, with a linewidth of < 200 Hz. Note that at this time a different probe laser system was being used than the one described in Chapter 3. Although this laser had been previously characterized with a linewidth of several Hz [159], it was later determined that during the following weeks of atomic spectroscopy, etaloning near the high finesse cavity had developed, compromising the laser stabilization to the cavity. This led to laser linewidth broadening which limited the atomic spectra to 200 Hz. Despite this limitation, the uncertainties in the fit of the center of the atomic spectra were typically smaller than the uncertainty in the absolute frequency axis, determined by the stability of the H-maser on the timescale of the scan (50-100 s). Many such line centers were averaged together for a particular parameter value (averaging scans in both the positive and negative frequency direction) and the parameter values were varied to determine dependence on a particular effect. Figure 4.4(b-d) shows the observed dependence on the magnetic field, the atomic density, and the lattice intensity (for this work $\lambda_{lattice} = 813.437$ nm). Figure 4.4(e) shows the dependence of the clock transition frequency for a fixed intensity as $\lambda_{lattice}$ was varied. Table 4.1 summarizes the measured systematic shifts and their uncertainties.

Further details on this measurement can be found in [21]. A detailed description of individual systematic effects will be reserved for the next chapter. I mention here a few of many differences between the system operation for the results here and that in Chapter 5. First, in the measurement discussed here, the atomic sample was probed at nearly zero B-field, with transitions from all spin states essentially degenerate. Second,

Table 4.1: Measurement 1 (2005): Systematic corrections and their associated uncertainties for the absolute frequency of the $^1S_0$ - $^3P_0$ clock transition.

Contributor	Correction (Hz)	Uncertainty (Hz)
AC Stark shift (lattice)	-17	8.3
AC Stark shift (probe)	7.0	0.9
Blackbody shift	2.2	0.05
Zeeman shift	0	12
Recoil/Doppler shift	0	1.9
Density shift	-2.0	12
Systematic total	-9.8	19

the probe laser illuminating the atoms was intentionally phase-modulated so that a weak first order sideband could probe the transition, while a far-detuned ($\sim$ 10 MHz) but stronger carrier could be used for optical path phase noise cancellation. During this first measurement, the fiber delivering the probe laser was angle-cleaved at the fiber output to reduce back reflections into the fiber. The reflected signal for noise cancellation was taken from the lattice retroreflector, which at that time had a 698 nm reflection of 70%. The benefit of this approach was that phase noise in the optical path after the fiber could be compensated for. However, as our measurement accuracy improved, the drawbacks of having probe standing wave effects and a strong, RF-detuned optical beam outweighed the benefit, and this was changed. Also during the earlier measurements, the probe beam and lattice beam were also focused to the same beam waist, $w_0 = 65$ μm. This resulted in stronger transverse spatial inhomogeneity of the Rabi excitation frequency, reducing the observed excitation fraction. To counteract this effect and enhance the spectroscopic signal (measuring the ground state population), after spectral probing on the clock transition for 10-40 ms, we illuminated the atoms with 2 ms of 679 nm light, pumping the excited $^3P_0$ population to the $^3S_1$ state for shelving to $^3P_2$. See Figure 1.2 in Chapter 1. This process of probing and pumping was repeated multiple times to enhance the ground state population dip on resonance.

In a second measurement (2006), we had implemented the improved stable laser

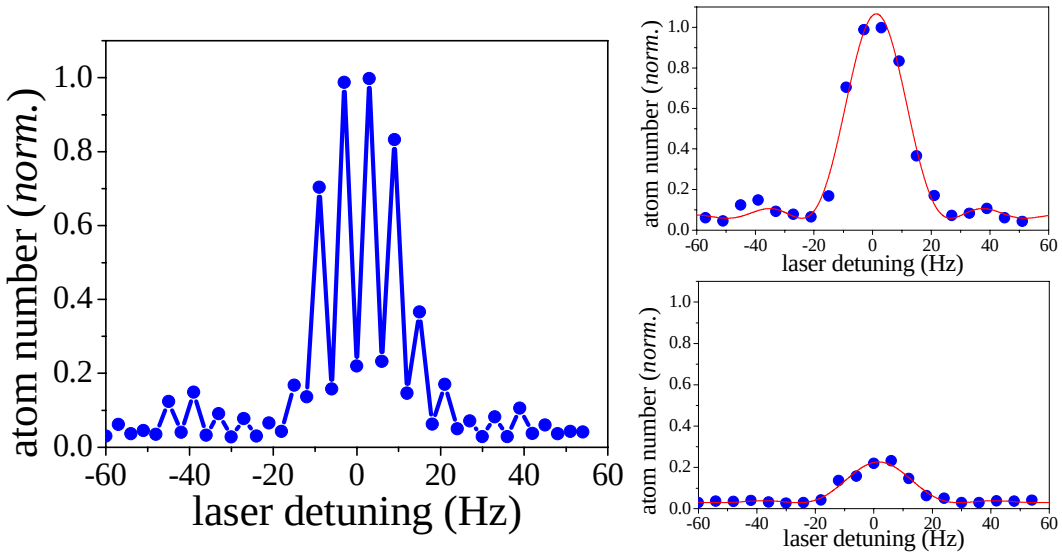

Figure 4.5: Measurement 2 uncertainty evaluation (2006). In order to measure shift sensitivities using the clock laser as a stable optical frequency reference, measurements of the clock transition were made interleaving different environmental parameters at the second timescale. As shown, we traced out the clock transition spectrum, alternating each point (approximately 1 s per point) with different atomic conditions. Here, the atomic number was varied as a handle on the density shift sensitivity. The collective spectrum is separated into the underlying spectrum for each condition and a fit determines the line center of each. A frequency difference is measured for the conditions. Collection of hundreds of spectra like these allowed determination of the relevant frequency shifts below the 10^{-15} level.

Table 4.2: Measurement 2 (2006): Systematic corrections and their associated uncertainties for the absolute frequency of the $^1S_0$ - $^3P_0$ clock transition.

Contributor	Correction (10^{-15})	Uncertainty (10^{-15})
AC Stark (Lattice)	0.25	0.60
AC Stark (Probe)	-0.02	0.12
AC Stark (BBR)	5.44	0.16
Zeeman Effect	0	0.53
Density Shift	-0.01	0.33
Total	5.66	0.88

system described in Chapter 3. Well aware from our first measurement of the painful averaging time required to characterize the systematic shifts with the limited stability of the H-maser, we were anxious to use an improved frequency reference. The evaluation of systematic shifts does not require an accurate reference, but typically only a stable one. The stability of the reference must be suitable on the timescale that is required to determine possible frequency shifts for different environmental parameter values. Knowing the impressive stability of the 698 nm probe laser itself (1×10^{-15} for timescales of 1-100 s with proper drift cancellation), we decided to characterize systematic shift mechanisms using the probe laser as the reference oscillator. To make this possible, a given environmental condition (density, probe intensity, magnetic field strength, etc.) was switched during each loading and spectroscopy cycle ($\sim$ 1 s) among different parameter values. The spectrum was scanned out as these parameters were varied. During data analysis, the spectrum consisting of multiple parameter values was separated into multiple spectra, one for each parameter value (see Figure 4.5). These spectra were fit, and the line center difference was determined as a function of the parameter. Many such spectra, scanning in both frequency directions, were averaged to determine the clock transition sensitivity to a given parameter. The results are summarized in Table 4.2. More details are found in [22]. As in the first measurement, spectroscopy was done by scanning the transition at near zero magnetic field, with all nuclear spin states degenerate.

4.4 Absolute frequency measurement of the $^1S_0$-$^3P_0$ transition

With the systematic shifts and uncertainties determined in the two measurements of Section 4.3, absolute frequency measurements of the ^{87}Sr $^1S_0$-$^3P_0$ transition frequency could be made using the Cs-calibrated H-maser reference. The absolute frequency measurement accompanying Measurement 1 (2005) is shown in Figure 4.6(a). In addition to the shifts and uncertainties in Table 4.1, measurement related shifts and their uncertainties for the H-maser calibration to Cs and the gravitational red shift between Sr and Cs were included. The $^1S_0$-$^3P_0$ transition frequency was measured to be 429 228 004 229 869 $\pm$19 (sys) $\pm$2.8 (stat) Hz, with the systematic and statistical uncertainties also in units of Hz. This was the highest precision measurement of the ^{87}Sr clock transition at the time, but disagreed with a different measurement published several months earlier [28]. The disagreement between the measurements was $\sim$ 80 Hz, corresponding to three times the combined uncertainty (see Figure 4.6(a)). This disagreement was later resolved by an independent measurement by the Paris group [24] as well as with a second measurement [29] by the authors of [28] which corrected a previous measurement error. Measurement 1 thus played an important role as the first high accuracy measurement of the lattice-trapped Sr $^1S_0$-$^3P_0$ transition, improving on the first direct excitation of this transition ([204], 20 kHz uncertainty) and the erroneous measurement of [28].

The improved systematic uncertainty evaluation of measurement 2 was also accompanied by an absolute frequency measurement of the clock transition. The results of almost 900 consecutive measurements (taken over a 24 hour period) of the transition frequency are shown in Figure 4.6(b). With the goal of measurement inaccuracy near the 1×10^{-15} level, we more carefully characterized measurement errors resulting from the H-maser transfer (such as that shown in Figure 4.3(a)). As discussed above, phase noise cancellation was implemented to compensate for group delay drift in the optical fiber link (see Figure 4.2). The fiber link was characterized to quantify additional frequency

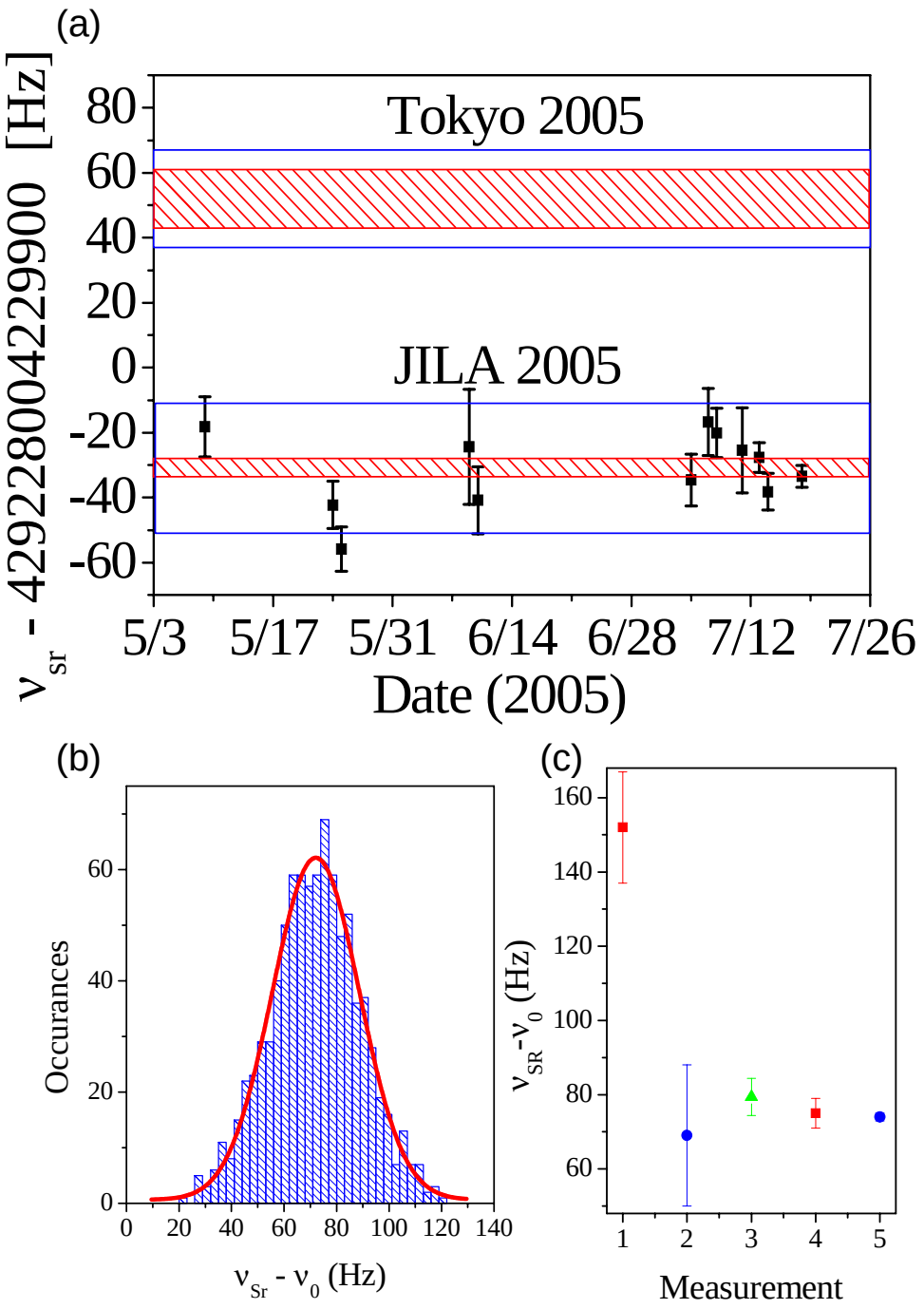

Figure 4.6: (a) Measurement 1 absolute frequency (2005). Our measurements are indicated by circles on the dates indicated on horizontal axis. The final weighted mean and statistical (systematic) error bars for the measurement are given by the filled (unfilled) blue bars. The final 2005 measurement by the University of Tokyo group is shown, again with the statistical and systematic error bars. The discrepancy is ~ 80 Hz. (b) Measurement 2 absolute frequency (2006). Histogram of frequency measurements binned in 30 s intervals over a 24 hour period. The data shown is not yet corrected for all systematic shifts. (c) Absolute frequency measurements of the Sr clock transition performed by JILA (circles), Tokyo (squares), and Paris (triangle). The first circle corresponds to Measurement 1 (2005) and the second to Measurement 2 (2006). Measurement by Paris, Tokyo, and JILA after 2005 confirmed the Measurement 1 result.

shifts and uncertainties of the remotely delivered Cs/H-maser reference. One critical shift mechanism was the temperature dependence of the synthesizer used for amplitude modulation in the H-maser link. This was determined by measuring the frequency shift of the synthesizer output (compared to a stable reference) while applying a known temperature ramp (K/hr) to the synthesizer [measured to be $4 \times 10^{-14} 1/(\mathrm{K/hr})$]. Then, during the absolute frequency measurement, the synthesizer was kept in a temperature stabilized enclosure and the ambient temperature was monitored. The measured shift and uncertainty was the measured time rate of temperature change scaled by the measured sensitivity coefficient, yielding a shift value of $-1.7(0.7) \times 10^{-15}$ during the 24 hour measurement run. Another shift uncertainty was imperfect fiber noise cancellation over the microwave link. An in-loop estimate of residual frequency shift from this effect was below the 10^{-17} level. A conservative estimate of 1×10^{-16} was assigned to this effect, and we later made a more rigorous out-of-loop evaluation confirming the absence of systematic shift at the 10^{-16} level. Microwave transfer from the H-maser lab to the Optical Frequency Measurements lab was estimated to be negligible on the 1×10^{-16} level (by comparing a high quality, low temperature dependent link with a separate link using standard RG-58 cable with a different path between the labs). Counter error and other synthesizer error was also determined to be negligible. As a final precaution, the absolute frequency measurement was made over a 24 hour period to average over diurnal environmental fluctuations. The $^1S_0$-$^3P_0$ transition frequency was measured to be 429 228 004 229 874.0 (1.1) Hz, with the uncertainty dominated by the H-maser calibration to the Cs-fountain. Figure 4.6(c) shows this result together with the first measurement, as well as comparable measurements made by the Tokyo and Paris groups. The final fractional uncertainty of 2.5×10^{-15} made this the highest accuracy optical frequency measurement for neutral atoms (at the time), at the time falling short of the Hg^+ ion measurement as the most accurate optical measurement of any system.

Chapter 5

The Strontium Optical Frequency Standard at 10^{-16} Uncertainty: Remote Optical Comparison of Optical Clocks

In the previous chapter, we saw high precision and high accuracy spectroscopy of the clock transition of ^{87}Sr atoms confined in a 1-D optical lattice. These results demonstrated the potential of Sr as an optical frequency standard and illuminated how refinement of the Sr system could yield improved performance. Aided by the agreement among the independent high-accuracy measurements of different groups (JILA, Paris, and Tokyo), the lattice trapped ^{87}Sr $^1S_0$-$^3P_0$ transition was recommended by the CIPM as a standard frequency "for applications including the practical realization of the metre and secondary representations of the (SI) second" [205]. Further improvements in the Sr standard could rival or surpass the uncertainties in the best Cs standards, the primary standard. Characterizing an improved Sr standard would benefit greatly from comparison with other optical standards, since the averaging time required to make high accuracy measurements against microwave standards was sometimes prohibitively long. For this reason, we developed a direct optical frequency link between JILA and NIST to enable a Sr clock comparison with other optical clocks at NIST (e. g. Ca, Yb, Hg^+, and Al^+). This chapter details the characterization of the improved Sr standard by remote optical comparison and an improved absolute frequency measurement of the clock transition, culminating in the evaluation of the overall uncertainty at the 10^{-16} level.

5.1 Design Improvements in the Sr Optical Standard

5.1.1 Atomic Polarization

As seen in the systematic shift and uncertainty evaluation in 2005 and 2006 (see Section 4.3), the first order Zeeman shift played a significant role in the final total systematic uncertainty. Between Measurement 1 (2005) and Measurement 2 (2006), the Zeeman shift uncertainty was reduced because of the improved capacity to maintain the magnetic field at or near zero value. The enhanced field determination was derived from the narrower spectra observed in Measurement 2, which more sensitively revealed B-field induced broadening of the nearly-degenerate, overlapping transitions from all magnetic sublevels. This yielded a factor of 50 improvement in the Zeeman shift uncertainty (similar to the ratio of the spectral linewidths observed in the two measurements). Besides continuing to improve the B-field characterization, reducing the clock transition sensitivity to the B-field would ideally reduce the uncertainty from this effect. As mentioned in Chapter 1, hyperfine interaction mixes the pure $^3P_0$ with a small admixture of $^1P_1$ and $^3P_1$. This accounts for the fact that $^1S_0$ and $^3P_0$, which would otherwise have identical g-factors, have relatively small but unequal energy dependence on B-field ($\Delta g = 7.7 \times 10^{-5}$) [151]. The first order shift for a π-transition is $\delta\nu = \mu_B \Delta g m_F B/h$, where μ_B is the Bohr magneton, and the magnetic field strength (along the quantization axis) is given by B. The first order Zeeman shift for magnetic sublevels with equal but opposite m_F is thus equal but opposite. Taking the average of two such transitions ($\pm m_F$) gives an effective transition frequency which is (1) equal to the zero field transition frequency and (2) has no first-order Zeeman dependence. Thus, the first-order Zeeman sensitivity can be greatly reduced. Techniques using different magnetic states to measure or cancel m_F-dependent shifts have been applied in a variety of different contexts (e. g. [206]).

The most straightforward way to average the Zeeman components would be to

sequentially interrogate the resolved transitions under a bias B-field, and average the individual measurement results. To avoid wasting atomic population, ideally all of the population would reside in the m_F state being interrogated. However, after lattice loading, the atomic population is approximately evenly distributed among the magnetic sublevels. For this reason, optical pumping may be employed to drive population to one or two sublevels for interrogation (as discussed in Section 2.7). Utilizing the $^1S_0$ $F = 9/2$ - $^3P_1$ $F' = 7/2$ transition with π-polarized light (with the light propagation along the lattice axis), the atomic population is pumped to two sublevels $m_F = \pm 9/2$ with experimental ease. A primary disadvantage to this dual spin state approach is that after one of the two spin states is interrogated, the population is read off using $^1S_0$-$^1P_1$ fluorescence. This broad transition does not discriminate the spin states, consequently heating away all spin states. Thus one half of the lattice trapped atoms are wasted in a measurement cycle (which remains much better than the 90% wasted in the unpolarized case, but still not ideal). Nonetheless, as seen from experimental data later in this chapter, this approach easily facilitates a Sr frequency standard with nominally no first order Zeeman shift. As will be further detailed in Section 5.4.2, the effect of the lattice-induced AC Stark shift includes a component depending linearly on m_F through the vector polarizability. This interaction can be thought of as between the atomic magnetic dipole and an effective magnetic field along the lattice k-vector [207]. Because of its m_F dependence, the $\pm m_F$ interrogation also enjoys cancellation of the vector Stark shift.

Another optical pumping approach is to use the $^1S_0$ $F = 9/2$ - $^3P_1$ $F' = 9/2$ transition with pure σ^+-polarized light (with light propagation along the quantization axis, which we set with a bias magnetic field along the lattice polarization axis). This drives all of the population to $m_F = +9/2$. These atoms are then interrogated and the clock state populations are read off. Then in the next experimental cycle (after loading a new group of atoms into the MOT and lattice) the optical pumping light is switched to σ^--polarized, driving all the population into $m_F = -9/2$ for interrogation. In this case,

100% of the atoms may contribute to spectroscopy. Experimentally, there are one or two additional details to this approach. We utilized a liquid crystal variable wave plate (Meadowlark Optics) to switch between σ^+ and σ^- polarization between experimental cycles. When stabilizing the clock laser to the atomic transition (discussed below) proper synchronization must be maintained between the clock laser feedback from the atoms and the σ^+ and σ^- experimental cycles. Figure 5.1(a-b) shows atomic polarization for both schemes and we have operated the clock with both schemes. Most of the uncertainty evaluation in this chapter uses the first scheme, the doubly-spin-polarized case of $m_F = \pm 9/2$. The spin state will also be relevant as we investigate collisional effects between the ultracold Sr atoms.

5.1.2 Laser Stabilization to the Atomic Transition

To operate as a standard, the clock laser frequency must reflect the atomic standard transition frequency. The clock laser derives its short-term frequency stability from locking to the high-finesse optical cavity. The longer-term frequency stability is derived by locking the laser frequency to the atomic transition. Methods to do this have been developed for various frequency standards over the decades. We implement a modulation based lock to the clock transition, which is largely insensitive to long term fluctuations in the atom excitation signal. Since we want to stabilize the laser to the average of the two $m_F = \pm 9/2$ transitions, we operate two independent locks which are time multiplexed and whose average frequency is calculated digitally. The basic approach for this two peak lock is illustrated in Figure 5.1(c). At first, for lock acquisition, the laser is frequency scanned across the doubly-polarized atomic sample. For efficiency, this scan typically skips a large range of frequencies known to be between the two peaks. This spectrum is fit to two peak-functions (usually Lorentzian). The laser frequency is then set to the low frequency half maximum of the first peak and spectroscopy is performed, detecting the population excitation, and recording it digitally.

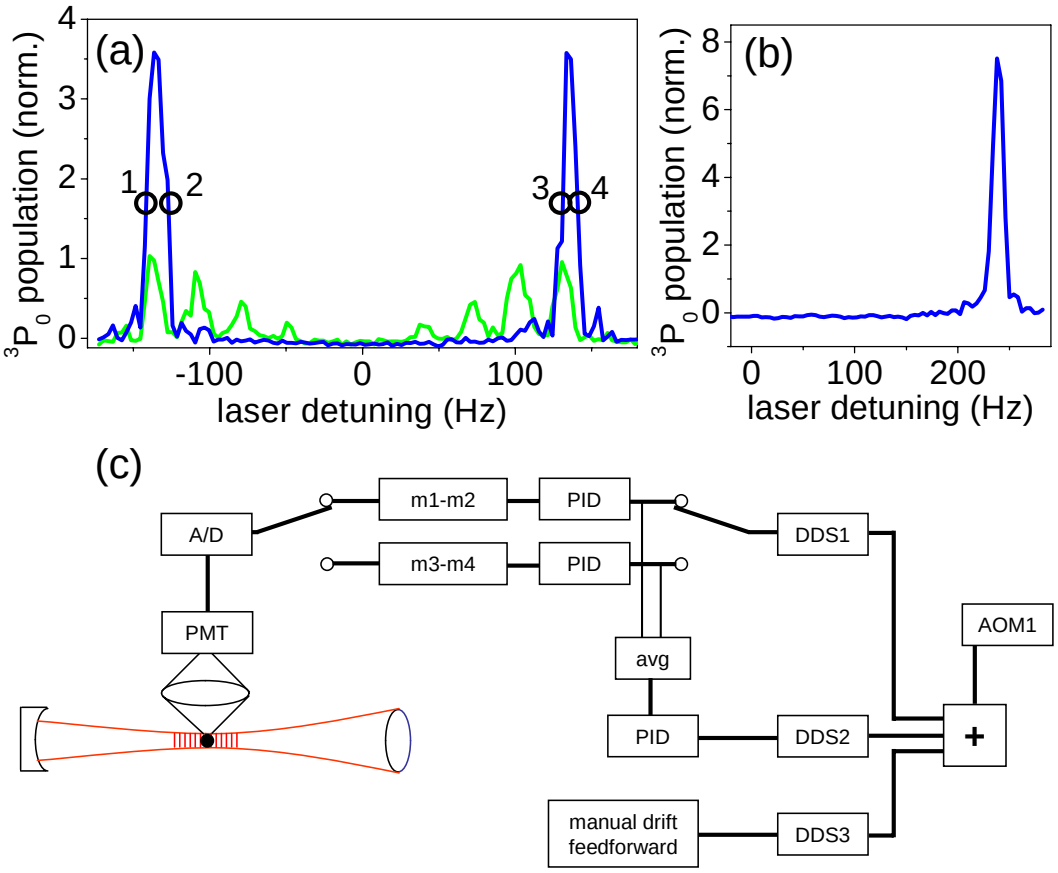

Figure 5.1: (a) Spectra of the π clock transitions under a bias magnetic field with (blue) and without (green) state preparation to the doubly spin-polarized $m_F = \pm 9/2$ states. The vertical axis gives the excited $^3P_0$ population and is normalized to the $m_F = 9/2$ peak height in the unpolarized case. (b) Spectra with spin polarization to a single spin state, $m_F = 9/2$. As in (a), other spin states contain $< 5\%$ residual population. Although negative detuning is not shown, no observable population resides in the negative m_F states. (c) Schematic for stabilization of the clock laser to the atomic transition. The ground and excited states are measured by fluorescence collected by the photomultiplier tube, PMT. After amplification and filtering, this signal is digitized by the A/D analog-to-digital converter. To stabilize to the average of the $m_F = \pm 9/2$ transitions, the four points are measured as shown in (a) over four experimental cycles (at the half maxima). The difference of the measurements on the first peak, $m1 - m2$, gives the error signal to lock to that peak, and likewise for the second peak ($m3 - m4$). These measurements are time multiplexed. The error signal for each peak has its own PID loop filter (proportional, integral, differential gain) to stabilize the clock laser to each peak in a time-multiplexed fashion. The average of the two correction frequencies for locking to each of the two peaks is calculated in software. A second PID loop filter is fed to DDS2 and is used to keep the original correction frequency drift near zero. A user operated manual drift feedforward (DDS3) is also implemented to compensate laser drifts.

In the next measurement cycle, the laser frequency is set to the other half maximum of the first peak. The difference in the excitation between these two peaks is computed and represents the first error signal. When the excitations are equal (difference = 0), then the laser is properly centered on the symmetric transition lineshape. A positive or negative difference indicates that the frequency must be adjusted to remain centered on the line. This error signal is filter by a PID (proportional, integral, derivative) filter to feedback on the AOM shifting the laser light into resonance with the atoms. In the third and fourth measurement cycles, the half maxima of the second peak are interrogated, the second error signal is calculated, and a second PID filter provides feedback to the AOM (over the time interval synchronized with interrogation of the second peak).

After the excitation signal is digitized using a fast, hardware re-triggerable 16-bit A/D converter, all of the error signal calculation, filtering, and transfer to the frequency transducer (DDS1, a GPIB controlled DDS synthesizer driving AOM1) is handled in software (LabVIEW). No analog biases are present in these digital operations. The output of the two PID filters is averaged together and fed in-series to a third PID filter. The output of this third filter actuates on a separate DDS synthesizer, DDS2. Rather than actuating on the frequency output of DDS2, DDS2 is set to have a linear frequency drift with controllable amplitude (Hz/s). This drift amplitude is feedback controlled, and has a primary function of compensating for any residual drift of the clock laser relative to the atoms. When operating properly, DDS2 keeps the drift of the control frequency in DDS1 below 1 mHz/s. Furthermore, DDS2 is summed with a third DDS synthesizer, DDS3, which is reserved for manual feedforward compensation of the laser drift relative to the atomic transition. During lock operation, we periodically update this feedforward value so that DDS2 does not accumulate too much drift amplitude as the clock laser drift changes over the course of a day (varies between ± 1 Hz/s). In this way, each DDS handles laser drift/noise on different timescales and the frequency sum of DDS1, DDS2, and DDS3 (using a frequency mixer) is applied to the AOM1. Note

that all critical frequency sources in the experiment are phase locked to the 10 MHz output of the HP Cs atomic frequency standard.

To tightly lock the clock laser to the atomic transition, the PID filters must be properly tuned. As a first effort at tuning the PID values, we implemented the Ziegler-Nichols tuning algorithm. We then optimized the filter by observing the error signal in both the time and frequency (FFT) domains, and varied the PID values to minimize the error signal, particulary at low frequencies. The primary lock (with feedback to AOM1) typically used an integrator with a PI corner at 20 s. The secondary lock (with feedback to AOM2) typically used an integrator corner at 200 s. After the two peaks were measured over four experimental cycles, the process is repeated. When operating with experimental cycles of approximately 1 s, this sets the Nyquist detection frequency as $\sim 1/(8\text{ s})$, limiting the servo bandwidth. Under these conditions we typically operated with a unity gain bandwidth of $\sim 1/(20\text{ s})$. We sometimes required faster servo response, trimming the experimental cycle down to a total of 600 ms. We were still limited by the extra time needed to measure both peaks, and in some cases, operated the lock on a single peak, for the fastest servo attack time. Since the benefit of the two peak is predominantly to cancel very slowly drifting magnetic-field induced Zeeman shifts, another way to achieve faster attack time is to simply make the multiplexing time between the two peaks much longer (lock on one peak for a given amount of time, and then switch to the next peak for the same amount of time).

5.1.3 Other System Improvements

In Section 3.3.1, we saw that laser stabilization to the high finesse cavity is limited by the measurement S/N ratio. The same holds true for laser stabilization to the atomic resonance (the S/N limitation in the atomic case is more severe). This is reflected in the stability of the frequency standard as given in Equation 1.1. A number of technical mechanisms exist which limit the achievable S/N ratio of the atom excitation

measurement, but which can be overcome or avoided with proper design. We determine the atomic excitation by measuring the remaining $^1S_0$ population after clock interrogation by collecting $^1S_0$-$^1P_1$ fluorescence. This transition is driven with an intense, nearly resonant 461 nm probing beam (10 MHz red-detuned, $s \simeq 3$) with a beam radius much larger than the lattice-trapped atom cloud radius, to avoid inhomogeneities, or noise from pointing instability. This 461 nm probing laser is intensity stabilized using an AOM, and then pulsed on with a second AOM (and a shutter). To ensure high TEM_{00} mode quality, before illuminating the atoms, the 461 probing beam is sent through a single mode fiber. The intensity stabilization does not correct for fluctuations due to the second pulsing AOM or the fiber coupling, so before entering the vacuum chamber, a fraction of the 461 nm probing light is split off with a pellicle beam splitter and monitored on a photodetector. We use this signal to ensure minimal intensity drift over many experimental cycles. Over the course of a day, intensity drifts are kept to $\sim \pm 10\%$. After illuminating the atoms to drive the $^1S_0$-$^1P_1$ transition, a fraction of the total 4π steradians of emitted photons ($\sim 1\%$) is collected by a large aperture (2 inch) lens and imaged onto a photo-multiplier tube (PMT, Hamamatsu R7400U-20). Here we enjoy the fact that a large number of photons are scattered because of the large spontaneous decay rate of $^1S_0$-$^1P_1$. Nevertheless, to ensure that we collect more than sufficient photon numbers so that we are not limited by the Poissonian photon shot noise, we typically collect photons for a full 5 ms. This is also sufficient time to resonantly heat the $^1S_0$ atoms out of the lattice.

Despite our efforts to reduce technical noise from the 461 nm probing, our excitation measurement remains limited by a technical source: atom number fluctuations in the lattice. After loading a lattice with X number of atoms, we make a $^1S_0$ population measurement proportional to X. Our locking procedure requires a measurement on each side of the peak to determine the line center. We start a new experimental cycle, loading a new group of atoms into the lattice. Unfortunately, shot-to-shot load-

ing fluctuation can give a new atom number $X + \Delta X$, where $\Delta X/X$ is typically near 10%. The next $^1S_0$ measurement is proportional to $X+\Delta X$, and the difference between the two, used for locking, has excess noise proportional to ΔX. To overcome this, we implement normalized excitation detection. After measuring the $^1S_0$ population and heating these atoms out of the trap, we illuminate the atoms with the 679 nm and 707 nm repumping laser, driving the $^3P_0$ population to decay to $^1S_0$. Now what was previously $^3P_0$ population can be measured identically as the original $^1S_0$ population - by scattering 461 nm photons on the $^1S_0$-$^1P_1$ transition. The excitation fraction is simply the $^3P_0$ signal divided by the sum of the $^3P_0$ and the $^1S_0$ signals. Fluctuations in the lattice-loaded atom number scale both measurements the same, and thus divide out. Furthermore, because the method for measuring the $^1S_0$ and $^3P_0$ is identical, other technical noises enjoy common mode rejection (for example, the 461 nm probing laser typically only fluctuates in power at the 1% level over the timescale between the $^1S_0$ and $^3P_0$ measurements). Using this normalization technique, excitation could be detected with a S/N ratio (~ 50) nearly that of the fundamental limit, the quantum projection noise (see next section).

In addition to the Zeeman shift uncertainties in Section 4.3, another dominant contributor to the final achievable frequency uncertainty originated from the AC Stark shift induced by the lattice confinement. We saw that for typical lattice trap depths, a lattice laser frequency 1 GHz from the "magic" operating point resulted in a ~ 1 Hz clock transition shift. For a frequency shift uncertainty at the 10^{-16} level, this requires stabilizing the laser frequency at or better than the 100 MHz level. We had previously used a CW, single mode Ti:Sapphire laser as the lattice laser source. With natural laser drift on a timescale of tens of minutes typically at or below the 100 MHz level, we previously provided this laser stabilization by simply monitoring the output frequency on a high accuracy (50 MHz) commercial wavemeter, and periodically adjusting the laser cavity to keep the output near the magic wavelength. To improve the lattice

laser stability, the laser frequency is now locked to the optical frequency comb, which itself is stabilized to the clock transition. In doing so, the lattice laser frequency is controlled more carefully than is needed for even 10^{-18} clock operation. To facilitate stabilization to the fs comb, we changed the lattice laser source from a CW Ti:Sapphire to a diode laser injection locking a Ti:Sapphire system. With feedback to the diode driving current and laser PZT, the diode laser was locked to the Ti:Sapphire cavity. With single-mode operation from the laser seeding, the Ti:Sapphire laser required no additional intracavity elements, such as a birefringent filter, optical diode, or thick and thin etalons [208]. The removal of these optical elements eliminated cavity loss, facilitating higher output power from the Ti:Sapphire system (as much as 1.5×). The heterodyne beat between the frequency comb and the lattice laser was stabilized to a 70 MHz RF frequency reference, by feeding back on the Ti:Sapphire intracavity PZT. By using the wavemeter as a course guide, and by operating the comb at the same repetition rate each day (made possible by adjusting a New Focus picomotor that translated one of the fs comb cavity mirrors), the lattice laser frequency could be controlled as close to the magic wavelength (frequency) as the Stark shift measurements could determine.

Finally, the other major contributor to previous frequency shift uncertainty was atomic collisions resulting in a density-dependent frequency shift. While no observable shift had been measured, the uncertainty was dictated by the measurement precision. Lacking the immediate means to magnify the potential density-related shift by simply increasing the atomic density one or two orders of magnitude beyond our normal operating density (e. g. as done in [91]), the brute-force use of higher measurement precision could better characterize these density related effects. This was made possible by the all optical comparison of two high stability optical atomic clocks, motivating the optical carrier remote transfer described in the next section.

5.2 Optical Carrier Remote Transfer

In Section 4.2.1, amplitude modulation of an optical carrier was used to transmit a stable microwave frequency over several km. This could be done with a stability level at short timescales comparable to the H-maser [79]. Excess noise at longer time scales could be avoided by implementing a low bandwidth fiber-stretcher to compensate for time varying group delay of the fiber link. These techniques have been refined and improved upon, where transfer over an 86 km link has now achieved instability of 5×10^{-15} at 1 s and 2×10^{-18} after one day [209, 210]. Just as the high operating frequency of an optical frequency standard offers an advantage over a microwave standard, frequency transfer using a coherent optical carrier can outperform its microwave counterparts. Combined with the broad spectral coverage of a fs frequency comb, optical transfer techniques are the best solution for comparing optical frequency standards. To this end, we developed a coherent optical phase transfer system for use over the BRAN fiber network, designed particularly for comparison of the Sr standard to other optical standards at NIST.

Figure 5.2 shows the experimental setup for phase coherent optical transfer. A CW 1064 nm Nd:YAG is phase-locked to the JILA frequency comb, which itself is phase-locked to the Sr clock. The 1064 nm light is transferred to NIST for measurement with the NIST frequency comb. To actively cancel the accumulated fiber phase noise, the transfer laser coherence time must exceed the fiber network round-trip travel time. Our transfer laser has an intrinsic linewidth of 1 kHz in 1 ms, sufficient for fiber noise cancellation over the (round trip) 7-km link. On the JILA end, $\sim$ 1 mW from the transfer laser is picked off by a polarizing beam splitter (PBS) and detected on a photodiode (PD), while up to $\sim$ 40 mW is coupled into the fiber (below threshold for stimulated Brillouin scattering) after being frequency shifted by an AOM. On the NIST end, the final length of fiber has a gold-coated, flat-polished tip which reflects 90% of the 1064 nm light back to JILA, and transmits 10% for heterodyne measurement

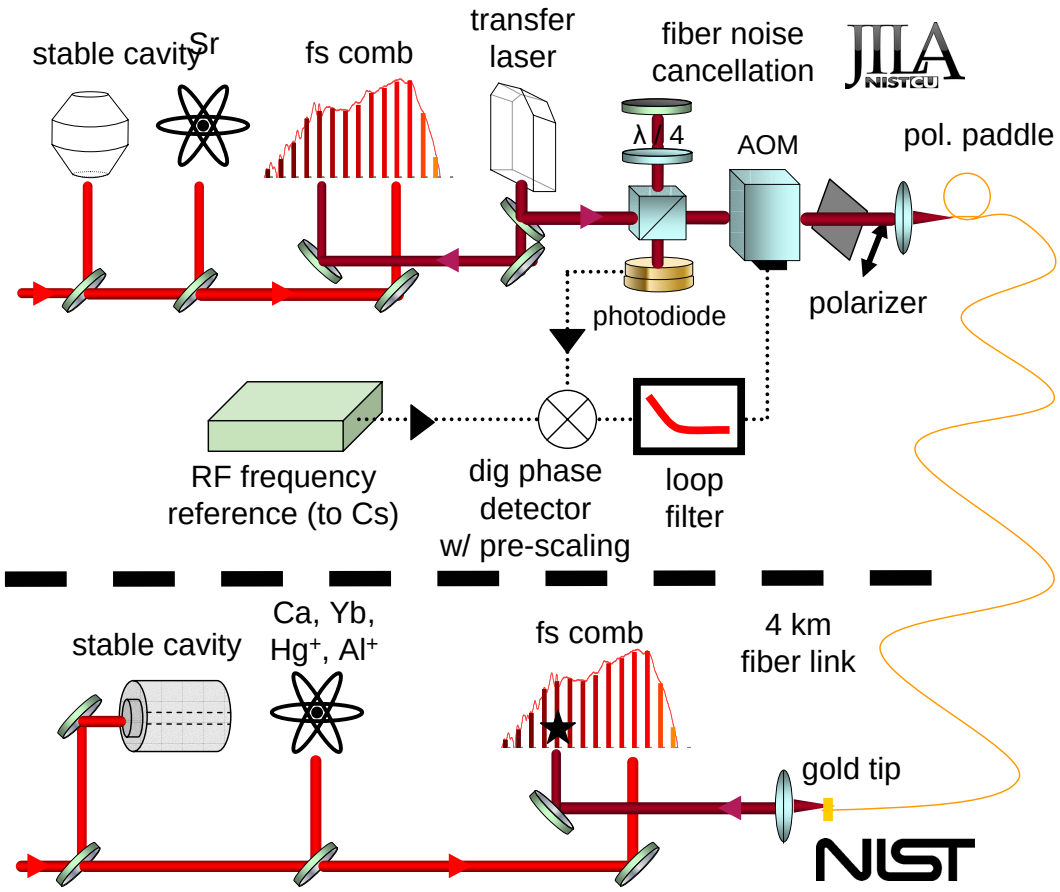

Figure 5.2: Schematic of the phase coherent optical carrier transfer system implemented to remotely compare the Sr standard at JILA to other optical standards at NIST. The clock laser, pre-stabilized to the high finesse ultra-stable cavity, is locked to the atomic transition. A self-referenced fs frequency comb is phase-locked to the Sr clock laser and subsequently a transfer laser, a Nd:YAG at 1064 nm, is phase-locked to the frequency comb. In this way, the comb serves as a "gear" linking the lasers in different parts of the optical spectrum. The Nd:YAG is injected into the fiber link eventually arriving at NIST $\sim$ 4 km later. To cancel carrier phase noise accumulated over the fiber link, phase noise cancellation is implemented using a heterodyne Michelson interferometer.

with the NIST fs frequency comb. Light returning from the remote end accumulates a round-trip phase, again passes through the AOM, and is heterodyned with the local 1064 nm light on the PD. Similar to the fiber phase noise cancellation used elsewhere for the clock laser (Chapter 3), the beat frequency is used for fiber noise cancellation by phase locking it to an RF reference (f_{NENIST}) via feedback to the AOM driving frequency [193, 192]. In this way, noise processes that are stationary during the round trip time are pre-compensated by the AOM. This is not the case for noise at Fourier frequencies corresponding to times shorter than the round trip time. A pre-scaling of the detected heterodyne beat frequency by a division factor of 50 is utilized to give the phase lock a large enough dynamic range to avoid cycle slips under burst noise. Furthermore, a set of birefringent fiber paddles is used on the input end of the fiber link to adjust the polarization state of the round-trip light to maximize the power of heterodyne beat signal. The beat signal power still fluctuates by 1 dB at frequencies of a few Hz, and slowly degrades by as much as 5 to 10 dB over the course of 1 day due to time-changing birefringence of the fiber link. Every few hours the fiber paddles are adjusted to maximize the beat signal strength. To help control polarization mode dispersion [211] on a fast timescale, a linear polarizer is placed just before the local fiber input.

To quantify the optical carrier transfer performance, rather than utilizing the gold fiber tip at the NIST end to terminate the fiber, the gold tip was removed and the fiber was spliced to a second fiber making the return trip to JILA. The gold tip was installed at the JILA end, so that the transfer scheme could operate with the local and remote ends co-located for out-of-loop comparison. This link has twice the fiber phase noise of the original JILA-NIST only link. Figure 5.3(a) shows the Allan deviation of the heterodyne beat (mixed down to 10 kHz) between the local and remote 1064 nm light. Also shown is the frequency stability with the noise cancellation inactive (i. e. free-running fiber noise) and the measured in-loop instability of the locked heterodyne beat

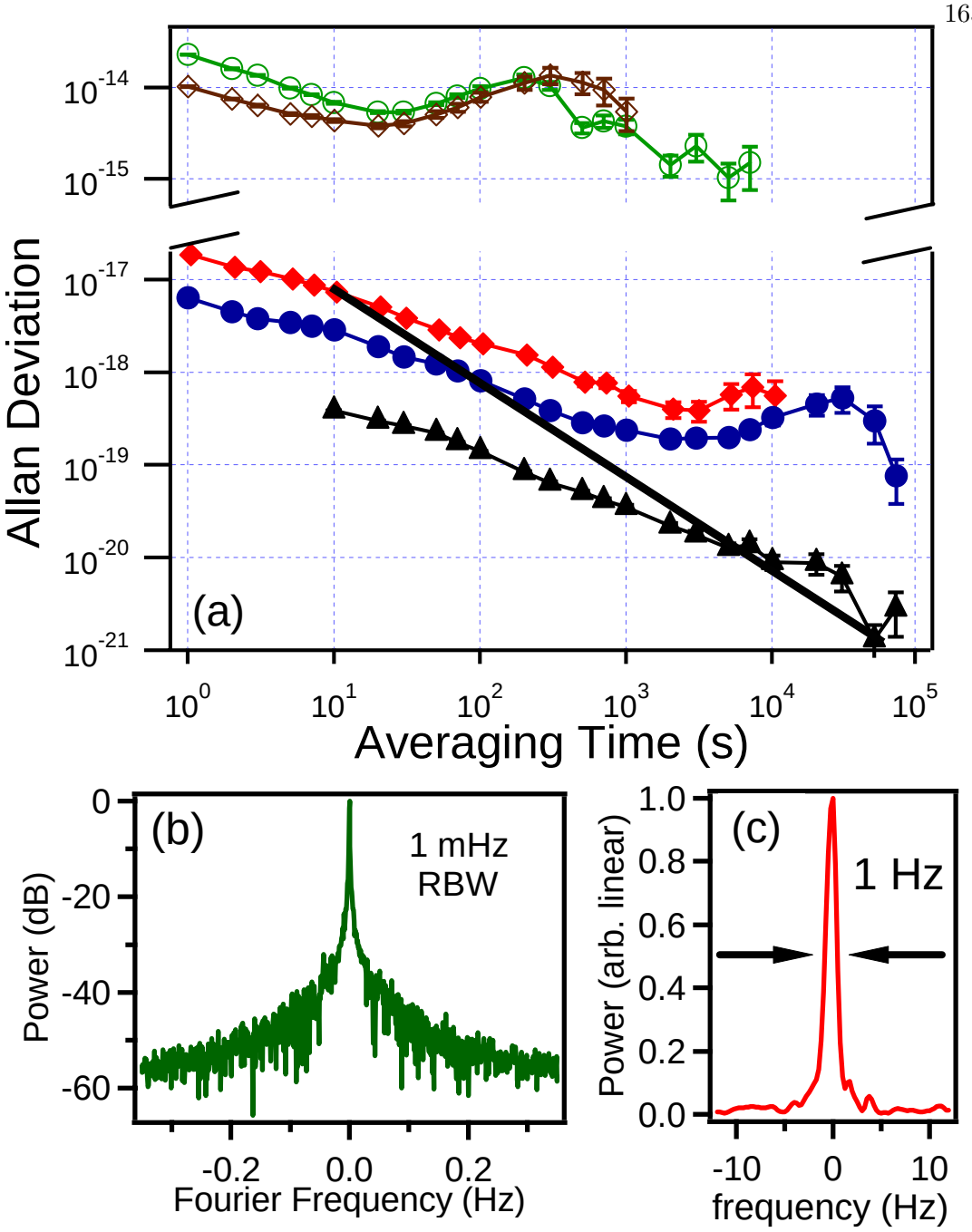

Figure 5.3: Measurements of the phase coherent optical carrier transfer. (a) Instability versus time of the remotely transferred optical carrier versus the original, local optical carrier. Open circles: No phase noise cancellation over 32 km fiber, Open diamonds: No phase noise cancellation over 7 km fiber, Closed diamonds: Phase-noise cancellation over 32 km fiber, Closed circles: Phase-noise cancellation over 7 km fiber, Closed triangles: In-loop estimate of phase noise cancellation. (b) Heterodyne beat between 7 km remotely transferred 1064 nm light and the frequency comb to which the local 1064 nm is phase-locked. (c) Heterodyne beat between the Hg^+ ion clock laser and the Sr clock laser remotely transferred from JILA to NIST with the phase coherent optical carrier transfer.

(divided by two for the one way instability). An impressive 1 s instability of $< 10^{-17}$ demonstrates that the transfer scheme can be used to compare optical standards with transfer noise well below the intrinsic noise of the current optical standards. The phase lock loop for the fiber transfer itself has demonstrated locking durations of 70 hours. Furthermore, the transferred frequency accuracy is 1×10^{-19}, consistent with the best measured instability.

The effectiveness of the fiber transfer scheme is also shown in Figure 5.3(b), which gives the measured power spectrum for the heterodyne beat between the remote 1064 nm light and the comb mode to which the local 1064 nm light is locked. The uncancelled transfer broadens the relative linewidth to $\sim$ 1 kHz, whereas the locked case reveals a resolution-bandwidth-limited linewidth of 1 mHz. For more details on the coherent optical carrier transfer, including the resulting phase spectral noise density and extending the transfer scheme to longer distances using a coherent repeater station, see [212, 201]. The choice of optical transfer at 1064 nm was convenient for the spectrum of the fs frequency combs at JILA and NIST. For longer distance comparisons, the optical power attenuation through the fiber link ($<$ 4 dB for 7 km roundtrip path) can be greatly reduced using telecom friendly wavelengths.

As an exhaustive out-of-loop evaluation of the optical carrier transfer scheme, Figure 5.3(c) shows the linewidth of the optical heterodyne beat between the 1064 nm light phase-locked to the Sr clock laser via the comb and transferred to NIST and the NIST fs frequency comb which is locked to the Hg^+ ion clock laser [212]. The recovered 1 Hz linewidth demonstrates the exquisite generation and transfer of optical phase control across the optical spectrum and across km-scale distances, despite the accumulated noise of more than a dozen phase-lock-loops.

Figures 5.4 and 5.5 give a summary schematic of frequency counting of the Sr standard using both the optical and microwave transfer with NIST. As is clear from Figure 5.4, the comb plays a critical, centralized role of allowing lasers at different parts

of the spectrum to be phase stabilized relative to each other, and does so with dramatic fidelity [202]. Note that the comb is phase-locked to the cavity-stabilized 698 nm light before AOM1 used to lock the cavity-stabilized light to the atomic transition. The synthesizer used as the phase/frequency reference for the comb lock to the 698 laser has a computer-controlled frequency output ($f_{SRSlock}$). The locking program (Section 5.1.2) updates $f_{SRSlock}$ (see frequency 8 in Figure 5.5) to keep the comb locked to the atomic transition, counteracting the cavity-stabilized laser frequency drift. This approach was taken to minimize the number of AOMs used to transfer the atomic transition lock to the fs comb (and the remote optical standard), but not transfer the lock modulation. Using the formulas in Figure 5.5, for absolute frequency measurements using the Cs-calibrated H-maser reference link, the Sr transition is found to be:

$$\nu_{Sr} = \left[\frac{N}{10}(f_{maser} + f_{count}) + f_{CEO}\right] + (f_{NEcomb} + f_{NESr}) - (f_{offset} + f_{ARP}) \quad (5.1)$$

For a frequency measurement using the optical transfer to NIST, the Sr frequency is given by:

$$\nu_{Sr} = \left[\frac{N}{M}(Y f_{YAGlock} + \nu_{YAG} - f_{CEO}) + f_{CEO}\right] + (f_{NEcomb} + f_{NESr}) - (f_{offset} + f_{ARP}) \quad (5.2)$$

where NIST measures $\nu_{YAG} - f_{NENIST}$ using their frequency comb stabilized to an optical (or microwave) standard. Note that as described in Section 4.1, the integer mode numbers N and M are determined using wavemeter readings for the clock laser and YAG transfer laser, respectively.

5.3 Stability Evaluation of the Sr Optical Frequency Standard

In Chapter 1, we looked at a generic expression for the fractional instability of an atomic frequency standard, which we repeat here for convenience:

$$\sigma_y(\tau) = \frac{\delta\nu}{\nu_0}\frac{\eta}{S/N\sqrt{\tau}} \quad (5.3)$$

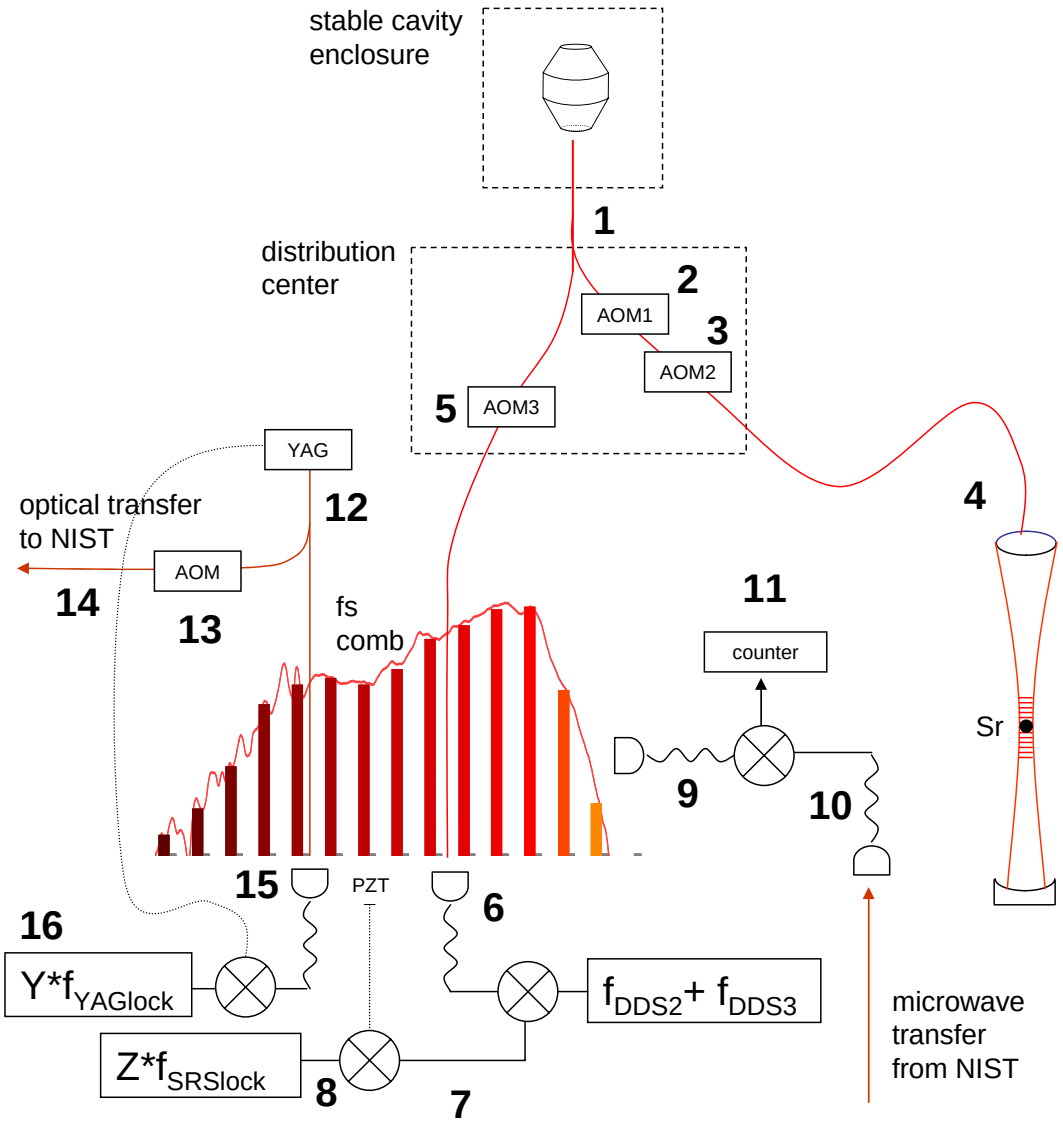

Figure 5.4: Summary schematic of Sr frequency counting with both optical and microwave references. Figure 5.5 gives the relevant frequency relationships at the numbered locations.

1: ν_{cavity}

2: AOM1 = $f_{DDS1}+f_{DDS2}+f_{DDS3}+f_{ARP}$

$f_{DDS2}+f_{DDS3} \approx 75$ MHz, $f_{ARP} = 22.3$ MHz

3: AOM2 = $f_{NESr} = ½ \times 155.46464$ MHz

4: $\nu_{Sr} = \nu_{cavity}-(f_{DDS1}+f_{DDS2}+f_{DDS3}+f_{ARP})+f_{NESr}$

5: AOM3 = $f_{NEcomb} = ½ \times 155.46464$ MHz

6: comb-698 beat = $(Nf_{rep}+f_{CEO})-(\nu_{cavity}-f_{NEcomb})$
$f_{CEO} = 70$ MHz

7: $(Nf_{rep}+f_{CEO})-(\nu_{cavity}-f_{NEcomb})+(f_{DDS1}+f_{DDS2})$

8: comb lock: $(Nf_{rep}+f_{CEO})-(\nu_{cavity}-f_{NEcomb})+(f_{DDS1}+f_{DDS2}) = Z\ f_{SRSlock} \approx 100$ MHz
for lock to Sr: $f_{SRSlock} = (f_{offset} - f_{DDS1})/Z$, Z=80

9: tenth harmonic of rep rate = $10\ f_{rep} \approx 950$ MHz

10: modulation from NIST H-maser: $f_{maser} \approx 950$ MHz

11: $f_{count} = 10f_{rep}-f_{maser} \approx 40$ kHz

12: transfer YAG = ν_{YAG}

13: AOM = f_{NENIST}

14: $\nu_{YAG} \pm f_{NENIST}$

15: comb-YAG beat = $(Mf_{rep}+f_{CEO}) \pm \nu_{YAG}$

16: YAG lock: $(Mf_{rep}+f_{CEO}) \pm \nu_{YAG} = Y\ f_{YAGlock} = 60$ MHz

Figure 5.5: Frequency relationships for Figure 5.4. For more details on f_{DDS1}, f_{DDS2}, and f_{DDS3}, see Figure 5.1(c). f_{ARP} is an arbitrary offset. f_{NESr}, f_{NEcomb}, and f_{NENIST} are the phase/frequency references used in the fiber noise cancellation for optical transfer from the distribution center to Sr apparatus, from the distribution center to the frequency comb, and from the frequency comb at JILA to NIST, respectively. $f_{SRSlock}$ is the reference for the phase lock of the frequency comb to the Sr clock laser and $f_{YAGlock}$ is the reference for the phase lock of the YAG transfer laser to the frequency comb. f_{maser} is the modulation frequency referenced to the NIST H-maser, as shown in Figure 4.2. The comb parameters f_{CEO} and f_{rep} are illustrated in Figure 4.1. For more details on the complete system details, see the main text.

We have assumed that the noise process dominating the instability is white. The parameter η is approximately unity and depends on the details of the spectroscopic lineshape. We saw that enhancing the signal-to-noise ratio S/N allows us to improve upon the measurement resolution (stability) provided by the transition line quality factor ($Q = \nu_0/\delta\nu$). The standard's instability can be expressed as the Allan deviation, as defined in Equation 3.11. A number of different noise processes work to limit the achievable instability, some of them eluded to in Section 5.1. As a starting point to consider the most relevant noise processes, we write the fractional instability as a sum of several effects [39]:

$$\sigma_y(\tau) = \frac{1}{\pi Q}\sqrt{\frac{T_c}{\tau}}\left(\frac{1}{N} + \frac{1}{Nn_{ph}} + \frac{2\sigma_N^2}{N^2} + \gamma\right)^{\frac{1}{2}} \tag{5.4}$$

Two pulse Ramsey spectroscopy is assumed here (similar but not identical to the case of Rabi spectroscopy given below). By comparison to Equation 1.1, it is clear that each term in parentheses is related to the signal to noise ratio (S/N) for different noise processes. The first term originates from quantum projection noise, the second from photon shot noise, the third from technical atom number fluctuations, and the fourth from frequency noise of the interrogation laser. T_c is the experimental cycle time (of which some fraction is spent interrogating the clock transition), N is the atom number, n_{ph} is the number of signal photons detected for each atom, σ_N is the uncorrelated rms (root mean squared) fluctuations of the atom number, and γ is the frequency noise of the probe laser.

Using the fluorescence-based measurement described in Section 5.1.3, typically $n_{ph} \gg 1$ so that photon shot noise (2^{nd} term) is below the quantum projection noise (1^{st} term). Atom loading fluctuations in the lattice limited the detection S/N to a value typically in the range of 10-15. However, the normalization procedure permitted measurement S/N up to ~ 50. This was estimated by exciting the atoms using a short, strong Rabi pulse which power and Fourier broadened the excitation (reducing

the effect of laser frequency noise). We then measured the normalized, shot-to-shot excitation fluctuations as we re-loaded the optical lattice with new samples.

The most fundamental limit to the atomic frequency standard instability is the quantum projection noise (also referred to as atom shot noise). It is a well known postulate of quantum mechanics that any physical measurement of a quantum system can be modelled by a Hermitian operator acting on the wave function of the system being measured, and that the result of that measurement is an eigenvalue of the operator. Thus a measurement on an atomic state which is a superposition of eigenstates yields a statistical result: one eigenvalue with a measurement probability given by the superposition weighting of its eigenstate. This implies fluctuation (noise) in the measurement as the wavefunction collapses and is projected onto a particular eigen-basis. For the two level system of an atomic frequency standard, this quantum projection noise for the measurement of the ground or excited state is equal to $\Delta exc = \Delta gnd = \sqrt{Np(1-p)}$, where N is the number of atoms interrogated and p is the excitation fraction [213]. The S/N for the excitation fraction, equivalent to the S/N of the excited state population, becomes $\sqrt{Np/(1-p)}$. For comparison to the experimentally measured S/N after normalization, $N \simeq 2000 - 4000$ and $p \simeq 0.4 - 0.5$, yielding an $S/N \simeq 50$, indicating that the observed S/N is consistent with that limited by quantum projection noise. The quantum projection noise limited instability for the case of Rabi spectroscopy of a Lorentzian lineshape with FWHM given by γ can be found to be:

$$\sigma_y(\tau) = \frac{\gamma}{2\nu_0}\sqrt{\frac{2(1-p)}{pN}\frac{T_{tc}}{\tau}} \tag{5.5}$$

where the transition frequency is ν_0 and the total cycle time is T_{tc} (for probing both half maxima of the Lorentzian). Using typical values for the operation of our Sr standard ($\gamma = 10$ Hz, $\nu_0 = 4.29 \times 10^{14}$ Hz, $p \simeq 0.4$, $N \simeq 4000/2$, $T_{tc} \simeq 2 \times 1$ s), the fundamental fractional instability limit is approximately 7×10^{-16}.

We have not yet considered measurement instability induced by the clock laser

frequency noise. We do not treat here the integrated laser frequency noise over the probe pulse time (typically $t_p = 80$ ms for the Sr standard) which is relevant for the instability at that timescale. Rather we focus on spectroscopic probing repeated every experimental cycle time T_c and separated by nonzero dead time, which contributes to long-term instability. The atomic excitation measurement corresponds to a temporally-binned, "digital" sampling with sampling rate of $f_c = 1/T_c$. With no means to low pass filter the excitation measurement resulting from the atom-laser interaction, excitation resulting from high frequency laser noise is aliased into the detection bandwidth, indistinguishable from excitation originating from laser noise in the detection bandwidth. The lock to the atomic transition, unable to distinguish the two, improperly compensates for the aliased noise and introduces extra instability into the frequency standard. All sequentially operated cold atom standards suffer from this effect as do any atomic standards with modulated interrogation around the line center. Larger dead time in the experimental cycle makes this effect more pronounced. Sequential cold atom samples have a minimum dead time associated with cooling and loading the atomic sample. The dead time of the Sr standard (typically from 0.5 to 1 s) also includes loading the optical lattice, polarizing the atomic sample, and reading off the populations after interrogation. The aliasing effect depends upon the particular spectroscopy implemented, which influences how sensitive the population excitation is to frequency fluctuations (in the general case, this is a time-dependent sensitivity). This effect, which can be viewed as resulting from time-dependent gain in the atom-laser feedback loop, was first illuminated by G. John Dick at the NASA Jet Propulsion Laboratory and is now referred to as the Dick effect.

The fractional instability resulting from this effect can be shown to be [214, 215]:

$$\sigma_y(\tau) = \frac{1}{\mu_0}\sqrt{\frac{1}{\tau}\sum_{m=1}^{\infty}\left(\frac{g_{c,m}^2}{g_0^2} + \frac{g_{s,m}^2}{g_0^2}\right) S_f\left(\frac{m}{T_c}\right)} \tag{5.6}$$

Here $S_f(m/T_c)$ is the one-sided power spectral density of the free running probe laser (local oscillator) at the Fourier frequency m/T_c. The factors $g_{c,m}$ and $g_{s,m}$ correspond

to the Fourier sine and cosine series coefficients giving the sensitivity spectral content at $f = m/T_c$ and are given by:

$$g_{s,m} = \frac{1}{T_c}\int_0^{T_c} g(\epsilon)\sin\left(\frac{2\pi m\epsilon}{T_c}\right)d\epsilon \tag{5.7}$$

$$g_{c,m} = \frac{1}{T_c}\int_0^{T_c} g(\epsilon)cos\left(\frac{2\pi m\epsilon}{T_c}\right)d\epsilon \tag{5.8}$$

and the normalization factor g_0 is:

$$g_0 = \frac{1}{T_c}\int_0^{T_c} g(\epsilon)d\epsilon \tag{5.9}$$

The physics of the atom laser interaction is hidden in the time-dependent sensitivity function $g(t)$. This function can be found for the particular spectroscopic details by solving for the population evolution as a function of probing time and detuning from the atomic transition. For the special case of coherent excitation from a Rabi π-pulse, the sensitivity function is:

$$g(t) = \frac{\Delta_{HM}}{(1+\Delta_{HM}^2)^{3/2}}\left[\sin\Omega_1(t)(1-\cos\Omega_2(t)) + \sin\Omega_2(t)(1-\cos\Omega_1(t))\right] \tag{5.10}$$

where $\Omega_1(t) = \beta t/t_p$, $\Omega_2(t) = \beta - \Omega_1(t)$, $\beta = \pi\sqrt{1+\Delta_{HM}^2}$ and the half maximum detuning is $\Delta_{HM} \simeq .799$. Figure 5.6(a) shows this Rabi π-pulse $g(t)$ for $t_p = 80$ ms and $T_c = 1$ s. Using this $g(t)$ and the known probe laser frequency noise spectrum (Figure 3.4(c)), Equation 5.6 can be solved for the Dick-effect-limited instability, found to be $\sim 2\times10^{-15}\ \tau^{-1/2}$, larger than the quantum projection noise instability. This sets a Dick effect limit on the Sr instability.

Looking at Equations 5.6-5.10, there are several ways to reduce the Dick noise instability limit. The first is to reduce the clock laser frequency noise. Some considerations for improving the laser frequency noise were discussed in Chapter 3. Interestingly, as the laser frequency noise is reduced, narrower transition linewidths will be observed for the atomic systems with this potential. This means that the quantum projection noise instability will also decrease. As a result, although reduced laser noise will reduce the instability, in some cases the Dick effect may continue to play a limiting role.

Fortunately, a quieter laser means that the probing time can be increased to a larger fraction of the total cycle time. A reduction in dead time results in further reduction of the Dick effect. Thus, whether the standard ends up being stability-limited by quantum projection noise or the Dick effect depends on the details.

Without improving the laser frequency noise, increasing the probing time can still decrease the Dick effect. In the Sr case, a typical probing time of 80 ms is chosen to give a very reliable ~ 10 Hz wide line. As seen in Chapter 3, we have probed for longer intervals. However, a tradeoff does seem to exist: going to too long probing times results in noisier, less well-defined spectra (becoming more sensitive to clock laser noise). This creates extra problems for the lock to the atomic transition. Note also that even in the limit when $t_p = T_c$, the Dick effect is nonzero because of the time dependence of the sensitivity function $g(t)$.

Another way to reduce the Dick effect is by reducing the cycle time T_c for a fixed probe time t_p. In the case of pure white frequency noise from the clock laser, the reduction is similar to that seen from increasing t_p for a fixed T_c. In other words, t_p/T_c or the fraction of dead time $(1 - t_p/T_c)$ is the important parameter. However, in the case of frequency noise which falls off at higher frequency, going to shorter cycle times has the extra advantage that the aliased laser noise originates from higher Fourier frequencies where the noise spectral density is reduced. This is partially the case for the Sr clock laser, which at the lowest frequencies has noise set by the thermal noise of the cavity, resulting in a frequency noise power spectral density that falls off as $1/f$ (see Figure 3.4(c)). Table 5.1 gives the Dick-limited instability of the Sr clock laser for several values of T_c and t_p.

Decreasing the dead time reduces the Dick effect by making the sensitivity function $g(t)$ more homogeneous over the cycle time T_c. This idea could be taken further by designing a pulse shape which has a more even $g(t)$ over the probe duration. This is the case for two-pulse Ramsey spectroscopy (as one might expect the sensitivity must

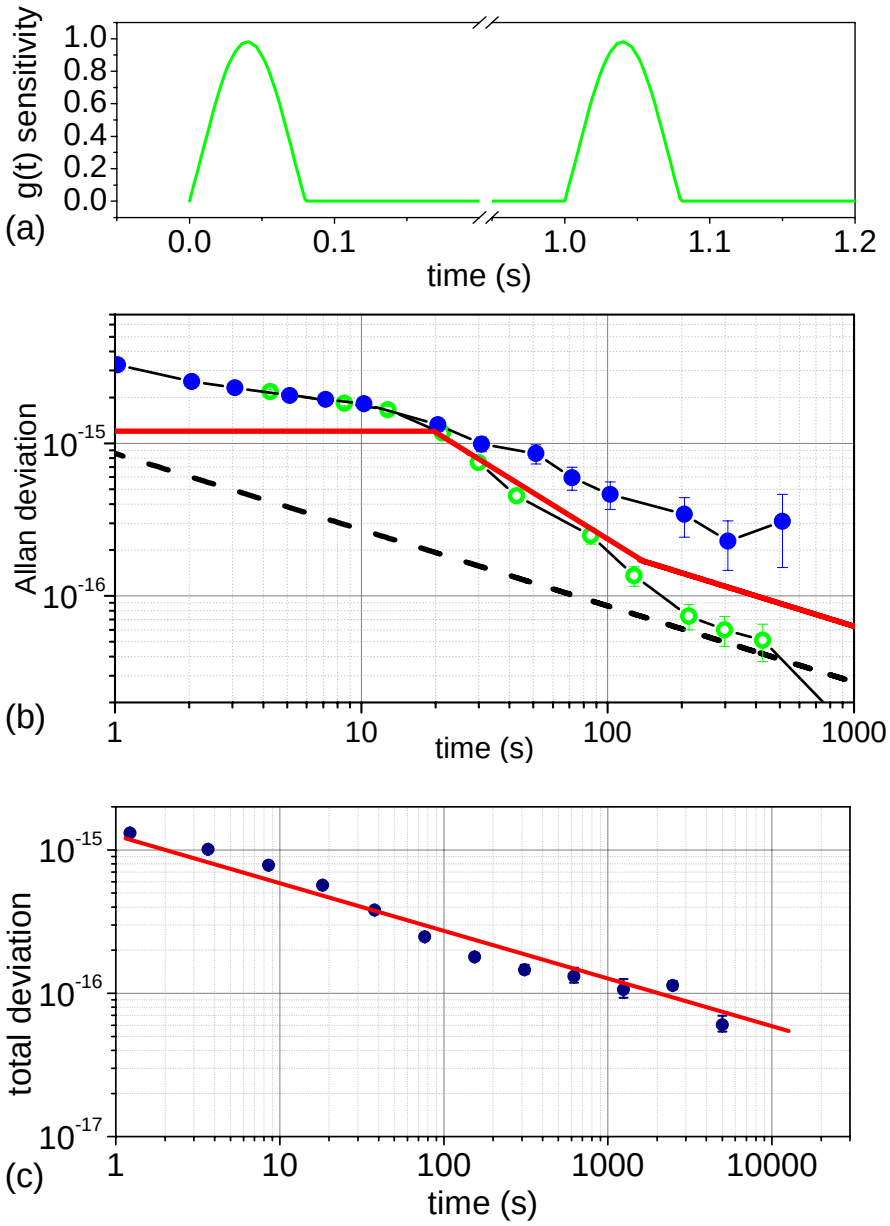

Figure 5.6: (a) The sensitivity function, $g(t)$, with an atomic probe time of $t_p = 80$ ms and an experimental cycle time of $T_c = 1$ s. During the probe time, the sensitivity function is given by the Rabi interrogation of the atoms. All other times are dead time, with $g(t) = 0$. The Dick effect results from time-dependence of the sensitivity function, introducing atom-laser interaction sensitivity at frequencies equal to $f_c = 1/T_c$ and its harmonics. This measurement noise is then aliased to DC where the servo to the atomic transition, unable to recognize its aliased origin, compensates for it. (b) Stability figures for the Sr atomic clock. Black dashed line: quantum projection noise limit. Solid red line: estimate for the Sr clock instability. At short times, this is the free-running instability of the Sr clock laser. At $\tau = 20$ s, the atom servo crosses unity gain with a single integrator, allowing the clock laser instability to average down with the atomic transition at nearly $1/\tau$. After 100 s, the Dick effect limit is reached, where the instability then averages down as $1/\sqrt{\tau}$. Green open circles: In-loop measure of the Sr clock instability based on the error signal. Blue filled circles: Measured instability between the JILA Sr system and the NIST Ca system, linked by the remote carrier transfer. (c) Instability between remotely transferred JILA Sr system and the NIST Yb system. Here, Sr is operated with a single peak lock to maximize the atom servo attack time.

Table 5.1: Dick effect limited instability of the JILA Sr standard for various values of experimental cycle time T_c and transition probing time t_p

t_p	T_c	$\sigma(\tau = 1s)$
80 ms	1 s	2×10^{-15}
80 ms	500 ms	1.2×10^{-15}
80 ms	160 ms	5×10^{-16}
80 ms	1 s	2×10^{-15}
160 ms	1 s	1.6×10^{-15}
320 ms	1 s	1.2×10^{-15}
1 s	1 s	4×10^{-16}
1 s	1 s	4×10^{-16}
80 ms	80 ms	2×10^{-16}

be constant during the Ramsey dark time). In the limit of a Ramsey dark time much longer than the pulse time of the two Ramsey pulses, $g(t)$ approaches a box function. As we considered the relative advantages of Rabi or Ramsey spectroscopy on our lattice-trapped Sr atoms, the atomic confinement puts the two methods on similar footing. One possible advantage of Ramsey spectroscopy (particularly when the Ramsey dark time is much longer than the pulse time) is a reduction in the Dick effect. However, the benefits of the shape of $g(t)$ during the spectroscopic interrogation are only substantial when the interrogation accounts for a large fraction of T_c, i. e. when the dead time is small. For our normal operating conditions, the smallest dead time is $\sim 85\%$ of T_c, and the corresponding Dick instability reduction for Ramsey spectroscopy is only at the 10% level [216]. However, as the experimental cycle is refined, decreases in T_c and especially increases in t_p may eventually merit worthwhile instability reduction from the use of Ramsey interrogation.

Finally, another approach to reducing the Dick effect is to have multiple atomic samples, so that the local oscillator can sequentially interrogate the different atomic samples and effectively reduce or eliminate the dead time. This solution is conceptually straightforward, however increases experimental complexity. For Cs fountains, this technique may be compatible with the multi-atomic-cloud juggling fountains proposed

to circumvent density related shifts [217]. The use of multiple traps to reduce the Dick effect has recently been demonstrated for a Cs microwave standard [218].

With insight into the relevant instability limitations, we now consider the performance of the Sr standard. Figure 5.6(b) shows different stability estimates for the Sr standard. The dashed black line indicates the fundamental limit given by the quantum projection noise. The solid red line gives the best known estimate of the current operational instability for the Sr standard. At short time scales, the instability is governed by the free-running instability of the clock laser (see Chapter 3). At approximately 20 s, the servo to the atomic transition crosses unity gain with a single integrator (20 dB/decade) with the instability improving almost as $1/\tau$ as the laser tracks the atoms. This continues until $\sim$ 100 s, where the white-frequency Dick noise limit is reached, at which point the instability averages down as $1/\sqrt{\tau}$. To reduce long timescale oscillations, we have at times operated the atom-laser servo aggressively, yielding a servo bump in the instability at 10-20 s. The green open circles (in Figure 5.6(b)) indicate an in-loop measure of the Sr instability, taken from the error signal of the lock to the atomic transition. Finally, the blue dots indicate an independent, out-of-loop evaluation made by comparing the Sr JILA standard to the NIST Ca standard, using the optical carrier fiber link described in Section 5.2.

To better characterize the potential stability, Figure 5.6(c) shows the measured fractional instability between the Sr JILA standard and the NIST Yb standard, again utilizing the optical fiber link. For the measurement shown, the Sr standard was operated by locking to just one of the $m_F = \pm 9/2$ transitions, helping to facilitate faster servo time. The instability of 1×10^{-16} near 1000 s and crossing into the 10^{-17} decade shows strong potential of both the Yb and Sr standards. At the current time, this represents the best stability for a neutral atom system and is comparable to the best stability observed in a single-trapped ion system. With the large atom number enjoyed by the neutral atom samples, the stability of the neutral atom system has the potential

to substantially exceed that of the single ion standards. As seen by the analysis of this section, doing so will foremost require a more stable clock laser, to reduce the Dick effect and allow narrower atomic transitions. Afterwards, enhancing the lattice-trapped atom number will bring the quantum projection noise further down.

5.4 Accuracy Evaluation of the Sr Optical Frequency Standard

5.4.1 Measurement Description

In Section 4.3, I described our systematic uncertainty evaluation of the Sr clock transition frequency utilizing an atomic microwave reference and later a stable laser reference. As seen in the last section, the measurement precision made possible by directly comparing two optical atomic standards gives an even higher resolution probe of the physics governing the Sr clock transition shifts. This enables a significantly improved characterization of the Sr clock frequency uncertainty. We make this characterization by remote comparison of the Sr standard to the NIST Ca standard (measurement scheme summarized in Figure 5.7). The Ca clock is a simple and robust system that uses freely expanding cold atoms. Like a hydrogen maser, it serves as a highly stable frequency reference, but with 100 times better stability at short times. As we just saw, the stability of the Sr-Ca comparison can reach below 3×10^{-16} after 200 s. However, the Ca clock is susceptible to long-term (> 1000 s) drifts due to residual Doppler effects associated with the free space Ca. As we evaluate frequency shifts from individual mechanisms, in order to optimize the shift uncertainties, frequency measurements are thus made in 100-s time windows. To remove sensitivity to long-term Ca drifts, these 100-s windows are interleaved as a particular parameter of the Sr clock is systematically varied. Typically, the parameter is toggled between two settings for two consecutive 100-s windows, and a Sr clock frequency shift is measured between them. Many such pairs are accumulated to average to a measurement precision below 1×10^{-16}, enabling rigorous evaluations of

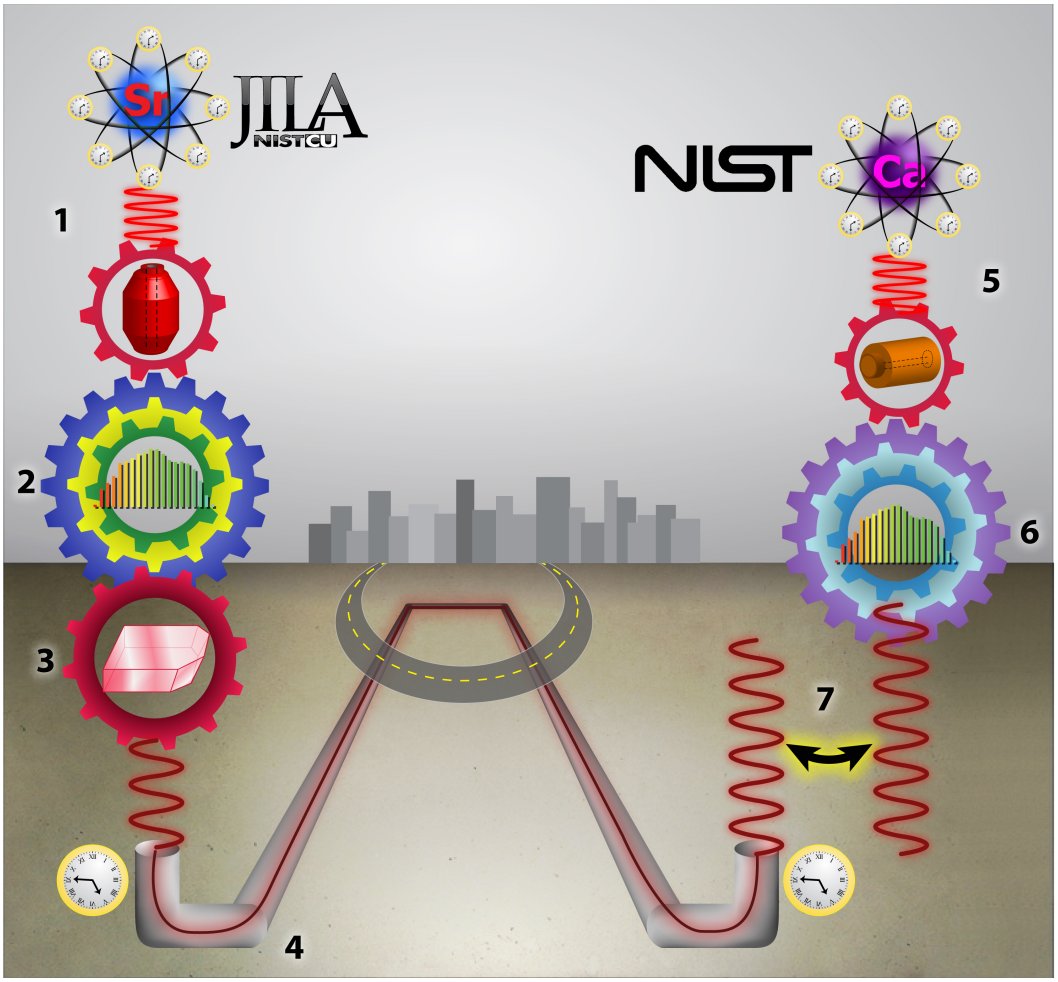

Figure 5.7: Summary of the experimental setup used for evaluation of systematic shifts of the Sr system by remote comparison with the NIST Ca optical frequency standard. The Sr atomic reference is counted and distributed in direct analogy to traditional clocks using mechanical gears, albeit at optical frequencies. The Sr atomic clock at JILA (1, consisting of lattice trapped Sr system and the cavity-stabilized clock laser) serves as the atomic standard to which an optical frequency comb (2) is phase-locked. A CW Nd:YAG laser at 1064 nm (3, a non-planar ring oscillator as shown in the figure) is phase-locked to the same frequency comb and transferred to NIST via a phase-noise-cancelled fiber link (4). The 1064 light emerges from the fiber at NIST and is phase coherent with the light originating from JILA, as symbolized by the syntonized clocks on either fiber end. The Ca optical clock at NIST (5, consisting of free space Ca system and a cavity-stabilized laser at 657 nm) is the atomic reference to which another optical frequency comb (6) operating at NIST is phase locked. The clock comparison (7) is made by a heterodyne measurement between the NIST frequency comb and the 1064 nm transmitted light.

key Sr clock frequency shifts at this level. This measurement approach is facilitated by the robustness of these optical clocks, as both systems are regularly operated on-demand for timescales of a day.

For the Sr clock operation reported here, approximately 4000 ^{87}Sr atoms are laser cooled to 2.5 μK and confined in the one-dimensional optical lattice with a longitudinal (transverse) trap frequency of 42 kHz (120 Hz), a lattice depth $U \simeq 35E_r$, and a single beam lattice intensity of $I_0 = 3$ kW/cm^2. With the optical pumping techniques previously described, the atoms are (doubly) spin polarized and occupy only the two states $m_F = \pm 9/2$. Under a weak bias field of $B = 200$ mG, we interrogate the isolated $m_F = \pm 9/2$ clock transitions for 80 ms, allowing Fourier-limited spectral linewidths of 10 Hz. The average atomic density is $\rho_0 \simeq 1 \times 10^{11}$ cm^{-3}.

We now consider systematic shifts and their uncertainties from a variety of physical origins:

5.4.2 Lattice AC Stark shift

In Section 2.6, we derived an expression for the dipole polarizability of an atomic state, which provided the means to confine the atoms in the lattice dipole potential. We implicitly made a simplifying assumption that the perturbing electric field was polarized along a particular axis. This enabled us to neglect anisotropic terms of the polarizability, which accounts for an induced dipole moment along an axis orthogonal to the electric field. Analogous to the classical picture, in a more general case the induced dipole must account for all contributions including anisotropic ones [219]:

$$\begin{pmatrix} d_x \\ d_y \\ d_z \end{pmatrix} = \begin{pmatrix} \alpha_{xx} & \alpha_{xy} & \alpha_{xz} \\ \alpha_{yx} & \alpha_{yy} & \alpha_{yz} \\ \alpha_{zx} & \alpha_{zy} & \alpha_{zz} \end{pmatrix} \begin{pmatrix} E_x \\ E_y \\ E_z \end{pmatrix} \tag{5.11}$$

The stark shift can be written as:

$$U = -\frac{1}{2}\vec{E} \overleftrightarrow{\alpha} \vec{E} = -\frac{1}{2}E_i \alpha_{ij} E_j = -\frac{1}{2}E_i d_i \tag{5.12}$$

where the double arrow denotes the tensor nature of α, and the last two lines use the Einstein summation convention where summation over repeated indices is presumed. In an atomic system, the polarizability operator can be derived from perturbation theory for a state a. When the fine structure splitting is much larger than the magnetic sublevel splitting (due to m dependent Stark effect), then this operator can be represented as a matrix in the subspace of the ground magnetic sublevels of J_a:

$$\langle J_a m_a | \hat{\alpha_{ij}} | J_a m'_a \rangle = \frac{1}{\hbar} \sum_{k \neq a} \frac{\langle J_a m_a | d_i | J_k m_k \rangle \langle J_k m_k | d_j | J_a m'_a \rangle}{\omega_{ak} - \omega_L} + \frac{\langle J_a m_a | d_j | J_k m_k \rangle \langle J_k m_k | d_i | J_a m'_a \rangle}{\omega_{ak} + \omega_L} \tag{5.13}$$

where k denotes the summation index over the intermediate states, and the other quantum numbers besides J and m are not explicitly shown. Furthermore, we have assumed large detuning from any atomic transition. Note also that while we are considering only total electronic spin J and fine structure here, under the appropriate conditions the formalism trivially extends to other angular momentum quantum numbers (e. g. total angular momentum F if the hyperfine structure splitting dominates the magnetic state splitting).

It is common to transform the Cartesian operator $\hat{\alpha}_{ij}$ into a sum of polarizability terms, known as the scalar (α_s), vector (α_v), and tensor (α_t) polarizabilities [219]. This is a transformation to the spherical tensor basis:

$$\hat{\alpha_{ij}} = \alpha_s \hat{\delta_{ij}} - \alpha_v (\hat{J}_i \hat{J}_j - \hat{J}_j \hat{J}_i) + \alpha_t \frac{\frac{3}{2}(\hat{J}_i \hat{J}_j + \hat{J}_j \hat{J}_i) - J_a(J_a+1)\hat{\delta_{ij}}}{J_a(2J_a - 1)} \tag{5.14}$$

$$\alpha_s = \frac{2}{3\hbar g_J} \sum_{k \neq a} \frac{|\langle J_a \| d \| J_k \rangle|^2 \omega_{ak}}{\omega_{ak}^2 - \omega_L^2} \left(\delta_{J_k, J_a - 1} + \delta_{J_k, J_a} + \delta_{J_k, J_a + 1} \right) \tag{5.15}$$

$$\alpha_v = \frac{1}{\hbar g_J} \sum_{k \neq a} \frac{|\langle J_a \| d \| J_k \rangle|^2 \omega_L}{\omega_{ak}^2 - \omega_L^2} \left(\frac{-1}{J_a} \delta_{J_k, J_a - 1} - \frac{1}{J_a(J_a+1)} \delta_{J_k, J_a} + \frac{1}{J_a + 1} \delta_{J_k, J_a + 1} \right) \tag{5.16}$$

$$\alpha_t = \frac{2}{3\hbar g_J} \sum_{k \neq a} \frac{|\langle J_a \| d \| J_k \rangle|^2 \omega_{ak}}{\omega_{ak}^2 - \omega_L^2} \left(-\delta_{J_k, J_a - 1} + \frac{2J_a - 1}{J_a + 1} \delta_{J_k, J_a} - \frac{J_a(2J_a - 1)}{(J_a + 1)(2J_a + 3)} \delta_{J_k, J_a + 1} \right) \tag{5.17}$$

Here $g_J = 2J_a + 1$ is the ground state degeneracy, and δ_{ij} is the Kronecker delta function. The Wigner-Eckart theorem has been applied, so that the scalar, vector, and tensor polarizabilities are functions of the reduced dipole matrix elements only. All of the geometrical details remain in Equation 5.14. Note also that $\alpha_t = 0$ for $J_a = 0, 1/2$, and while it is not obvious from Equation 5.16, $\alpha_v = 0$ for $J_a = 0$. To find the AC stark shift for a state with J_a, the scalar, vector, and tensor polarizabilities can be calculated using Equations 5.15 - 5.17. The polarizability operator matrix for the relevant ij dimensions (determined by the electric field) can then be calculated with Equation 5.14 in the m_a subspace of J_a. In general, this matrix is not diagonal. Diagonalization yields the total polarizability for each m_a state in J_a and a given direction ij. By choosing the particular sub-level of interest together with the electric field $\vec{E}$, the AC-stark shift is determined by Equation 5.12.

In some cases, the polarizability matrix is already diagonal in the m basis for the important dimensions, leading to a straightforward AC stark shift calculation. For example, for light which is linearly polarized along the quantization axis, the AC stark shift is found to be (e. g. [220]):

$$U = -\frac{E_0^2}{4} \left[\alpha_s(\omega_L) + \alpha_t(\omega_L) \frac{3m_a^2 - J_a(J_a + 1)}{J_a(2J_a - 1)} \right] \tag{5.18}$$

On the other hand, circularly polarized light with the k-vector along the quantization axis has an AC stark shift given by (e. g. [221]):

$$U = -\frac{E_0^2}{4} \left[\alpha_s(\omega_L) + \frac{m_a}{2J_a} \xi \alpha_v(\omega_L) - \frac{3m_a^2 - J_a(J_a + 1)}{J_a(2J_a - 1)} \alpha_t(\omega_L) \right] \tag{5.19}$$

where $\xi = 2\gamma/(1 + \gamma^2) = \pm 1$ (circular polarization) and γ is the ellipticity parameter. References [220, 207] points out additional geometrical factors for the more general case where the linear polarization is at an angle to the quantization axis or the circularly-polarized k-vector is at angle relative the quantization axis [207]. Note that in Equations

5.13, 5.14, 5.18, and 5.19, F can replace J when the hyperfine structure energy also dominates the Stark shift. Equations relating $\alpha(J)$ to $\alpha(F)$ can be found in multiple references (e. g. [219, 220]).

For $J = 0$, the vector and tensor polarizabilities are zero. It can be seen that Equation 2.62 corresponds to the scalar polarizability. However, we remember that the Sr clock states are not perfectly $J = 0$ because of hyperfine interaction. This makes the calculation of the vector and tensor polarizability terms more complex. To be done properly, rather than using the polarizability operator (Equation 5.13) which originates from perturbation theory to second order in the electric field, the atom-light and hyperfine interaction can be treated simultaneously as a perturbation. A solution to third order (two orders in the electric field, and one order of hyperfine interaction) can yield the vector and tensor polarizabilities for $^3P_0$ [222]. This was done for the case of Yb. The magnetic dipole hyperfine interaction was seen to introduce only a non-zero vector polarizability, with the vector Stark shift given by:

$$U = \frac{E_0^2}{4}\xi\frac{m_F}{2F}\alpha_v(\omega_L) \tag{5.20}$$

It has been further seen that the electric quadrupole hyperfine interaction introduces at least a non-zero tensor polarizability [220]. Another approach to calculation of these effects may include the effective operator formalism [223].

To estimate the size of the vector and tensor polarizabilities, one may consider the effects of the hyperfine interaction on the polarizability. The first is that the higher-lying intermediate states coupling to the clock states exhibit hyperfine splitting. As the different clock state sublevels couple to these higher lying hyperfine split states, the polarizability of the individual sublevels differs by an amount scaling with the hyperfine splitting. A Taylor expansion of Equation 2.62 with the hyperfine splitting included leads to a correction term of order $\Delta_{hfs}/(\omega_{ak} - \omega_L)$. Dominated by the $^3S_1$ effect on $^3P_0$, this correction term is on the order of 10^{-4} [100]. The authors of [100] used the

hyperfine splitting to estimate the vector AC stark shift, finding it to be $< 10^{-4}$ of the scalar shift (< 10 Hz). The hyperfine interaction also mixes a small fraction of $^3P_1$ into $^3P_0$, which with $J = 1$ is much more sensitive to vector and Stark shifts. This admixture can also be used to approximate a further contribution to the vector and tensor shifts [222, 16].

For Sr clock operation using $\pm m_F$ spin-polarized samples, the vector and tensor shifts do not play a major limitation. This is partly because of their small estimated magnitude, but further because of the design of the interrogation. Optical confinement of the Sr atoms occurs at the "magic" wavelength where the polarizabilities of the two clock states are equal [100]. As seen above, the scalar Stark shift exhibits no m_F dependence, the vector shift exhibits linear m_F dependence, and the tensor shift exhibits quadratic m_F dependence. The opposite symmetries of the vector and tensor shifts facilitate orthogonalization of their effects experimentally. Because of the antisymmetric m_F-dependence of the vector shift, clock stabilization to the average of the $m_F = \pm 9/2$ transitions eliminates dependence of the clock frequency on the vector light shift, just as for the 1^{st} order Zeeman shift. Its effect would instead be observed as a change in the frequency separation between the two $\pm 9/2$ transitions added to the Zeeman splitting from the bias magnetic field. The averaged clock transition retains dependence on the symmetric tensor shift. However, the tensor shift simply adds a $|m_F|$-dependent offset to the much more dominant scalar term. Thus, for a given lattice polarization, each spin state has a well-defined magic wavelength for insensitive confinement. By experimentally ensuring that we operate at λ_{magic} for our given pair of nuclear spin states, we can safely eliminate the scalar, vector, and tensor shifts.

The lattice laser providing the atomic confinement is frequency stabilized to the optical frequency comb which itself is locked to the Sr clock laser. At a lattice peak intensity of $I_0 = 3$ kW/cm^2 and at the typical operating lattice laser frequency (368554.324 GHz), we observe a $6.5(5) \times 10^{-16}$ shift in the clock frequency compared to zero in-

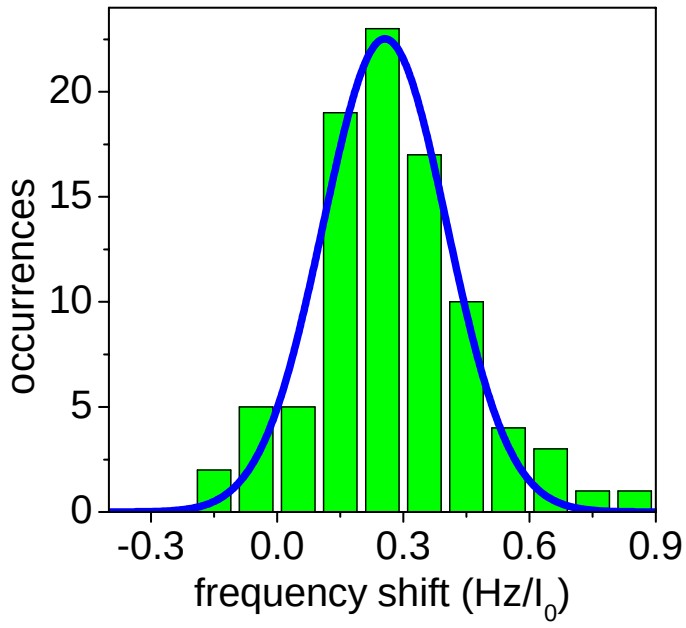

Figure 5.8: Histogram of the experimentally measured frequency shift sensitivity of the Sr clock transition due to the AC Stark shift from the lattice laser intensity. $I_0 = 3$ kW/cm^2.

Table 5.2: Experimentally measured values of λ_{magic}.

λ (nm)	Reference
813.420(7)	[29]
813.418(10)	[21]
813.428(1)	[143]
813.4283(12)	[22]
813.4274(4)	[23]

tensity (see Figure 5.10). Note that because of a non-zero density shift (see below), it is difficult to completely separate density related effects from measurement of the lattice Stark effects as the lattice intensity is changed. For example, as the lattice depth and thus trap frequency is reduced, the spatial extent of a given motional state increases (see Equation 2.33 and the surrounding equations). Assuming all other things remaining constant, this results in a density reduction (as the effective trap volume increases). However, a reduced lattice trap typically traps less atoms, and in many cases the trapped sample is colder. The reduced temperature corresponds to a smaller spatial extent of the wavefunction, partially counteracting a density reduction. We have typically observed a constant blue and red longitudinal sideband amplitude ratio while changing the lattice depth. In this case, the mean density scales with the square root of each trap frequency. With the added complexity that the electronic excitation depends on the confinement, a non-zero density shift can muddy the measurement waters of the lattice Stark shift. For this reason, it was useful to measure the lattice Stark shift below the highest achievable densities (reduced atom number). Nonetheless, a correction to the observed lattice Stark shift was included to account for the density change induced shift.

Combining this lattice Stark shift measurement with our previous measurement of the weak clock sensitivity to the lattice frequency (Figure 4.4), we extrapolate the magic lattice frequency to be 368,554.68(18) GHz, corresponding to a vacuum wavelength of 813.4274(4) nm. Table 5.2 shows the measured λ_{magic} values since high precision

interrogation of the $^1S_0$-$^3P_0$ transition in an optical lattice was begun. Although tensor shifts are estimated to be small, it should be remembered that the magic frequency we report here is specified for the π-transitions from the $m_F = \pm 9/2$ nuclear spin states.

Even though the total electric dipole polarizability contribution to the transition shift is cancelled to zero, the shift of each clock state is large (100 kHz). This large state shift motivates the question of how large the next order contribution is: the dipole hyperpolarizability (fourth order in E). The hyperpolarizability is somewhat complicated, with dependence on both one and two photon atomic resonances [222, 224]. For ^{87}Sr, one worrisome contributor to the hyperpolarizability is a two-photon transition $^3P_0$-$^3F_2$ which is 5 nm detuned from the λ_{magic} at 818.6 nm. This contribution has been experimentally investigated [143]. Furthermore, by probing the clock transition under very high lattice intensity, the authors of [143] made a measurement of the fourth-order Stark shift, finding a coefficient of $< 10(10)$ μHz$/E_r^2$. This experimental measurement is approximately an order of magnitude larger than theoretical calculations based on the calculated magic wavelength at 795 nm [136, 100]. For our operating conditions and based upon the experimentally determined shift coefficient, the shift is 2×10^{-17}, with the same uncertainty.

The Stark effect from higher order multipoles can provide additional shifts to the clock transition. The magnetic dipole (M1) and electric quadrupole (E2) polarizabilities are suppressed by at least the fine structure constant squared compared to the electric dipole polarizability [222, 100]. Numerical estimates put $\alpha_{M1} \simeq \alpha_{E2} \simeq 10^{-7}\alpha_{E1}$. These higher multipole contributions are particularly important in the standing wave of an optical lattice: the Stark shift spatial dependence from the higher-order multipole polarizability differs from that of the larger electric dipole polarizability and frustrates the existence of perfectly well-defined magic frequency for all multipoles [225].

Before leaving the lattice-induced Stark shift, it is worth mentioning that during the experimental measurement of the shift of the $m_F = \pm 9/2$ averaged clock transi-

tion, while varying the lattice intensity, we also observed a small (10^{-15}) change in the frequency separation between the $m_F = \pm 9/2$ transitions. As mentioned above, one possible explanation for this is the vector Stark shift. Unfortunately we have not yet had the opportunity to further investigate this observation. Other possible explanations include an inhomogeneous magnetic field which, as a varied lattice intensity changes the spatial confinement of the interrogated atoms, the atoms sample this field differently yielding a lattice-dependent 1^{st} order Zeeman shift. Furthermore, an m_F antisymmetric density shift could also play a role, due to unwanted density change as the lattice is varied. If the observed shift was assumed to be the vector Stark shift, knowledge of the stress-induced birefringence of the vacuum window would be important. This observation merits further investigation, particularly with well-controlled circularly polarized lattice light.

5.4.3 1^{st}- and 2^{nd}- order Zeeman shifts

As with the lattice vector Stark shift on the clock transition, the 1^{st} order Zeeman shift on the clock transition ($-108.4(4) \times m_F$ Hz/G [151]) is cancelled due to the antisymmetric linear dependence of the $\pm 9/2$ states on the magnetic field. To individually address spin states, we choose a bias field ($B_0 = 20$ μT $= 200$ mG) large enough to resolve π-transitions and reduce line pulling from residual populations of other spin states, but small enough to keep the spin-symmetric 2^{nd} order Zeeman shift small. The B-field is calibrated by measuring the frequency spacing between the two spin state transitions. To determine the 2^{nd}-order sensitivity and the 1^{st}-order insensitivity, we measure clock frequency shifts as a function of B. An example of one such measurement is shown in Figure 5.9(a). Each set of data is fit to a second-order polynomial. To extract the 2^{nd} order coefficient, we constrain the linear term to zero and perform the fit. To extract the 1^{st} order coefficient, we constrain the quadratic term to the well-established theoretical estimate. The fit parameters of many such sets of data are

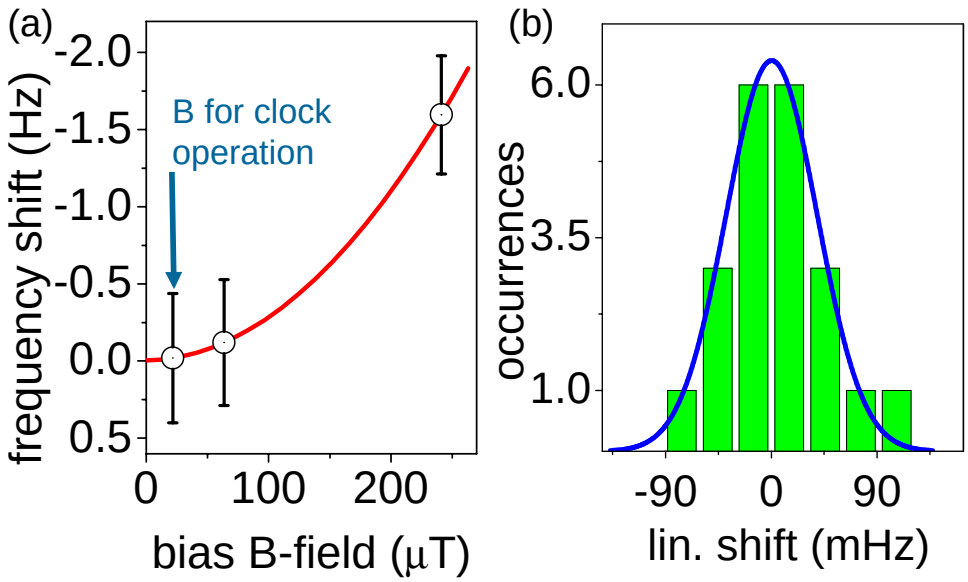

Figure 5.9: Experimentally measured frequency shift sensitivity of the Sr clock transition due to the Zeeman shift. (a) Measurement of the shift at three magnetic field values. The data is fit to a 2^{nd} order polynomial to extract the 1^{st} and 2^{nd} order Zeeman shift coefficient. (b) Histogram of the linear (1^{st} order) Zeeman shift coefficients. The mean, consistent with zero, indicates that the two-peak lock to the $m_F = \pm 9/2$ states effectively eliminates sensitivity to the linear Zeeman effect. A similar histogram for the quadratic term gives the 2^{nd} order Zeeman sensitivity.

averaged (see Figure 5.9(b)) and the 1^{st}-order shift is found to be $2(2) \times 10^{-17}$ (for B_0), consistent with zero. The second order shift is $2.3(2) \times 10^{-17}$ and the measured shift coefficient is $5.8(8) \times 10^{-8}$ T^{-2}, consistent with other measurements [26]. This number also agrees with previous theoretical calculations (e. g. [226, 151]). Note that this 2^{nd} order Zeeman shift is significantly smaller than that observed in Cs and other microwave standards [227]. This is in part because the Sr clock states, with $J = 0$, have no hyperfine structure and so the intermediate states contributing to this second order shift (principally $^3P_1$) have much larger atomic detuning (fine structure splitting) than the nearby hyperfine states in microwave standards. While the B-field was a dominant contributor in previous shift evaluations near zero field, note that the averaging technique of the $m_F = \pm 9/2$ transitions under a small bias field makes this shift uncertainty quite small, with room for further improvement.

5.4.4 Density shift

While an ensemble of neutral atoms enables large signal-to-noise measurements for high precision and stability, interactions among colliding atoms can result in frequency shifts that degrade the system accuracy. Density dependent collisional shifts play an important role in the operation of the highest accuracy Cs fountain standards (e. g. [7, 228, 229]). The reduced collisional interaction of cold Rb atoms is the principal motivation for the development of Rb fountain standards [230, 231]. For the case of lattice clocks, unity (or less)-filled sites in a 3-D lattice can keep atomic spacing to at least half an optical wavelength and thus reduce interatomic interactions [100, 232], keeping the expected density shift small. For the 1-D lattice, use of identical ^{87}Sr fermions at ultracold temperature can exploit the Pauli-exclusion principle to reduce interactions by eliminating even-wave collisions [233, 234]. If the atomic sample is sufficiently cold, the lowest odd-wave (p-wave) collisions are frozen out. With the s-wave collisions remaining forbidden by the Pauli exclusion principle, the density shift could

be very small even at high ultracold densities. Because of this property, fermions have been anticipated as good candidates for atomic frequency standards. Pauli-blocking resulting in the absence of collisional frequency shifts has been observed experimentally at high densities for RF transitions [234, 235].

In the experimental situation described for our normal clock operation, although only one nuclear spin state is interrogated at a given time, the presence of a second spin state in the ground electronic state means that the atomic sample is not composed of identical fermions. Collisions between identical spin states would presumably be suppressed, while collisions with the secondary spectator spin state would not be. With or without Pauli-suppression and the presence of a second spin state, the details of the resulting density shifts require knowledge of the interatomic potentials. Ground ($^1S_0$-$^1S_0$) and excited ($^3P_0$-$^3P_0$) state inter-atomic potentials have been theoretically calculated [236, 237], but the only experimental measurements exist in photoassociation spectroscopy of the even isotopes of Sr [238] pertaining to ground state interactions.

Our previous investigations of unpolarized, nuclear-spin-degenerate ^{87}Sr revealed no indication of collision related frequency shifts. Using the high measurement precision afforded by the optical-optical comparison, we now observe a non-zero density-dependent frequency shift in our doubly-spin-polarized sample. This measurement was made using a fixed lattice environment, and observing clock transition shifts as the number of trapped atoms was varied. Typically, low atom numbers were achieved by removing a loading mechanism on the $^1S_0$-$^1P_1$ MOT, either the Zeeman slower or the atomic beam transverse cooling. As discussed below, the measured frequency shift value depends on a number of details including the excitation fraction and the nuclear spin state. By proper control of these parameters ($\rho_0 = 1 \times 10^{11}$ cm^{-3}, $m_F = \pm 9/2$, excitation fraction $\sim 16\%$), we are able to measure and control this shift to $8.9(8) \times 10^{-16}$ (see Figure 5.10).

As a result of the shift dependence on several experimental details, further control

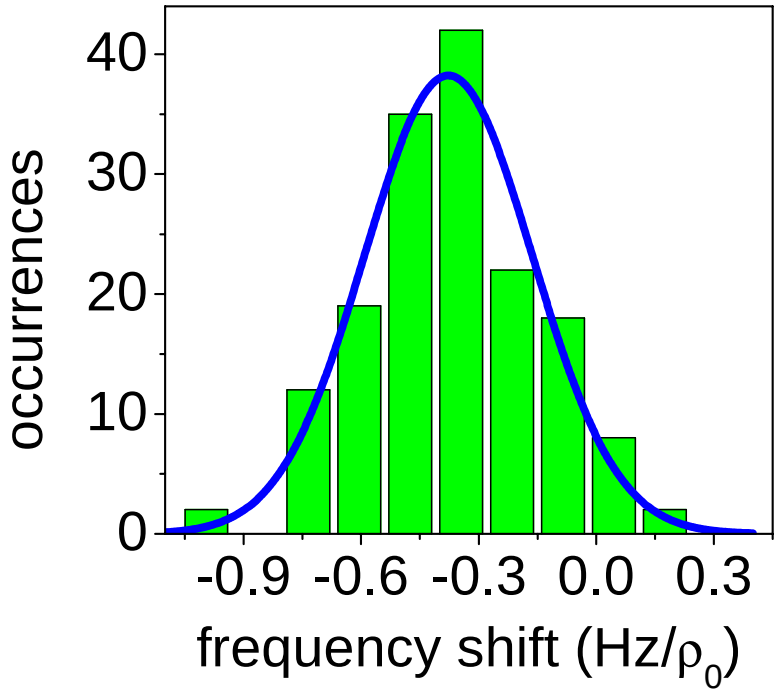

Figure 5.10: Experimentally measured frequency sensitivity of the Sr clock transition to the atomic density. $\rho_0 = 1 \times 10^{11}$ cm^{-3}. These measurements were made by varying the atom number loaded into a fixed lattice environment.

or characterization of the density shift requires a quantitative understanding of the relevant collision mechanisms yielding the shift. Study of these ultracold collisions [239] can yield important interaction details relevant both to Sr and more broadly to other systems, and are worthwhile in their own right. Furthermore, understanding these effects can be useful for quantum information applications such as quantum simulation or multi-particle entanglement for universal quantum logic gates (e. g. [240, 241, 242, 243, 244, 245]), which try to exploit atomic collisions. To this end, we utilized the ^{87}Sr frequency standard as a sensitive tool for studying interatomic collisions by measuring their corresponding density-dependent shifts under different conditions.

At sufficiently cold temperatures, where higher-order partial waves are frozen out due to their centrifugal barrier, the collision process of two particles can be described by their dominant s-wave interaction. Here we consider only two body collisions. In this case, the interaction strength, which depends upon the internal state of each atom, can be characterized by a single parameter, the s-wave scattering length. For two-level atoms, the transition frequency shift due to cold collisions can be derived by application of the quantum Boltzmann equation [246, 247] or by consideration of the mean field interaction [248, 249, 250], and is found to be:

$$\Delta\nu_{12} = \frac{2\hbar n}{m}\left[g_{22}a_{22}\rho_{22} - g_{11}a_{11}\rho_{11} + (\rho_{11} - \rho_{22})g_{12}a_{12}\right] \tag{5.21}$$

Here m is the atomic mass, a_{xy} is the scattering length describing collisions between particles in the x and the y internal states, ρ_{11} (ρ_{22}) is the ground (excited) state population fraction, and n is the atomic density. g_{xy} is the two particle correlation function at zero separation and is given by the wavefunction overlap integrals:

$$g_{xy} = \frac{\langle\Psi_x^\dagger\Psi_y^\dagger\Psi_x\Psi_y\rangle}{\langle\Psi_x^\dagger\Psi_x\rangle\langle\Psi_y^\dagger\Psi_y\rangle} \tag{5.22}$$

The value of the g_{xx} correlation function can be neatly divided into four cases: (1) for two identical bosons in a thermal gas, $g_{xx} = 2$ (2) for two atoms in a Bose-Einstein

Condensate (BEC), $g_{xx} = 1$ (3) for two distinguishable particles, $g_{xx} = 1$ (4) for two identical fermions, $g_{xx} = 0$. In the case of excited state population originating from coherent excitation from the ground state (or vice versa), then the spatial correlations are transferred between the atomic states and $g_{11} = g_{22} = g_{12} = g$ [249, 248]. In this case, the density shift can be simplified to:

$$\Delta\nu_{12} = \frac{2\hbar n}{m} g \left[a_{22}\rho_{22} - a_{11}\rho_{11} + (\rho_{11} - \rho_{22})a_{12}\right] \tag{5.23}$$

In general, the scattering lengths a can be positive (attractive) or negative (repulsive), and the density shift depends on the excitation fraction. We have assumed sufficiently cold temperature that s-waves dominate. Sometimes referred to as the Wigner threshold regime, s-waves dominate with the condition $a/\lambda_T \ll 1$, where a is the largest relevant scattering length, and $\lambda_T = h(2\pi m k_b T)^{-1/2}$ is the thermal deBroglie wavelength [239, 250]. Note that when the deBroglie wavelength exceeds the scattering length, the quantum statistics of the particles influence the scattering properties (through g, the two-particle correlation function). For this reason, $a/\lambda_T \ll 1$ is also the condition for quantum scattering effects [251, 239, 250]. In general, this condition is easier met than the quantum degeneracy condition requiring the "average" particle spacing to be smaller than the deBroglie wavelength [251, 250].

From Equation 5.23, the benefit of identical fermions is clear - they do not interact and no collisional shift is present. If we take the s-wave collisions of identical fermions to be identically zero, then we must consider the residual effects from the next higher order wave, the p-wave. The shift resulting from p-wave interactions takes on a form similar to Equation 5.23 and is given by [252]:

$$\Delta\nu_{12} = \frac{\pi\hbar n}{m}\langle k_T^2\rangle \left[v_{22}\rho_{22} - v_{11}\rho_{11} + (\rho_{11} - \rho_{22})v_{12}\right] \tag{5.24}$$

Here v_{xy} is the p-wave scattering volume given by $v_{xy} = (a_{xy}^{\mathrm{p-wave}})^3$ and $\hbar^2\langle k_T^2\rangle/m$ is the average collision energy.

With these basic models in place, to better clarify the role of dual spin states in our observed density-dependent clock shift, we operate the clock with a single spin state. This was done by replacing the dual-spin-state preparation by optical pumping yielding a single spin state only (see Sections 2.7 and 5.1). The remaining operational conditions were left the same. Before giving the results of these shift measurements, I first describe two important experimental details. Unlike Ramsey spectroscopy with long dark times and short $\pi/2$-pulses, typically used in microwave standards, during the Sr Rabi spectroscopy, the ground and excited state populations are changing during the collision process. This is an extra complication beyond the measurements demonstrated in Cs [229], where the density shift is measured as a function of the excited state fraction during the Ramsey dark time. In our case, the population evolution during collisions make the resulting density shift a non-linear function of the excitation after the Rabi pulse. In other words, in a simple picture, the density shift in Equation 5.23 or 5.24 should include time dependent populations $\rho_{11}(t)$ and $\rho_{22}(t)$ which must be integrated over the Rabi pulse to determine the resulting shift.

Furthermore, as eluded to in Section 2.6.5, the population does not evolve as simple Rabi flopping. Instead, weak transverse confinement outside of the Lamb-Dicke regime results in motional-state-dependent dipole couplings. Unfortunately, the probe laser has a small k-vector component along the transverse direction, exciting the atom along this weak confinement axis. This is due not only to technical limitations (imperfect overlap of the lattice and probe beams and their foci), but a fundamental reason as well. At the probe and lattice foci, the Heisenberg uncertainty principle dictates that the finite beam waist yields a spread in k-vectors (at the waist). This has been observed in a variety of Bragg scattering measurements (e. g. [253]). Although our probe beam focus is designed to be relatively large ($\sim$ 100 μm) to homogeneously probe the transverse spatial extent of the trapped atoms, the lattice focus is much tighter (original diffraction limited design radius of 20 μm, measurement of the trap frequencies typically indicated a

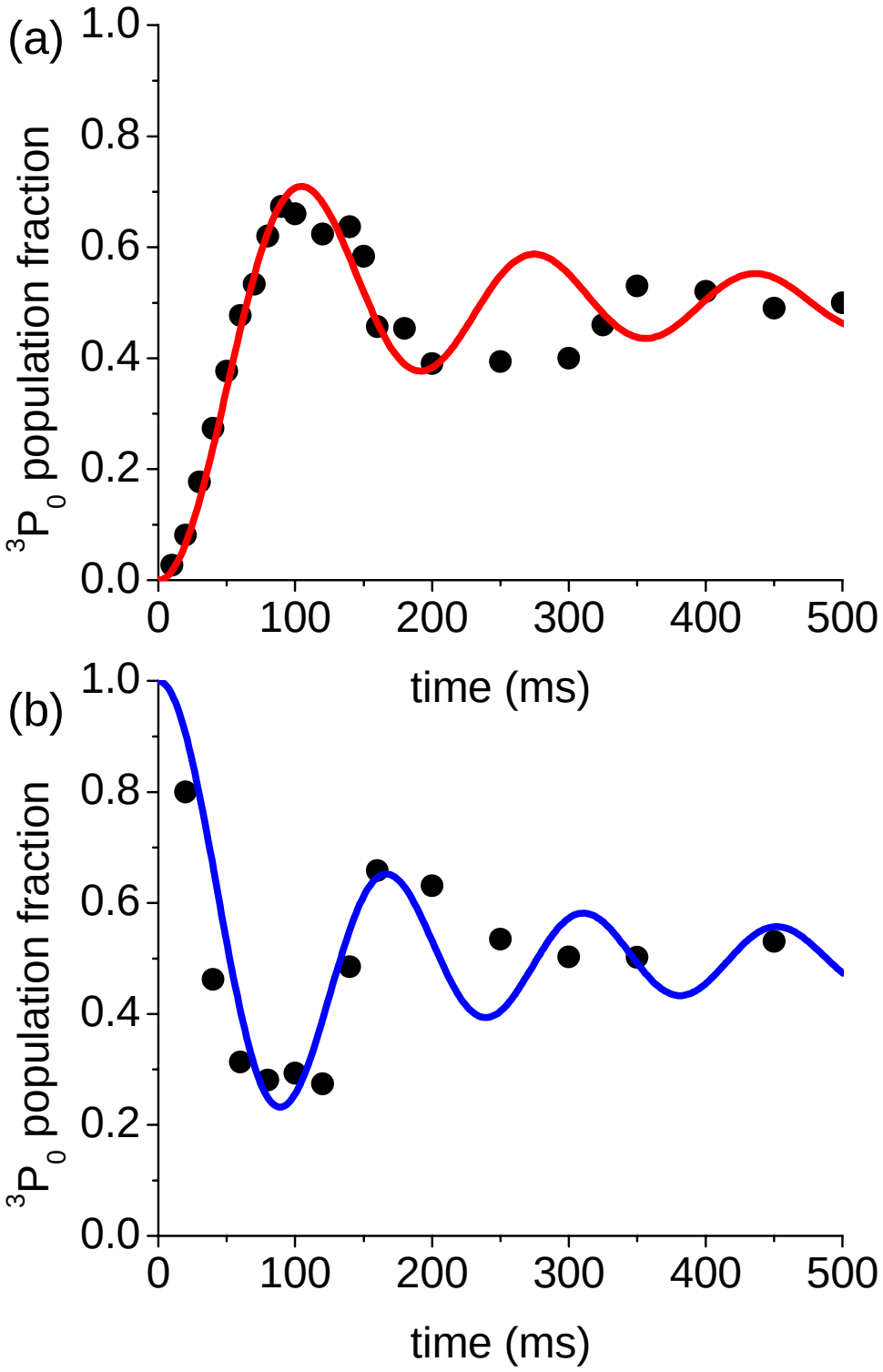

Figure 5.11: Atomic excitation as a function of time with Rabi frequencies similar to those used for clock operation. (a) Excitation of a single spin state ($m_F = 9/2$) starting in the ground state $^1S_0$ (b) De-excitation of a single spin state starting in $^3P_0$, as described in the text. In both cases, the measured excitation is shown by black circles, and the theoretical fits based on Rabi inhomogeneity from dephasing among different motional states are shown as solid curves. The model matches the data very well for at least one full Rabi cycle, but is less reliable on the second. When these measurements are made with much higher Rabi frequencies, the fit matches over many more cycles.

65 μm radius, although recent improvements indicate a radius of 35 μm). The relative k-vector alignment of the lattice and probe determine the transverse excitation component. The k-vector uncertainty due to small lattice beam focus leads to an rms probe-lattice misalignment as large as a several mrad. This inhomogeneous excitation of the atomic sample among transverse motional states (in dramatic case, see Figure 2.16) leads to dephasing of the Rabi flopping process, exhibiting an excitation damping. Experimental measurement of the excitation ($^3P_0$) as a function of time as well a theoretical estimate based upon this Rabi inhomogeneity from misalignment is shown in Figure 5.11(a). Here, I have assumed a Rabi inhomogeneity taking into account a residual k-vector component along one transverse dimension (here a generous 8 mrad). A more realistic 3-D treatment increases the Rabi dephasing, so that less misalignment is required to achieve the same damping. Note that at long enough times, t, the Rabi contrast revives in the calculation.

With these details in mind, Figure 5.12 shows the observed density shift as a function of the final excitation fraction (after the Rabi pulse) for the single spin state (red squares) described above. These measurements were taken using the typical lock to the atomic transition and looking for shifts relative to Ca. In order to change the final excitation fraction, the modulation depth of the lock to the atomic transition was changed, i. e. the symmetrically-probed detuning on either side of transition center was changed (small detuning for higher excitation). Because of the Rabi contrast reduction, as well as the need to lock at a detuning large enough from the line center so that the laser sampled a monotonic discriminator, the density shift at high final excitation could not be probed. For this reason, we took a second set of data under different initial conditions. After double spin polarization to the $m_F = \pm 9/2$ states, a strong clock pulse was applied under bias B-field with the purpose of pumping a single spin state of $^1S_0$ into $^3P_0$ (the pulse was strong to excite the atoms with less frequency sensitivity). At this point, the 461 nm laser was applied to cycle the $^1S_0$-$^1P_1$ transition and heat away

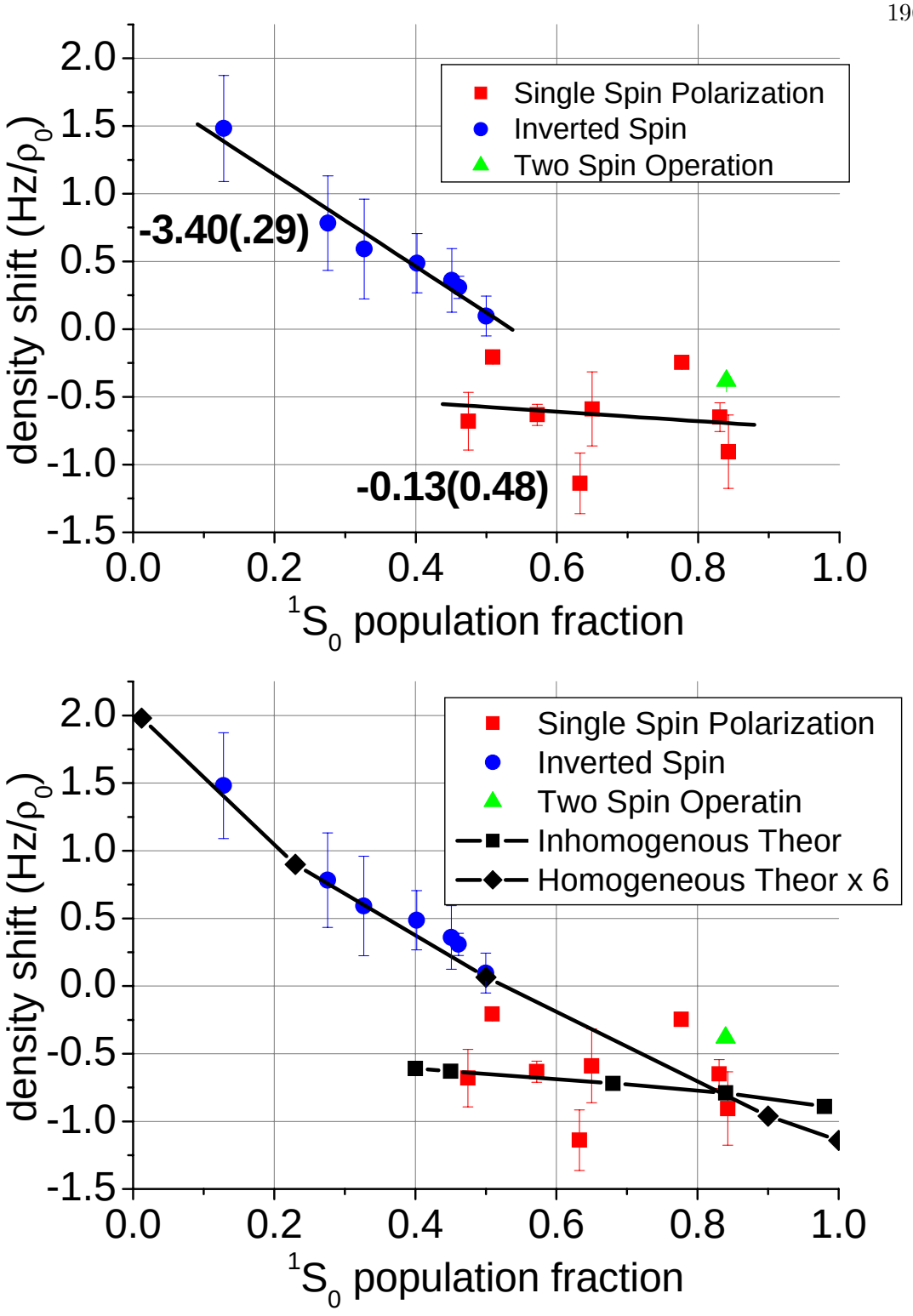

Figure 5.12: Measured density shift sensitivity as a function of ground state $^1S_0$ population. Probing time $t_p = 80$ ms. Red squares: A single nuclear spin state starting from $^1S_0$. Blue circles: A single nuclear spin state starting from $^3P_0$, as described in the text. Green triangle: Normal clock operational conditions with double spin polarization ($m_F = \pm 9/2$). (a) includes linear fits to the data, with slope and uncertainty indicated, while (b) includes theoretical models of the density shift, for the cases of homogeneous and inhomogeneous Rabi excitation.

the remaining $^1S_0$ population, including all of the other nuclear spin states originally present. Done directly before spectroscopy, this gave a sample of $^3P_0$ atoms with a single spin state and somewhat different motional state distribution than prior to the optical pumping (due to Rabi inhomogeneity). Standard spectroscopy was then performed on this inverted population. This was alternatively done for one spin state and then the other, so that the atomic lock operated on the average of the $\pm m_F$ transition. The time dependent excitation is shown in Figure 5.11(b), along with the theoretical fit based on Rabi inhomogeneity. The measured density shift for this case, again as a function of final excitation fraction, is shown in Figure 5.12 as blue circles, along with a linear fit to guide the eye. Also shown is the measurement corresponding to traditional clock operation with both spin states present (green triangle).

The first item to note from Figure 5.12 is that a density shift remains for the case of only one spin state during spectroscopy (either red squares or blue circles). The origin of this shift seems likely to be from one or both of two mechanisms. The first is p-wave interactions. As stated above, p-wave collisions freeze out at cold temperatures due to the centrifugal barrier. Based on the theoretical ground and excited state potentials, the threshold for freezing out p-wave interactions is ~ 30 μK, substantially warmer than $2-3$ μK sample temperature. Below the p-wave threshold, the p-wave collision cross section scales as $\sigma_p/\sigma_s \propto (k_T a)^4$ where $k_T = 2\pi/\lambda_T$ is the wavenumber corresponding to the relative thermal collision energy [251]. This yields more than 100 fold reduction in p-wave collision cross section. Based upon the experimentally determined scattering lengths for ^{88}Sr and ^{86}Sr [238], an isotope mass scaling gives an s-wave scattering length estimate of $a_{11} \simeq 4.3$ nm [252] for ^{87}Sr. This implies that the ultracold Sr collides in the Wigner-threshold regime. The size of the observed shift, if accounted for by p-wave interactions, would require a p-wave scattering length of many nanometers.

Another possible explanation is that the single spin state ^{87}Sr atoms are not identical fermions and that s-wave collisions occur. Indistinguishability originates from

the internal wavefunction of the atom (identical set of quantum numbers for the internal degrees of freedom). Because of the motional state dependent Rabi excitation, atoms within one lattice site evolve as different superpositions of clock electronic states, and are therefore not identical. Neither are they perfectly distinguishable, as the superposition of each atom is not orthogonal to the others. In this sense, collisions between the ^{87}Sr atoms could be described by the time dependent Equation 5.23 with a time-dependent, effective correlation function $g(t)_{eff}$ with a value between 0 (perfectly indistinguishable) and 1 (perfectly distinguishable). This would result in partial, but not complete, s-wave collision suppression. This is in dramatic contrast to the experimental results of [234, 235], where atoms were excited uniformly as the interrogation was made far in the Lamb-Dicke regime for the RF transition being probed.

Another interesting result seen in Figure 5.12 is the remarkable difference between the two single spin cases in the slope of the density shift as a function of excitation fraction. The first case, with an initial $^1S_0$ ground state population, has much weaker dependence than the atoms starting from $^3P_0$. I mentioned one difference in this latter case is that "pumping" the population to $^3P_0$ before spectroscopy favors some motional states as a consequence of the Rabi inhomogeneity. This can lead to a decrease in the inhomogeneity and thus reduced dephasing of the excitation in time. While not dramatic, comparison of Figures 5.11(a) and 5.11(b) show that, in fact, the latter case shows higher Rabi contrast. This was coarsely estimated in the theoretical fit with a slightly colder sample temperature of 2 μK. Note that to rule out effects from differences in the atomic samples from the two-spin an one-spin polarization techniques (using optical pumping along different lattice axes), a single spin state was prepared and then pumped to $^3P_0$. Spectroscopy was then performed on this inverted population. One of the blue circles in Figure 5.11 is actually this case, indicating that the difference between blue circles and red squares was not the spin-state polarization prior to spectroscopy.

Assuming p-wave interactions, to model these effects we use the time dependent

version of Equation 5.24 and calculate the density shift as a function of final excitation fraction. To match the experimental conditions, the different excitation fractions correspond to different detunings from the line center. Different degrees of dephasing due to Rabi inhomogeneity are allowed for the two single spin state cases. For simplicity, we assume $v_{12} = 0$. Unfortunately, because of the huge difference in slopes for the two cases plotted in Figure 5.12(a), no ratio of v_{22}/v_{11} was found that can fit the two data curves, despite the difference in population evolution between the two cases (as shown in Figure 5.11). Instead, a good fit was found by taking $v_{22}/v_{11} \simeq .55$ and allowing v_{11} to be six times larger for the inverted population case than for the case of excitation from the ground state. Furthermore, while single ground spin state excitation was assumed to have a Rabi inhomogeneity as seen in Figure 5.11(a), for the inverted population case it was necessary to assume a homogeneous Rabi evolution (more homogenous than that shown in Figure 5.11(b)). Results of this calculation are shown in Figure 5.12(b). For the inverted population case, the data indicates $a_{11}^{\mathrm{p-wave}} \simeq 20$ nm, and six times smaller for the other case.

It is necessary to consider the qualitative motivations for the above described fit model. For the inverted population case, it is seems from Figure 5.11(b) that the population evolution implies a more homogeneous Rabi excitation than other case. However, it is not obvious to justify more dramatic homogeneity than that implied in Figure 5.11(b), other than to say that the optical pumping which creates the inverted population does not necessarily preserve a simple Boltzmann distribution among motional states (which is assumed in the theoretical fit of Figure 5.11(b)). With the resulting shift coming from an integrated population, a more careful analysis of the actual time dependent population for the motional states occupied in the inverted population case would be useful.

Another possible effect of the Rabi inhomogeneity is particle distinguishability allowing s-wave collisions. One would expect that in the more homogenous case, the

distinguishability would be smaller, reducing the s-wave collision. We see a much larger effect for the inverted case, thought to be more homogeneous. One possible explanation for this is that the s and p-wave interactions have opposite sign, so that the addition of s-waves in the case of evolution from the ground state partly cancels the purer p-wave effect observed in the inverted population case. If this were the case, however, it would imply that the mass-scaled approximation of the s-wave scattering length for ^{87}Sr, $a_{11} \simeq 4$ nm, is underestimated. Note also that it is sometimes difficult to experimentally determine the absolute density of a cold atomic sample, which scales the scattering lengths. While several methods were used here and yielded similar results, it would be worthwhile to make a direct optical absorption measurement to confirm the absolute density. With the rather complex experimental conditions during the density shift measurement (motional state inhomogeneity, time dependent populations), many details remain unanswered. However the data shown in Figure 5.11 gives many hints at the underlying physics. We are currently considering the quantitative effect of distinguishability. Furthermore, we are exploring sideband cooling of the atomic sample to observe the temperature dependence of the density shift (e. g. Equation 5.24). Unfortunately, temperature also influences the Rabi inhomogeneity among motional states. Two changes to the current experiment which would simplify analysis include two pulse Rabi spectroscopy (with short pulses, population is fixed during collisions) and cooling to a single motional state (eliminate inhomogeneity) in the longitudinal and transverse directions.

One very important result shown in Figure 5.12 is the existence of a zero crossing in the density shift [229, 233], for the inverted population case. While it is highly interesting to use the remarkable precision of the Sr standard as a tool to explore the atomic interaction physics, for clock operation we prefer as small a density shift as possible. The presence of a zero crossing implies that the current density shift uncertainties may be substantially reduced with further investigation. For the case of a 3-D lattice with unity or less filled sites, collisions are suppressed by atomic confinement.

The density shift in the 1-D lattice case gives insight into requirements for the 3-D lattice case. The 3-D lattice also enjoys much more uniform atomic excitation, since all three dimensions are strongly confined in the Lamb-Dicke regime.

Before leaving the topic of density related effects, we also considered the dependence of the collision interaction strength on spin state m_F (e. g. [247]). As a simple probe of the m_F dependence, we measured the frequency shift as the density of an unpolarized ^{87}Sr sample was varied (with roughly equal population in the ten m_F levels). We first did this under a bias magnetic field (B = 470 mG). In this scenario, we still addressed individual $m_F = \pm 9/2$ nuclear spin states spectroscopically, so that only one nuclear spin state was excited at a time ($m_F = 9/2$ or $-9/2$) to $^3P_0$. This constrained $^3P_0$-$^3P_0$ interactions to a single spin state, but allowed all spin combinations of $^1S_0$-$^1S_0$ interactions as well as many possible $^1S_0$-$^3P_0$ interactions. This yielded a density-dependent shift similar to, but slightly smaller, than the polarized case. Even more dramatic, we probed an unpolarized sample around zero B-field, so that transitions from all spin transitions were degenerate. This was similar to the experimental conditions during our previous evaluations of the density shift (see Section 4.3 [22, 21]), except that we the lock the clock laser to the atomic transition rather than tracing across the line and fitting the center. In this case, all combinations of allowed $^1S_0$-$^1S_0$, $^1S_0$-$^3P_0$, and $^3P_0$-$^3P_0$ collisions from the different spin states were present, as all spin states experienced some excitation. In this case, we observed a density shift 2-3 times smaller (for the same total density) than the polarized case (also smaller than the polarized case at zero B-field). Although the large number of spin states and possible interactions makes this measurement difficult to interpret quantitatively, the reduced shift indicated that smaller interaction strengths may exist for spin states besides $m_F = \pm 9/2$. Further investigation of individual spin state interactions is another avenue worthy of consideration in an effort to reduce the observed density dependent shift.

5.4.5 Blackbody radiation induced Stark shift

The room temperature black body radiation (BBR) field induces a Stark shift on the clock states. This can be found from Equations 2.62 and 2.63, except one must integrate over the BBR spectral density (e. g. [254]):

$$\Delta\omega_a = -\frac{1}{6\pi^2\epsilon_0\hbar c^3}\left(\frac{kT}{\hbar}\right)^3 \sum_{b,i} |\langle b|d_i|a\rangle|^2 \int_0^\infty dx \frac{x^3}{e^x-1}\left(\frac{1}{y_b+x}+\frac{1}{y_b-x}\right) \tag{5.25}$$

where $x = \hbar\omega_{BBR}/kT$ and $y_b = \hbar\omega_{ab}/kT$, T is the temperature of the blackbody environment, and ω_{BBR} is the blackbody radiation frequency being integrated over. In Section 2.6.2, we calculated the dipole polarizability and discussed the importance of continuum contributions for the $^3P_0$ state, particularly near long wavelengths where the BBR distribution is peaked. The highest accuracy calculation of the BBR shift considers both bound- and continuum-state contributions, dynamical corrections to the static polarizability, and higher-order multipole contributions [20]. With higher order multipole contributions found to be smaller than the present uncertainty in the dipole contributions, the BBR shift was expressed as:

$$\Delta\omega_a = -\frac{2}{15}(\alpha_{fs}\pi)^3 T^4 \alpha_a^{E1}(0)\,(1+\eta) \tag{5.26}$$

where α_{fs} is the fine structure constant, $\alpha_a^{E1}(0)$ is the static dipole polarizability, and η is a dynamic correction term accounting for the fact that the BBR Stark interaction is not exactly static. Using an ab initio, many body perturbation calculation (with a link to experimental data) the static polarizabilities were found to be $\alpha_{^1S_0} = 197.2(2)$ au and $\alpha_{^3P_0} = 458.3(3.6)$ au [20]. At $T = 23^oC$, the BBR shift for our Sr clock is 2.24 Hz, a fractional frequency of 5.21×10^{-15}. The uncertainty of this shift is 7×10^{-17}, originating from uncertainty in the differential polarizability for the clock states (1%). Further experimental uncertainty in the BBR shift originates from lack of control and homogeneity of the blackbody environment (at room temperature, T). By monitoring the temperature of many positions on the Sr vacuum chamber, we determine

the blackbody environment to $T \simeq 1$ K (rms), leading to a shift uncertainty of 7.5×10^{-17}. Combining the two effects yields a 1×10^{-16} total BBR uncertainty. Note that although the atomic oven nozzle is kept at 850 ^{o}C, it is far removed from the atoms and mostly shielded by the atomic collimator at all times. Furthermore, during spectroscopy, a mechanical shutter blocks the atomic beam altogether, also blocking the BBR line of sight from the oven. The long vacuum tube for the atomic beam contacts several different water cooling blocks to maintain cool temperature. Also, approximately 15 cm from the atoms is a heated sapphire window (200 ^{o}C, to prevent Sr corrosion from the incident atomic beam) which contributes at total BBR shift of $< 2 \times 10^{-17}$.

To further improve the Sr accuracy, the differential static polarizability of the clock states must be known to better than 1% (with the dynamical correction η contributing $< 5\%$ to the total shift). Such a measurement could be approached from several angles. One technique is to measure the static polarizability directly by observing a clock shift as a well-controlled DC electric field is applied to the atoms [134]. Another is to constrain the static polarizability value with knowledge of the dynamic polarizability. From Equation 5.25, it is found that more than five dipole couplings contribute to the $^3P_0$ BBR shift above the 1% level ($5s4d\ ^3D_1$, $5p^2\ ^3P_1$, $5s5d\ ^3D_1$, $5s6s\ ^3S_1$, $5s6d\ ^3D_1$, and the sum of the higher-lying/continuum contributions). The influence of so many levels complicates an accurate extrapolation of the dynamic polarizability to DC, and would require improved experimental data for the dipole coupling strengths. Measuring the dynamic polarizability with lasers at longer, BBR-like wavelengths could be more effective (particulary at several different λ), as the uncertainties needed for extrapolation are more reasonable. A polarizability measurement at a long wavelength combined with an improved lifetime measurement from the dominant shift state $5s4d^3D_1$ (currently known at the 10% level experimentally) could also further constrain the polarizability important for BBR. Such measurements might benefit from nearby well-known atomic transitions that could be used to self-calibrate the optical

field strength (e. g. using the measured Stark shift), or from other methods [255]. To improve upon the 1% uncertainty, any measurement will require careful design.

Another measurement approach is to measure the BBR shift directly by enclosing the atoms in a well-characterized blackbody environment and recording the clock shift as the environment temperature is systematically varied (such an approach would simultaneously decrease the shift uncertainty due to the BBR environment). The technical challenge lies in the control of temperature homogeneity over various functional areas of the vacuum chamber while accommodating sufficient optical access for a variety of atomic manipulations. Without active temperature control, we measure temperature differences between different areas of the vacuum chamber surrounding the Sr of ~ 1 K (rms). Furthermore, at the highest clock accuracy level, it is important to account for the effect of the transmissivity of glass viewports for visible and infrared wavelengths on the blackbody environment. For example, as a rough estimate, if we model the BBR environment for wavelengths above $\lambda = 4$ μm to be for $T = 300$ K (the chamber temperature), whereas for below $\lambda = 4$ μm, the transmissivity of the vacuum windows allow the atoms to sample the room BBR field (let's say at 293 K), then the BBR induced shift is ~ 1 part per thousand (ppt) different than for the pure $T = 300$ K environment. This represents a substantial difference in the BBR shift relative to a goal of 10^{-18} clock operation. Ray-tracing Monte-Carlo algorithms can be used to accurately determine the effective emissivity of a particular cavity geometry and material at different λ (e. g. [256]), and may become important for these measurements.

Perhaps a much cleaner and workable solution is to cool and trap atoms in a standard chamber, and then transport them in a moving lattice [257, 258] to a secondary BBR chamber, where an ideal, well-defined blackbody environment is established (see Figure 5.13). The small chamber needs accurate temperature control at the 10 mK level and would require the use of only small, far-removed optical access to introduce the optical lattice and probe beams. With the appropriate geometry, the effective black-

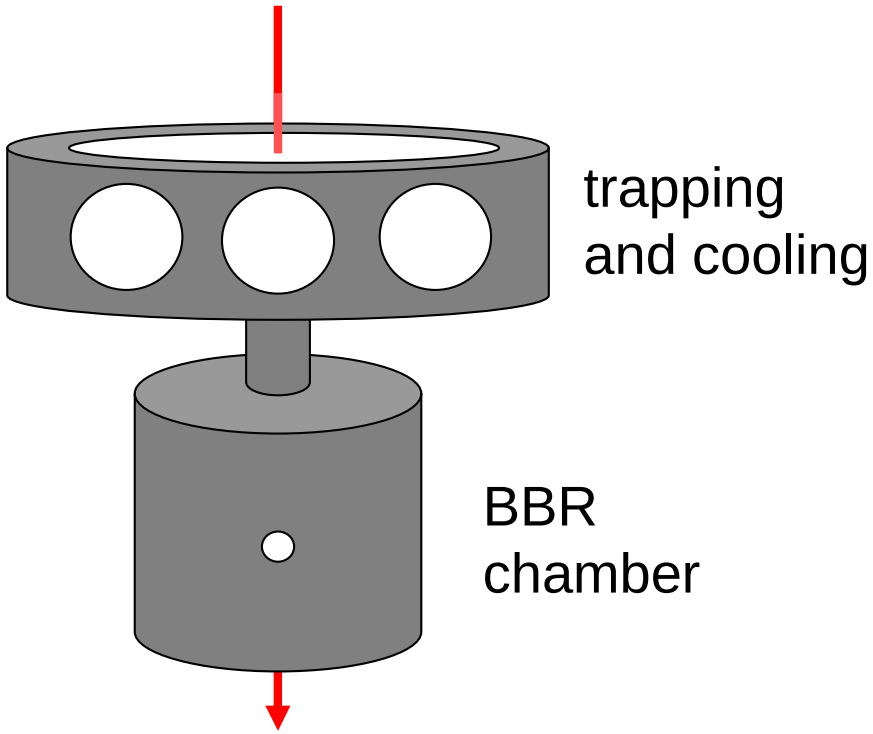

Figure 5.13: One approach to measuring and controlling the BBR shift in Sr at an improved level. The atoms are cooled and trapped in the traditional vacuum chamber with sufficient optical access for atomic manipulation. Once loaded into the lattice, the atoms are transported by the lattice to a secondary chamber, a BBR cavity. This small BBR chamber has excellent and accurate temperature control. Furthermore, there is limited optical access, so that viewport transmission of the room blackbody field (in the NIR and optical region) has limited effect on the internal blackbody environment. In other words, the geometry is well-suited for maintaining an effective emissivity extremely close to unity. Here the atoms are probed spectroscopically and measured. The BBR induced AC Stark shift is directly measured by systematically changed the well-controlled chamber temperature.

body emissivity of the interior can reach nearly unity and the total BBR environment can be known at the 1×10^{-4} level, necessary for 10^{-18} clock uncertainty. The accurately controlled temperature of this BBR chamber could then be systematically varied to measure the induced BBR shift, and determine the polarizability with reduced uncertainty. Such an approach avoids the complexity of cryogenic operation and can be generalized to other lattice clock species. These improvements can potentially reduce the BBR-related uncertainty to far below 10^{-16}. Note that sizeable BBR shifts in many atomic standards has motivated pursuing atomic species with a reduced BBR sensitivity, including lattice trapped neutral Hg [32, 33] and the single trapped Al^+ ion [255, 259].

5.4.6 Probe laser induced AC Stark shift

The two clock states have different polarizabilities at the clock transition frequency (see Figure 2.13). Consequently, the clock probe laser introduces a minute AC Stark shift. In other words, the atom is only approximately a two-level system, and coupling of the clock levels to outside levels allows for a probe induced Stark shift. The small detuning of the probe laser from couplings to other motional states can lead to such shifts, but this effect is much smaller than coupling to other electronic states. As discussed previously, imperfect alignment between the probe and the lattice axes leads to degradation in the transverse Lamb-Dicke condition and necessitates an increased probe power to excite the clock transition. By strongly saturating the transition with excess probe intensity, we measure a non-zero shift. Determining the laser intensity using the measured power and beam waist, the measured shift is consistent with the dynamic polarizabilities at 698 nm. By scaling to the intensity value typically used for clock operation, the shift is found to be $2(1) \times 10^{-17}$. More careful probe alignment, interrogation in a 3-D lattice (stronger confinement along all axes), and longer probe times can further decrease the required probe power and the resulting shift.

5.4.7 Line-pulling

Quantum confinement in the well-resolved-sideband limit means that Doppler effects are manifested in the sideband structure which can be isolated from the clock transition. These effects are further reduced in the Lamb-Dicke regime where photon recoil is transferred to the optical potential and the sidebands are suppressed. However, off-resonant, weakly excited motional transitions can pull the center frequency of the clock transition. More relevant is line-pulling originating from transitions of other spin states with residual populations after imperfect atomic polarization (typically $< 5\%$). Fortunately, many such effects largely occur in a (m_F) symmetric fashion such that the line-pulling, already small, is reduced. Furthermore, the 20 μT bias B-field separates excitation of neighboring spin states by more than two linewidths. The overall line-pulling effect is conservatively estimated to be $< 2 \times 10^{-17}$.

5.4.8 Servo Error

Servo errors in steering the clock laser to the atomic transition can also result in frequency offsets. Our digital servo operates via standard modulation techniques by probing the half maxima of the resonance. Noise processes around the modulation frequency, round-off error, and an asymmetric probe laser power spectrum are potential contributors to the servo error (e. g. [260, 261]). In our system, we are mostly concerned with residual laser drifts and finite loop gain. As described in Section 5.1.2, we typically implement a linear feed-forward frequency compensation for drift of the stable cavity to which the clock laser is locked. This feed-forward value is estimated by measuring the laser drift relative to the NIST H-maser via the frequency comb. To overcome imperfect feed-forward compensation, we utilize two integration stages in the laser-atom feedback loop. Operating properly, this approach keeps residual drifts compensated by the primary servo integrator (actuating on AOM1) to a measured value of < 1 mHz/s.

For a single integrator servo loop, the average drift-induced servo error can be estimated as $t_{servo}df/dt$ where t_{servo} is the servo time constant and df/dt is the constant linear drift [262]. From our measured drift, as well as from analysis of the overall servo signal record for residual offsets, we conservatively estimate the servo error to be $< 5 \times 10^{-17}$.

5.4.9 Other residual 1^{st}-order Doppler shifts

Line-pulling is one way that residual 1^{st}-order Doppler (and recoil) effects could introduce a systematic shift of the clock transition. Other mechanisms can also play a role. The first, as discussed in Section 2.6.5, is the residual Doppler and recoil effect due to tunnelling in the lattice potential. Exploiting gravity to lift degeneracy among different lattice sites and suppress tunnelling, for our lattice parameters this effect is estimated to be below the 10^{-17} shift level. As we consider interrogation of atoms in a 3-D optical lattice, it remains beneficial to probe the atoms along the gravitational axis.

Another residual 1^{st}-order Doppler effect, as discussed in Section 3.4.2, originates from relative shaking between the lattice potential and the clock laser. With the possibility to give a frequency offset, we are concerned with relative motion during probing synchronized with the experimental cycle at the frequency $f = 1/T_c$ (T_c being the experimental cycle time) and its harmonics. For example, the NIST Ca clock has observed problematic frequency shifts associated with turning on and off the quadrupole MOT field which systematically shakes the optical table. They have circumvented this problem by isolating the vacuum chamber from the table [86]. The NIST ion group was recently concerned with a Doppler shift synchronized to their atomic probing induced by photo-electron buildup on their trap electrodes due to illumination by the UV clock laser. To average out this effect, they alternated probing from opposite directions [259]. This leaves residual Doppler sensitivity at the frequency $f = 1/2T_c$, where any motional noise is presumably much smaller. In the case of lattice trapped neutral atoms,

the neutral atom is not strongly pushed by charged particles (which, except for vacuum particles, are neither present) and the relative lattice-probe motion is set by large, heavy optical components which can be designed to be very stable and placed on an isolated optical table. We investigated some of these effects as we probed narrow lines and did not observe any influence at the Hz level. Beyond this, our experience with phase noise cancellation for free space optical paths in our laboratory indicates that laboratory seismic noise and airborne fluctuations degrade laser instability from Doppler noise in the free space optical path well-below the 10^{-16} level at 1 s (approximately T_c). However, while mechanically switching optical shutters are typically isolated from the optics table, we do use switching magnetic fields like the Ca experiment. Fortunately, with our long T_c, this field switching is temporally far removed from the atomic interrogation time. Also, vacuum chamber motion is much less critical than for the lattice and probe laser optical components, which are further distanced from any switching fields. As discussed in Section 3.4.2, future interrogation will exploit active noise cancellation, where the lattice retroreflector is stabilized to make a weak lattice cavity resonant with the lattice laser, and fiber noise cancellation of the clock laser can be implemented all the way to the first lattice cavity mirror. In this way, the clock laser phase is locked to the atomic confinement reference frame.

A related Doppler effect involves switching the RF power in an AOM to pulse the clock laser for spectroscopy. This pulsing is known to induce phase chirps of the spectroscopic pulses, both from RF ringing and thermal effects [263]. The AOM we use for switching the clock pulse is the same used for the fiber-noise-cancellation path bringing the clock laser to the atoms. This means that with the fiber noise cancellation servo engaged, the optical phase is stabilized and Doppler frequency excursions are cancelled to < 10 mHz. After turning the RF power on, the fiber noise cancellation servo takes ~ 100 μs to properly engage, a small fraction of the pulse length time $t_p = 80$ ms. Additionally, we also use a liquid-crystal shutter to give time for this

servo to engage before illuminating the atoms. Interferometric techniques can be used to further characterize this effect.

5.4.10 2^{nd}-order Doppler shift

The 2^{nd}-order Doppler shift originates from expansion of the relativistic Doppler shift, accounting for time dilation. It is simply:

$$\Delta\omega = \frac{1}{2}\beta^2\omega_L \tag{5.27}$$

where $\beta = v/c$ is proportional to the atomic velocity and ω_L is the laser (angular) frequency. The atomic velocity of our ultracold lattice-trapped strontium is characteristically given by the sample temperature, $T = 2.5$ μK, corresponding to a velocity of ~ 15 cm/s. This results in a 2^{nd}-order Doppler shift below 100 μHz ($< 10^{-18}$). Shaking of the trap results in much smaller velocities and thus an even more negligible 2^{nd}-order Doppler shift.

5.4.11 Other effects

Although gravitational fields are not known to change the local operation of an atomic clock [264], general relativity dictates that comparison of clocks in different gravitational potentials is subject to the gravitational red shift:

$$\Delta\omega = \frac{gL}{c^2}\omega_L \tag{5.28}$$

where g is the local gravitational acceleration, L is the distance (component along gravity) between the standards, ω_L is the laser radiation frequency, and radiation travelling towards a weaker gravitational field is red-shifted. In Equation 5.28, we have assumed that g is constant at and between both clocks in the comparison. At the earth's surface the fractional gravitational red shift is $\sim 1 \times 10^{-18}$/cm. Because of their amazing stability and accuracy, optical clocks in the future may exploit this effect to perform geodesy.

The presence of a DC electric field induces a static Stark shift. The grounded vacuum chamber acts as a Faraday cage around the atoms as well as keeps charged objects far removed from the atoms. However, charge can build up on the dielectric coated glass viewports. If charge is collected on the large viewports closest to the atoms (top and bottom of chamber) sufficient to yield even a large 1 V potential difference, based on the DC polarizability (Section 5.4.5), the resulting clock transition shift would be $< 10^{-18}$.

No significant AC magnetic fields are present, the largest probably at the 60 Hz electrical line frequency. With the small 2^{nd}-order Zeeman shift for the clock transition (Section 5.4.3), AC Zeeman shifts are negligible. This effect is sometimes considered for the trapped ion case, due to the RF trapping potential (e. g. [265]).

To prevent AC Stark shifts from the unwanted presence of other laser beams used for the strontium experiment (laser cooling, optical pumping, etc.), mechanical shutters and acousto-optic shutters are typically used together to impede this laser radiation from reaching the atoms. Furthermore, the vacuum chamber is covered by an optically opaque curtain.

Finally, the clock states possess no permanent electric quadrupole moment, so that field-gradient induced shifts are negligible.

5.4.12 Uncertainty Summary

Table 5.3 summarizes the systematic shifts and uncertainties in realizing the natural Sr atomic transition frequency [23]. The total uncertainty of 1.5×10^{-16} represents the smallest frequency uncertainty for any neutral atom system to-date, including the Cs primary standard. It falls short of impressive Hg^+ and Al^+ trapped ion results as the smallest uncertainty for any type of frequency standard. The largest Sr uncertainty originates from the blackbody Stark shift, with the next largest being the density shift. Progress towards more fully characterizing and controlling these shift mechanisms will

Table 5.3: Systematic shifts and their uncertainties for the ^{87}Sr $^1S_0$-$^3P_0$ clock transition (2007)

Contributor	Correction (10^{-16})	Uncertainty (10^{-16})
Lattice Stark (scalar/tensor)	-6.5	0.5
Hyperpolarizability (lattice)	-0.2	0.2
BBR Stark	52.1	1.0
AC Stark (probe)	0.2	0.1
1^{st} order Zeeman	0.2	0.2
2^{nd} order Zeeman	0.2	0.02
Density	8.9	0.8
Line pulling	0	0.2
Servo error	0	0.5
2^{nd} order Doppler	0	$\ll$0.01
Systematic total	54.9	1.5

facilitate determination of the Sr standard in the 10^{-17} range. The 10^{-16} uncertainty demonstrated here is an important milestone towards the 10^{-18} accuracy goal shared by many optical standards.

5.5 Absolute Frequency Measurement

With the reduced uncertainty of the Sr optical standard, we performed a new absolute frequency measurement of the Sr clock transition using the H-maser based fiber link to the NIST-F1 Cs fountain. With the anticipated uncertainty at or below the 10^{-15} fractional frequency level, we re-characterized the microwave link from JILA to the H-maser ensemble. This included a full out-of-loop evaluation of the microwave electronics used for the microwave phase-stabilized, fiber-based transfer scheme from the laboratory of Drs. Leo Hollberg and Scott Diddams to JILA (this evaluation used a short piece of test fiber). This revealed a transfer instability of 10^{-14} at 1 s which averaged down to 10^{-17} for $> 10^4$ s, with no observable offset. In addition to the temperature sensitivity of the H-maser-referenced synthesizer used for amplitude modulation of the transfer laser, temperature sensitivity for a variety of microwave components (mixers, frequency doublers, cable, amplifiers) was found to be at the several 10^{-16}/(K/hr) level, and we could thus apply a small but complete temperature based correction to the frequency measurement.

The Sr system was run under conditions similar to, but not exactly the same as, those of the uncertainty evaluation described in the previous section. The measurement was made over 50 consecutive hours. Accounting for small breaks during which the microwave transfer link or a Sr laser was un-locked and then re-locked, the final measurement data set included $\sim 184,000$ s. The measurement instability averaged down predominantly characteristic of the H-maser. The NIST-F1 fountain was operated with a total fractional frequency uncertainty (systematic and statistical) of 6×10^{-16}. An additional 6×10^{-16} uncertainty originated from dead time in the strontium measurement

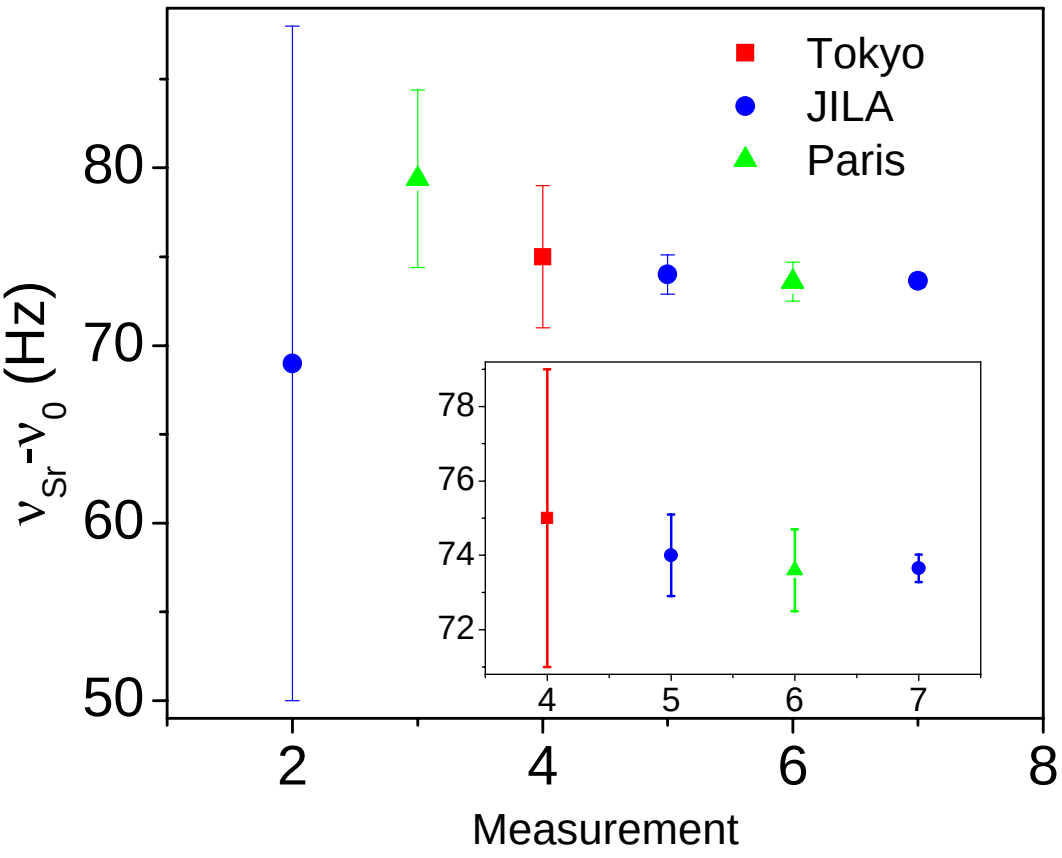

Figure 5.14: Plot of high accuracy absolute frequency measurements of the Sr clock transition. 1: JILA 2005, 2: Paris 2006, 3: Tokyo 2006, 4: JILA 2006, 5: Paris 2007, 6: JILA 2007, based on 48 hour measurement with the NIST F1 Cs fountain. The inset is a magnification of the last four points.

during which the Cs continued to average down with the H-maser. The measurement yielded a Sr transition frequency of 429 228 004 229 873.8 (4) Hz, with a fractional frequency uncertainty $< 10^{-15}$, making it one of the most accurately determined optical transitions (similar to measurement level of the Hg^+ optical clock transition [6]) [266]. This measurement, combined with other recent measurements of the Sr clock transition, is shown in Figure 5.14. The excellent agreement among groups makes strontium the best-agreed upon optical standard. In fact, this excellent agreement allows for analysis of the combined international Sr frequency data set for time dependent frequency changes that could be put additional constraints on possible variation of the fundamental constants [264].

5.6 Outlook

In 2003, the ^{87}Sr $5s^2\ ^1S_0$- $5s5p\ ^3P_0$ clock transition was directly excited for the first time and its frequency was determined with a 20 kHz uncertainty ($\sim 5 \times 10^{-11}$) [204]. Less than five years later, its absolute frequency has been measured to $< 10^{-15}$ and its frequency uncertainty has been characterized at the 10^{-16} level, representing five orders of magnitude improvement. This rapid progress has been facilitated by an atomic system well-suited for high precision and high accuracy spectroscopy. Another key ingredient was the ability to manipulate and control the strontium to generate large atomic samples uniformly confined in the well-resolved sideband and Lamb-Dicke regimes. The neutral lattice-trapped strontium system demonstrates many qualities which are well-suited for its continued development towards the 10^{-18} accuracy level. Paramount to this goal, near-future steps for the strontium system must include better control and characterization of the BBR and density shifts. Operation in a 3-D lattice has immediate implications for the collisional interactions as well as the benefit of strong confinement in all axes. An important enabling step will be the development of a clock laser system with coherence times exceeding 10 s. This will not only make ultra-

narrow resonance atomic interrogation possible, but will allow neutral atom systems to emerge as ultra-stable optical frequency standards. No major clock limitations have so far originated from the added complexity of the hyperfine interaction in the odd-isotope alkaline earth standards. Nevertheless even isotopes (with no hyperfine interaction) using external magnetic field state mixing [226] or electromagnetically-induced transparency [267, 268] may be an interesting exploration. Already recommended as a secondary representation of the SI second, strontium will surely continue to play an important role in high accuracy time and frequency standards. Together with interesting possible applications in ultracold molecular association and spectroscopy [269, 270], cold collisions [23, 269, 68], measurement of fundamental constants [264, 270], quantum non-demolition measurements [271], quantum simulations, quantum computation, quantum degeneracy [84, 68, 269], ultracold plasmas [272], coherent population trapping [268, 267], and more, strontium will continue to help both better define and better understand the world around us.

Bibliography

[1] R. Davis, The SI unit of mass, *Metrologia* **40**, 299 (2003).

[2] I. M. Mills, P. J. Mohr, T. J. Quinn, B. N. Taylor, and E. R. Williams, Redefinition of the kilogram: a decision whose time has come, *Metrologia* **42**, 71 (2005).

[3] P. Forman, Atomichron - The Atomic Clock From Concept To Commercial Product, *Proceedings Of The Ieee* **73**, 1181 (1985).

[4] J. Levine, Introduction to time and frequency metrology, *Review Of Scientific Instruments* **70**, 2567 (1999).

[5] T. P. Heavner, S. R. Jefferts, E. A. Donley, J. H. Shirley, and T. E. Parker, Recent improvements in NIST-F1 and a resulting accuracy of $\delta f/f = 0.61 \times 10^{-15}$, *Ieee Transactions On Instrumentation And Measurement* **54**, 842 (2005).

[6] J. E. Stalnaker *et al.*, Optical-to-microwave frequency comparison with fractional uncertainty of 10^{-15}, *Applied Physics B-Lasers And Optics* **89**, 167 (2007).

[7] R. Wynands and S. Weyers, Atomic fountain clocks, *Metrologia* **42**, S64 (2005).

[8] A. Bauch and H. R. Telle, Frequency standards and frequency measurement, *Reports On Progress In Physics* **65**, 789 (2002).

[9] S. Bize *et al.*, Cold atom clocks and applications, *Journal Of Physics B-Atomic Molecular And Optical Physics* **38**, S449 (2005).

[10] C. Santarelli, P. Laurent, P. Lemonde, A. Clairon, A. G. Mann, S. Chang, A. N. Luiten, and C. Salomon, Quantum projection noise in an atomic fountain: A high stability cesium frequency standard, *Physical Review Letters* **82**, 4619 (1999).

[11] M. E. Tobar *et al.*, Long-term operation and performance of cryogenic sapphire oscillators, *Ieee Transactions On Ultrasonics Ferroelectrics And Frequency Control* **53**, 2386 (2006).

[12] A. Bauch, Caesium atomic clocks: function, performance and applications, *Measurement Science & Technology* **14**, 1159 (2003).

[13] E. Peik, G. Hollemann, and H. Walther, Laser Cooling And Quantum Jumps Of A Single Indium Ion, *Physical Review A* **49**, 402 (1994).

[14] G. Breit and L. A. Wills, Hyperfine structure in intermediate coupling, *Physical Review* **44**, 0470 (1933).

[15] A. Lurio, M. Mandel, and R. Novick, Second-Order Hyperfine And Zeeman Corrections For An (Sl) Configuration, *Physical Review* **126**, 1758 (1962).

[16] M. M. Boyd, High Precision Spectroscopy of Strontium in an Optical Lattice: Towards a New Standard for Frequency and Time, Ph.D. thesis, University of Colorado, 2007.

[17] K. H. Ko, Y. K. Lim, D. Y. Jeong, H. Park, T. S. Kim, G. Lim, and H. K. Cha, Measurement of the isotope selectivity of the strontium magneto-optical trap by a time-of-flight mass spectrometer, *Journal Of The Optical Society Of America B-Optical Physics* **23**, 2465 (2006).

[18] M. G. Mayer, Nuclear Configurations In The Spin-Orbit Coupling Model .1. Empirical Evidence, *Physical Review* **78**, 16 (1950).

[19] A. Lurio, Configuration Interaction And Hfs Of Sl Configuration, *Physical Review* **142**, 46 (1966).

[20] S. G. Porsev and A. Derevianko, Multipolar theory of blackbody radiation shift of atomic energy levels and its implications for optical lattice clocks, *Physical Review A* **74**, 020502 (2006).

[21] A. D. Ludlow, M. M. Boyd, T. Zelevinsky, S. M. Foreman, S. Blatt, M. Notcutt, T. Ido, and J. Ye, Systematic study of the ^{87}Sr clock transition in an optical lattice, *Physical Review Letters* **96**, 033003 (2006).

[22] M. M. Boyd, A. D. Ludlow, S. Blatt, S. M. Foreman, T. Ido, T. Zelevinsky, and J. Ye, ^{87}Sr lattice clock with inaccuracy below 10^{-15}, *Physical Review Letters* **98**, 083002 (2007).

[23] A. D. Ludlow *et al.*, Sr Lattice Clock at 1×10^{16} Fractional Uncertainty by Remote Optical Evaluation with a Ca Clock, *Science* **319**, 1805 (2008).

[24] R. Le Targat, X. Baillard, M. Fouche, A. Brusch, O. Tcherbakoff, G. D. Rovera, and P. Lemonde, Accurate optical lattice clock with ^{87}Sr atoms, *Physical Review Letters* **97**, 130801 (2006).

[25] X. Baillard, M. Fouche, R. Le Targat, P. G. Westergaard, A. Lecallier, Y. Le Coq, G. D. Rovera, S. Bize, and P. Lemonde, Accuracy evaluation of an optical lattice clock with bosonic atoms, *Optics Letters* **32**, 1812 (2007).

[26] X. Baillard *et al.*, arXiv:0710.0086v1 (unpublished).

[27] H. Katori, in *Proceedings of the 6th Symposium on Frequency Standards and Metrology*, edited by P. Gill (World Scientific, ADDRESS, 2002), Chap. Spectroscopy of strontium atoms in the Lamb-Dicke confinement, pp. 323–330.

[28] M. Takamoto, F. L. Hong, R. Higashi, and H. Katori, An optical lattice clock, *Nature* **435**, 321 (2005).

[29] M. Takamoto, F. L. Hong, R. Higashi, Y. Fujii, M. Imae, and H. Katori, Improved frequency measurement of a one-dimensional optical lattice clock with a spin-polarized fermionic ^{87}Sr isotope, *Journal Of The Physical Society Of Japan* **75**, 104302 (2006).

[30] C. W. Hoyt, Z. W. Barber, C. W. Oates, T. M. Fortier, S. A. Diddams, and L. Hollberg, Observation and absolute frequency measurements of the $^1S_0$-$^3P_0$ optical clock transition in neutral ytterbium, *Physical Review Letters* **95**, 083003 (2005).

[31] Z. W. Barber, C. W. Hoyt, C. W. Oates, L. Hollberg, A. V. Taichenachev, and V. I. Yudin, Direct excitation of the forbidden clock transition in neutral Yb-174 atoms confined to an optical lattice, *Physical Review Letters* **96**, 083002 (2006).

[32] F. Chapeletet, J. Guena, D. Rovera, P. Laurent, P. Rosenbusch, G. Santarelli, S. Bize, A. Clairon, M. E. Tobar, and M. Abgrall, in *Proceedings of the Joint IEEE-FCS and EFTF Meeting* (PUBLISHER, ADDRESS, 2007).

[33] H. Hachisu, K. Miyagishi, S. G. Porsev, A. Derevianko, V. D. Ovsiannikov, V. G. Pal'chikov, M. Takamoto, and H. Katori, Trapping of Neutral Mercury Atoms and Prospects for Optical Lattice Clocks, *Physical Review Letters* **100**, 053001 (2008).

[34] J. J. Snyder, J. L. Hall, and M. S. Sorem, Measurement Of Relativistic Doppler-Shift, *Ieee Journal Of Quantum Electronics* **QE10**, 692 (1974).

[35] W. D. Phillips, Laser cooling and trapping of neutral atoms, *Reviews Of Modern Physics* **70**, 721 (1998).

[36] D. W. Allan, N. Ashby, and C. C. Hodge, Technical report, Hewlett-Packard Application Note 1289 (unpublished).

[37] E. A. Curtis, Quenched narrow-line laser cooling of ^{40}Ca with application to an optical clock based on ultracold neutral Ca atoms, Ph.D. thesis, University of Colorado, 2003.

[38] S. Schiller and et al., , *Nuc. Phys. B (Proc. Suppl.)* **166**, 300 (2007).

[39] P. Lemonde *et al.*, Cold-atom clocks on Earth and in space, *Frequency Measurement And Control Advanced Techniques And Future Trends* **79**, 131 (2000).

[40] C. N. Cohen-Tannoudji, Manipulating atoms with photons, *Reviews Of Modern Physics* **70**, 707 (1998).

[41] P. D. Lett, W. D. Phillips, S. L. Rolston, C. E. Tanner, R. N. Watts, and C. I. Westbrook, Optical Molasses, *Journal Of The Optical Society Of America B-Optical Physics* **6**, 2084 (1989).

[42] Y. Castin, H. Wallis, and J. Dalibard, Limit Of Doppler Cooling, *Journal Of The Optical Society Of America B-Optical Physics* **6**, 2046 (1989).

[43] D. J. Wineland and W. M. Itano, Laser Cooling Of Atoms, *Physical Review A* **20**, 1521 (1979).

[44] H. J. Metcalf and P. van der Straten, *Laser Cooling and Trapping* (Springer, ADDRESS, 1999).

[45] C. S. Adams and E. Riis, Laser cooling and trapping of neutral atoms, *Progress In Quantum Electronics* **21**, 1 (1997).

[46] T. W. Hansch and A. L. Schawlow, Cooling Of Gases By Laser Radiation, *Optics Communications* **13**, 68 (1975).

[47] D. Wineland and H. Dehmelt, Proposed 1014 Delta Upsilon Less Than Upsilon Laser Fluorescence Spectroscopy On T1+ Mono-Ion Oscillator Iii, *Bulletin Of The American Physical Society* **20**, 637 (1975).

[48] D. E. Pritchard, E. L. Raab, V. Bagnato, C. E. Wieman, and R. N. Watts, Light Traps Using Spontaneous Forces, *Physical Review Letters* **57**, 310 (1986).

[49] E. L. Raab, M. Prentiss, A. Cable, S. Chu, and D. E. Pritchard, Trapping Of Neutral Sodium Atoms With Radiation Pressure, *Physical Review Letters* **59**, 2631 (1987).

[50] J. Dalibard and C. Cohen-Tannoudji, Laser Cooling Below The Doppler Limit By Polarization Gradients - Simple Theoretical-Models, *Journal Of The Optical Society Of America B-Optical Physics* **6**, 2023 (1989).

[51] A. Aspect, E. Arimondo, R. Kaiser, N. Vansteenkiste, and C. Cohentannoudji, Laser Cooling Below The One-Photon Recoil Energy By Velocity-Selective Coherent Population Trapping - Theoretical-Analysis, *Journal Of The Optical Society Of America B-Optical Physics* **6**, 2112 (1989).

[52] H. J. Lee, C. S. Adams, M. Kasevich, and S. Chu, Raman cooling of atoms in an optical dipole trap, *Physical Review Letters* **76**, 2658 (1996).

[53] T. H. Loftus, Laser Cooling and Trapping of Atomic Ytterbium, Ph.D. thesis, University of Oregon, 2001.

[54] K. R. Vogel, Laser Cooling on a Narrow Atomic Transition and Measurement of the Two-Body Collision Loss Rate in a Strontium Magneto-Optical Trap, Ph.D. thesis, University of Colorado, 1999.

[55] A. N. Nesmeyanov, in *Vapor Pressure of the Chemical Elements*, edited by R. Gary (Elsevier Publishing Company, ADDRESS, 1963).

[56] T. E. Barrett, S. W. Daporeschwartz, M. D. Ray, and G. P. Lafyatis, Slowing Atoms With σ^--Polarized Light, *Physical Review Letters* **67**, 3483 (1991).

[57] A. Noble and M. Kasevich, Uhv Optical Window Seal To Conflat Knife Edge, *Review Of Scientific Instruments* **65**, 3042 (1994).

[58] M. Bode, I. Freitag, A. Tunnermann, and H. Welling, Frequency-tunable 500-mW continuous-wave all-solid-state single-frequency source in the blue spectral region, *Optics Letters* **22**, 1220 (1997).

[59] X. Y. Xu, T. H. Loftus, J. L. Hall, A. Gallagher, and J. Ye, Cooling and trapping of atomic strontium, *Journal Of The Optical Society Of America B-Optical Physics* **20**, 968 (2003).

[60] M. Yasuda and H. Katori, Lifetime measurement of the $^3P_2$ metastable state of strontium atoms, *Physical Review Letters* **92**, 153004 (2004).

[61] S. G. Porsev and A. Derevianko, Hyperfine quenching of the metastable $^3P_{0,2}$ states in divalent atoms, *Physical Review A* **69**, 042506 (2004).

[62] T. Loftus, J. R. Bochinski, R. Shivitz, and T. W. Mossberg, Power-dependent loss from an ytterbium magneto-optic trap, *Physical Review A* **61**, 051401 (2000).

[63] T. P. Dinneen, K. R. Vogel, E. Arimondo, J. L. Hall, and A. Gallagher, Cold collisions of Sr*-Sr in a magneto-optical trap, *Physical Review A* **59**, 1216 (1999).

[64] S. B. Nagel, C. E. Simien, S. Laha, P. Gupta, V. S. Ashoka, and T. C. Killian, Magnetic trapping of metastable $^3P_2$ atomic strontium, *Physical Review A* **67**, 011401 (2003).

[65] D. P. Hansen, J. R. Mohr, and A. Hemmerich, Magnetic trapping of metastable calcium atoms, *Physical Review A* **67**, 021401 (2003).

[66] J. Stuhler, P. O. Schmidt, S. Hensler, J. Werner, J. Mlynek, and T. Pfau, Continuous loading of a magnetic trap, *Physical Review A* **6403**, 031405 (2001).

[67] A. Derevianko, S. G. Porsev, S. Kotochigova, E. Tiesinga, and P. S. Julienne, Ultracold collision properties of metastable alkaline-earth atoms, *Physical Review Letters* **90**, 063002 (2003).

[68] V. Kokoouline, R. Santra, and C. H. Greene, Multichannel cold collisions between metastable Sr atoms, *Physical Review Letters* **90**, 253201 (2003).

[69] R. Santra and C. H. Greene, Tensorial analysis of the long-range interaction between metastable alkaline-earth-metal atoms, *Physical Review A* **67**, 062713 (2003).

[70] A. V. Avdeenkov and J. L. Bohn, Collisional dynamics of ultracold OH molecules in an electrostatic field, *Physical Review A* **66**, 052718 (2002).

[71] H. J. Lewandowski, D. M. Harber, D. L. Whitaker, and E. A. Cornell, Simplified system for creating a Bose-Einstein condensate, *Journal Of Low Temperature Physics* **132**, 309 (2003).

[72] H. J. Metcalf and P. van der Straten, Laser cooling and trapping of atoms, *Journal Of The Optical Society Of America B-Optical Physics* **20**, 887 (2003).

[73] H. Wallis and W. Ertmer, Broad-Band Laser Cooling On Narrow Transitions, *Journal Of The Optical Society Of America B-Optical Physics* **6**, 2211 (1989).

[74] X. Y. Xu, T. H. Loftus, M. J. Smith, J. L. Hall, A. Gallagher, and J. Ye, Dynamics in a two-level atom magneto-optical trap, *Physical Review A* **66**, 011401 (2002).

[75] T. H. Loftus, T. Ido, A. D. Ludlow, M. M. Boyd, and J. Ye, Narrow line cooling: Finite photon recoil dynamics, *Physical Review Letters* **93**, 073003 (2004).

[76] T. H. Loftus, T. Ido, M. M. Boyd, A. D. Ludlow, and J. Ye, Narrow line cooling and momentum-space crystals, *Physical Review A* **70**, 063413 (2004).

[77] R. W. P. Drever, J. L. Hall, F. V. Kowalski, J. Hough, G. M. Ford, A. J. Munley, and H. Ward, Laser Phase And Frequency Stabilization Using An Optical-Resonator, *Applied Physics B-Photophysics And Laser Chemistry* **31**, 97 (1983).

[78] R. J. Jones, I. Thomann, and J. Ye, Precision stabilization of femtosecond lasers to high-finesse optical cavities, *Physical Review A* **69**, 051803 (2004).

[79] J. Ye *et al.*, Delivery of high-stability optical and microwave frequency standards over an optical fiber network, *Journal Of The Optical Society Of America B-Optical Physics* **20**, 1459 (2003).

[80] K. W. Holman, D. J. Jones, D. D. Hudson, and J. Ye, Precise frequency transfer through a fiber network by use of 1.5-μm mode-locked sources, *Optics Letters* **29**, 1554 (2004).

[81] H. Katori, T. Ido, Y. Isoya, and M. Kuwata-Gonokami, Magneto-optical trapping and cooling of strontium atoms down to the photon recoil temperature, *Physical Review Letters* **82**, 1116 (1999).

[82] I. Courtillot, A. Quessada-Vial, A. Brusch, D. Kolker, G. D. Rovera, and P. Lemonde, Accurate spectroscopy of Sr atoms, *European Physical Journal D* **33**, 161 (2005).

[83] S. Blatt, monte-carlo simulation of optical pumping carried out by S. Blatt (unpublished).

[84] T. Mukaiyama, H. Katori, T. Ido, Y. Li, and M. Kuwata-Gonokami, Recoil-limited laser cooling of ^{87}Sr atoms near the Fermi temperature, *Physical Review Letters* **90**, 113002 (2003).

[85] P. Bouyer, P. Lemonde, M. Bendahan, A. Michaud, C. Salomon, and J. Dalibard, An Atom Trap Relying On Optical-Pumping, *Europhysics Letters* **27**, 569 (1994).

[86] G. Wilpers *et al.*, Absolute frequency measurement of the neutral ^{40}Ca optical frequency standard at 657nm based on microkelvin atoms, *Metrologia* **44**, 146 (2007).

[87] C. Degenhardt *et al.*, Calcium optical frequency standard with ultracold atoms: Approaching 10^{-15} relative uncertainty, *Physical Review A* **72**, 062111 (2005).

[88] G. Wilpers, C. Degenhardt, T. Binnewies, A. Chernyshov, F. Riehle, J. Helmcke, and U. Sterr, Improvement of the fractional uncertainty of a neutral-atom calcium optical frequency standard to 2×10^{-14}, *Applied Physics B-Lasers And Optics* **76**, 149 (2003).

[89] G. Wilpers, T. Binnewies, C. Degenhardt, U. Sterr, J. Helmcke, and F. Riehle, Optical clock with ultracold neutral atoms (vol 89, art no 230801, 2002), *Physical Review Letters* **90**, 089901 (2003).

[90] U. Sterr, C. Degenhardt, H. Stoehr, C. Lisdat, H. Schnatz, J. Helmcke, F. Riehle, G. Wilpers, C. Oates, and L. Hollberg, The optical calcium frequency standards of PTB and NIST, *Comptes Rendus Physique* **5**, 845 (2004).

[91] T. Ido, T. H. Loftus, M. M. Boyd, A. D. Ludlow, K. W. Holman, and J. Ye, Precision spectroscopy and density-dependent frequency shifts in ultracold Sr, *Physical Review Letters* **94**, 153001 (2005).

[92] A. Gorlitz, T. L. Gustavson, A. E. Leanhardt, R. Low, A. P. Chikkatur, S. Gupta, S. Inouye, D. E. Pritchard, and W. Ketterle, Sodium Bose-Einstein condensates in the F=2 state in a large-volume optical trap, *Physical Review Letters* **90**, 090401 (2003).

[93] J. J. Sakurai, in *Modern Quantum Mechanics*, edited by S. F. Tuan (Addison-Wesley, ADDRESS, 1994).

[94] D. Leibfried, R. Blatt, C. Monroe, and D. Wineland, Quantum dynamics of single trapped ions, *Reviews Of Modern Physics* **75**, 281 (2003).

[95] D. J. Wineland, C. Monroe, W. M. Itano, D. Leibfried, B. E. King, and D. M. Meekhof, Experimental issues in coherent quantum-state manipulation of trapped atomic ions, *Journal Of Research Of The National Institute Of Standards And Technology* **103**, 259 (1998).

[96] C. A. Blockley, D. F. Walls, and H. Risken, Quantum Collapses And Revivals In A Quantized Trap, *Europhysics Letters* **17**, 509 (1992).

[97] J. L. Hall and M. Zhu, in *International School of Physics Enrico Fermi, Course CXVIII, Laser Manipulation of Atoms and Ions*, edited by E. Arimondo, W. Phillips, and S. F. (North Holland, ADDRESS, 1992), Chap. An Introduction to Phase-Stable Optical Sources, pp. 671–702.

[98] W. Neuhauser, M. Hohenstatt, P. Toschek, and H. Dehmelt, Optical-Sideband Cooling Of Visible Atom Cloud Confined In Parabolic Well, *Physical Review Letters* **41**, 233 (1978).

[99] J. Ye, D. W. Vernooy, and H. J. Kimble, Trapping of single atoms in cavity QED, *Physical Review Letters* **83**, 4987 (1999).

[100] H. Katori, M. Takamoto, V. G. Pal'chikov, and V. D. Ovsiannikov, Ultrastable optical clock with neutral atoms in an engineered light shift trap, *Physical Review Letters* **91**, 173005 (2003).

[101] J. Ye, H. J. Kimble, and H. Katori, science (invited review), in press (2008). (unpublished).

[102] D. J. Wineland, W. M. Itano, J. C. Bergquist, and R. G. Hulet, Laser-Cooling Limits And Single-Ion Spectroscopy, *Physical Review A* **36**, 2220 (1987).

[103] S. Stenholm, The Semiclassical Theory Of Laser Cooling, *Reviews Of Modern Physics* **58**, 699 (1986).

[104] R. H. Dicke, The Effect Of Collisions Upon The Doppler Width Of Spectral Lines, *Physical Review* **89**, 472 (1953).

[105] R. L. Mossbauer, The discovery of the Mossbauer effect, *Hyperfine Interactions* **126**, 1 (2000).

[106] D. J. Wineland, R. E. Drullinger, and F. L. Walls, Radiation-Pressure Cooling Of Bound Resonant Absorbers, *Physical Review Letters* **40**, 1639 (1978).

[107] D. J. Griffiths, *Introduction to Electrodynamics* (Prentice-Hall, ADDRESS, 1999).

[108] I. I. Sobelman, *Theory of Atomic Spectra* (Alpha Science, ADDRESS, 2006).

[109] B. W. Shore and D. H. Menzel, *Principles of Atomic Spectra* (John Wiley and Sons, Inc., ADDRESS, 1968).

[110] E. U. Condon and G. H. Shortley, *The Theory of Atomic Spectra* (Cambridge University Press, ADDRESS, 1964).

[111] P. M. Farrell and W. R. MacGillivray, On The Consistency Of Rabi Frequency Calculations, *Journal Of Physics A-Mathematical And General* **28**, 209 (1995).

[112] C. Degenhardt, H. Stoehr, U. Sterr, F. Riehle, and C. Lisdat, Wavelength-dependent ac Stark shift of the $^1S_0$-$^3P_1$ transition at 657 nm in Ca, *Physical Review A* **70**, 023414 (2004).

[113] C. E. Moore, *Atomic Energy Levels (Vol. II)* (National Bureau of Standards, ADDRESS, 1971).

[114] M. Yasuda, T. Kishimoto, M. Takamoto, and H. Katori, Photoassociation spectroscopy of ^{88}Sr: Reconstruction of the wave function near the last node, *Physical Review A* **73**, 011403 (2006).

[115] S. B. Nagel, P. G. Mickelson, A. D. Saenz, Y. N. Martinez, Y. C. Chen, T. C. Killian, P. Pellegrini, and R. Cote, Photoassociative spectroscopy at long range in ultracold strontium, *Physical Review Letters* **94**, 083004 (2005).

[116] H. G. C. Werij, C. H. Greene, C. E. Theodosiou, and A. Gallagher, Oscillator-Strengths And Radiative Branching Ratios In Atomic Sr, *Physical Review A* **46**, 1248 (1992).

[117] D. A. Miller, L. You, J. Cooper, and A. Gallagher, Collisional Energy-Transfer Between Excited-State Strontium And Noble-Gas Atoms, *Physical Review A* **46**, 1303 (1992).

[118] R. C. Hilborn, Einstein Coefficients, Cross-Sections, F Values, Dipole-Moments, And All That, *American Journal Of Physics* **50**, 982 (1982).

[119] B. H. Bransden and C. J. Joachain, *Physics of Atoms and Molecules* (Prentice Hall, ADDRESS, 2003).

[120] S. U. Haq, S. Mahmood, M. A. Kalyar, M. Rafiq, R. Ali, and M. A. Baig, Photoionization cross section and oscillator strength distribution in the near-threshold region of strontium, *European Physical Journal D* **44**, 439 (2007).

[121] C. Barrientos and I. Martin, Oscillator Strength Distribution In The Alkaline-Earth Elements, *Canadian Journal Of Physics* **66**, 29 (1988).

[122] C. Barrientos and I. Martin, Oscillator-Strength Distribution In The Discrete And Continuous Spectra Of The Alkali Elements, *Canadian Journal Of Physics* **65**, 435 (1987).

[123] C. H. Greene and M. Aymar, Spin-Orbit Effects In The Heavy Alkaline-Earth Atoms, *Physical Review A* **44**, 1773 (1991).

[124] R. D. Hudson, V. L. Carter, and P. A. Young, Absorption Spectrum Of Sr I In Region Of Autoionization From 1646-A To 2028-A, *Physical Review* **180**, 77 (1969).

[125] W. H. Parkinson, E. M. Reeves, and F. S. Tomkins, Neutral Calcium, Strontium And Barium - Determination Of F-Values Of Principal Series By Hook Method, *Journal Of Physics B-Atomic Molecular And Optical Physics* **9**, 157 (1976).

[126] U. Fano and J. W. Cooper, Spectral Distribution Of Atomic Oscillator Strengths, *Reviews Of Modern Physics* **40**, 441 (1968).

[127] M. Inokuti, J. L. Dehmer, T. Baer, and J. D. Hanson, Oscillator-Strength Moments, Stopping Powers, And Total Inelastic-Scattering Cross-Sections Of All Atoms Through Strontium, *Physical Review A* **23**, 95 (1981).

[128] W. Mende and M. Kock, Oscillator strengths of the Sr I principal series, *Journal Of Physics B-Atomic Molecular And Optical Physics* **30**, 5401 (1997).

[129] W. Mende and M. Kock, Oscillator strengths of Ba I and Sr I Rydberg transitions, *Journal Of Physics B-Atomic Molecular And Optical Physics* **29**, 655 (1996).

[130] C. H. Greene, private communication (unpublished).

[131] E. J. Angstmann, V. A. Dzuba, and V. V. Flambaum, Frequency shift of hyperfine transitions due to blackbody radiation, *Physical Review A* **74**, 023405 (2006).

[132] S. Micalizio, A. Godone, D. Calonico, F. Levi, and L. Lorini, Blackbody radiation shift of the Cs-133 hyperfine transition frequency, *Physical Review A* **69**, 053401 (2004).

[133] F. Levi, D. Calonico, L. Lorini, S. Micalizio, and A. Godone, Measurement of the blackbody radiation shift of the Cs-133 hyperfine transition in an atomic fountain, *Physical Review A* **70**, 033412 (2004).

[134] E. Simon, P. Laurent, and A. Clairon, Measurement of the Stark shift of the Cs hyperfine splitting in an atomic fountain, *Physical Review A* **57**, 436 (1998).

[135] W. M. Itano, L. L. Lewis, and D. J. Wineland, Shift Of 2s1/2 Hyperfine Splittings Due To Blackbody Radiation, *Physical Review A* **25**, 1233 (1982).

[136] V. G. Pal'chikov, Y. S. Domnin, and A. V. Novoselov, Black-body radiation effects and light shifts in atomic frequency standards, *Journal Of Optics B-Quantum And Semiclassical Optics* **5**, S131 (2003).

[137] J. R. Mowat, Stark Effect In Alkali-Metal Ground-State Hyperfine-Structure, *Physical Review A* **5**, 1059 (1972).

[138] R. D. Haun and J. R. Zacharias, Stark Effect On Cesium-133 Hyperfine Structure, *Physical Review* **107**, 107 (1957).

[139] E. J. Angstmann, V. A. Dzuba, and V. V. Flambaum, Frequency shift of the cesium clock transition due to blackbody radiation, *Physical Review Letters* **97**, 040802 (2006).

[140] K. Beloy, U. I. Safronova, and A. Derevianko, High-accuracy calculation of the blackbody radiation shift in the Cs-133 primary frequency standard, *Physical Review Letters* **97**, 040801 (2006).

[141] L. Guidoni and P. Verkerk, Optical lattices: cold atoms ordered by light, *Journal Of Optics B-Quantum And Semiclassical Optics* **1**, R23 (1999).

[142] S. Friebel, C. D'Andrea, J. Walz, M. Weitz, and T. W. Hansch, CO2-laser optical lattice with cold rubidium atoms, *Physical Review A* **57**, R20 (1998).

[143] A. Brusch, R. Le Targat, X. Baillard, M. Fouche, and P. Lemonde, Hyperpolarizability effects in a Sr optical lattice clock, *Physical Review Letters* **96**, 103003 (2006).

[144] P. Lemonde and P. Wolf, Optical lattice clock with atoms confined in a shallow trap, *Physical Review A* **72**, 033409 (2005).

[145] R. Le Targat, Horloge a reseau optique au Strontium : une 2eme generation dhorloges a atomes froids, Ph.D. thesis, l'Observatoire de Paris, 2007.

[146] V. Letchumanan, P. Gill, E. Riis, and A. G. Sinclair, Optical Ramsey spectroscopy of a single trapped $^{88}Sr^{+}$ ion, *Physical Review A* **70**, 033419 (2004).

[147] L. Marmet and A. A. Madej, Optical Ramsey spectroscopy and coherence measurements of the clock transition in a single trapped Sr ion, *Canadian Journal Of Physics* **78**, 495 (2000).

[148] J. D. Miller, R. A. Cline, and D. J. Heinzen, Far-Off-Resonance Optical Trapping Of Atoms, *Physical Review A* **47**, R4567 (1993).

[149] J. E. Bjorkholm, Collision-Limited Lifetimes Of Atom Traps, *Physical Review A* **38**, 1599 (1988).

[150] S. Bali, K. M. O'Hara, M. E. Gehm, S. R. Granade, and J. E. Thomas, Quantum-diffractive background gas collisions in atom-trap heating and loss, *Physical Review A* **60**, R29 (1999).

[151] M. M. Boyd, T. Zelevinsky, A. D. Ludlow, S. Blatt, T. Zanon-Willette, S. M. Foreman, and J. Ye, Nuclear spin effects in optical lattice clocks, *Physical Review A* **76**, 022510 (2007).

[152] R. J. Rafac, B. C. Young, J. A. Beall, W. M. Itano, D. J. Wineland, and J. C. Bergquist, Sub-dekalhertz ultraviolet spectroscopy of $^{199}Hg^{+}$, *Physical Review Letters* **85**, 2462 (2000).

[153] F. Schmidt-Kaler, S. Gulde, M. Riebe, T. Deuschle, A. Kreuter, G. Lancaster, C. Becher, J. Eschner, H. Haffner, and R. Blatt, The coherence of qubits based on single Ca^{+} ions, *Journal Of Physics B-Atomic Molecular And Optical Physics* **36**, 623 (2003).

[154] E. D. Black, An introduction to Pound-Drever-Hall laser frequency stabilization, *American Journal Of Physics* **69**, 79 (2001).

[155] T. Day, E. K. Gustafson, and R. L. Byer, Sub-Hertz Relative Frequency Stabilization Of 2-Diode Laser-Pumped Nd-Yag Lasers Locked To A Fabry-Perot-Interferometer, *Ieee Journal Of Quantum Electronics* **28**, 1106 (1992).

[156] M. Zhu and J. L. Hall, Stabilization Of Optical-Phase Frequency Of A Laser System - Application To A Commercial Dye-Laser With An External Stabilizer, *Journal Of The Optical Society Of America B-Optical Physics* **10**, 802 (1993).

[157] D. S. Elliott, R. Roy, and S. J. Smith, Extra-Cavity Laser Band-Shape And Bandwidth Modification, *Physical Review A* **26**, 12 (1982).

[158] B. C. Young, F. C. Cruz, W. M. Itano, and J. C. Bergquist, Visible lasers with subhertz linewidths, *Physical Review Letters* **82**, 3799 (1999).

[159] A. D. Ludlow, X. Huang, M. Notcutt, T. Zanon-Willette, S. M. Foreman, M. M. Boyd, S. Blatt, and J. Ye, Compact, thermal-noise-limited optical cavity for diode laser stabilization at 1×10^{-15}, *Optics Letters* **32**, 641 (2007).

[160] L. Z. Duan and K. Gibble, Locking lasers with large FM noise to high-Q cavities, *Optics Letters* **30**, 3317 (2005).

[161] H. Stoehr, E. Mensing, J. Helmcke, and U. Sterr, Diode laser with 1 Hz linewidth, *Optics Letters* **31**, 736 (2006).

[162] A. Schoof, J. Grunert, S. Ritter, and A. Hemmerich, Reducing the linewidth of a diode laser below 30 Hz by stabilization to a reference cavity with a finesse above 10^5, *Optics Letters* **26**, 1562 (2001).

[163] C. W. Oates, F. Bondu, R. W. Fox, and L. Hollberg, A diode-laser optical frequency standard based on laser-cooled Ca atoms: Sub-kilohertz spectroscopy by optical shelving detection, *European Physical Journal D* **7**, 449 (1999).

[164] C. W. Oates, Z. W. Barber, J. E. Stalnaker, C. W. Hoyt, T. M. Fortier, S. A. Diddams, and L. Hollberg, in *Proc. 2007 Joint Mtg. IEEE Intl. Freq. Cont. Symp. and EFTF Conf.* (PUBLISHER, ADDRESS, 2007), pp. 1274–1277.

[165] M. Notcutt, L. S. Ma, J. Ye, and J. L. Hall, Simple and compact 1-Hz laser system via an improved mounting configuration of a reference cavity, *Optics Letters* **30**, 1815 (2005).

[166] S. A. Webster, M. Oxborrow, and P. Gill, Subhertz-linewidth Nd : YAG laser, *Optics Letters* **29**, 1497 (2004).

[167] C. Ishibashi, J. Ye, and J. L. Hall, in *Quantum Electronics and Laser Science Conference, 2002. QELS '02. Technical Digest. Summaries of Papers Presented at the* (PUBLISHER, ADDRESS, 2002).

[168] N. C. Wong and J. L. Hall, Servo Control Of Amplitude-Modulation In Frequency-Modulation Spectroscopy - Demonstration Of Shot-Noise-Limited Detection, *Journal Of The Optical Society Of America B-Optical Physics* **2**, 1527 (1985).

[169] M. Notcutt and J. L. Hall, unpublished (unpublished).

[170] P. R. Saulson, *Fundamentals of Interferometric Gravitational Wave Detectors* (World Scientific, ADDRESS, 1994).

[171] M. Notcutt, C. T. Taylor, A. G. Mann, and D. G. Blair, Temperature Compensation For Cryogenic Cavity Stabilized Lasers, *Journal Of Physics D-Applied Physics* **28**, 1807 (1995).

[172] P. Dub, A. A. Madej, J. E. Bernard, and A. D. Shiner, in *Time and Frequency Metrology Proc. SPIE, Vol. 6673, 667305*, edited by R. J. Jones (PUBLISHER, ADDRESS, 2007), Chap. High-resolution spectroscopy of the $^{88}Sr^{+}$ single ion optical frequency standard.

[173] J. Alnis, A. Matveev, N. Kolachevsky, T. Wilken, T. Udem, and T. W. Hansch, arXiv:0801.4199, submitted to Applied Physics B (unpublished).

[174] C. T. Taylor, M. Notcutt, E. K. Wong, A. G. Mann, and D. G. Blair, Measurement of the thermal expansion coefficient of an all-sapphire optical cavity, *Ieee Transactions On Instrumentation And Measurement* **46**, 183 (1997).

[175] S. Seel, R. Storz, G. Ruoso, J. Mlynek, and S. Schiller, Cryogenic optical resonators: A new tool for laser frequency stabilization at the 1 Hz level, *Physical Review Letters* **78**, 4741 (1997).

[176] J. P. Richard and J. J. Hamilton, Cryogenic Monocrystalline Silicon Fabry-Perot Cavity For The Stabilization Of Laser Frequency, *Review Of Scientific Instruments* **62**, 2375 (1991).

[177] V. Dattilo, The VIRGO suspensions: design and recent performance measurements, *Physics Letters A* **318**, 192 (2003).

[178] M. V. Plissi, C. I. Torrie, M. E. Husman, N. A. Robertson, K. A. Strain, H. Ward, H. Luck, and J. Hough, GEO 600 triple pendulum suspension system: Seismic isolation and control, *Review Of Scientific Instruments* **71**, 2539 (2000).

[179] P. F. Zhao, J. Luo, Z. B. Zhou, and J. X. Tang, Ultra-low frequency passive vertical vibration isolation system, *Science In China Series A-Mathematics Physics Astronomy* **42**, 660 (1999).

[180] L. S. Chen, J. L. Hall, J. Ye, T. Yang, E. J. Zang, and T. C. Li, Vibration-induced elastic deformation of Fabry-Perot cavities, *Physical Review A* **74**, 053801 (2006).

[181] T. Nazarova, F. Riehle, and U. Sterr, Vibration-insensitive reference cavity for an ultra-narrow-linewidth laser, *Applied Physics B-Lasers And Optics* **83**, 531 (2006).

[182] S. A. Webster, M. Oxborrow, and P. Gill, Vibration insensitive optical cavity, *Physical Review A* **75**, 011801 (2007).

[183] A. Di Virgilio *et al.*, Experimental upper limit on the estimated thermal noise at low frequencies in a gravitational wave detector, *Physical Review D* **76**, 122004 (2007).

[184] S. Rowan, J. Hough, and D. R. M. Crooks, Thermal noise and material issues for gravitational wave detectors, *Physics Letters A* **347**, 25 (2005).

[185] K. Numata, A. Kemery, and J. Camp, Thermal-noise limit in the frequency stabilization of lasers with rigid cavities, *Physical Review Letters* **93**, 250602 (2004).

[186] H. B. Callen and R. F. Greene, On A Theorem Of Irreversible Thermodynamics, *Physical Review* **86**, 702 (1952).

[187] T. Uchiyama *et al.*, Mechanical quality factor of a cryogenic sapphire test mass for gravitational wave detectors, *Physics Letters A* **261**, 5 (1999).

[188] D. F. Mcguigan, C. C. Lam, R. Q. Gram, A. W. Hoffman, D. H. Douglass, and H. W. Gutche, Measurements Of Mechanical Q Of Single-Crystal Silicon At Low-Temperatures, *Journal Of Low Temperature Physics* **30**, 621 (1978).

[189] K. Yamamoto *et al.*, Measurement of the mechanical loss of a cooled reflective coating for gravitational wave detection, *Physical Review D* **74**, 022002 (2006).

[190] G. M. Harry *et al.*, Titania-doped tantala/silica coatings for gravitational-wave detection, *Classical And Quantum Gravity* **24**, 405 (2007).

[191] M. Notcutt, L. S. Ma, A. D. Ludlow, S. M. Foreman, J. Ye, and J. L. Hall, Contribution of thermal noise to frequency stability of rigid optical cavity via Hertz-linewidth lasers, *Physical Review A* **73**, 031804 (2006).

[192] L. S. Ma, P. Jungner, J. Ye, and J. L. Hall, Delivering The Same Optical Frequency At 2 Places - Accurate Cancellation Of Phase Noise Introduced By An Optical-Fiber Or Other Time-Varying Path, *Optics Letters* **19**, 1777 (1994).

[193] J. C. Bergquist and et al., in *Proceedings of the International School of Physics "Enrico Fermi"*, edited by T. W. Hansch and M. Inguscio (North Holland, ADDRESS, 1992), p. 359.

[194] D. W. Allan, Time And Frequency (Time-Domain) Characterization, Estimation, And Prediction Of Precision Clocks And Oscillators, *Ieee Transactions On Ultrasonics Ferroelectrics And Frequency Control* **34**, 647 (1987).

[195] J. A. Barnes *et al.*, Characterization Of Frequency Stability, *Ieee Transactions On Instrumentation And Measurement* **IM20**, 105 (1971).

[196] S. Blatt, J. Thomsen, and et al., unpublished (unpublished).

[197] D. A. Jennings, K. M. Evenson, and D. J. E. Knight, Optical Frequency Measurements, *Proceedings Of The Ieee* **74**, 168 (1986).

[198] H. Schnatz, B. Lipphardt, J. Helmcke, F. Riehle, and G. Zinner, First phase-coherent frequency measurement of visible radiation, *Physical Review Letters* **76**, 18 (1996).

[199] D. J. Jones, S. A. Diddams, J. K. Ranka, A. Stentz, R. S. Windeler, J. L. Hall, and S. T. Cundiff, Carrier-envelope phase control of femtosecond mode-locked lasers and direct optical frequency synthesis, *Science* **288**, 635 (2000).

[200] K. W. Holman, Distribution of an Ultrastable Frequency Reference Using Optical Frequency Combs, Ph.D. thesis, University of Colorado, 2005.

[201] S. M. Foreman, Femtosecond Frequency Combs for Optical Clocks and Timing Transfer, Ph.D. thesis, University of Colorado, 2007.

[202] L. S. Ma, Z. Y. Bi, A. Bartels, L. Robertsson, M. Zucco, R. S. Windeler, G. Wilpers, C. Oates, L. Hollberg, and S. A. Diddams, Optical frequency synthesis and comparison with uncertainty at the 10^{-19} level, *Science* **303**, 1843 (2004).

[203] S. M. Foreman, K. W. Holman, D. D. Hudson, D. J. Jones, and J. Ye, Remote transfer of ultrastable frequency references via fiber networks, *Review Of Scientific Instruments* **78**, 021101 (2007).

[204] I. Courtillot, A. Quessada, R. P. Kovacich, A. Brusch, D. Kolker, J. J. Zondy, G. D. Rovera, and P. Lemonde, Clock transition for a future optical frequency standard with trapped atoms, *Physical Review A* **68**, 030501 (2003).

[205] A. Wallard, News from the BIPM - 2006, *Metrologia* **44**, 97 (2007).

[206] P. Dube, A. A. Madej, J. E. Bernard, L. Marmet, J. S. Boulanger, and S. Cundy, Electric quadrupole shift cancellation in single-ion optical frequency standards, *Physical Review Letters* **95**, 033001 (2005).

[207] M. V. Romalis and E. N. Fortson, Zeeman frequency shifts in an optical dipole trap used to search for an electric-dipole moment, *Physical Review A* **59**, 4547 (1999).

[208] E. A. Cummings, M. S. Hicken, and S. D. Bergeson, Demonstration of a 1-W injection-locked continuous-wave titanium : sapphire laser, *Applied Optics* **41**, 7583 (2002).

[209] C. Daussy *et al.*, Long-distance frequency dissemination with a resolution of 10^{-17}, *Physical Review Letters* **94**, 203904 (2005).

[210] F. Narbonneau, M. Lours, S. Bize, A. Clairon, G. Santarelli, O. Lopez, C. Daussy, A. Amy-Klein, and C. Chardonnet, High resolution frequency standard dissemination via optical fiber metropolitan network, *Review Of Scientific Instruments* **77**, 064701 (2006).

[211] S. C. Rashleigh and R. Ulrich, Polarization Mode Dispersion In Single-Mode Fibers, *Optics Letters* **3**, 60 (1978).

[212] S. M. Foreman, A. D. Ludlow, M. H. G. de Miranda, J. E. Stalnaker, S. A. Diddams, and J. Ye, Coherent optical phase transfer over a 32-km fiber with 1 s instability at 10^{-17}, *Physical Review Letters* **99**, 153601 (2007).

[213] W. M. Itano, J. C. Bergquist, J. J. Bollinger, J. M. Gilligan, D. J. Heinzen, F. L. Moore, M. G. Raizen, and D. J. Wineland, Quantum Projection Noise - Population Fluctuations In 2-Level Systems, *Physical Review A* **47**, 3554 (1993).

[214] G. Santarelli, C. Audoin, A. Makdissi, P. Laurent, G. J. Dick, and A. Clairon, Frequency stability degradation of an oscillator slaved to a periodically interrogated atomic resonator, *Ieee Transactions On Ultrasonics Ferroelectrics And Frequency Control* **45**, 887 (1998).

[215] G. J. Dick, in *Proceedings Precise Time and Time Interval Meeting* (PUBLISHER, ADDRESS, 1987), pp. 133–147.

[216] G. J. Dick, J. D. Prestage, C. A. Greenhall, and L. Maleki, in *Proceedings of the 22nd Precise Time and Time Interval Meeting* (PUBLISHER, ADDRESS, 1990), pp. 487–508.

[217] R. Legere and K. Gibble, Quantum scattering in a juggling atomic fountain, *Physical Review Letters* **81**, 5780 (1998).

[218] M. Kasevich and et al., international Conference on Laser Spectroscopy, 2007, poster presentation (unpublished).

[219] K. D. Bonin and V. V. Kresin, *Electric-Dipole Polarizabilities of Atoms, Molecules and Clusters* (World Scientific, ADDRESS, 1997).

[220] J. R. P. Angel and P. G. H. Sandars, Hyperfine Structure Stark Effect .I. Theory, *Proceedings Of The Royal Society Of London Series A-Mathematical And Physical Sciences* **305**, 125 (1968).

[221] V. D. Ovsiannikov, V. G. Pal'chikov, H. Katori, and M. Takamoto, Polarisation and dispersion properties of light shifts in ultrastable optical frequency standards, *Quantum Electronics* **36**, 3 (2006).

[222] S. G. Porsev, A. Derevianko, and E. N. Fortson, Possibility of an optical clock using the 6^1S_0-¿ 6^3P_0 transition in ^{171}Yb, ^{173}Yb atoms held in an optical lattice, *Physical Review A* **69**, 021403 (2004).

[223] W. Happer and B. S. Mathur, Effective Operator Formalism In Optical Pumping, *Physical Review* **163**, 12 (1967).

[224] N. L. Manakov, V. D. Ovsiannikov, and L. P. Rapoport, Atoms In A Laser Field, *Physics Reports-Review Section Of Physics Letters* **141**, 319 (1986).

[225] A. V. Taichenachev, V. I. Yudin, V. D. Ovsiannikov, and V. G. Palchikov, arXiv:0803.1039 (unpublished).

[226] A. V. Taichenachev, V. I. Yudin, C. W. Oates, C. W. Hoyt, Z. W. Barber, and L. Hollberg, Magnetic field-induced spectroscopy of forbidden optical transitions with application to lattice-based optical atomic clocks, *Physical Review Letters* **96**, 083001 (2006).

[227] D. B. Sullivan *et al.*, Primary atomic frequency standards at NIST, *Journal Of Research Of The National Institute Of Standards And Technology* **106**, 47 (2001).

[228] F. P. Dos Santos, H. Marion, S. Bize, Y. Sortais, A. Clairon, and C. Salomon, Controlling the cold collision shift in high precision atomic interferometry, *Physical Review Letters* **89**, 233004 (2002).

[229] K. Szymaniec, W. Chalupczak, E. Tiesinga, C. J. Williams, S. Weyers, and R. Wynands, Cancellation of the collisional frequency shift in caesium fountain clocks, *Physical Review Letters* **98**, 153002 (2007).

[230] S. J. J. M. F. Kokkelmans, B. J. Verhaar, K. Gibble, and D. J. Heinzen, Predictions for laser-cooled Rb clocks, *Physical Review A* **56**, R4389 (1997).

[231] Y. Sortais, S. Bize, C. Nicolas, A. Clairon, C. Salomon, and C. Williams, Cold collision frequency shifts in a Rb-87 atomic fountain, *Physical Review Letters* **85**, 3117 (2000).

[232] D. E. Chang, J. Ye, and M. D. Lukin, Controlling dipole-dipole frequency shifts in a lattice-based optical atomic clock, *Physical Review A* **69**, 023810 (2004).

[233] K. Gibble and B. J. Verhaar, Eliminating Cold-Collision Frequency-Shifts, *Physical Review A* **52**, 3370 (1995).

[234] M. W. Zwierlein, Z. Hadzibabic, S. Gupta, and W. Ketterle, Spectroscopic insensitivity to cold collisions in a two-state mixture of fermions, *Physical Review Letters* **91**, 250404 (2003).

[235] S. Gupta, Z. Hadzibabic, M. W. Zwierlein, C. A. Stan, K. Dieckmann, C. H. Schunck, E. G. M. van Kempen, B. J. Verhaar, and W. Ketterle, Radio-frequency spectroscopy of ultracold fermions, *Science* **300**, 1723 (2003).

[236] R. Santra, K. V. Christ, and C. H. Greene, Properties of metastable alkaline-earth-metal atoms calculated using an accurate effective core potential, *Physical Review A* **69**, 042510 (2004).

[237] S. G. Porsev and A. Derevianko, High-accuracy relativistic many-body calculations of van der Waals coefficients C-6 for alkaline-earth-metal atoms, *Physical Review A* **65**, 020701 (2002).

[238] P. G. Mickelson, Y. N. Martinez, A. D. Saenz, S. B. Nagel, Y. C. Chen, T. C. Killian, P. Pellegrini, and R. Cote, Spectroscopic determination of the s-wave scattering lengths of ^{86}Sr and ^{88}Sr, *Physical Review Letters* **95**, 223002 (2005).

[239] J. Weiner, V. S. Bagnato, S. Zilio, and P. S. Julienne, Experiments and theory in cold and ultracold collisions, *Reviews Of Modern Physics* **71**, 1 (1999).

[240] G. K. Brennen, I. H. Deutsch, and P. S. Jessen, Entangling dipole-dipole interactions for quantum logic with neutral atoms, *Physical Review A* **6106**, 062309 (2000).

[241] G. K. Brennen, C. M. Caves, P. S. Jessen, and I. H. Deutsch, Quantum logic gates in optical lattices, *Physical Review Letters* **82**, 1060 (1999).

[242] I. H. Deutsch, G. K. Brennen, and P. S. Jessen, Quantum computing with neutral atoms in an optical lattice, *Fortschritte Der Physik-Progress Of Physics* **48**, 925 (2000).

[243] G. K. Brennen, I. H. Deutsch, and C. J. Williams, Quantum logic for trapped atoms via molecular hyperfine interactions, *Physical Review A* **65**, 022313 (2002).

[244] R. Stock, I. H. Deutsch, and E. L. Bolda, Quantum state control via trap-induced shape resonance in ultracold atomic collisions, *Physical Review Letters* **91**, 183201 (2003).

[245] D. Hayes, P. S. Julienne, and I. H. Deutsch, Quantum logic via the exchange blockade in ultracold collisions, *Physical Review Letters* **98**, 070501 (2007).

[246] B. J. Verhaar, J. M. V. A. Koelman, H. T. C. Stoof, O. J. Luiten, and S. B. Crampton, Hyperfine Contribution To Spin-Exchange Frequency-Shifts In The Hydrogen Maser, *Physical Review A* **35**, 3825 (1987).

[247] E. Tiesinga, B. J. Verhaar, H. T. C. Stoof, and D. Vanbragt, Spin-Exchange Frequency-Shift In A Cesium Atomic Fountain, *Physical Review A* **45**, R2671 (1992).

[248] D. M. Harber, H. J. Lewandowski, J. M. McGuirk, and E. A. Cornell, Effect of cold collisions on spin coherence and resonance shifts in a magnetically trapped ultracold gas, *Physical Review A* **66**, 053616 (2002).

[249] M. O. Oktel, T. C. Killian, D. Kleppner, and L. S. Levitov, Sum rule for the optical spectrum of a trapped gas, *Physical Review A* **65**, 033617 (2002).

[250] M. O. Oktel and L. S. Levitov, Collective dynamics of internal states in a Bose-Einstein gas, *Physical Review A* **65**, 063604 (2002).

[251] B. DeMarco and D. S. Jin, Exploring a quantum degenerate gas of fermionic atoms, *Physical Review A* **58**, R4267 (1998).

[252] P. Naidon and P. S. Julienne, private communication (unpublished).

[253] P. J. Martin, B. G. Oldaker, A. H. Miklich, and D. E. Pritchard, Bragg Scattering Of Atoms From A Standing Light-Wave, *Physical Review Letters* **60**, 515 (1988).

[254] J. W. Farley and W. H. Wing, Accurate Calculation Of Dynamic Stark Shifts And Depopulation Rates Of Rydberg Energy-Levels Induced By Blackbody Radiation - Hydrogen, Helium, And Alkali-Metal Atoms, *Physical Review A* **23**, 2397 (1981).

[255] T. Rosenband, W. M. Itano, P. O. Schmidt, D. B. Hume, J. C. J. Koelemeij, J. C. Bergquist, and D. J. Wineland, arXiv:physics/0611125 (unpublished).

[256] M. J. Ballico, Modelling of the effective emissivity of a graphite tube black body, *Metrologia* **32**, 259 (1996).

[257] S. Schmid, G. Thalhammer, K. Winkler, F. Lang, and J. H. Denschlag, Long distance transport of ultracold atoms using a 1D optical lattice, *New Journal Of Physics* **8**, 159 (2006).

[258] T. L. Gustavson, A. P. Chikkatur, A. E. Leanhardt, A. Gorlitz, S. Gupta, D. E. Pritchard, and W. Ketterle, Transport of Bose-Einstein condensates with optical tweezers, *Physical Review Letters* **88**, 020401 (2002).

[259] T. Rosenband *et al.*, Frequency Ratio of Al^+ and Hg^+ Single-Ion Optical Clocks; Metrology at the 17th Decimal Place, *Science* **319**, 1808 (2008).

[260] W. D. Lee, J. H. Shirley, and R. E. Drullinger, in *Proceedings of the IEEE International Frequency Control Symposium* (PUBLISHER, ADDRESS, 1997).

[261] W. D. Lee, J. H. Shirley, J. P. Lowe, and R. E. Drullinger, The Accuracy Evaluation Of Nist-7, *Ieee Transactions On Instrumentation And Measurement* **44**, 120 (1995).

[262] E. Peik, T. Schneider, and C. Tamm, Laser frequency stabilization to a single ion, *J. Phys. B: At. Mol. Opt. Phys* **39**, 145 (2006).

[263] C. Degenhardt, T. Nazarova, C. Lisdat, H. Stoehr, U. Sterr, and F. Riehle, Influence of chirped excitation pulses in an optical clock with ultracold calcium atoms, *Ieee Transactions On Instrumentation And Measurement* **54**, 771 (2005).

[264] S. Blatt *et al.*, New Limits on Coupling of Fundamental Constants to Gravity Using ^{87}Sr Optical Lattice Clocks, *Physical Review Letters* **100**, 140801 (2008).

[265] W. H. Oskay *et al.*, Single-atom optical clock with high accuracy, *Physical Review Letters* **97**, 020801 (2006).

[266] G. K. Campbell and et al., manuscript in preparation, to be submitted Metrologia (unpublished).

[267] R. Santra, E. Arimondo, T. Ido, C. H. Greene, and J. Ye, High-accuracy optical clock via three-level coherence in neutral bosonic ^{88}Sr, *Physical Review Letters* **94**, 173002 (2005).

[268] T. Zanon-Willette, A. D. Ludlow, S. Blatt, M. M. Boyd, E. Arimondo, and J. Ye, Cancellation of stark shifts in optical lattice clocks by use of pulsed Raman and electromagnetically induced transparency techniques, *Physical Review Letters* **97**, 233001 (2006).

[269] T. Zelevinsky, M. M. Boyd, A. D. Ludlow, S. M. Foreman, S. Blatt, T. Ido, and J. Ye, Optical clock and ultracold collisions with trapped strontium atoms, *Hyperfine Interactions* **174**, 55 (2007).

[270] T. Zelevinsky, S. Kotochigova, and J. Ye, Precision Test of Mass-Ratio Variations with Lattice-Confined Ultracold Molecules, *Physical Review Letters* **100**, 043201 (2008).

[271] D. Meiser, J. Ye, and M. J. Holland, arXiv:0707.3834, to be published in Phys. Rev. Lett. (unpublished).

[272] T. C. Killian, T. Pattard, T. Pohl, and J. M. Rost, Ultracold neutral plasmas, *Physics Reports-Review Section Of Physics Letters* **449**, 77 (2007).